Atomistics of Defect Nucleation and Mobility: Dislocations and Twinning

by

Jinpeng Chang

Submitted to the Department of Nuclear Engineering
in partial fulfillment of the requirements for the degree of

Doctor of Philosophy of Nuclear Engineering

at the

MASSACHUSETTS INSTITUTE OF TECHNOLOGY

June 2003

Author . . . .
Department of Nuclear Engineering
February 10, 2003

Certified by. . . . .
Sidney Yip
Professor of Nuclear Engineering
Thesis Supervisor

Read by . . . .
Sow-Hsin Chen
Professor of Nuclear Engineering
Thesis Reader

Read by . . . .
Ali S. Argon
Professor of Mechanical Engineering
Thesis Reader

Accepted by . . . .
Jeffrey A. Coderre
Chairman, Department Committee on Graduate Students

Atomistics of Defect Nucleation and Mobility:
Dislocations and Twinning

by

Jinpeng Chang

Abstract

Multiscale materials modeling has emerged in recent years as a significant concept and the only viable approach to understand the mechanical response of materials by linking modeling research at different length scales and time scales, including quantum mechanics, atomistics modeling, mesoscale modeling and continuum modeling together. The role that atomistic modeling plays is important and indispensable in that it can generate understanding of the physics and pass this mechanistic understanding as well as important parameters to higher level simulations. This thesis presents theories and simulations of defect nucleation and mobility in BCC transition metal molybdenum using atomistic methods, with the two primary defects of interest being dislocations and deformation twinning, and emphasis on the atomistic mechanisms and measures. The contributions presented in the thesis may be regarded as advances in both methods development and mechanistic understanding of dislocation mobility and twinning nucleation.

For atomistic studies of dislocations in a simulation cell of finite size, new methods have been derived to (1) calculate the atomic displacement field under PBC and generate atomic dislocation configuration from this displacement field; (2) quantify artificial image effect for a dislocation moving within the periodic cell and optimize geometry of simulation cell to minimize such effects. These methodological breakthroughs serve as the basis for atomistic studies of dislocations and are used repeatedly in this thesis.

To understand the complex plasticity behavior of BCC metal molybdenum, we need to first understand the most fundamental problem of core structure and lattice resistance of straight dislocations before considering more complicated structures including kinks, jogs, junctions, etc. In this thesis, we examine the two major types of dislocations that are of primary interest in BCC molybdenum: screw dislocations, which is the major plasticity carrier at low temperatures, and edge dislocations, which become important at elevated temperatures. For screw dislocations, the issue of whether core is polarized or not is explored by a static calculation of core structure for the first time by a tight-binding potential. The screw core structure is determined to be non-polarized; however, the magnitude of Peierls stress, which

is a measure of the lattice resistance to dislocation motion and is calculated accurately using a local-driving-force method in this thesis, remains rather high despite of the non-polarized core, suggesting that core polarization is a secondary and less important effect compared to core planarity. For edge dislocations in molybdenum, the core structure and Peierls stress is calculated using a Finnis-Sinclair potential and it is shown that edge dislocation in Mo has a planar core structure and a core width of approximately 11Å, is indeed very mobile and has a Peierls stress of only 25 MPa, after correction for image effects due to boundary conditions. This new result is consistent with experimental observations of high mobility of edge dislocations and clearly rejects the proposal of kink mechanisms operating on edge dislocations that arose in the literature as a result of previous inaccurate Peierls stress calculations yielding an unrealistically high value of 700 MPa. These static calculations on core structure and Peierls stress for edge and screw dislocations clarifies two fundamental issues and is a major step towards understanding of the complex plasticity behavior of BCC metals.

Furthermore, the dynamics of dislocations under stress is examined. The motion of edge dislocations is simulated at a range of temperatures and stresses. At stresses above Peierls stress and below $500MPa$, dislocation mobility is controlled mainly by phonon drag which is evident from the linear relation between stress and velocity as well as the decreasing velocity with increasing temperature. At stresses above $500MPa$, relativistic effect appears and the linear relation between stress and velocity is replaced by an asymptotic behavior.

The above studies focus on the atomistics of dislocation motion in molybdenum; however, deformation twinning, as the alternative plastic deformation mechanism, deserves equal amount of attention and is studied atomistically in this thesis. Homogeneous twin nucleation and growth in molybdenum is examined atomistically for the first time in 3D molecular dynamics (MD) simulations, where the geometry of the nucleated twin is determined and the growth of the twin is analyzed. To understand the twin nucleation and growth phenomena better in a low-dimensional space, a physically-motivated 1D atomic chain model is developed. Using the 1D chain model, it is found that the minimum twin structure has two layers instead of three as found in previous pair-potential calculations. Furthermore, the model provides simple energy measures for the competition between dislocation-based slip and twinning, describes the minimum-energy path leading to twin embryo as well as its bifurcation from the slip path, and allows us to study the 4-stage wave-steepening process that is inherent to the nucleation of twin embryos and any other homogeneous defect nucleation phenomena.

Thesis Supervisor: Sidney Yip
Title: Professor of Nuclear Engineering

Acknowledgments

This is an ideal place for me to express my gratefulness to the people who helped me a lot during my five years of PhD study at MIT.

I want to first thank Professor Sidney Yip, my mentor and supervisor, for helping me during the last five years on every small step I needed to make as I gradually become more mature and experienced both as an individual and as a researcher. I was lucky to join the group five years ago upon arrival at MIT and today I feel even more so to have him as my Thesis advisor. I am grateful for having the opportunity to work with him, and for spending the best part of my life in our friendly and exciting group that he brought together.

I owe my special thanks to Dr. Vasily Bulatov, whom I have been working with in my first year at MIT. He guided me in my very earliest stage of scientific research with great patience and encouragement. Although he left the group and joined LLNL one year later, I still benefited a lot by consulting him for his expert opinions on dislocation modeling.

I want to thank Professor Ali Argon and Sow-hsin Chen for serving on my thesis committee, for the knowledge that I have learned from them both in and out of classes, and for their tremendous help as a source of consultation during my Ph.D. research.

I would like to thank my colleagues, Dr. Ju Li, Dr. Wei Cai, and Dr. Dongyi Liao, for the support and happiness they bring to me constantly during my five years in the group.

I would also like to thank my collaborators, Dr. Caizhuang Wang from Ames Lab, Dr. Dongsheng Xu from Chinese Institute of Metals Research, Dr. Shigenobu Ogata from Osaka University, Japan, and Dr. Ting Zhu from MIT, for their friendly exchange and for their constant support offered during my thesis research.

My research has been supported by Lawrence Livermore National Laboratory under an ASCI-Level 2 project. Without them this work would have be impossible. I would also like to thank AFOSR who provided funding in the last year of this

research.

I dedicate this thesis my beloved wife, Meng Yan, for her love and support throughout the years.

Contents

List of Figures

14

15

17

19

List of Tables

Chapter 1

Introduction

1.1   Background

The world that we live in is made of materials. Everywhere we look we see products made from materials of different kinds: metals, semiconductors, ceramics, plastics, composites. All of these have been made possible by various developments in materials science and engineering. As a matter of fact, materials have the milestones of progress during the evolution of mankind. All civilizations have been categorized by the materials they used: the Stone Age, the Bronze Age, the Iron Age, etc. (see Figure 1-1.) From metal making in the ancient times to the development of steel and aluminum alloys that made the industrial age possible, from the discoveries of plastics and other polymers in the early 20th century to the invention of semiconductors in the middle of the 20th century that created worldwide industrial developments in communications, computers and consumer electronics, each breakthrough in materials science has had a tremendous impact on human civilization, just like the old saying goes, *a grain of sand can change the world.* As we strive to live a better life and build a better world, constant advances and inventions in materials science is a must.

Throughout its history, materials science has been largely an experimental science. However, with the introduction of computers and the exponential growth of
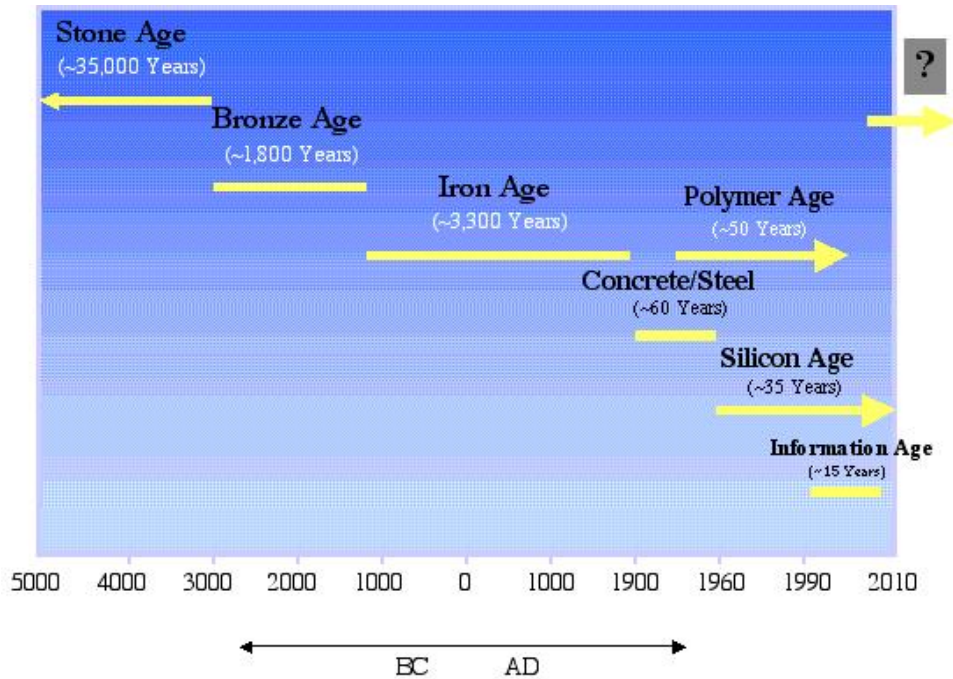
Figure 1-1: Evolution of mankind. Each stage of civilization is categorized by the material they use.

CPU speed ever since, computer modeling and simulation of large systems have been made feasible and have found wide applications in many important fields, such as weather forecasting, logistic optimizations, DNA sequencing and genomic analyses, etc. The same goes true for the materials science research field. Computational materials science quickly emerged as a new research field by itself. Different from the traditional trial-and-error approach in designing new materials with desired properties, computational materials science applies high performance computing to materials research and seeks both understanding of materials behavior and predicting power in a wider range of parameter space than previously available to achieve the same goal – to design new material with improved performance. This is still a young field and there is still only a limited number of researchers in this field; however, it has been in constant growth as it becomes more accepted both by academic researchers and by industrial users, and as powerful computers become more easily available.

The goal of computational materials science is towards design of new materials of

desired properties. It is a theoretical approach, whose primary function is two-fold:

(1) To explain and suggest experiments.

Many problems in materials science are too complex for analytical methods to be very useful. Computational materials science provides the theory that is needed to understand current experiments and help plan new experiments. This is what we refer to as "understanding". Computer modeling is a powerful tool to probe material behavior under various conditions and it can provide insight into the controlling mechanisms that are responsible for material properties of interest.

The future of computational materials science in explaining experiments largely depend on the improvements on both the computing power and the computational models that is used. For the former aspect, current available computer processing speed and memory on a typical shared-memory cluster or Beowulf PC cluster (32 or more processors, 1-2 gigabyte per processor) are large enough to do many computations that were simply impossible in the past, but they are still far from large enough to do large computations with high accuracy that is required in many problems. For example, density functional theory (DFT) calculations can now only handle calculations of up to several hundred atoms and the situation would get only marginally better with higher computing speed and larger memory since computing resources required by DFT calculations scale as $\sim N^3$. For less accurate methods such as molecular dynamics (MD) or dislocation dynamics (DD), the scaling situation is better but the thirst for more computing power does not change much. For the latter aspect, the success of the model in explaining experimental results largely relies on how much the modeled system deviated from the real experimental conditions. To make the connection between theoretical calculations and experimental results, one must improve the model to better resemble the real condition. However, theoretical models typically have various constraints that one can not avoid such as boundary conditions, size constraints, time-scale constraints, etc. It then become the researcher's task to try to capture the essence of the problem by using appropriate models under these constraints.

Macroscopic
(PDE)

Mesoscopic
(KMC)

Atomistic
(MD/MC)

Electronic
Structure
(first principle)

length[A]

1 $\qquad$ 10^2 $\qquad$ 10^4 $\qquad$ 10^7

understanding
and prediction

applications
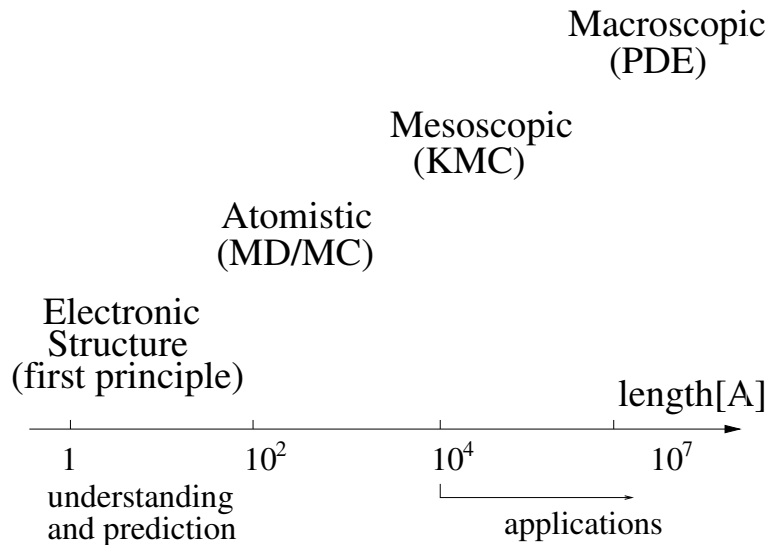
Figure 1-2: Different length scale of modeling methods.

(2) To predict material behavior and replace experiments with modeling.

Once the validity of a computer model is unequivocally demonstrated, one can progress to replace some experiments with models. Tremendous savings in both time and money can be achieved once this stage is reached. For industrial users, this will hopefully speed up the R&D process to develop new materials as well as cut down the associated cost; this is the main reason why we see a constant growth in industrial interest and presence in material modeling research. Comparing to the first function as we mentioned above ("understanding"), we refer to this function as "prediction" and it is even more ambitious than the first one. However, this two aspects are closely connected and "prediction" can only come after a good "understanding" of the physics behind the problem that we are trying to solve.

It is a major breakthrough in material science and engineering that computer modeling is now capable of providing valuable help in reducing experimental efforts, shortening product development cycles and offering deeper fundamental understandings. Attracting talents from diverse backgrounds (physics, mechanical engineering, chemical engineering, computer science ...), the young field of computational materi-

als science has shown a great prospect and is growing fast. Although computational materials experimental validation of material modeling and simulations will remain a necessity in the foreseeable future and it should not be expected that computers would eventually make materials developments in the laboratory obsolete, constant developments in the modeling concepts and ideas as well as the computing power will surely bring the field of computational materials science forward in an unprecedented pace.

Computer modeling of materials is mainly limited by the length and time scales of the processes that can be studied. As shown in Figure 1-2, different modeling techniques can handle only a specific range of length scale. *Ab initio* method, also called first principles, is the most accurate method of all because it uses quantum mechanics of electrons to describe interactions between atoms; however, it is very expensive computationally and can only handle up to several hundred atoms with computing capabilities as of today. Molecular Dynamics (MD) method uses semi-empirical potential models to describe atomic interactions and therefore can model systems with up to billion atoms and therefore covers a length scale of approximately $10^1 - 10^3$ Å. In short, microscopic methods are more accurate in describing the material responses but is severely limited by available time and length scale. On the other hand, the mesoscopic and macroscopic methods are coarse-grained methods and are less accurate, but they make larger length and time scales accessible and are much closer to real applications.

If only the theories and models at different scales can be connected and macroscopic material behavior be understood through fundamental physics, the challenge to understand the immense complexity of real material behavior can be answered. This naturally leads to the multiscale approach [1]. Multiscale materials modeling aims to develop improved description of material behavior through the incorporation of information about materials structures and processes from various length and time scales as necessary. Many important problems could be attacked under this multiscale scheme efficiently. Modeling materials strength against deformation and failure is one
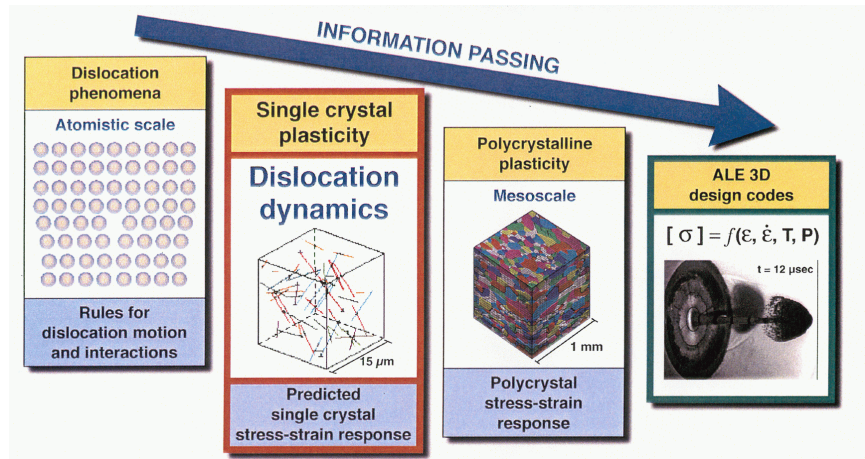
Figure 1-3: Multiscale Modeling of Material Strength. Courtesy of Lawrence Livermore National Laboratory.

of the most prominent problems that hopefully can be addressed with this multiscale approach.

Mechanical strength of materials not only differs from one material to another, but more importantly, is sensitively dependent on material microstructures. In crystalline materials, the microstructures are made up of all kinds of lattice defects: point defects, dislocations, twins, grain boundaries, voids, cracks, etc. The deformation behavior of each individual type of defect and how they interact with each other during the deformation process have to be understood from the atomistic scale before this information is passed onto larger scale models towards developing a constitutive model of material strength [2]. As shown in Figure 1-3, multiscale strength modeling links models from different length scales and time scales together. True physics is preserved by information passing from the lower length and time scale models to higher length and time scale models, and it can provide a mechanistic-informed strength model with predicting power.

The role that atomistic modeling plays in the grand picture of multiscale modeling is important and indispensable. It can generate understanding of the physics and pass this mechanistic understanding as well as important parameters to higher-level

simulations. Without this understanding and parameters, the higher-level simulations would become buildings without base and will not be able to reflect the true physics, therefore lacking of predictive power is guaranteed. However, producing physical understanding from atomistic models is difficult due to several reasons: (1) The atomistic model may not be accurate enough to capture the physics; (2) More accurate methods, though, is computationally expensive and can only treat highly limited systems, sometimes their results contain artifacts of the limited size; (3) Due to the large dimension involved, in order to comprehend the generated results and translate it into a physical picture that human beings can comprehend and make use of, it is often necessary to reduce the problem size to either a small number of degrees of freedom (DOF) or small number of order parameters that is a function of the general coordinations yet captures the essence of the problem, and this is not a easy task.

1.2 Problem Statement

This thesis presents theories and simulations of defect nucleation and mobility in BCC transition metal molybdenum using atomistic methods, with the two primary defects of interest being dislocations and deformation twinning, and emphasis on the atomistic mechanisms and measures.

There are two important types of dislocations in Mo: screw dislocation controls the low temperature plasticity while edge dislocations are important at high temperatures. Despite the amount of research on dislocations in bcc metals, there are still a number of unresolved issues and inconsistencies that have not been properly addressed in previous studies. An example is that the Peierls values reported in the literature are often higher (in some cases lower) than their true values, e.g., previous calculations in the literature yielded a Peierls stress of 700 MPa for edge dislocations [3], which is against the experimental observation that edges are highly mobile even at very low stresses, and kink mechanism was proposed to reconcile the obvious discrepancy. Another example is the screw dislocation core structure polarization

33

controversy. These controversies in core structure and Peierls stress hinder the true physical understanding of the plasticity problem and shall be resolved in an accurate and reliable manner by designing more accurate simulation models and improving simulation methods.

While the above discussion concerns property of dislocations at $0K$, it is also important to understand dislocation mobility under given temperature and stress conditions. Due to various reasons (simulation settings, computational constraints, etc.), not much has been done in this area except for the early work of Baskes and Clapp [4, 5] and recent work of Gumbsch and Gao [6]. Yet one has to realize that such work will not only provide valuable insights into the dynamic behavior of dislocations but can also provide larger-scale modeling, e.g., dislocation dynamics, with parameters that can not be acquired otherwise, e.g., drag coefficients. This is another area calling for exploration.

On the other hand, deformation twinning, as an alternative plastic deformation mode, is relatively under-studied and not well understood when compared with dislocations. The competition between twinning and dislocation-based slip is not yet understood atomistically, and the atomistic details of twin nucleation and migration are still unclear. It is evident that we need to acquire understanding to these fundamental phenomena from atomistic models.

The above mentioned problems serve as motivations and objectives for this thesis work and will be discussed and treated in detail in the following chapters.

In this thesis, we describe five related contributions which may be regarded as advances in both methods development and mechanistic understanding of dislocation mobility and twinning nucleation.

(1) New methods have been derived to: (a) calculate the atomic displacement field under PBC and generate atomic dislocation configuration from this displacement field; (b) quantify artificial image effect for a dislocation moving within the periodic cell and optimize geometry of simulation cell to minimize such effects.

(2) The core structure and Peierls stress of screw dislocations in BCC molybdenum, which is a major plasticity carrier at low temperatures, is calculated for the first time using a tight-binding potential and the results are compared with semi-empirical potentials where core polarization and its influence on Peierls stress is examined.

(3) Core structure and Peierls stress for edge dislocations in BCC molybdenum is calculated using Finnis-Sinclair potential and it is shown that edge dislocation in Mo which has a planar core structure and a core width of approximately 10Å, is indeed very mobile and has a Peierls stress of only 25 MPa. This clearly rejects the proposal of kink mechanisms operating on edge dislocations that arose in the literature because of previous inaccurate Peierls stress calculations yielding an unrealistically high value of $400 - 700$ MPa.

(4) The motion of edge dislocations is simulated at a range of temperatures and stresses. At stresses above Peierls stress and below ~ 500MPa, dislocation mobility is controlled mainly by phonon drag which is evident from the linear relation between stress and velocity, the decreasing velocity with increasing temperature, as well as the constant drag coefficient. At stresses above 500MPa, relativistic effect appears. The linear relation between stress and velocity is broken, and drag coefficient increases approximately linearly.

(5) The mechanism of twin nucleation and growth is examined in 3D molecular dynamics (MD) settings and then a physically-motivated 1D atomic chain model is developed and it provides simple energy measures for the competition between dislocation-based slip and twinning, describes the transition path leading to twin embryo as well as its bifurcation from the slip path, and allows us to study the 4-stage wave-steepening process that is inherent to the nucleation of twin embryos.

The thesis is structured exactly in the same order as the above contributions.

We start our discussion in Chapter 2 by first introducing the methodologies of creating dislocations under PBC and correctly treating image effect due to PBC. These methodologies serve as the technical foundation for the atomistic studies on

dislocations that follow. Chapter 3 and 4 presents my results on core structure and Peierls stress for edge and screw dislocations in molybdenum respectively. Chapter 5 deals with dynamic motion of edge dislocations. Chapter 6 presents the very recent work of mine on atomistic analysis of deformation twinning in Mo. It contains two main sections – the MD analysis part and the 1-D Chain Model part, whereas a four-stage strain localization model is also presented. I found great joy in writing this chapter and recommend readers who are short of time to skip the previous chapters and read this one. Chapter 7 summarizes the thesis and discusses the future work directions beyond single defect nucleation and mobility.

Chapter 2

Dislocations under Periodic Boundary Conditions

In this chapter, we discuss one of the most important methodological issues in atomistic modeling of dislocations - how to treat boundary conditions and its effects. We present recent contributions on the study of effect of one specific boundary condition, periodic boundary conditions (PBC), on modeling dislocation core energy and mobility.

In the first section, we will introduce the problem of conditional convergence in modeling of dislocations under PBC and present our solution. In the next three sections, we present three applications of the method: (1) calculate the atomic displacement field under PBC, which is directly used to prepare arbitrary dislocation configurations; (2) quantify artificial image energies in dislocation simulations and arrive at an accurate core energy; (3) quantify artificial image energy barrier for a dislocation moving within the periodic cell, where such barriers for edge and screw dipole configurations under PBC have been evaluated for different cell geometries and optimal aspect ratio of the cell has been identified to minimize the artificial energy barrier.

This work has been published and more detailed discussions can be found in

[7, 8, 9].

2.1 Conditional Convergence and the Solution

In atomistic modeling studies, because of the discreteness (atoms) and finiteness (limited number of atoms that can be simulated), some type of boundary condition has to be used. Popular boundary conditions include periodic boundary conditions (PBC), fixed boundary conditions, and more recently, atomistic-continuum boundaries. When using one of these boundary conditions, one important question one must ask before getting any modeling results and interpreting the results is: what effects does the boundary condition have on the modeling results and can we quantify it? Unfortunately, this question often does not receive its share of attention due to a popular view held by many researchers that as long as the simulation cell size is big enough, the boundary effect should diminish and can be ignored. As will be proved once and again in this chapter and Chapter 3, this argument is wrong. For atomistic modeling of dislocations, boundary effect can lead to artificial results that significantly deviates from true numbers.

In this study, we focus on one specific type of boundary condition: PBC. It has many advantages: (1) PBC makes it possible to preserve the translational symmetry of crystal lattice with a finite cell size; (2) PBC can be used to avoid surface effects; (3) PBC is simple to implement. Because of these merits, it is widely used in Density Functional Theory (DFT) and Molecular Dynamics (MD) calculations as well as Dislocation Dynamics (DD). However, as with any other boundary conditions, PBC introduces artificial things to the model. What it does is that it introduces infinite number of identical images of the simulation supercell and the artificial effect due to these images must be quantified.
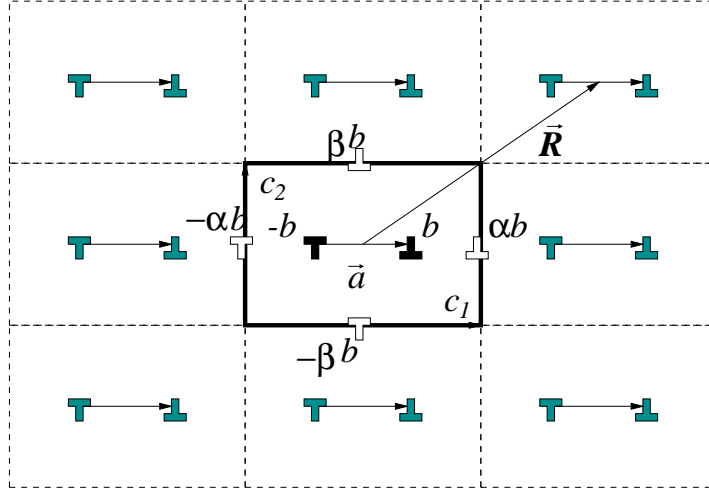
Figure 2-1: Schematic of an atomistic simulation cell (solid rectangle) containing a dislocation dipole with Burgers vector $\pm\vec{b}$ and separated by $\vec{a}$ under PBC along $\vec{c}_1$, $\vec{c}_2$ and $\vec{c}_3$ (out of plane). To facilitate calculation of the image energy, we introduce "ghost" dislocations (in white) at the cell boundaries.

2.1.1 PBC and Conditional Convergence

Let us consider an atomistic simulation supercell that contains a dislocation dipole. As shown in Figure 2-1, the simulation supercell is periodic along $\vec{c}_1, \vec{c}_2$ and $\vec{c}_3$ directions ($\vec{c}_3$ is normal to paper). The dislocation lines are parallel to $\vec{c}_3$. The Burgers vectors of the dislocation dipole are $\vec{b}$ and $-\vec{b}$, respectively; the separation between the dipole is $\vec{a}$.

The stress field in the PBC cell is the sum of the stress fields of the primary dipole in the simulation supercell and the infinite number of image dipoles located on a periodic lattice characterized by $\vec{c}_1$ and $\vec{c}_2$:

$$\sigma_{ij}(\vec{r}) \equiv \sum_{\vec{R}} \sigma_{ij}^{dipole}(\vec{r} - \vec{R}) \ , \tag{2.1}$$

where $\vec{r}$ specifies the position of the evaluated point, $\vec{R}$ specifies positions of the image dipoles with respect to the primary dipole, and the summation runs over the two-dimensional lattice $\vec{R} = n_1 \vec{c}_1 + n_2 \vec{c}_2$ (n_1, n_2 are integers and $-\infty < n_1, n_2 < \infty$).

Since the stress field of a straight dislocation decays as R^{-1} while the stress field of a dislocation dipole decays as R^{-2}, the sum of stress fields of the image dipoles by their absolute values diverges logarithmically and therefore the series in Eq. 2.1 is not absolutely convergent.

$$\sum_{\vec{R}} |\sigma_{ij}^{dipole}(\vec{r} - \vec{R})| \sim \int^{\infty} \frac{1}{R^{-2}} \cdot 2\pi R \cdot dR \sim \int^{\infty} \frac{dR}{R} \sim \infty \qquad (2.2)$$

This does not mean the summation in Eq. 2.1 does not converge; indeed it does converge due to partial cancellations of terms with opposite signs. Therefore, the summation in Eq. 2.1 converges conditionally, i.e., for any real number c, there is a rearrangement of the summation series such that the new resulting series will converge to c. In other words, by changing summation ordering, e.g., choosing different summation boundary shapes, the straightforward (naive) summation will converge to different numbers. Therefore, the naive summation cannot provide a definite solution for the true stress field in the periodic cell.

Shown in Figure 2-2 is an example of such conditional convergence behavior when calculating stress field at $(x = 0.1L, y = 0.5L)$ for an edge dislocation dipole located at $(x = 0.25L, y = 0.25L)$ and $(x = 0.75L, y = 0.75L)$, respectively, in a cell with dimensions $c_1 = c_2 = L$. The stress is plotted in units of $\frac{b \cdot G}{2\pi(1-\nu)}$. We show results for three different summation orderings: summation by expanding concentric circles, by expanding ellipses, and by expanding rectangles. Each summation ordering results in a converged series, but the value they converge to are wildly different.

The same conditional-convergence problem occurs in the evaluation of strain field because stress and strain are linked by the elastic constants. Similarly, summation of displacement field whose derivative is strain, is also conditional convergent.

We will now show the interaction energy between the primary dipole and the image dipoles also has the conditional-convergence problem.
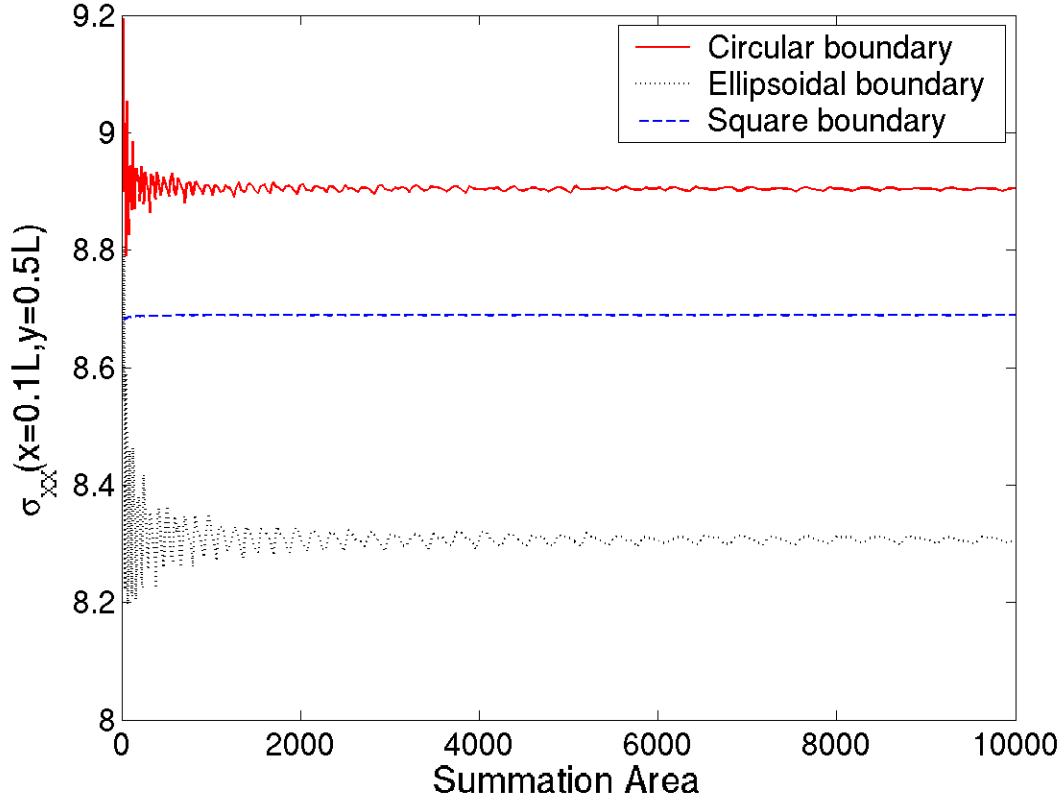
Figure 2-2: Conditional convergence of stress field summation. Naive summation results in different converged numbers when three different summation orderings are used: expanding circles, expanding ellipses and expanding rectangles. One can reasonably expect even much wilder behavior since it has been mathematically proven that the conditional convergence series can converge to any real number when summation order is varied.

The physical meaning of such interaction energy can be clearly seen if we consider an atomic configuration corresponding to the schematic plot in Figure 2-1. The total energy of the atomistic configuration E_{atm} (in excess of the energy of perfect lattice with same number of atoms) is well-defined and can be directly calculated using atomistic methods (MD or DFT). Two terms contribute to E_{atm}: the core energy and the elastic energy, with the division between the two determined by core cut-off radius (r_c). Further dissecting the elastic energy contribution to primary-primary interaction and primary-image interaction, one can see that E_{atm} consists of three

parts: core energy of the two dislocations ($2E_{core}$), interaction energy between the two primary dislocations (E_{prm}), and the interaction energy between the primary dipole and image dipoles (E_img):

$$E_{\text{atm}} = 2E_{\text{core}}(r_c) + E_{\text{prm}}(r_c) + E_{\text{img}} , \qquad (2.3)$$

In order to calculate core energy for a given r_c, one shall evaluate $E_{\text{prm}}(r_c)$ and E_{img} with elasticity theory [10, 11]. Evaluating $E_{\text{prm}}(r_c)$ is straightforward; however, calculating E_{img} is less so and is again a conditional-convergence problem:

$$E_{\text{img}} = \frac{1}{2}\sum_{\vec{R}}{}' E_{\text{dd}}(\vec{R}) \qquad (2.4)$$

$E_{dd}(\vec{R})$ is the interaction energy between two dipoles separated by vector $\vec{R}$ and the summation runs over $\vec{R} = n_1\vec{c_1} + n_2\vec{c_2}$ (n_1, n_2 are integers and $-\infty < n_1, n_2 < \infty$) which specifies positions of the image dipoles with respect to the primary dipole. The prime symbol indicates the exclusion of the self-interaction ($n_1 = n_2 = 0$). Since only half the interaction energy should be ascribed to the primary cell while the other half should belong to the image cell, the factor $1/2$ was added before the summation.

$E_{dd}(\vec{R})$ can be readily calculated from elasticity theory. Let us consider a screw dipole in isotropic media:

$$E_{\text{dd}}(\vec{R}) = \frac{\mu b^2}{2\pi}\ln(|\vec{R}+\vec{a}| \cdot |\vec{R}-\vec{a}|/R^2) . \qquad (2.5)$$

For large R, $E_{dd}(\vec{R}) \simeq \frac{\mu b^2}{2\pi}\frac{a^2}{R^2}cos2\theta \sim R^{-2}$. Therefore,

$$\begin{aligned}\sum_{\vec{R}} E_{\text{dd}}(\vec{R}) &\sim \int^{\infty}\frac{1}{R^2}\cdot 2\pi R \cdot dR \\ &\sim \int^{\infty}\frac{dR}{R} \\ &\sim [\ln R]^{\infty} \to \infty\end{aligned} \qquad (2.6)$$

42

Again, this series is a convergent series because of cancellation of terms with opposite signs but it is only conditional convergent and its value depends on the summation ordering [1]. Attempts to obtain the value of E_{img} with a straightforward summation will only result in an arbitrary number being reported. Most of the earlier reports dealing with dislocation image sums in PBC ignored the issue of conditional convergence and did not specify the summation order. The credit-worthiness of the reported numbers are therefore highly suspicious.

2.1.2 Image Summation Method

Available methods to resolve the conditional convergence problem include summing dislocation walls for edge dislocations [12, 13, 14] and performing fast multipole calculations [13] or Ewald-like summations for screw dislocations [15]. However, all the proposed methods are applicable only to isotropic media, leaving the effects of anisotropy without scrutiny. In this section, we present our new solution to the problem which is fully applicable to anisotropic media.
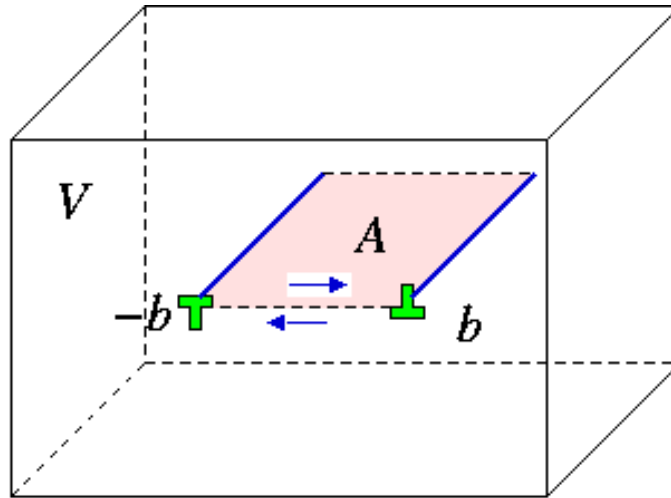
Figure 2-3: Create a dislocation dipole by making a cut and displacing the two sides of the cut surface relative to each other.

---

[1]Similar problems arises in evaluating Coulomb interactions of dipole lattices and typically treated using Ewald method.

By evaluating the reversible work to create a dislocation dipole in the periodic cell, we obtain an expression for the elastic energy of the dipole, expressed in terms of its stress field $\sigma(\vec{r})$ in the PBC cell.

$$E_{\text{el}} = -\frac{1}{2} \int dA_j b_i \sigma_{ij}^0(\vec{r}) + \frac{1}{2} S \bar{\sigma}^2 V, \qquad (2.7)$$

where the integral extends over the area enclosed by the dislocation dipole, $\bar{\sigma} = \langle \sigma(\vec{r}) \rangle_V$ is the stress averaged over the cell volume V, $\sigma^0(\vec{r}) = \sigma(\vec{r}) - \bar{\sigma}$, and S is the elastic compliance tensor.

Eq. (2.7) follows from the combination of two steps, first creating a perfect lattice under a uniform stress field and then creating a dislocation dipole by making a cut on a surface (under stress) and displacing the two sides of the surface relative to each other, as shown in Fig. 2-3. The elastic energy is therefore composed of a defect contribution, which depends only on the stress field variation $\sigma^0(\vec{r})$, and a bulk contribution varying quadratically with the average stress $\bar{\sigma}$.

One can express $\sigma^0(\vec{r})$ as the summation of variations in the stress due to the individual dislocation dipoles. Denote the stress field of a dipole at $\vec{R}$ by $\sigma_{ij}^{\text{dipole}}(\vec{r} - \vec{R})$; this summation is absolutely convergent since the stress difference between two field points decays like R^{-3}. To connect with the existing approach mentioned above, we note that the integral of the stress field of one dipole over the region enclosed by the primary dipole equals to minus the interaction between the two dipoles, so that

$$E_{\text{prm}} = -\frac{1}{2} \int dA_j b_i \sigma_{ij}^{\text{dipole}}(\vec{r}) \qquad (2.8)$$

and

$$E_{\text{dd}}(\vec{R}) = -\int dA_j b_i \sigma_{ij}^{\text{dipole}}(\vec{r} - \vec{R}). \qquad (2.9)$$

It then follows that E_{img} can be rigorously written as

$$E_{\text{img}} = \frac{1}{2} \sum_{\vec{R}}{}' E_{\text{dd}}(\vec{R}) + \frac{1}{2} A_j b_i \sigma_{ij}^{\text{err}} + \frac{1}{2} S \bar{\sigma}^2 V, \qquad (2.10)$$

44

where $\sigma_{ij}^{\text{err}} = \left\langle \sum_{\vec{R}} \sigma_{ij}^{\text{dipole}}(\vec{r} - \vec{R}) \right\rangle_V$, and the summation here involves the same collection of image dipoles as in the first term of Eq. (2.10) plus the primary dipole contribution ($\vec{R} = 0$). Eq. (2.10) shows that what is missing in Eq.(2), besides a term describing the bulk stress effect, $\frac{1}{2} S \bar{\sigma}^2 V$, is a dipole correction $\frac{1}{2} A_j b_i \sigma_{ij}^{\text{err}}$, which is $-1/2$ of the interaction between the primary dipole and the average stress introduced by the primary and image dipoles. This is similar to that derived by Wolf [16] in treating Coulomb interaction summations in electric dipole lattices. The correction is non-zero only if the primary cell contains a nonzero dipole moment [17]. If one can group every two neighboring cells to form a dislocation quadrupole array [18], its image summation is then free from this dipole correction. It is important to note the difference between σ^{err} and $\bar{\sigma}$. The former is average stress arbitrarily introduced into the PBC cell when summing the image dislocations, whose effect has to be subtracted out completely. On the other hand, $\bar{\sigma}$ is the "physical" average stress determined by atomistic simulations, whose contribution to the total energy is expressed in the quadratic term in Eq. (2.7).

One can show that the dipole correction can be exactly canceled by introducing a set of specially chosen "ghost" dislocations to interact with all the dipoles. This is analogous to the fictitious charges introduced in [19] to cancel the dipole correction in the lattice of electric dipoles. As shown in Figure 2-1, "ghost" dislocation with Burgers vector $\alpha \vec{b}$ can be placed at $\vec{c}_1/2$, $-\alpha \vec{b}$ at $-\vec{c}_1/2$, $\beta \vec{b}$ at $\vec{c}_2/2$, and $-\beta \vec{b}$ at $-\vec{c}_2/2$, with α, β satisfying $\vec{a} = \alpha \vec{c}_1 + \beta \vec{c}_2$. In this way E_{img} becomes,

$$E_{\text{img}} = \frac{1}{2} \sum_{\vec{R}}{}' (E_{\text{dd}}(\vec{R}) - E_{\text{dg}}(\vec{R})) - \frac{1}{2} E_{\text{dg}}(0) + \frac{1}{2} S \bar{\sigma}^2 V, \qquad (2.11)$$

where $E_{\text{dg}}(\vec{R})$ represents the interaction energy between a dislocation dipole (at offset $\vec{R}$) and the "ghost" dislocations. The summation in Eq. (2.11) is absolutely convergent because the "ghost" dislocations have exactly the same dipole moment as the primary dipole, so that $E_{\text{dd}}(\vec{R}) - E_{\text{dg}}(\vec{R}) \sim R^{-3}$ for large R. Since Eq. (2.11) does not depend on the explicit form of dislocation interactions, our method is applicable

to dislocations of any character in a general anisotropic elastic medium.

The above solution is presented for evaluation of elastic energy due to image interactions. However, the same method can be applied to evaluate stress, strain, or displacement field of dislocations in PBC. More generally, the solution is for reconstruction of the total elastic field of a periodic array of field sources. A simple recipe has been presented where one first compute the lattice sum of the field sources following some arbitrarily summation order, then measure and subtract the spurious part of the field that appears due to conditional convergence. This approach restores the translational periodicity of the supercell and guarantees the uniqueness of the solution. In the following section, this method is used to different stages of atomistic modeling of dislocations and one will realize the importance of the method by then.

2.2   Creating Atomic Configurations of Dislocations

The first step of modeling dislocations atomistically is to create an atomic configuration of dislocations. This task may seem trivial because according to the mathematical models of dislocations, we can follow a simple 3-step recipe to accomplish our task: (1) Make a cut in the cell, the cut may range from a whole half plane, if you are creating a single dislocation in infinite medium or with fixed boundaries, to a circular disk, if you are creating a dislocation loop within your simulation cell; (2) Shift the atoms on the two sides of the half planes relatively by a Burgers vector, and move the other off-core atoms by amounts prescribed by elasticity; (3) Insert or delete atoms if needed. However, there are many troubles associated with this process. First, the implementation of the procedures may seem relatively straightforward for simple edge or screw dislocations, but become cumbersome for mixed dislocations. Second, moving atoms using elasticity is good, but one will get unwanted mismatches, sometimes even stacking faults, at the boundary if a simple elastic solution assuming the dislocation being in infinite medium is applied. Third, insertion and deletion of atoms are somewhat arbitrary and if not done properly, can lead to point defects near

created dislocations. Furthermore, because the prepared configuration is so far from equilibrium configuration, it usually takes a long time for it to relax to minimum energy state. Finally, still because of the crudeness of the prepared configurations, the dislocation introduced may move away from the intended sites during the process of relaxation. In summary, this simple recipe is very crude, cumbersome, and may lead to serious problems in some cases.
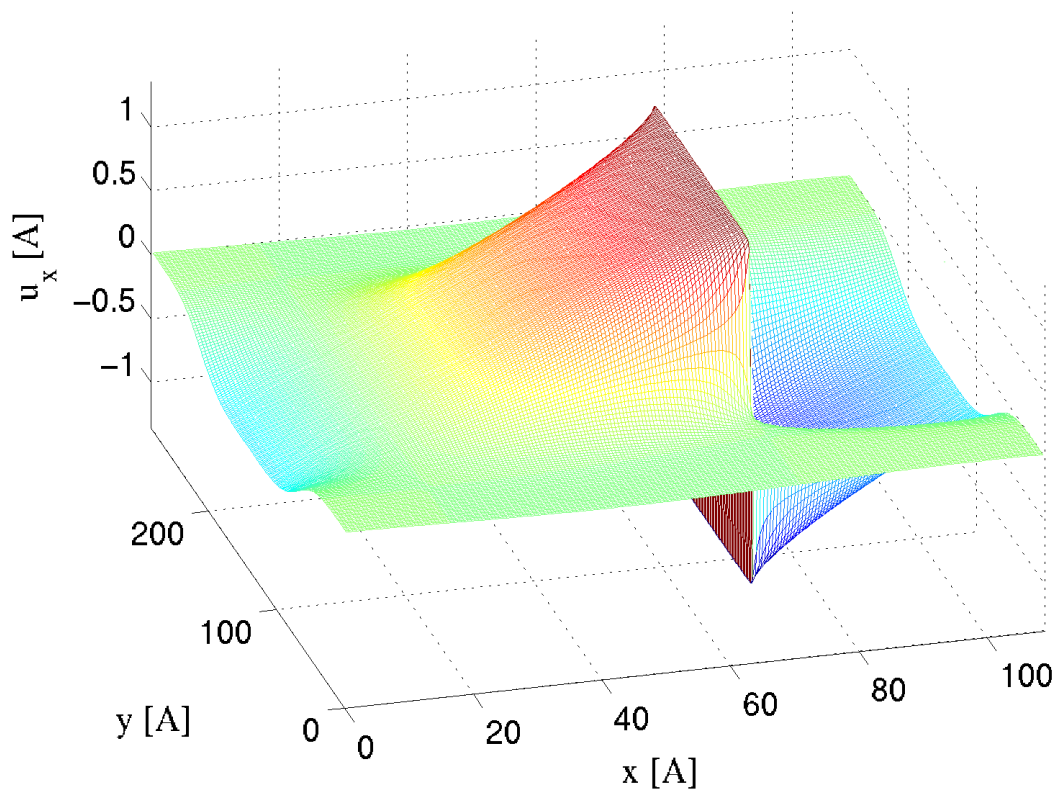
Figure 2-4: Displacement field generated for a screw dislocation dipole under PBC.

Instead, one should apply the image summation method to obtain the true displacement field considering the effect of the periodic images of the primary dislocations, using anisotropic elasticity. With this accurate displacement field (certainly only for regions away from the core), one move the atoms accordingly and can create an initial configuration which is very close to ground energy state. Since the core

region can not be well described by elasticity, the dislocation core atoms need further relaxation. However, for the atoms far from core region, the prescribed displacement are already very close to equilibrium values, if not exactly the same.

This two-step process is shown in Figure 2-4 and Figure 2-5, where the displacement field is first calculated using image summation method, and then a discrete atomic representation of this field is generated as the atomic configuration.
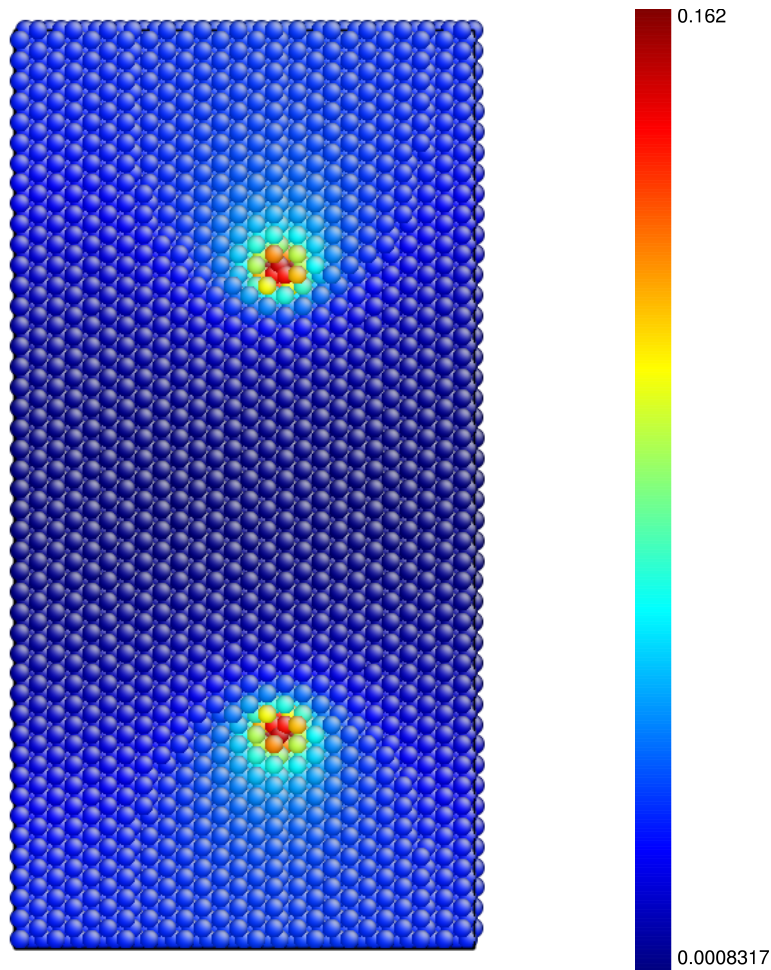
Figure 2-5: After obtaining the displacement field using image summation method, this continuous field is mapped to discrete lattice to produce an real atomic configuration.

2.3 Calculating Core Energy of Dislocations

We apply the image summation method to extract the core energy of the edge dislocations in BCC metal Mo using the Finnis-Sinclair (FS) potential [20]. We use a simulation cell with $\vec{c}_1,\vec{c}_2,\vec{c}_3$ along $[111],[\bar{1}01],[1\bar{2}1]$ directions respectively, with $\vec{a} = \vec{c}_2/2$ and $\vec{b} = \pm[111]/2$. The dislocation dipole is created by following the procedures described in the previous section and the configuration obtained is then relaxed under zero stress. (After the relaxation, there is an overall strain on the cell to accommodate the plastic strain introduced by the dislocation dipole, so that it has zero average stress and the last term in Eq. (2.11) vanishes. The atomic structure is shown in Figure 2-6. The elastic constants for the potential model are $C_{11} = 464.7\mathrm{GPa}$, $C_{12} = 161.5\mathrm{GPa}$, $C_{44} = 108.9\mathrm{GPa}$, and Voigt average values are $\mu = 125.98\mathrm{GPa}$, $\nu = 0.2932$.

Figure 2-7 shows the variation of total energy per unit dislocation length (E_{atm}) with cell dimension $\vec{c}_2$, while $\vec{c}_1$ is fixed. For a given simulation cell, we calculate the corresponding elastic energy $E_{\mathrm{prm}} + E_{\mathrm{img}}$ through Eq. (2.11) and use anisotropic elasticity theory for individual dislocation interaction energies. The expression for the interaction energy are obtained by integration of the stress expression from[10]. For two parallel dislocations separated by (x, y), their interaction takes the form $E \sim \ln(x + p_\alpha y)$, with p_α being roots of a sixth order polynomial. The elastic constants used for elasticity calculations are taken from the reported values for the FS potential.

The core energy predicted by anisotropic elasticity is $E_{\mathrm{core}} = 0.324 \pm 0.002\mathrm{eV/\mathring{A}}$, at $r_c = b = 2.7256\mathring{A}$, (corresponding to $\alpha = 1.66$). On the other hand, using μ as a free parameter, isotropic elasticity gives $E_{\mathrm{core}} = 0.382 \pm 0.002\mathrm{eV/\mathring{A}}$, (corresponding to $\alpha = 1.81$), significantly different from anisotropic results. Thus dislocation core energies obtained under the assumption of elastic isotropy can be in appreciable error even when the energy prefactor is fitted to atomistic data.
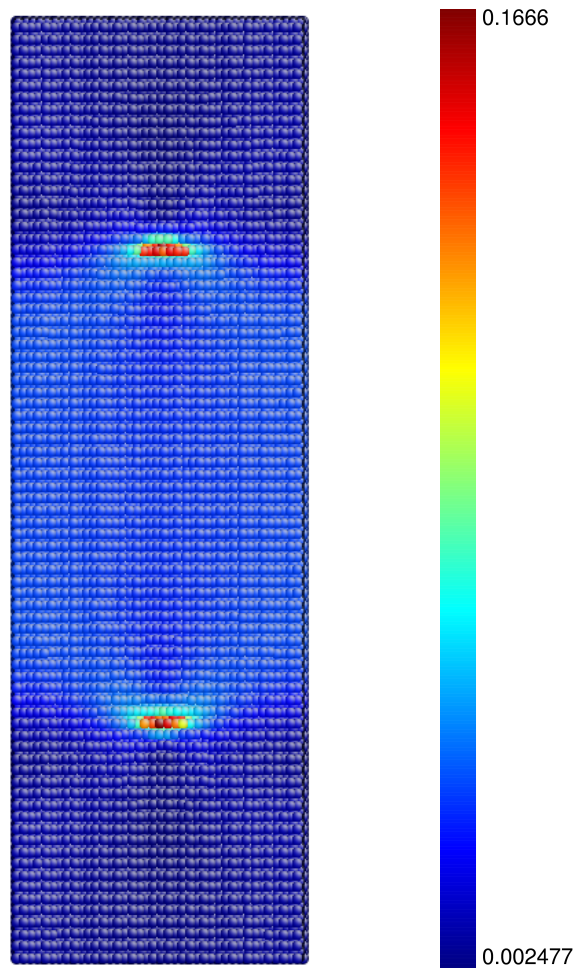
Figure 2-6: Atomic structure of edge dislocation dipole in Mo a simulation cell under PBC. The dipole is created by removing a layer of atoms between the two dislocations. The high energy atoms in the dislocation core are plotted in dark color.

2.4 Quantifying Artificial Image Energy Barriers

The previous section shows that the image summation method can be applied to accurately calculate core energies of dislocations. In this section, we concern ourselves with identifying the image effects for simulating dynamic motion of dislocations under PBC. We will use the image summation method to calculate the artificial energy barrier due to image interactions and compare the results with atomistic calculations. Important implications for simulation geometry design is discovered and will be discussed at the end of section.
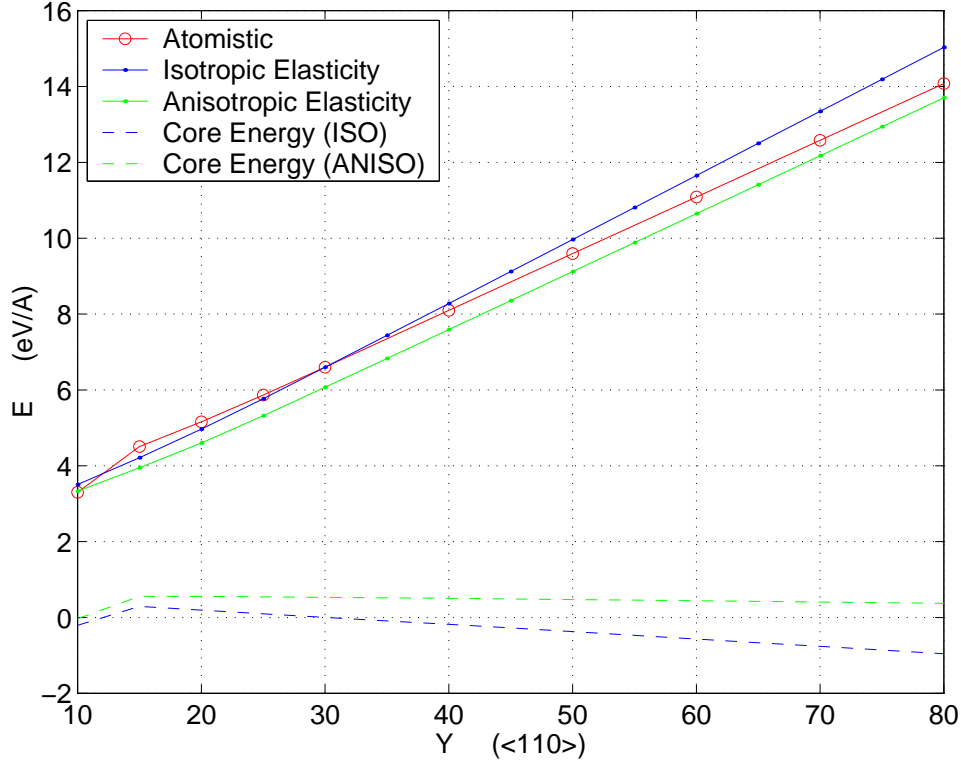
Figure 2-7: Calculating core energy of an edge dislocation in Mo using an edge dislocation dipole configuration under PBC cell. Core energy is obtained by subtracting linear elastic energy E_{el} (isotropic $\square$) and anisotropic $\diamond$) from atomistic total energy E_{atm} ($\circ$), and then divide by 2. Anisotropic elasticity is shown to give a very accurate core energy result.

In simulating dynamic motion of dislocations under PBC, an issue of practical concern is whether there exists an optimal cell geometry for atomistic simulation studies of dislocations. Linear elasticity predicts that when $\vec{a}$ is kept at $\vec{c}_1/2$, E_{img} is only dependent on the cell aspect ratio. Figure 2-8 shows the predicted image interactions not only decrease with increasing aspect ratio, as one would expect, with anisotropy effects reducing the magnitude, but also the energies can change sign. This information is noteworthy because a simulation cell with small magnitude of image energy E_{img} would have higher accuracy in determining both the core energy and the Peierls stress τ_{PN}, both of which are static parameters of dislocation core that can be used to infer dislocation mobility at finite temperature and finite stress conditions.
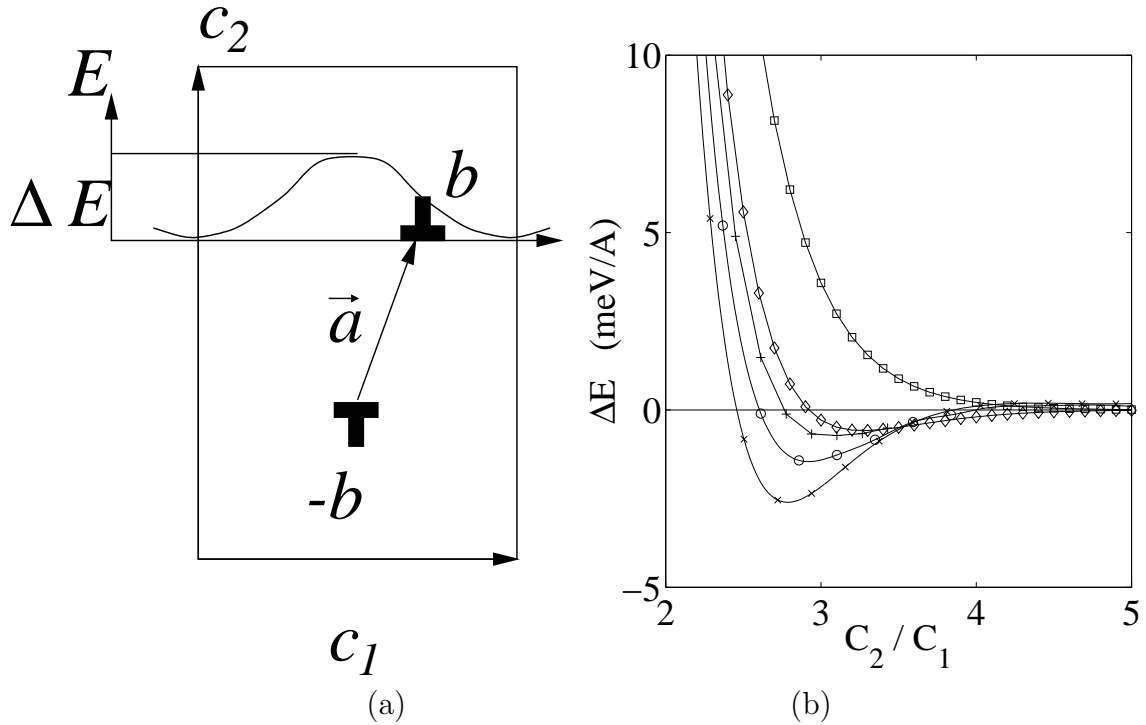
Figure 2-8: (a) Schematic of the total energy variation with relative displacement x, ΔE being the maximum. (b) Variation of ΔE with cell aspect ratio c_2/c_1 for edge dislocations in Mo, with the same set up as in Figure 2-7. Anisotropic elasticity predicts $\Delta E = 0$ at $c_2/c_1 = 2.918$ ($\diamond$). Isotropic elasticity predicts a monotonic decrease of ΔE with increasing c_2/c_1 ($\square$). Atomistic simulations with $c_1 = 15, 20$ and $30[111]$ are shown in $\times$, $\circ$ and $+$ respectively.

Cell geometry will also affect the dynamics of simulated dislocations. Indeed, cell geometry generally affects the total elastic interactions and hence the dynamics of dislocations in atomistic simulations. A question of practical interest is whether there exists an optimum cell geometry for which the elastic interactions are minimized. Consider a simulation cell (Figure 2-8(a)) containing two edge dislocations separated by $\vec{a} = \vec{c}_2/2$; each of the dislocations can only glide along $\vec{c}_1$. The system energy is then a periodic function of their relative displacement x along $\vec{c}_1$ direction, the energy barrier being a result of an oscillatory image stress field superimposed on any applied external stress. Linear elastic considerations show that the energy variation has extrema at $x = 0$ and $x = c_1/2$, so that $\Delta E = E(x = 0) - E(x = c_1/2)$, a function only of the cell aspect ratio, is an appropriate measure of the internal

52

dislocation interaction. For dislocation mobility simulations [21] a minimum value ΔE is desirable for obtaining an accurate relation between the dislocation velocity and the applied stress.
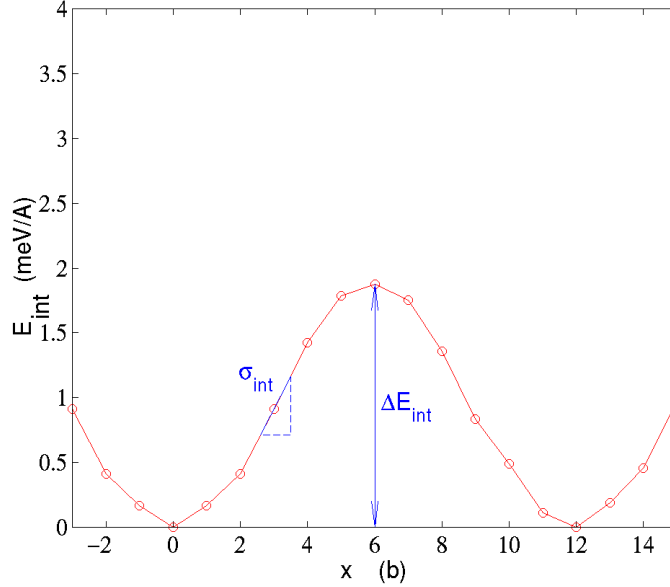
Figure 2-9: Calculating ΔE directly from atomistics. First we prepared a number of atomic configurations corresponding to different relative displacement values, $0b$, $1b$, $2b$,...,etc. Then these configuration are relaxed and the final energy of each one is represented by a data point in this picture. This gives us the atomistically reproduced image energy variation curve, which is more accurate than the isotropic predictions, but requires much more computational efforts.

Results for the energy barrier determined separately by isotropic and anisotropic elasticity calculations are compared in Figure 2-8(b). Isotropic linear elasticity predicts ΔE to decrease monotonically with increasing aspect ratio without becoming negative, whereas the anisotropic calculation predicts ΔE to vanish at the aspect ratio of $c_2/c_1 = 2.918$. Also shown in Figure 2-8(b) are direct atomistic simulation results (see Figure 2-9 for details) for the artificial image energy barrier for three cell sizes, showing a converging behavior toward the elasticity result.

The vanishing of the energy barrier at the special aspect ratio implies a complete
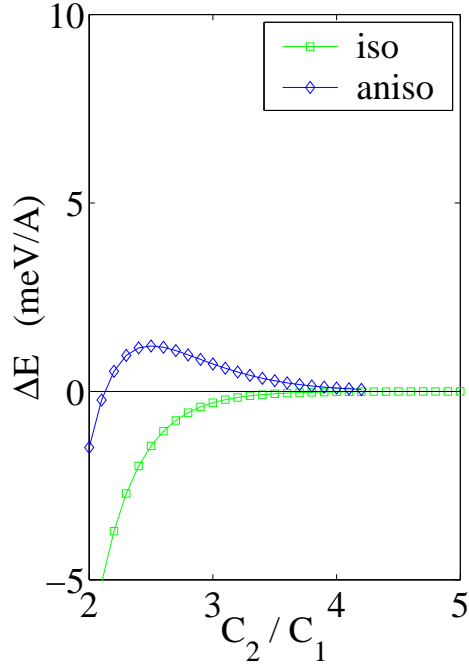
Figure 2-10: Variation of ΔE with cell aspect ratio c_2/c_1 for screw dislocations in Mo. Anisotropic elasticity predicts a reverse of sign at $c_2/c_1 \approx 2.2$ while isotropic elasticity predicts a monotonic increase of ΔE approaching zero.

cancellation among the primary and image interactions, thus allowing unhindered dislocation glide in the PBC simulation cell. Direct atomistic simulations confirm that ΔE indeed is greatly reduced at a cell geometry close to the predicted c_2/c_1. For example, at $\vec{c}_1 = 20[111]$ and $\vec{c}_2 = 64[\bar{1}01]$, simulation gives $\Delta E = 0.091\text{meV/Å}$, corresponding to a maximum internal stress of about 0.3MPa. In contrast, typical stresses applied in mobility simulations are in the range of $10 - 1000\text{MPa}$ [21].

It may appear that the atomistic results in Figure 2-8(b) indicate a significant size dependence. Indeed, a contributing factor could be the higher order (e.g. $\sim 1/r$) terms in the elastic interactions which is not in place if ones uses linear elastic theory. However, the difference due to higher-order elastic terms appear to be rather small.

One may have noticed that the energy scale in the same figure is about 2 orders of magnitude smaller than typical values for migration barriers for dislocations and conclude that the effect here is rather small. However, be aware that as aspect ratio

further decreases, a more-than-linear increase in ΔE will lead to significantly higher image energy barriers.

The existence of special geometries, arising from elastic anisotropy, is not a unique phenomena for edge dislocations. Indeed, for screw dislocation dipole in Mo, we have discovered similar behavior, as shown in Figure 2-10. The special aspect ratio in this case is different from the previous case of edge dipole, meaning that this special value of aspect ratio is not a universal number and have to be computed separately for different systems.

According to Figure 2-8(b), for edge dislocation mobility simulations in Mo using periodic boundary conditions, the aspect ratio c_2/c_1 of the simulation cell need to be larger than $3 \sim 4$ to make image interaction effects negligibly small. This prediction is confirmed by direct Molecular Dynamics simulations. Figure 2-11 shows the Virial stress oscillation during MD simulations of moving edge dislocation dipoles with cell aspect ratio at 3.8 and 1.65 respectively [22]. The simulations are performed at 20K with a constant shear rate of $0.4 \times 10^{-9} \text{s}^{-1}$. The Virial stress oscillation for the large aspect ratio is very small and mainly comes from thermal fluctuation, while that for the small aspect ratio clearly shows a sinusoidal pattern, which is an artifact due to the image interactions. In the edge mobility studies that we are going to discuss in Chapter 5, an aspect ratio of 3.5 is chosen to minimize the image effect and give a better description of dislocation velocity response under finite temperature and finite stress conditions.
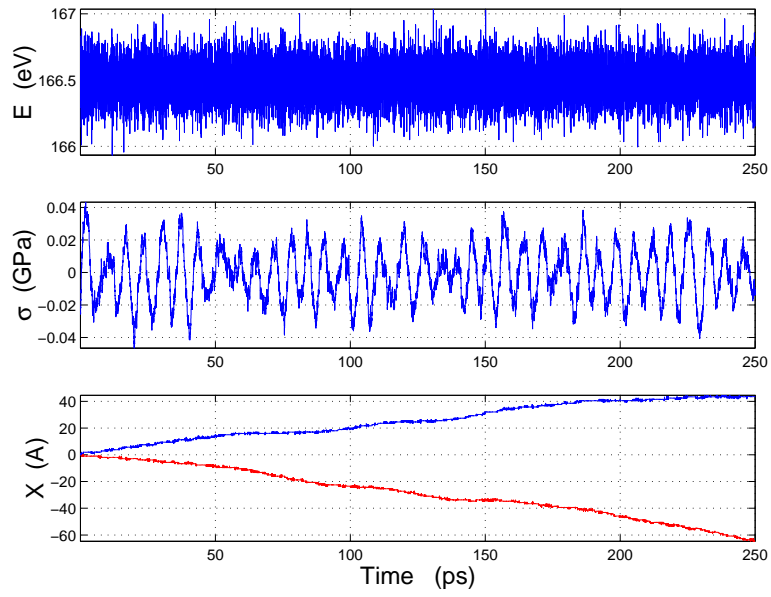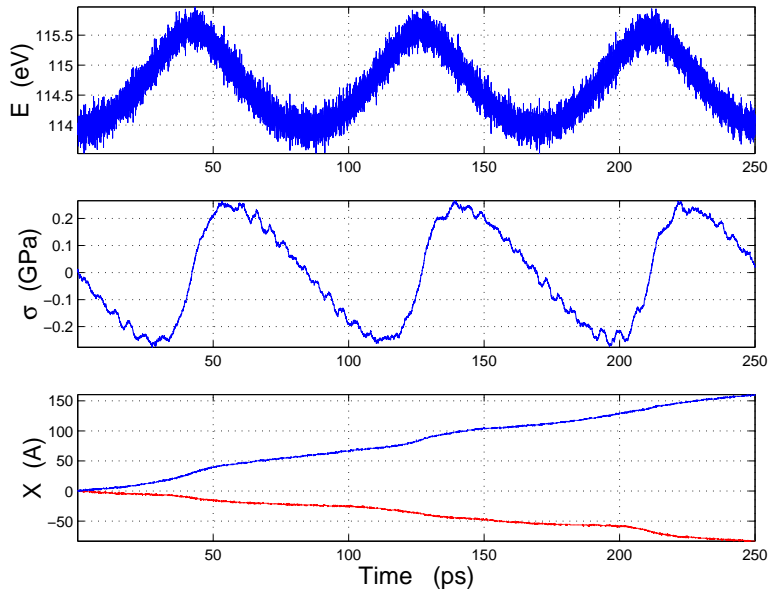
Figure 2-11: Variation of total energy E and Virial stress σ, and dislocation displacement X in MD simulations of edge dislocation motion, with cell aspect ratio c_2/c_1 at (a) 3.8 and (b) 1.65. The fluctuation in (a) is small and is mainly due to thermal noise, while the large oscillations in (b) is clearly due to the image interaction artifact.

Chapter 3

Core Structure and Peierls Stress: Screw Dislocations in Mo

In this chapter, atomistic results on core structure and Peierls stress, τ_P, for screw dislocations in BCC metal molybdenum are presented. In the first section I review the experiments on deformation behavior of BCC metals, which serve as background knowledge for this chapter as well the following two chapters both of which deal with edge dislocations in BCC metal molybdenum. In the second and third section, the core structure and Peierls stress of screw dislocations in Mo are calculated using an environment-dependent tight-binding potential and are compared to results obtained using empirical potentials; furthermore, the importance and validity of this study is evaluated by putting it into a larger picture that has been built up by a great number of previous atomistic and experimental studies. In the final section, atomistic results on mobility of kinks on screw dislocation are presented and current understanding of kink mobility and its relation to screw dislocation mobility is reviewed by considering recent atomistic, experimental and theoretical findings.

It is worth noting that the plasticity behavior of BCC metals is quite complicated and it is not the purpose of this thesis to resolve all the issues in the atomistic framework. Instead, we are going to focus on a small number of topics and try to clarify the issues there as cleanly as possible. In this chapter and the following chapter, two issues will be addressed using atomistic calculations. One is the core structure

and Peierls stress for straight screw dislocations, the other is the core structure and Peierls stress for straight edge dislocations. There are quite a large number of other important issues, e.g., anomalous slip, effect of kinks, jogs, and junctions, etc., that are not covered in entirety or not covered at all in this thesis. The author will try to give brief discussions about current understandings of these issues where appropriate; in the meantime, interested readers should refer to [2, 23, 24, 25] for complete coverage of these topics.

3.1 Experiments on Deformation Behavior of BCC Metals

3.1.1 BCC Metals

BCC (body-centered cubic) metals and alloys have been heavily used by human kind ever since the Iron Age. Their most useful property is high strength over a wide range of temperature and straining conditions, which makes them the ideal candidates for structural applications and high temperature conditions. Indeed, BCC iron alloys are the most widely used and the most important structure material, mainly due to the abundance of iron ores on earth, as well as the relatively straightforward technologies for metal extraction and high formability at reasonable temperatures. BCC metals, e.g., the refractory metals Mo, W, Nb, Ta and others, also served as important elements for more specialized applications: when used in combinations with Fe, they can greatly improve the quality of structural materials.

Compared to other types of metals, i.e., FCC (face-centered cubic) metals and HCP (hexagonal close packed) metals, BCC metals exhibit certain general plasticity behaviors such as the prominent temperature and strain-rate dependence of the yield stress, features of slip crystallography, and the existence of a ductile-to-brittle transition at low temperatures. These plasticity behaviors of BCC metals have the root in their common lattice crystallography and are closely related to the defect microstructure and dislocation activities, e.g., the ductile-to-brittle transition is a

Table 3.1: Bulk properties of BCC transition metals [26, 27, 10, 28]. Elastic constants C_{11}, C_{12}, C_{44} in GPa, melting temperature in K, cohesive energy E_{coh} in eV, and thermal conductivity κ in Wm^{-1}K^{-1}. Note that Group 6 metals Cr, Mo and W generally have a larger shear modulus C_{44} and thermal conductivity κ than Group 5 metals V, Nb and Ta.

	Z	ele. conf.	C_{11}	C_{12}	C_{44}	T_m	T_b	E_{coh}	κ
V	23	$[Ar]3d^34s^2$	227.9	118.7	42.6	2163	3680	5.31	30.7
Nb	41	$[Kr]4d^45s^1$	246.6	133.2	28.1	2742	5017	7.57	53.7
Ta	73	$[Xe]4f^{14}5d^36s^2$	266.0	161.2	82.4	3293	5731	8.10	57.5
Cr	24	$[Ar]3d^54s^1$	387.1	103.5	100.8	2130	2944	4.10	93.7
Mo	42	$[Kr]4d^55s^1$	464.7	161.5	108.9	2896	4912	6.82	138
W	74	$[Xe]4f^{14}5d^46s^2$	522.4	204.4	160.6	3695	5828	8.90	174
Fe	26	$[Ar]3d^64s^2$	242	146.5	112	1808	3134	4.29	80.2

manifestation of the inability of dislocations to multiply and/or move fast enough, at low temperatures, to relieve the stress concentrations that are the causes of cracking.

Transition metals in group 5(VB), such as V, Nb, Ta, and group 6(VIB) such as Cr, Mo, W, and Fe in group 8 (VIII) all have BCC structure. A comparison of the bulk properties of these BCC metals including V, Nb, Ta, Cr, Mo, W, and Fe is shown in Table 3.1. In this thesis, we will focus on the properties of molybdenum, as a representative of BCC transition metals.

In the following text, we will discuss several important aspects of BCC plasticity, namely features of slip crystallography, temperature and orientation dependence of plasticity, anomalous slip, and dislocation microstructure. Individual dislocation mobility measurements, which we discuss at the beginning of Chapter 5, will be also be discussed briefly here. One can also refer to [29, 30, 31, 32, 33, 34, 35, 26, 36, 9], where the experiments on the temperature and orientation dependence of plasticity of BCC metals, as well as their relationship with the core structure of screw dislocations are discussed in great details.
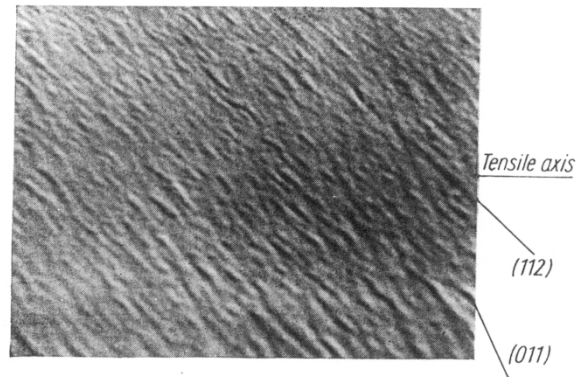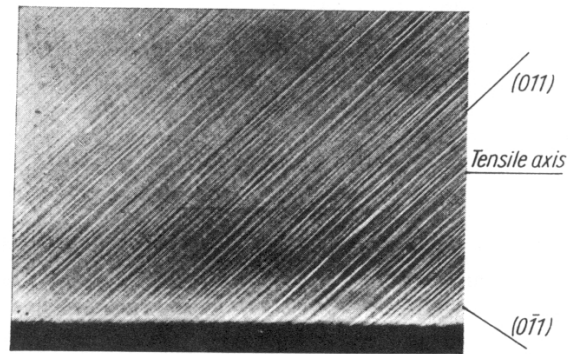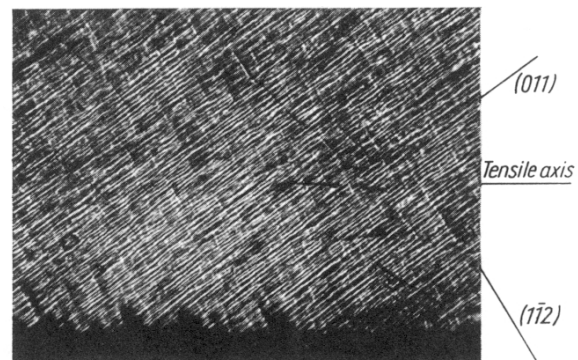
Figure 3-1: Slip traces of BCC Mo deformed at 353 and 413K under uniaxial tension along the direction near the center of the standard triangle. (a) Slip lines on face 1 after 0.045 tensile strain. (b) Slip lines on face 2 after 0.045 tensile strain. (c) Slip lines on face 2 after 0.175 tensile strain [37].

3.1.2 Slip Crystallography and Slip Asymmetry

The dominant dislocation type has Burgers vector of $\frac{a}{2}\langle 111\rangle$, which is the smallest repeat vector of the BCC lattice. $a\langle 100\rangle$ dislocations are also observed. The latter are usually considered to be reaction products between $\frac{a}{2}\langle 111\rangle$ dislocations, e.g., $\frac{a}{2}[111] + \frac{a}{2}[1\bar{1}\bar{1}] = a[100]$.

Slip trace analysis (for example, see Figure 3-1) reveals slip in $\{110\}$, $\{112\}$ and even $\{123\}$ planes of the $\langle 111\rangle$ zone [37, 38, 39, 10]. At higher temperatures, the so-called pencil or non-crystallographic slip is observed such that the slip plane, on average, follows the maximum resolved shear stress (MRSS) plane, with the slip traces having a wavy appearance [40, 41, 42]. The waviness of the slip traces can be interpreted as the result of cross slip of screw dislocations between $\{110\}$ and $\{112\}$ planes.

Both atomistic calculations and experimental observations suggest that there are no stable stacking faults in BCC metals, at least in ambient conditions. This suggests that dislocations in BCC metals should not dissociate in a planar, FCC-like fashion. Combining this with the fact that the BCC screw dislocation cores are observed to be rather compact (disregard of the fine structure of the screw core, i.e., whether it is polarized or not), and the pre-dominance of screw dislocations already mentioned, one can see that plasticity in BCC metals should be strongly influenced by cross-slip processes. [1]

As shown in Figure 3-2, under pure shear deformation at temperatures between 77 and 293K, shearing along two opposite directions on (112) plane have different responses and are labeled "soft" (favorable for twinning) and "hard" (anti-twinning) respectively. On the other hand, shearing on (110) plane did not generate visible asymmetry. Figure 3-2(a) shows the stress-strain curves for three different shear

---

[1]The very term "cross-slip" coined to describe rather infrequent events where the dislocation changes glide plane in FCC metals, could be somewhat misleading when used to describe the motion of screw dislocations in BCC metals. Given its compact core, a screw dislocation does not have to first constrict in order to change its glide plane; there would be always more than one glide plane that is available. The selection of glide plane and resulting slip crystallography are likely to be governed by rather more subtle effects in the core of the screw dislocation than the planar dissociation invariably observed in FCC metals.
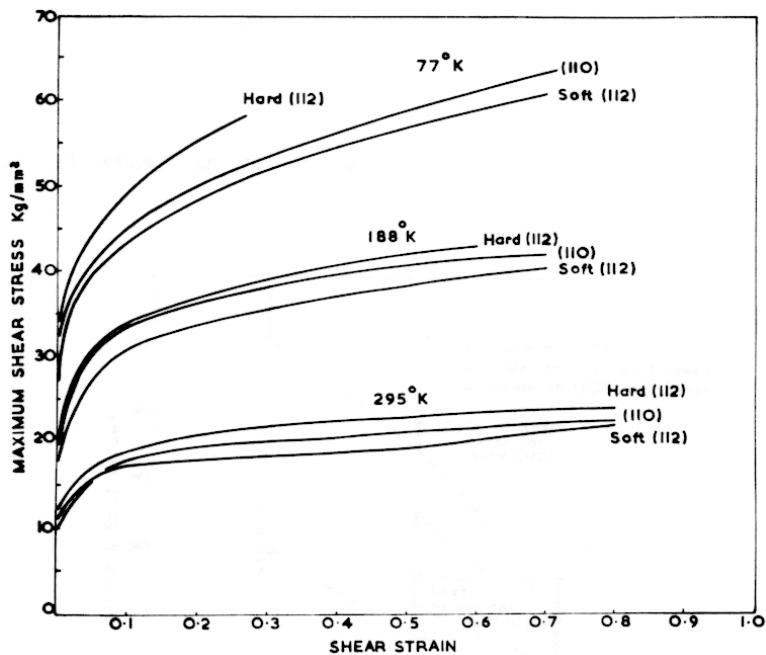
(a)
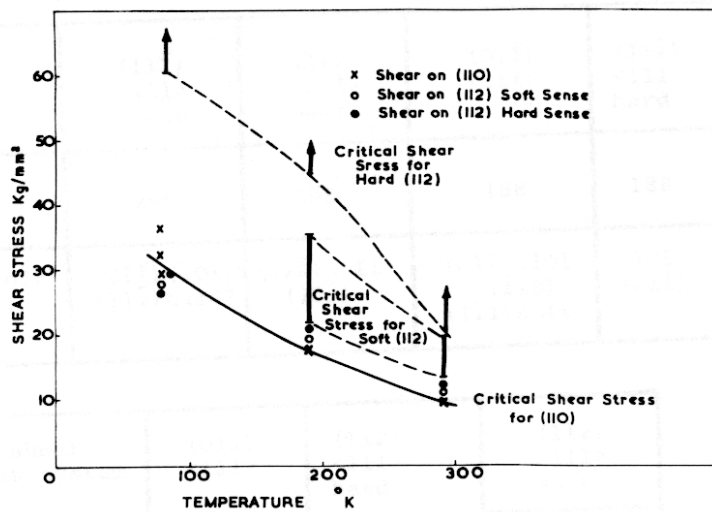
(b)

Figure 3-2: (a) Stress strain curve of Mo under direct shear. (b) Estimated bounds for critical resolved shear stress to nuclear slip on different planes [43].

62
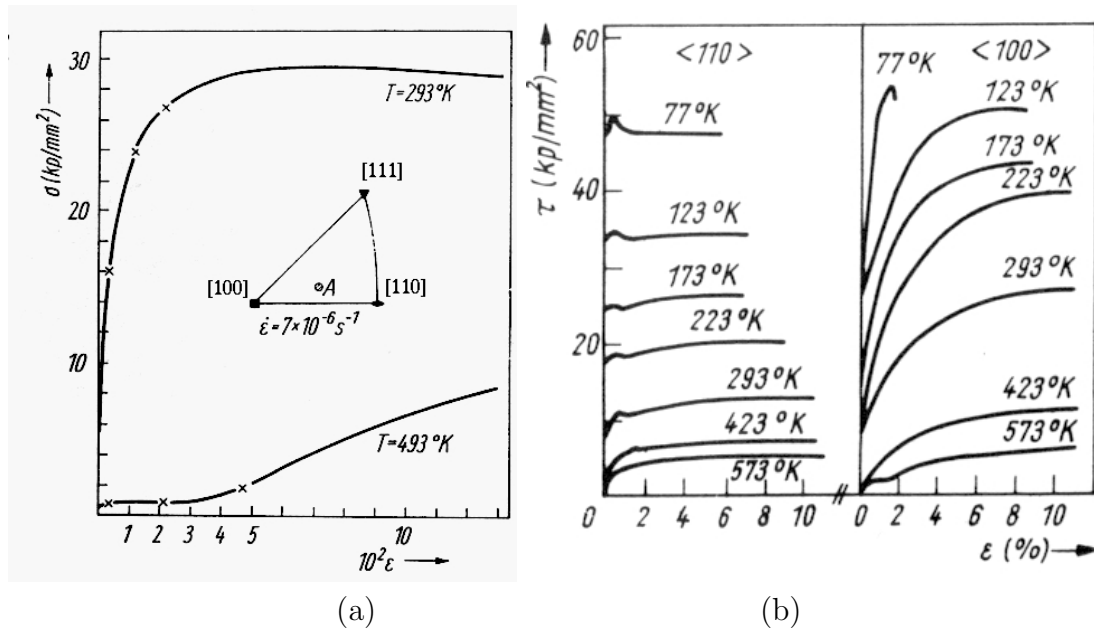
Figure 3-3: Tensile stress-strain curve of Mo. (a) Uniaxial tension along A direction (inside the standard triangle) at 293 and 493K. (b) Uniaxial tension along $\langle 110 \rangle$ and $\langle 100 \rangle$ from 77 to 573K [44, 45].

orientations at three different temperatures, while the estimated CRSS of different slip systems is shown in Figure 3-2(b). The twinning anti-twinning asymmetry observed when shearing on (112) plane has its root in the BCC lattice crystallography and can be actually predicted by atomistic calculations as will be shown later in Chapter 6 of this thesis.

3.1.3 Temperature and Orientation Dependence of Plasticity

In contrast to FCC metals where intrinsic lattice resistance to dislocation motion is vanishingly small and the resistance to plastic deformation mainly comes from dislocation interactions with impurities or other dislocations, BCC metals generally exhibit a strong lattice resistance to dislocation motion. As a result, the yield stress of BCC metals rises dramatically as temperature approaches zero. In addition, slip in BCC metals also exhibit strong orientation dependence, most of which can be accounted for by the anisotropy of intrinsic lattice resistance to dislocations.
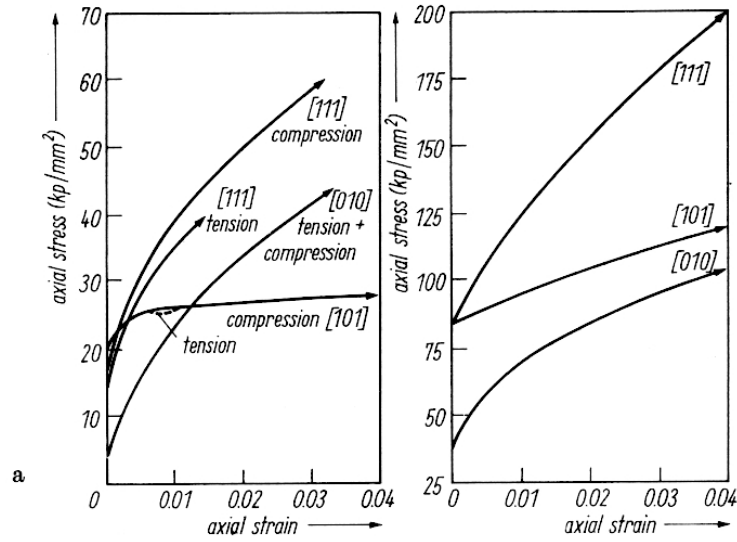
Figure 3-4: Tensile stress-strain curve of Mo along $\langle 101 \rangle, \langle 010 \rangle, \langle 111 \rangle$ directions under (a) 293K and (b) 77K [46].

Figure 3-3(a) shows stress-strain curves of Mo at two different temperatures [44]. The sample was under uniaxial tension along the direction marked as A inside the standard triangle. This loading condition favors single slip on $\{110\}\langle 111 \rangle$ system with Schmid factor ≈ 0.5. While at 493K three-stage hardening was observed, the crystal at 293K is much stronger and exhibits parabolic hardening. Figure 3-3(b) shows the stress-strain curves at high symmetry tensile directions [45] such as $\langle 110 \rangle$ and $\langle 100 \rangle$, where multiple slip systems are favored. The increase of yield stress with decreasing temperature is also clearly seen in multiple slip orientations. As shown in Figure 3-4, a slight asymmetry in stress between tension and compression is found at low temperature (77K) but not at higher temperature (293K).

The critical resolved shear stress (CRSS) τ_0 for Mo single crystals as a function of temperature was measured using tension and compression tests by Kaufmann et al. [47], as shown in Figure 3-5. As temperature approaches zero, the CRSS goes to 750MPa. More recent experiments by Seeger et al [49, 48] presents a more reliable and complete set of data on temperature dependence of CRSS using two types of tests, i.e., isothermal straining tests and incremental-strain-temperature-lowering
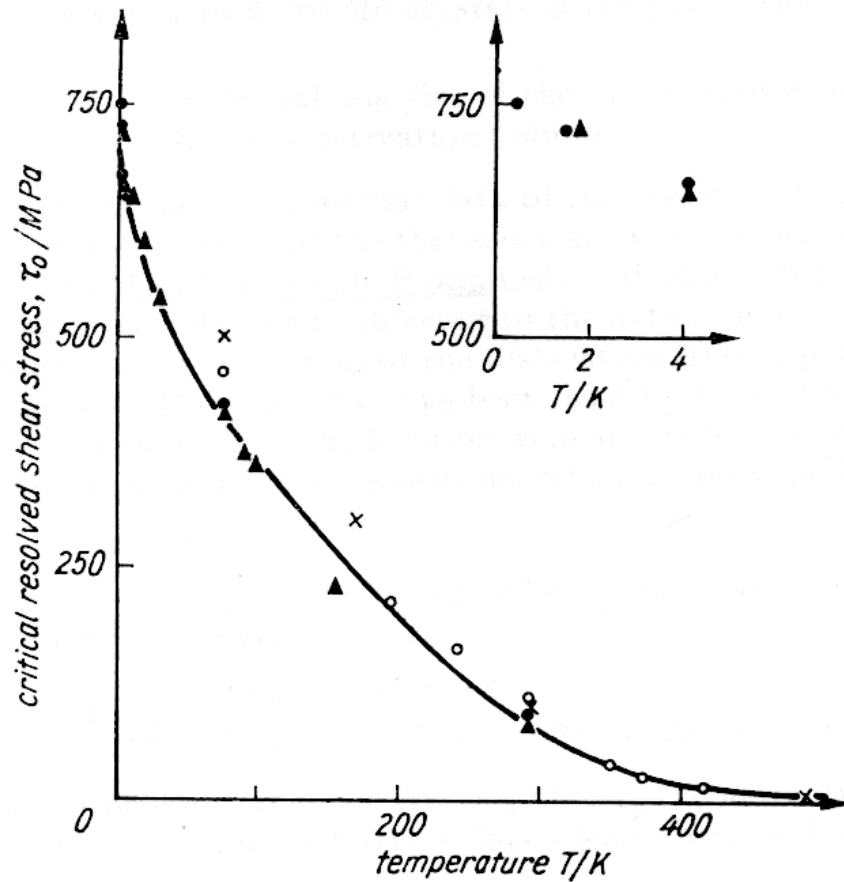
Figure 3-5: Temperature dependence of the critical resolved shear stress of $\langle 110 \rangle$ Mo single crystals for tension ($\bullet$) and compression ($\blacktriangle$) [47].

tests, as shown in Figure 3-6 where the extrapolated CRSS for zero temperature is ~ 870MPa. [2] These experimental results on temperature dependence of CRSS have been explained well using kink-pair theory by Seeger et al in [49]. However, as shown by Professor Ali S. Argon in [50], of the three temperature regimes outlined in [49] and shown in Figure 3-6, Regime II and III indeed should be one and a carefully derived double kink nucleation model fits very well with the experimental data in Figure 3-6.

Stress-strain relations have also been measured for other BCC metals, such as

---

[2]This value is usually regarded as the experimental indication of the minimum stress to move the dislocation across the lattice, namely the Peierls stress, and can be compared with atomistic calculations which will be discussed in following sections.
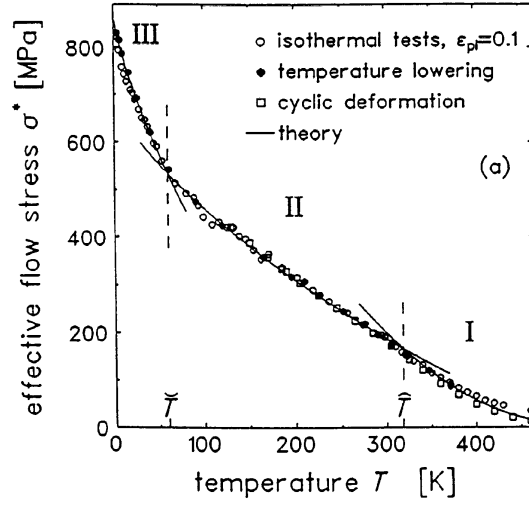
Figure 3-6: Temperature dependence of flow stress for $\langle 110 \rangle$ Mo single crystals by Seeger et al [48].

Table 3.2: Orientation dependence of the CRSS (in MPa, resolved on the M.R.S.S. plane) for BCC metals at 77K. [uvw] represent directions near the corner or the center of the standard triangle. (Table 1 of [35].)

	Tension				Compression				
	[110]	[100]	[111]	[uvw]	[110]	[100]	[111]	[uvw]	Ref.
W	730	353	416	485					[51]
W	584	283	255						[52]
Ta	323	179			172	273			[53]
Ta	353	283			264	221			[54]
Ta	406	297	337	338					[55]
Ta	400	278	293	275	259	221	309	300	[56]
Fe	270		200						[57]
Mo	471	151			393	137			[53]
Mo					577	214	647	320	[58]
Mo	500	170		250					[37]
Nb	254	165			108	214			[53]

66
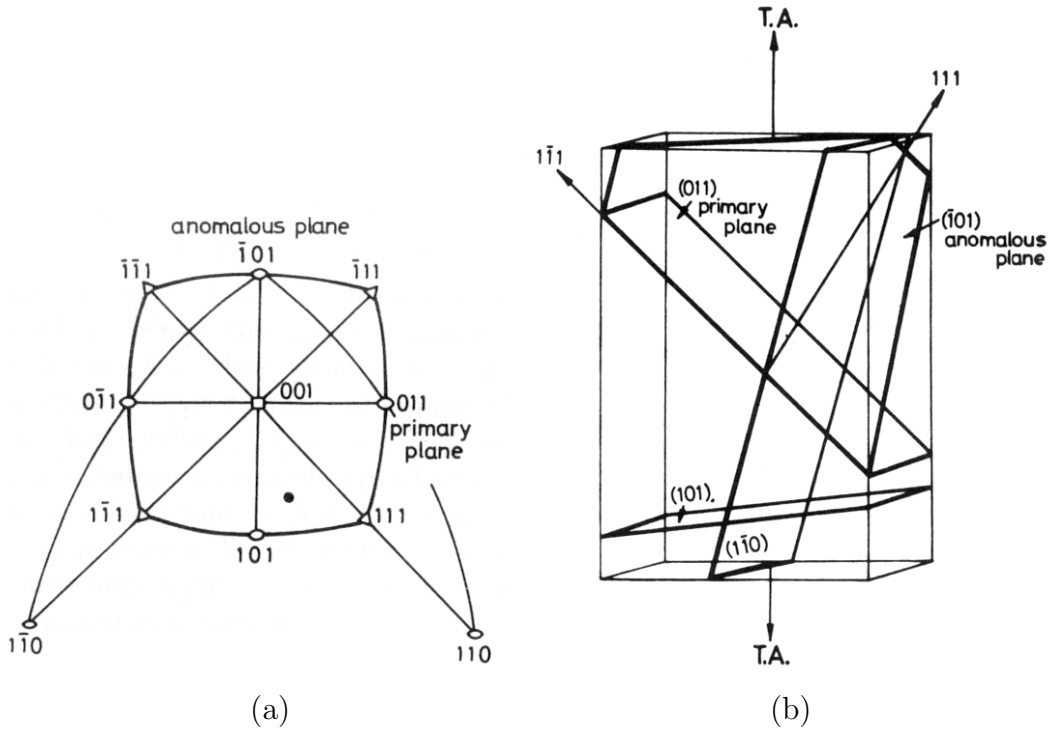
Figure 3-7: Orientation of the primary slip plane and the anomalous plane with respect to the tensile axis. (a) Stereographic plot. (b) 3-dimensional plot [68]. For the specified tensile direction, the Schmid factor on the primary slip plane (011) is ~ 0.5, while on anomalous slip plane ($\bar{1}01$) it is only $0.25 \sim 0.3$ [68].

Nb [59, 60], W[52], Fe[61, 62, 63], etc, and strong temperature and orientation dependence of yield stress has been found as a general behavior. The orientation dependence of CRSS for several BCC metals at 77K are compiled by Duesbery et al. [35], which is reproduced here in Table 3.2.

3.1.4 Anomalous Slip

First discovered in VB metals such as Nb and Ta [64, 65, 66] and later for Mo under low temperature at small strains [67], anomalous slip [67] occurs at low temperature in high purity BCC metals, and derives its name from the fact that its Schmid factor is much lower than that of the primary slip system, so that its occurrence is "unexpected" (see Figure 3-7).
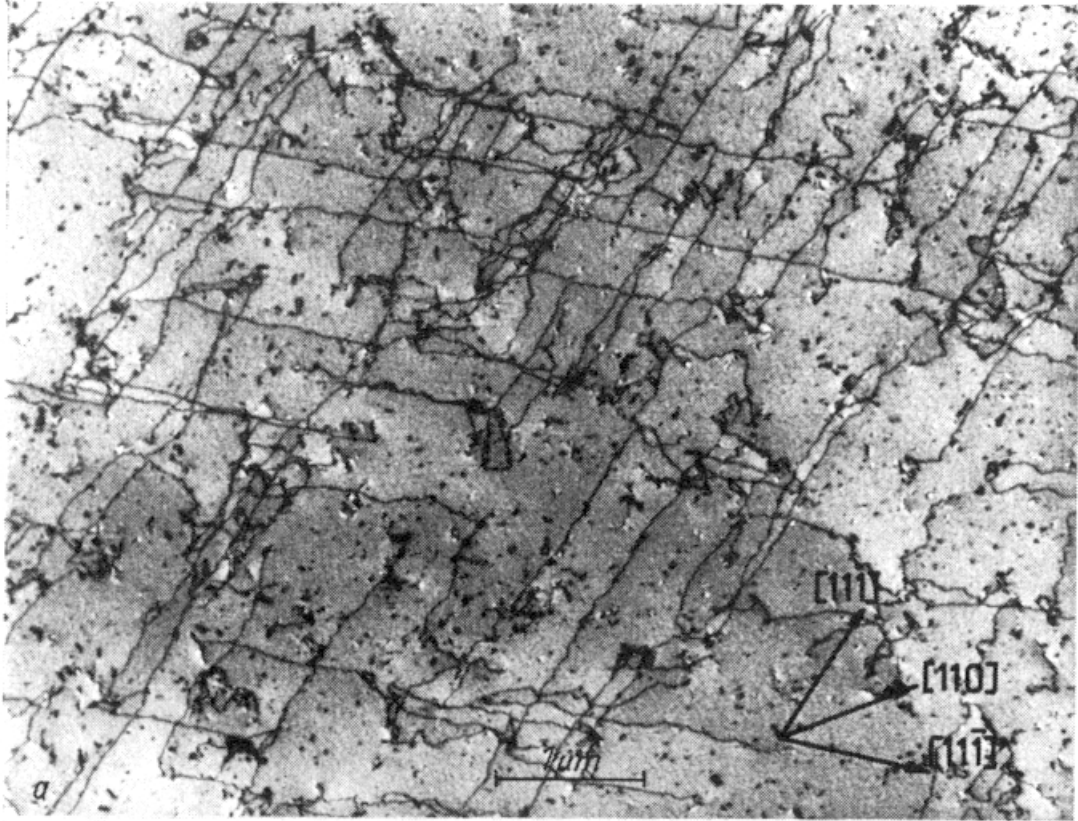
Figure 3-8: Dislocation microstructure in Mo under 2% tensile strain along [110] at 77K [47]. The many long screw dislocation segments that one sees directly reflects the low mobility of screw dislocation compared with other types of dislocations, which is a result of anisotropy of the BCC lattice.

3.1.5   Low Temperature Dislocation Microstructure

As shown in Figure 3-8 [47], TEM micrographs of deformed molybdenum sample show characteristic features of long screw dislocations often stretching along many microns, with no or very little deviation from the perfect screw orientation. This anisotropy of dislocation microstructure directly reflects the anisotropy of dislocation mobility. In other words, the dominance of screw dislocations in the sample reflects their low mobility compared to other species of dislocations, e.g., edge dislocations. The pre-strained microstructure dominated by long screw segments is produced by rapidly moving edge dislocations under stress. This is verified by *In situ* TEM observations [69] where it has been shown very clearly that screw dislocations move much
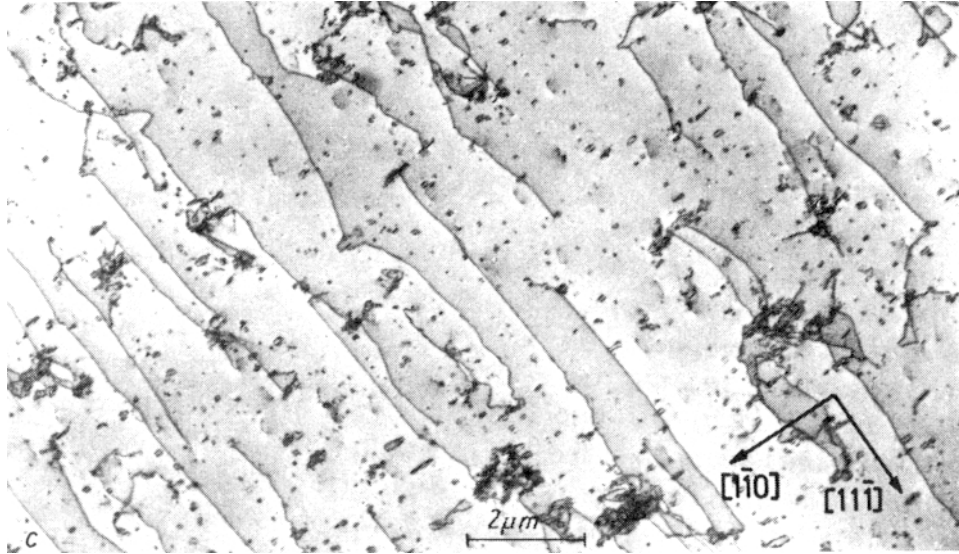
Figure 3-9: Dislocation microstructure in Mo under 5.8% tensile strain at 293K [47]. With higher strain and higher temperature, aside from the long screw segments, large amounts of debris are found in the form of vacancy and interstitial loops. Simulations [25] suggest this may be the result of cross slip of screw dislocations.

slower than edge and mixed dislocations at low and moderate temperatures. For example, in pure molybdenum at room temperature the velocity of screw dislocation has been estimated to be 40 times lower than that of edge dislocations [70, 71].[3]

Another common element of the low temperature microstructure in BCC metals is a high concentration of debris in the form of vacancy and interstitial loops, which are often observed after deformation, as shown in Figure 3-9 [47]. The debris concentration typically increases with increasing straining rate. As shown in kinetic Monte Carlo simulations by Cai et al [75, 25], this could be due to cross-slip of screw dislocations, where kink-pairs on different planes are nucleated on the same screw dislocation, non-planar defects (which is referred to by some as "cross-kinks" [76]) is formed as the kinks collide, and eventually the dislocation extracts itself from the

---

[3]It is worth mentioning that some early experimental measurements of dislocation velocities in Mo have suggested that screws actually move faster than edges [72, 73, 74]. Firstly, these measurements suffered from surface related enhancement of screw dislocation mobility; secondly, the method of using chemical etching on the surface to monitor dislocation motion in the bulk itself is highly inaccurate and prone to artifacts. Therefore we consider these measurements unreliable and not necessarily representative of dislocation mobility in the bulk.
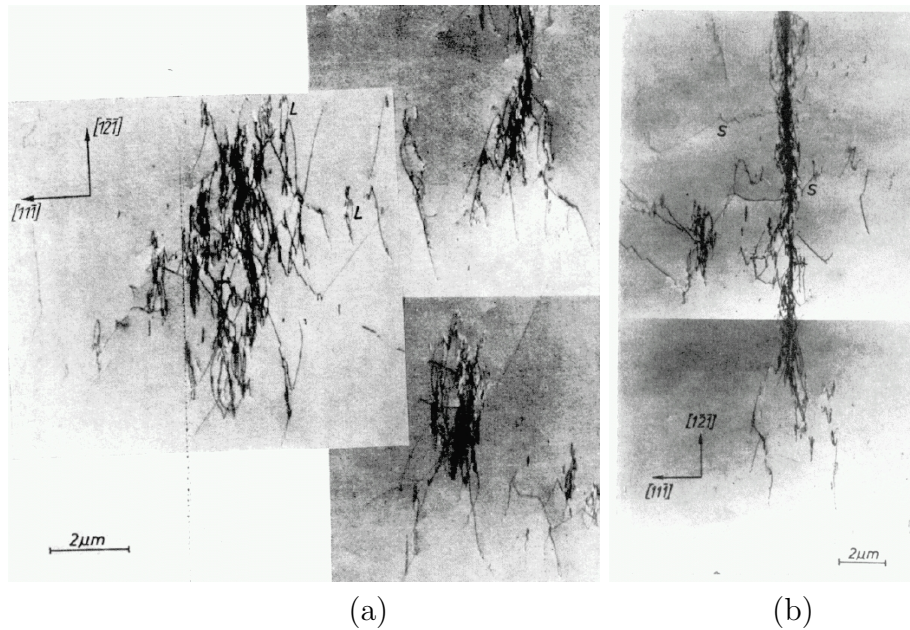
Figure 3-10: At 493K with 2.1% strain, dislocation microstructure of Mo differs substantially from that at 293K: (a) Edge dipoles and elongated loops. (b) Long bundle of primary edge dislocations [44].

conflict by moving by purely conservative double-kink nucleation, leaving a prismatic loop behind.

3.1.6 High Temperature Dislocation Microstructure

As shown in Figure 3-10, the dislocation microstructure at 493K differs substantially from that at 77K and 293K (Figure 3-8 and Figure 3-9). Screw dislocations can no longer be found, because the screws have gained high mobility at this elevated temperature and due to their ability to cross slip, they have annihilated with each other. What is left are the edge dislocations that are constrained to their glide planes and can not easily annihilate with each other. In Figure 3-10(a), the dislocation microstructure consists of edge dipoles and elongated loops; in Figure 3-10(b), dislocations are organized into long bundles of primary edge dislocations that are not connected with each other. At larger strains, formation of cellular structure have also been observed [45].

70

3.2 Core Structure of Screw Dislocations in Mo

At low temperatures the plasticity of BCC metals is controlled by screw dislocations. To understand the complex deformation behavior of BCC metals that have been discussed in the previous section, one first needs to understand the core structure and lattice resistance to straight screw dislocations. As one may soon find out, this problem, though of fundamental importance, have been discussed for a long time in the literature yet no convincing conclusions have been reached. This is indeed the motivation for this work where the issue of screw core structure will be addressed by a thorough review of existing research as well as careful atomistic calculations using a tight-binding potential model [77, 78].

3.2.1 Previous Research on Screw Core Structure in Mo

The rich research on core structure of screw dislocations in BCC metals is a direct reflection of the importance of the problem as well as the difficulty of solving it. Although the problem has not been completely solved yet, the long history of human's understanding of screw core in BCC has already become a classic and is worth while discussing here. The early ideas about the structure of screw dislocation core are centered around the hypothesis of FCC-like planar splitting for explaining the observed slip phenomenology [79, 80, 81]. In a drastic departure, Hirsch in the year of 1960 suggested that screws can actually dissociate in more than one plane and that such a non-planar dissociation behavior can explain the observed high Peierls barrier and the strong temperature dependence of the yield stress [82]. Initially, several variants of screw dislocation splitting were proposed (see Vitek's review article on this: [31]); however, with the advent of computer simulations, the thinking eventually converged to the well-known three-way dissociation into three equivalent {110} planes. Vitek et al [83, 31] and Duesbery et al [35, 26] have clearly shown that such a dissociation [4] can

---

[4] The term "dissociation" implies that the perfect screw dislocation splits into several partials or fractional dislocations, which does not seem to be appropriate for describing the screw core, we will refer to dislocation core spreading as "polarization", resulting from a symmetry-breaking core reconstruction.
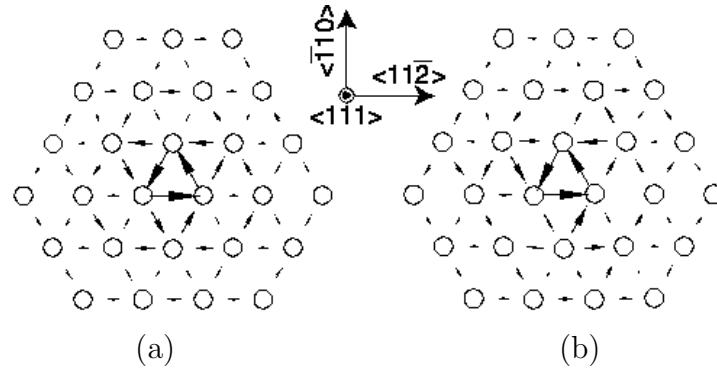
Figure 3-11: Differential displacement map of screw dislocation core in BCC metals, (a) unpolarized core [15, 84, 85], (b) polarized core [31].

occur even when no plane of the {111} zone contains a stable stacking fault. Vitek used differential displacement map to show the polarization of the screw dislocation core. As shown in Figure 3-11(b), it is quite clear from the differential displacement vectors (which plots an arrow between atoms, with the length of the arrow proportional to the relative displacement of these two atoms using perfect crystal lattice as reference) that the screw dislocation core in BCC Mo is polarized. Until this point, it seems that human thinking (Hirsch's idea) and computer modeling results (Duesbery and Vitek) have perfectly converged and the problem is solved; however, due to the inaccurate nature of the fitted semi-empirical potentials that Duesbery and Vitek used in their calculations, the results that they obtained can never be fully validated before it is checked by more accurate models, i.e., *ab initio* calculations. However, since modeling dislocation requires relative large number of atoms (at least in hundreds for screw problems and more for edges due to the spreading of the edge core in directions parallel to the Burgers vector), the checking had been practically impossible.

Not surprisingly, with the continuous-growth of available computing power and the growing availability of *ab initio* codes, the checking is finally made possible. In 2000, the *ab initio* calculation of screw core structure in molybdenum by Ismail-Beigi and Arias [15] surprisingly gives a different picture. Using a $5a[110]$ by $3[112]$ cell (90 atoms) that contains a dislocation quadrupole, this pioneering study resulted in

a relaxed core structure of screw dislocation that shows no D_3 symmetry breaking, i.e., the spreading of the core along only three out of the six possible $\langle 112 \rangle$ directions that was observed in previous calculations using Finnis-Sinclair or MGPT potential is now replaced by an even spreading of the core along all size $\langle 112 \rangle$ directions. Because of the extremely high dislocation density in this calculation (one dislocation per 25 atoms), this calculation may be subject to artificial effects and the results obtained are therefore not reliable. On the other hand, this calculation brings about a new picture of the screw core that can not be ignored. Indeed, this served as the motivation that drove several different research groups, including us, to calculate by themselves the core structure and Peierls stress of screw core structure.

In the following section, we will show that our calculation of the core structure for straight screw dislocations in bcc molybdenum actually verified the unpolarized core structure and a discussion will be in place as to the core polarization issue.

3.2.2 Setting Up the Atomic Configuration

Before setting up the atomic configuration, we need to first determine the geometry of the simulation cell. There are two major considerations:

(1) Since we are using periodic boundaries, we are bound to make the total Burgers vector zero, i.e., $\sum \vec{b_i} = 0$.

(2) We would like to make the stress field at the location of the simulated dislocation due to other dislocations in the primary cell and the image dislocations in the image cells zero. In other words, the forces on one dislocation from all other dislocations should cancel each other to arrive at zero.

Consider a screw quadrupole configuration as shown in Figure 3-12. The primary simulation box, which is shown with blue lines, has a square shape, i.e., $L_x = L_y = L$. X axis being the horizontal direction, Y the vertical direction, and Z normal to paper. The two positive dislocations are positioned at $(\frac{L}{4}, \frac{L}{4})$ and $(\frac{3L}{4}, \frac{3L}{4})$, while the negative dislocations at at $(\frac{L}{4}, \frac{3L}{4})$ and $(\frac{3L}{4}, \frac{L}{4})$. This quadrupole arrangement offsets the positive dislocation lattice and the negative dislocation lattice by exactly $(\frac{L}{2}, \frac{L}{2})$ and therefore makes all the image stress cancel to zero. The quadrupole setting
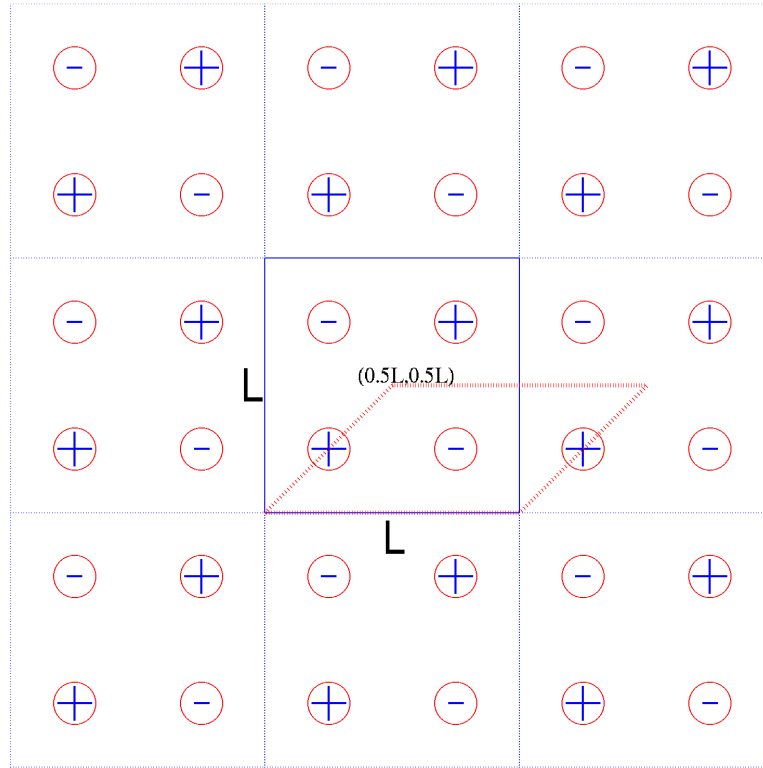
Figure 3-12: A quadrupole configuration with a square box shape makes the image stress zero and therefore is an ideal setting for simulating screw dislocations with small cells. However, the size of the cell can actually be reduced by half simply by redefining the box vector in Y as shown with red dotted lines.

is therefore an ideal choice for modeling dislocations in small cells. Indeed this is similar to the configuration that Ismail-Beigi and Arias used in their calculation. It is exactly because of the cancellation of the image forces on each dislocation that made the relaxation within such a tiny cell converge.

However, it should not be hard for one to notice that the simulation box can be redefined in many ways to cut the box size by half yet producing exactly the same configurational settings. Shown in the figure (red dotted lines) is one way of redefining the box where $\vec{L_X}$ remains unchanged but $\vec{L_Y}$ are redefined. Not only the

X component of $\vec{L_Y}$ is added by $\frac{L_X}{2}$, but also the Z component of $\vec{L_Y}$ need to be added by $\frac{b}{2}$, where b is the Burgers vector. This can be seen from the fact (L, L) is a lattice repeating vector whereas $(\frac{L}{2}, \frac{L}{2})$ is not. In order that no artificial defect is being created due to incompatibility of the box vector, $\frac{b}{2}$ must be either added or subtracted from $\vec{L_Y}$'s Z component.

After redefining the box vector, one can simply keep half of the original atoms who satisfy $0 < Y_i \leq \frac{L}{2}$ and map them into the new box which now contains a screw dislocation dipole instead of a quadrupole but have a tilted shape.

Similarly, one can also redefine a dipole box that has its vertices at $(\frac{L}{4}, \frac{L}{4})$, $(\frac{3L}{4}, \frac{3L}{4})$, $(\frac{5L}{4}, \frac{L}{4})$, $(\frac{3L}{4}, -\frac{L}{4})$. In this case, the Z component of L_X and L_Y both need to be adjusted by $\frac{b}{2}$.

Although seemingly trivial, this reduction of size is vital for the size-sensitive DFT studies. Since now we can study exactly the same problem with half number of atoms and the scaling of DFT computational cost with number of atoms is approximately 3, we have saved the computational cost by roughly 87 percent!

3.2.3 Preselection of Cell Size

In this study, the coordinate system is aligned as: $\vec{X}$: $[11\bar{2}]$, $\vec{Y}$: $[\bar{1}10]$, $\vec{Z}$: $[111]$. The dislocation line is along $\vec{Z}$. Since we study straight screw dislocations only, there is no need for L_Z to be big. In all the tight-binding studies, we use $\vec{Z}=\frac{1}{2}[111]$, i.e., exactly 1 layer in Z direction. For the empirical potential calculations, since there is a requirement that box dimension must be at least two times potential cutoff length, we have adopted 3 layers, therefore the total atom number is also 3 times that of tight-binding system.

Before the tight-binding calculations, we first looked at the size-dependence of the relaxed core structure using empirical potentials. Using Finnis-Sinclair potential, we created and relaxed several configuration of different sizes: Config $A_{3\times5}$: $3a[11\bar{2}] \times 5a[[\bar{1}10]$ Config $A_{5\times7}$: $5a[11\bar{2}] \times 7a[[\bar{1}10]$ Config $A_{7\times11}$: $7a[11\bar{2}] \times 11a[[\bar{1}10]$

Relaxation of these structures yielded different results. For Config $A_{3\times5}$, the created quadrupole configuration is not stable and the structure relaxes back to perfect
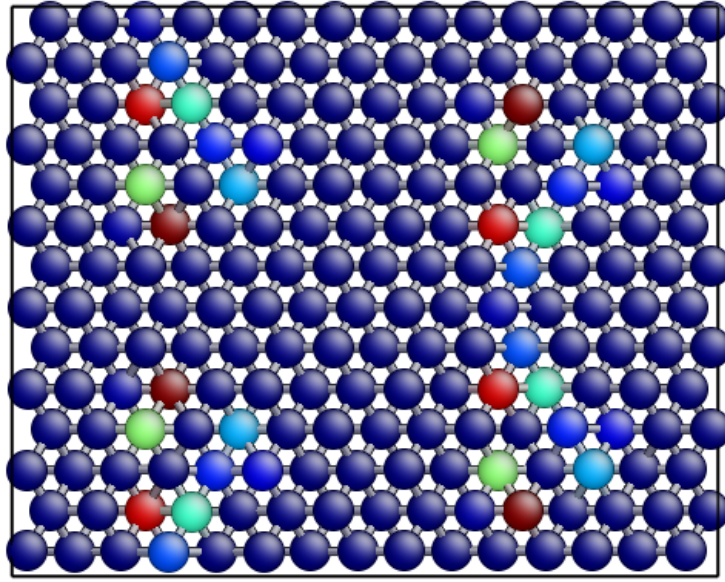
Figure 3-13: Config $A_{5\times7}$ relaxed using Finnis-Sinclair. Atoms color-encoded by local shear strain.

BCC crystal structure. This implies that the dislocations under this setting is indeed too close to each other and the size of the cell (proportional to the distance between the dislocations) should be increased. Interestingly, this structure is actually stable in the DFT calculations by Ismail-Beigi and Arias as well as our tight-binding calculations, which will be shown soon. Under Finnis-Sinclair model the screw core will extend along 3 of the 6 possible $\langle 112 \rangle$ directions and that makes the annihilation of the screw dislocations separated by only 10Å unavoidable.

The other two configurations do properly relax and the relaxed configuration is shown in Figure 3-13 and Figure 3-14 respectively, with the atoms color-encoded by local strain. For the ease of viewing, the dipole configuration is restored to the quadrupole orthogonal coordinate system.

Color-encoding with local strain helps us see the core qualitatively, but does not give us quantitative details about the core structure. Similar to plotting misregistry between two atomic rows for a planar edge dislocation core to analyze the core profile, we shall plot the differential displacement map to visualize the screw core structure,
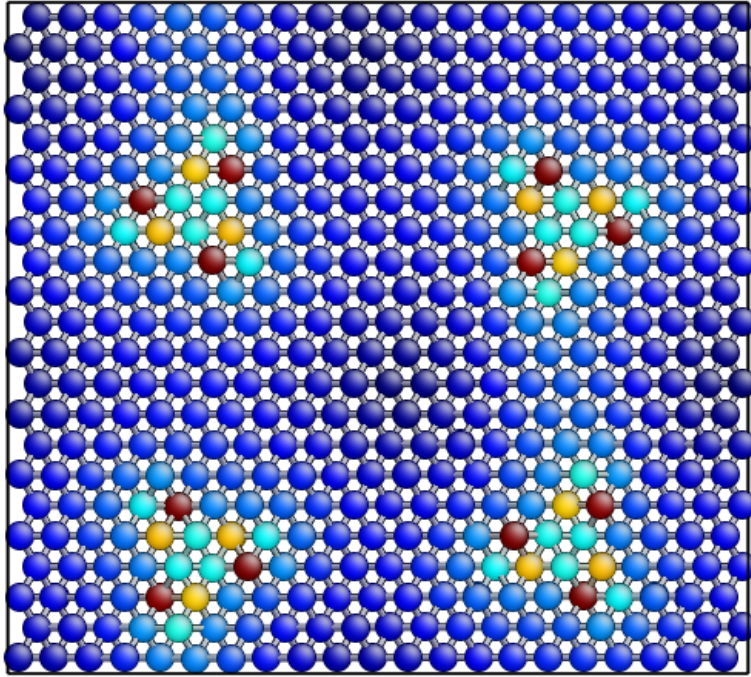
Figure 3-14: Config $A_{7\times 11}$ relaxed using Finnis-Sinclair potential.

as is explained below.

Figure 3-11 shows differential displacement maps (DDM) [86] of screw disloca-
tions. Each circle represents a column of atoms. The dislocation line and Burgers
vector are parallel to the atom columns, i.e. along z direction (out of the plane). The
DDM map is constructed by first computing the atom displacement (along z direc-
tion) with respect to perfect lattice for each column. The arrows then indicate the
difference between displacements of neighboring columns. The length of the arrow
is proportional to the magnitude of displacement difference and the direction of the
arrow indicate the sign of the displacement difference, i.e. the column that the arrow
points to has a larger displacement than the column on the other end of the arrow.
Because the lattice is periodic in z direction by Burgers vector b, the displacement
difference, i.e. the differential displacement, between any two columns can be only
defined *modulo b*. By convention, the differential displacement is always mapped into
the domain of $(-b/2, b/2]$ by adding or subtracting multiples of b. Among the three
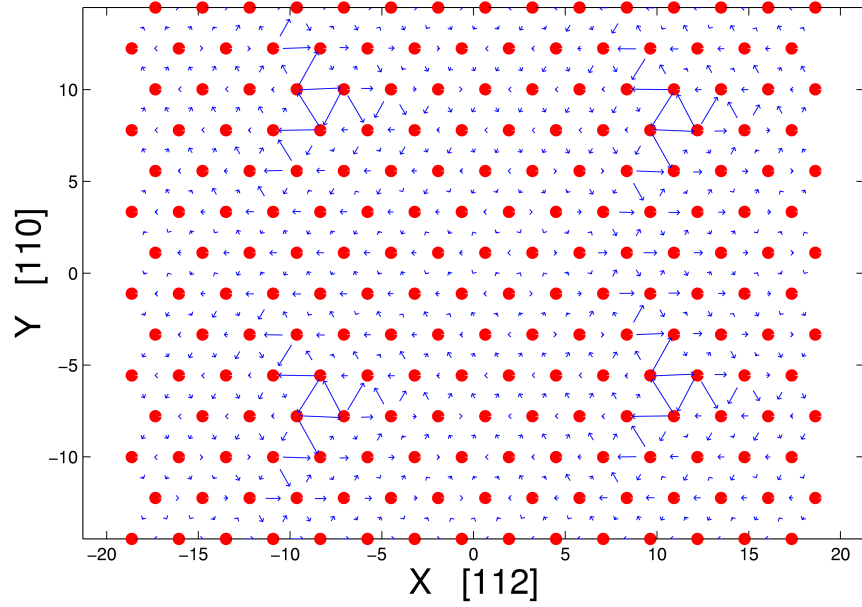
Figure 3-15: DDM for Config $A_{5\times 7}$ relaxed using Finnis-Sinclair.

atoms in Figure 3-11(a) that surround the center of dislocation, the DDM arrows form a closed circuit. The differential displacement between any two atoms out of these three, going counterclockwise, is $b/3$. By going around any circle containing the dislocation center, one accumulates a total displacement b. We should emphasize that while the arrows in the DDM are all in the plane for convenience of visualization, the displacement component they represent is strictly out of the plane.

Now we plot the differential displacement maps for the two relaxed configurations that we obtained using Finnis-Sinclair potential. The results are shown in Figure 3-15 and Figure 3-16, respectively.

From the DDM of the 5×7 configuration, one can see that the extended arms of screw cores have obviously touched each other and may cause inaccuracies in both predicting the core structure and the Peierls stress (τ_P). Therefore we choose 7×11 configuration as the one used in the following tight-binding studies.

78
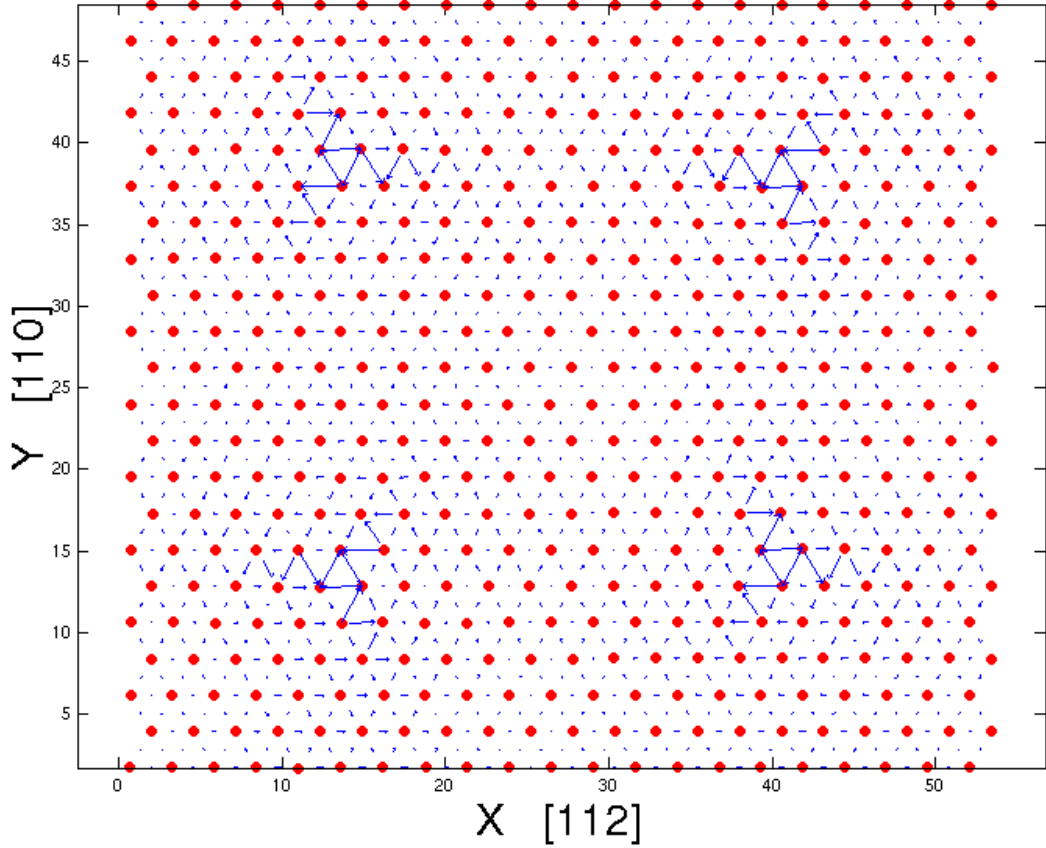
Figure 3-16: DDM for Config $A_{7\times11}$ relaxed using Finnis-Sinclair potential.

3.2.4 Core Structure from Tight-Binding Model

Starting from the configuration that we pre-selected from FS calculations, i.e., $\vec{X} = 7a[11\bar{2}]$, $\vec{Y} = 11a[\bar{1}10]$, $\vec{Z} = 1b$, we calculate screw core structure in Mo using an environment-dependent tight-binding potential model [77, 78]. The differential displacement map of the relaxed configuration is plotted in Figure 3-17. The screw core is evidently unpolarized as compared to the polarized core in Figure 3-16.

Looking in more details at the two different kinds of screw cores given by empirical potential and tight-binding, one finds that regardless of the details of misfit distribution, the core is rather compact. Similar to the core spreading predicted by Peierls-Nabarro model in the planar core case, the screw core spreads into the planes
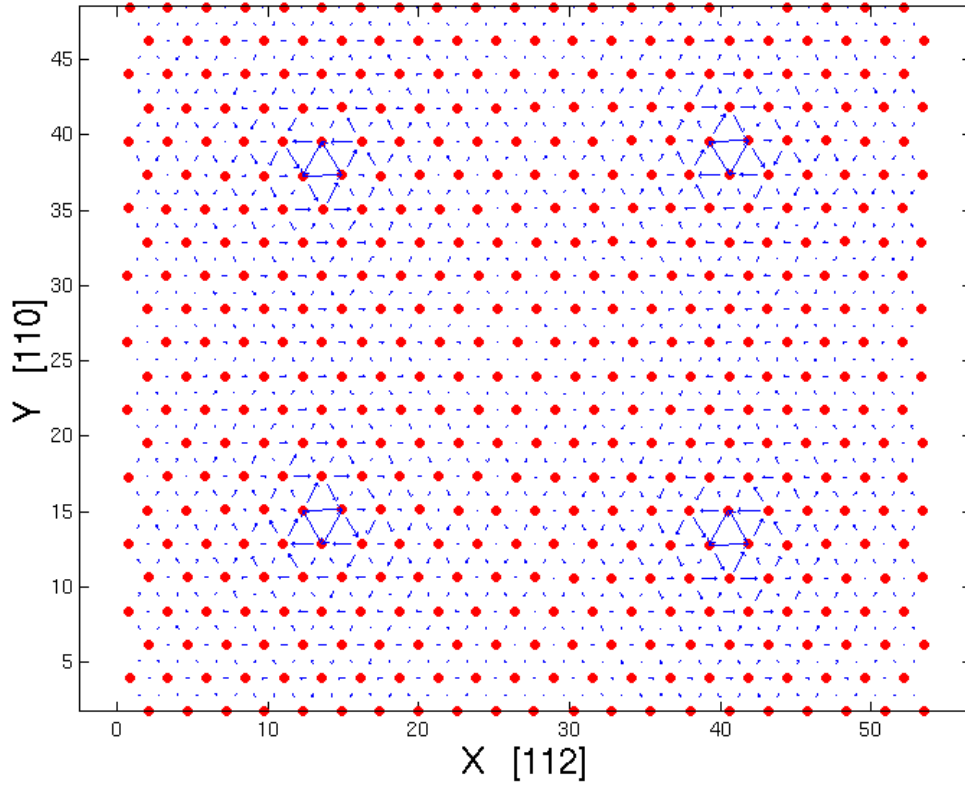
Figure 3-17: DDM for 7×11 configuration relaxed using an environment-dependent tight-binding potential [77, 78].

of the {111} zone to reduce elastic-energy. Unlike in the 1D planar core case, it is not directly obvious in which directions and planes does the spreading entail. The fine structure of the core is dependent on subtle details of atomic interactions in the core. As already discussed, some atomistic models predict nearly equal core extensions in all directions (therefore giving a unpolarized core) while others show a characteristic splitting into three $\langle 112 \rangle$ directions on {110} planes of the zone (predicting a polarized core). Regardless of whether the core is polarized or not, the compactness of the screw core is expected to give rise to a large Peierls stress, which is an effect described by the Peierls model of dislocation core. It is evident that, for a dislocation to translate from one lattice position to the one adjacent, the more extended the core the less each atom in the core has to move relative to its neighbors. While clearly

more atoms take part in the translation of a wider core, the Peierls barrier for the wider core is lower because of the highly non-linear character of interatomic interactions in the core. This effect is also seen from a well known correlation between the core width and Peierls stress in FCC metals [87]. The opposite effect can also occur - a dislocation with narrow core, notably in Si, can have very high Peierls stress, approaching the ideal shear resistance of the crystal [88].

The detailed structure of screw dislocation core in BCC metals has been examined extensively through atomistic simulations [89, 90, 15, 91, 92, 93, 85], particularly with regard to the effects of in-core relaxation. Most of the earlier calculations predicted a polarized core structure that was seemingly observed in HREM experiments [94], while some recent calculations predicted an unpolarized core, as in this tight-binding calculation. The reason why polarization is considered an important issue and have attracted such intense research efforts is that the details of the atomic rearrangement in the dislocation are believed to have an effect on the lattice resistance to dislocation motion, i.e., Peierls stress τ_P. As we proceed to quantify the Peierls stress for the polarized core, we shall soon uncover whether core polarization plays an important role in determining τ_P or not.

3.3   Lattice Resistance to Screw Dislocations in Mo

Peierls stress, a simple measure of lattice resistance, can be measured by atomistic models. However, two major errors may arise in such a calculation: interatomic potential and boundary conditions. On one hand, empirical potentials are usually fitted to equilibrium properties, so there is no guarantee it will work properly at large strains. On the other hand, more accurate methods, i.e., tight-binding models (TB) and density functional theory (DFT) provide accurate energetics but it has severe size limits, so core overlapping and image stress effects are significant and may introduce significant error to modeling results. Added to these are the difficulties in extracting the Peierls stress from atomistic calculation results in periodic boundary conditions (PBC) where both image stress due to PBC and inaccuracy in virial stress can give

rise to significant errors, as will be shown in the next chapter, where the calculated critical virial stress for edge dislocation varies by more than one order of magnitude when cell geometry is changed.

A systematic scheme circumventing the above difficulties is to use so-called First-Principles Greens Function Boundary Condition (FP-GFBC) to study a single dislocation [85]. This method eliminates the need of using the periodic boundaries and can be used to model a single dislocation. Alternatively, we have developed formalisms for PBC calculations to extract the core energy and Peierls stress [95, 7, 8] that manifests invariance with respect to supercell geometry, position and direction of the dislocation dipole.

On the current problem of screw dislocations in BCC molybdenum, we apply these methods to model both core energy and Peierls stress using both the Finnis-Sinclair potential [20, 96] and the tight-binding model [77, 78].

The Finnis-Sinclair potential [20, 96], which have been shown to predict a polarized screw core, gives a core energy of 0.300 eV/Å at $r_0 = b$ and a Peierls stress of 1.9 GPa. The energy (E) and energy difference (ΔE) curve used in the local driving force method calculation of Peierls stress is shown in Figure 3-18.

The tight-binding potential, which predicts an unpolarized screw core, gives a core energy of 0.371 eV/Å at $r_0 = b$, and a Peierls stress of ~ 3.6 GPa. The energy (E) and energy difference (ΔE) curve used in the local driving force method calculation of Peierls stress is shown in Figure 3-19.

Upon careful examination of the core structure evolution as the strain is gradually increased, we have found that the unpolarized core structure which is calculated to be the ground state at zero stress soon changes from non-planar to almost planar, as shown in Figure 3-20. This suggests that whether the core is polarized or not at zero stress state may not be important to its mobility at all, whether it is planar or not is. Non-polarization is much more a minor issue compared with non-planarity.
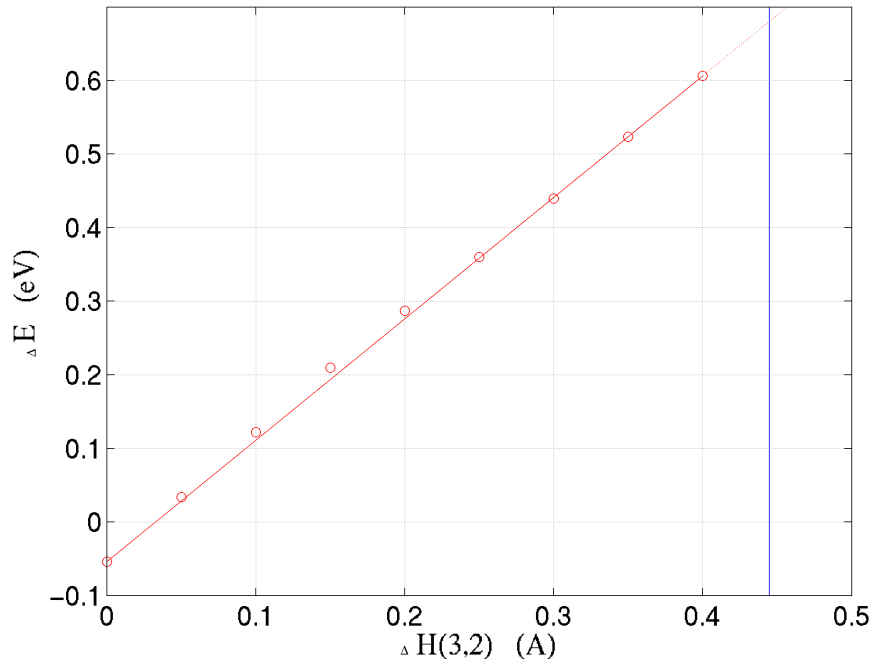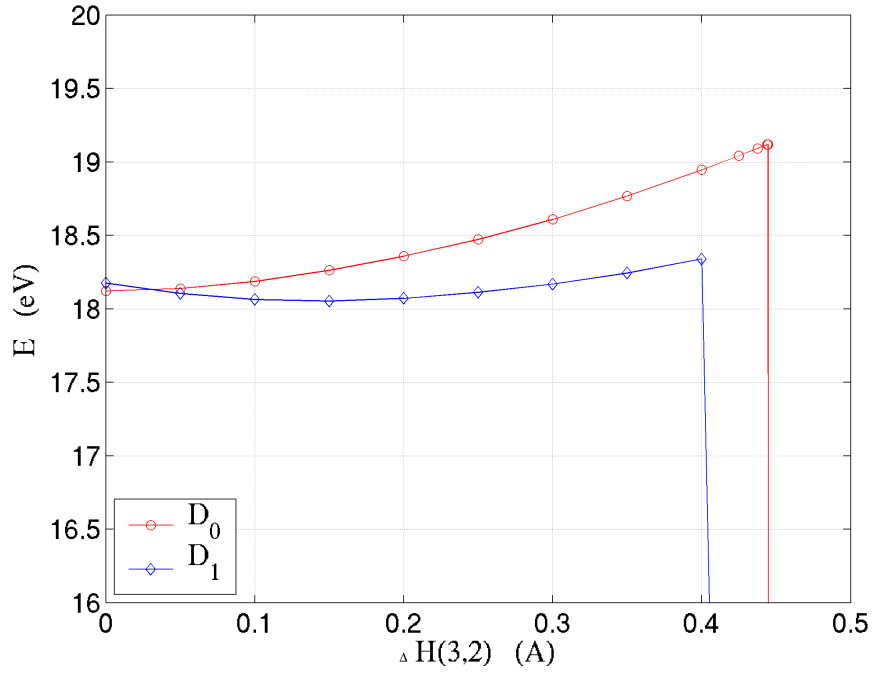
Figure 3-18: Evaluating τ_P with the local driving force method using Finnis-Sinclair potential model relaxation results. (a) E. (b) ΔE. D_0 and D_1 correspond to the two dislocation configurations where the dislocation sits at $x = 0$ and $x = b$, respectively.
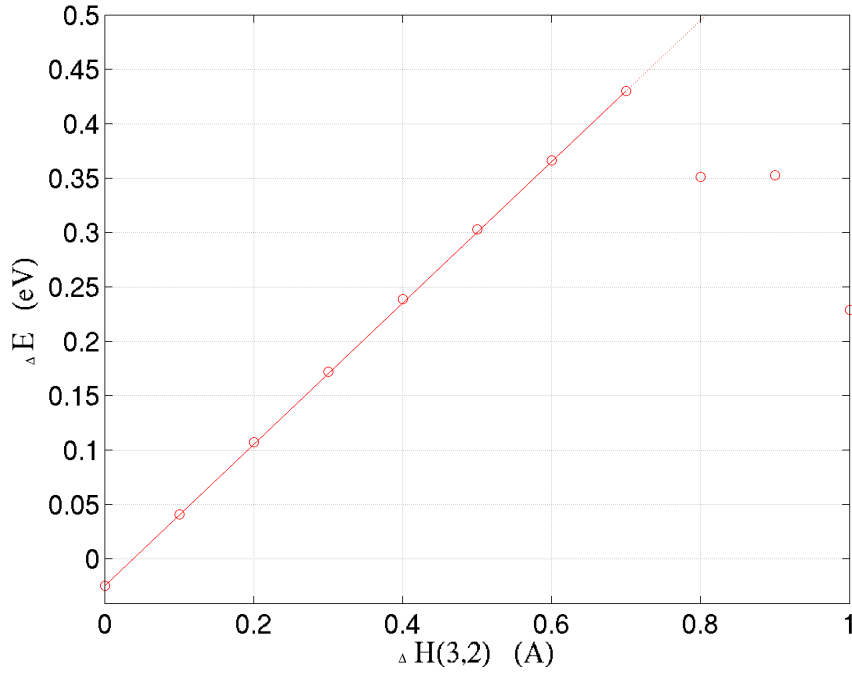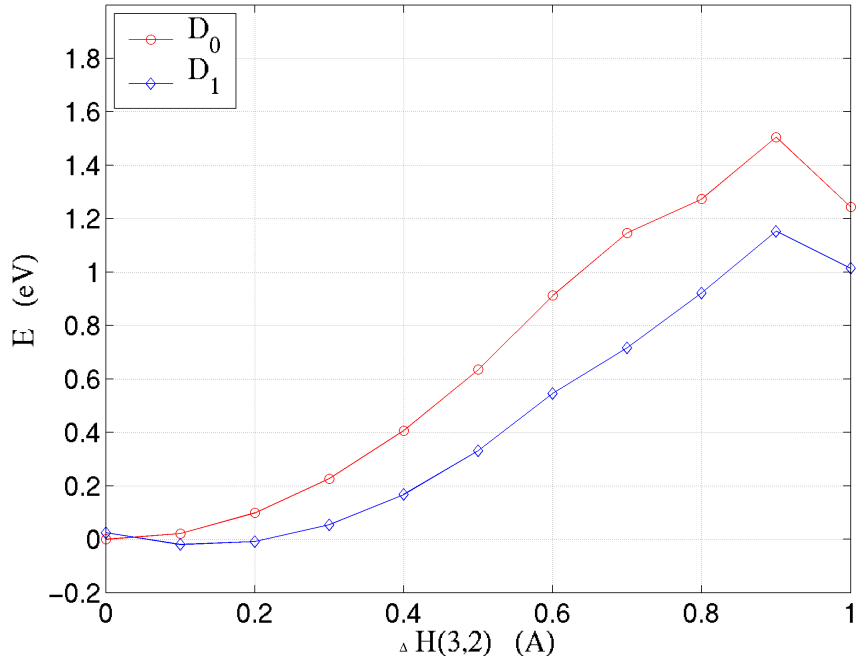
(a)

(b)

Figure 3-19: Evaluating τ_P with the local driving force method using tight-binding model relaxation results. (a) E. (b) ΔE. D_0 and D_1 correspond to the two dislocation configurations where the dislocation sits at $x = 0$ and $x = b$, respectively.
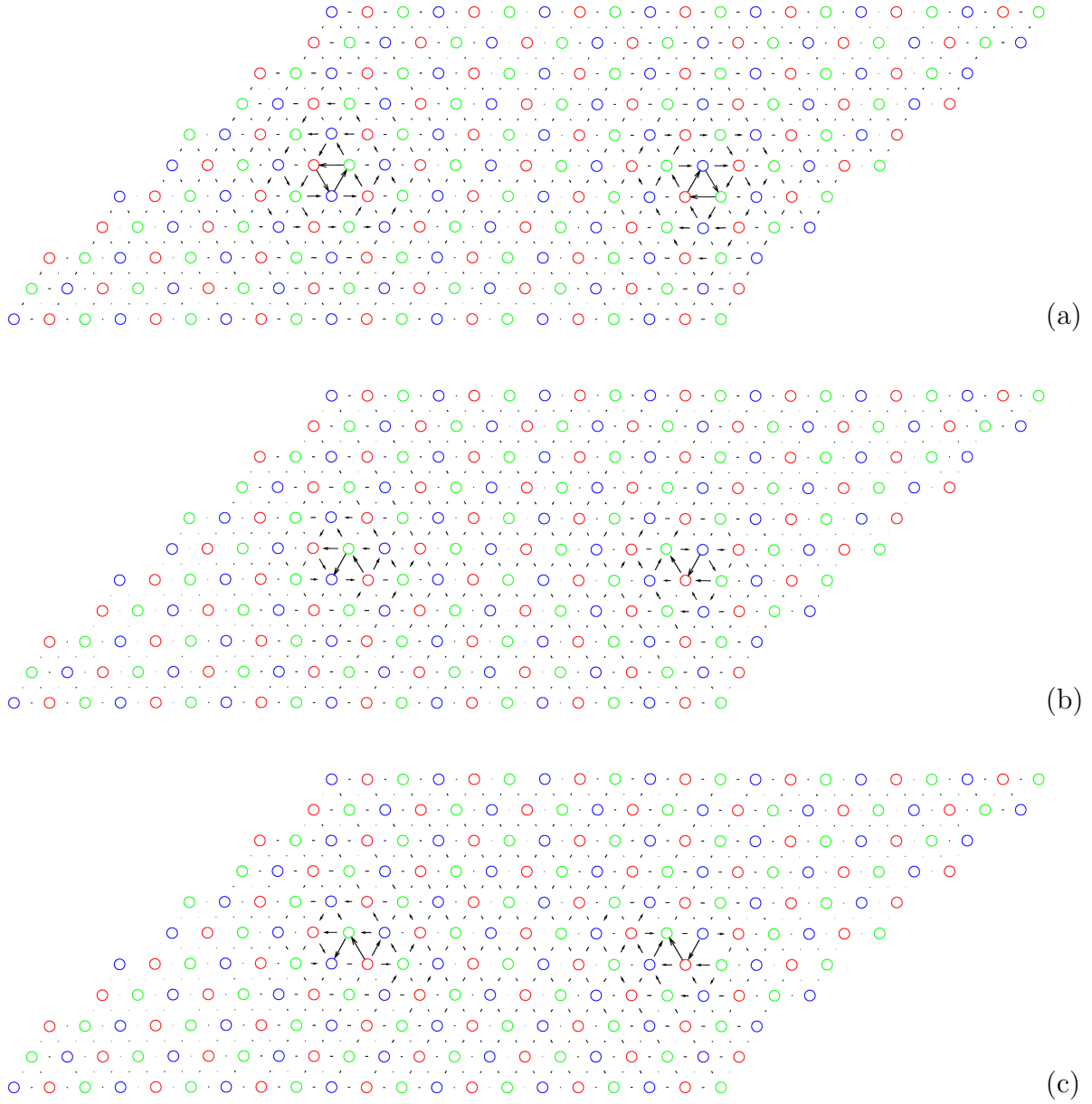
Figure 3-20: Differential displacement map of Mo screw dislocation under stress. As stress increases, the Mo screw core changes from non-planar to almost planar.

3.4 Summary on Core Structure and Peierls Stress for Straight Screw Dislocations

Using a tight-binding model, we have calculated the core structure, core energy, and the Peierls stress for straight screw dislocation in BCC Mo. In contrast to the results given by previous empirical potential calculations that predicted polarized screw core, and in agreement with recent *ab initio* calculations that predicted non-polarized core structure, the core structure we have obtained at zero stress state is not polarized. This leads us to believe that the polarization effect predicted by the empirical potentials may be an artifact of the potential models.

However, the core polarization issue may not be an important factor in determining the mobility of the screw dislocation. This view is supported by our calculation of Peierls stress at 3.6 GPa and the calculation by Rao and Woodward as well [85]. Our observation that the core undergoes profound changes from non-planar to almost planar shape as applied stress is increased further validates our view that whether the core is polarized at zero stress state is not of primary importance in the screw mobility picture. Similar effects indeed have been reported before by Duesbery and Vitek [30, 32] where the dislocation core structure changes profoundly under shear stress approaching the maximum (Peierls) sustainable level effectively wipe out the features of core structure observed at zero stress.

In this tight-binding study, we have applied shear stress strictly on {110} plane. However, if we vary the orientation of the shear loading and therefore the orientation of the maximum resolved shear stress plane (MRSSP), it is expected that the variation of CRSS will be in violation of Schmid law. Due to constraints in available computational power, an atomistic study of non-Schmid effects using tight-binding model is beyond our reach at this stage. In the following text, we will review and discuss existing results obtained by semi-empirical potentials in the literature.

In atomistic simulations when the applied stress reaches the Peierls value, a screw dislocation responds by moving along one of the crystallographic planes of the $\frac{1}{2}\langle 111 \rangle$ Burgers vector zone, most often a {110} plane closest to the MRSS plane. Depending
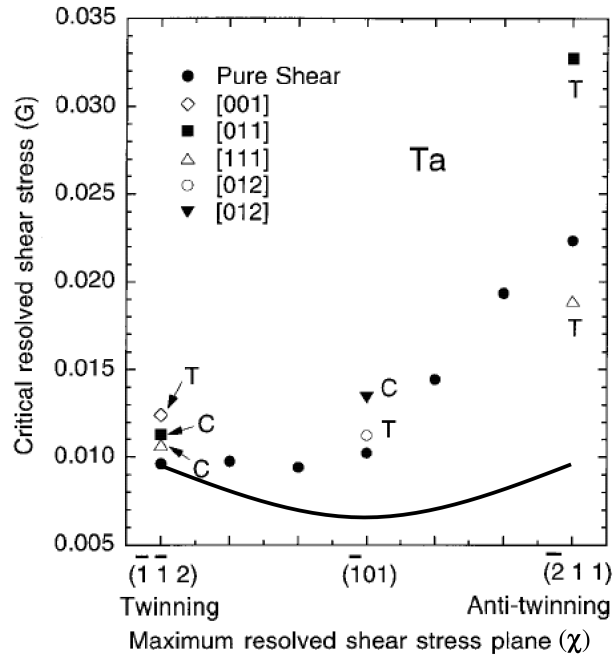
Figure 3-21: Screw dislocation Peierls stress for different loading stress directions in the {111} zone. The solid line shows the prediction of Schmid law and the symbols show typical atomistic simulation results [91].

on the interatomic potential, the translation plane can be {112} [32] as well. For example, the FS model potential predicts that screw dislocations in Mo move along {110}, but in Ta they move along {112} [26]. Also, screw dislocations simulated by using Finnis-Sinclair's model of bcc-Fe are observed to move on either a {112} or a {110} plane depending on the orientation of the MRSS plane [97]. The slip-plane selection and critical stress condition for screw dislocations are clearly in violation of the Schmid law [98]. For example, in cases where the screw dislocations show a definite preference to glide, say, on {110} plane the Schmid law specifies which of the three {110} planes of the zone will be selected, as well as the level of applied stress σ_{ij} at which the dislocation should begin to move, the latter being given by

$$\sigma_{ij}s_{ij} = \tau_{PN} \; , \tag{3.1}$$

where τ_{PN} is the Peierls stress and s_{ij} is the Schmid tensor of the given plane. For a

pure shear stress σ applied along the Burgers vector, the relation reduces to

$$\sigma = \tau_{PN} / \cos(\chi), \tag{3.2}$$

where χ is the angle between the MRSS plane and the nearest {110} plane. Relative to the Peierls stress for $\chi = 0$, the Peierls stress variation specified by the Schmid law is shown in Fig. 3-21. The variation simulated using an atomistic model of Mo, also shown, is clearly in considerable disagreement with the Schmid law [99, 98]. This and almost all other atomistic calculations reported so far showed that the motion of screw dislocation in BCC metals at low temperature does not follow the prescriptions of Schmid law [98]. The origin of the non-Schmid behavior is largely due to the twining-anti twining asymmetry of the BCC lattice, which makes $\chi = 30°$ and $\chi = -30°$ drastically different from each other. In addition to the non-Schmid χ-dependence, other stress components have been found to affect the critical stress, most notably the components perpendicular to the Burgers vector [100, 101, 102]. Duesbery and Vitek [26] traced such non-Schmid effects to a coupling between the applied stress and a small but resolvable edge components of displacement observed in the core of the screw dislocations. An extensive and thorough analysis of various non-Schmid couplings affecting the motion of screw dislocations in BCC metals was presented by Duesbery in [24].

3.5 Kinks on Screw Dislocations

As we have inferred from experimental observations [69] as well as direct calculations using atomistic methods, the Peierls stress of a screw dislocation is considerably higher than that of non-screw components; therefore, it is usually assumed that the macroscopic yield stress at low temperatures is closely related to this stress, or more generally, the critical stress to move the screw dislocation.

A Peierls stress of GPa order signifies a correspondingly high energy (Peierls) barrier and motion of screw dislocation at non-zero temperatures via thermally and

stress-activated kink mechanisms.

The model we have used so far have been of quasi-2D nature that has no thickness in dislocation line direction. To model kink mechanisms, we have set up a 3D MD simulation where a pre-existing kink has been put on to the straight dislocation dipole, as shown in Figure 3-22.
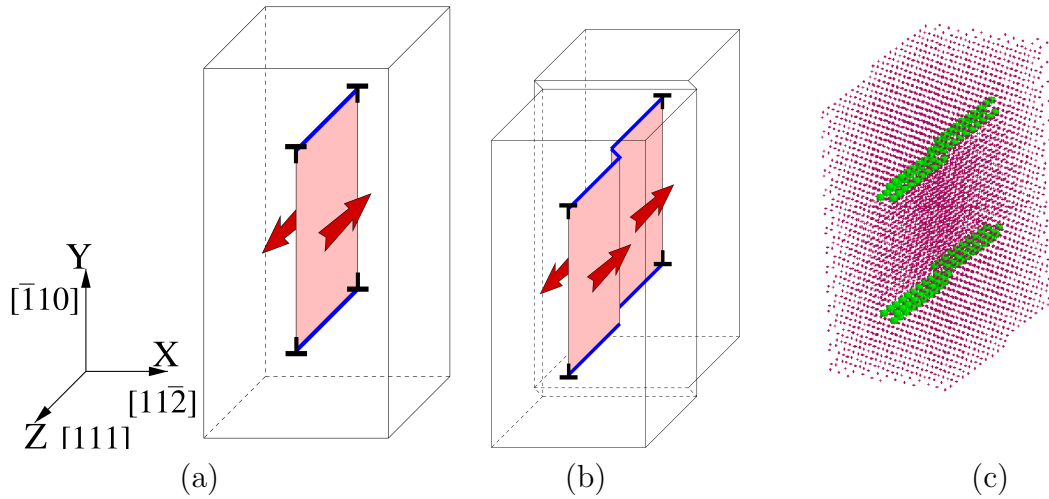
Figure 3-22: (a) Creation of screw dislocation dipole in a PBC simulation cell by displacing the two layers of atoms besides the cut plane by b relative to each other, followed by force relaxation. (b) Creation of kinks on screw dislocation by putting two copies of cells in (a) with an $1/2[11\bar{1}]$ in between. (c) Atomic arrangement of (b).

As shown in Figure 3-22(a), taking a cell with box vectors $4[11\bar{2}]$, $14[1\bar{1}0]$ and $5[111]$, we make a cut on the $(11\bar{2})$ plane and displace the two adjacent layers of atoms by $b = 1/2[111]$ relative to each other. The remaining atoms are displaced according to the linear elastic displacement field of the dislocation dipole under PBC, and the atomic arrangement relaxed using conjugate gradient. As shown in Figure 3-22(b), we create kinks on the two screw dislocations by placing two copies of the cell in (a) with an $1/2[11\bar{1}]$ offset between them. The basis vector along the dislocation line is redefined; it is no longer parallel to [111], so that the kink leaving the cell at one end re-enters the cell from the other end [5] The configuration is then relaxed by conjugate

___

[5]In fact, an additional number of atoms need to be inserted between the cut planes of the two

gradient method yielding the atomic arrangements in Fig 3-22(c).

The critical stress to move the kink at zero temperature is estimated to be $\sim$ 20MPa using static relaxation method. This value is comparable to the Peierls stress for straight edge dislocations ($\sim$ 25 MPa, as will be presented in the next chapter), indicating the high mobility of kinks on screw dislocations. This is also in agreement with Duesbery's early observations that that nucleated kinks experience very low resistance to their motion along the screw line [33].

This also means that the kink migration barrier is indeed low relative to the kink-pair nucleation barrier and the energy of a stand-alone kink [90, 28].

Furthermore, we apply a shear stress of $\tau = 40$ MPa to the simulation cell at $T = 300K$ and zero pressure and find the pre-existing kink on screw is highly mobile and the drag coefficient is estimated from its velocity and the applied stress to be $B = 4.5 \times 10^{-5} Pa \cdot s$, even slightly lower than that of straight edge dislocations under the same condition ($1.8 \times 10^{-4} Pa \cdot s$).

What we have learned from above calculations is that the lattice resistance to kinks on screw dislocations is negligibly small, comparable to that of edge dislocations. This finding, verified by both static relaxations and finite-temperature calculations, infers that kink nucleation rather than kink migration is the controlling mechanism for screw dislocations in BCC metals. Indeed, the experimental data of temperature dependence of CRSS shown in Figure 3-6 is found to be in excellent agreement with a kink nucleation model proposed by Argon [50].

---

cells. This is because the cut plane between the two cells are not parallel to the Burgers vector. The number of atoms to be inserted can be calculated from [10].

Chapter 4

Core Structure and Peierls Stress: Edge Dislocations in Mo

This chapter presents atomistic studies on core structure and Peierls stress, τ_{PN}, for edge dislocations in BCC metal molybdenum. Using a Finnis-Sinclair potential [20, 96], the core structure of the edge is found to be planar and $\sim 11\text{Å}$ wide. The critical stress to move an edge dislocation is calculated using different simulation cell geometries and it is found that the calculation results varies significantly with the aspect ratio of the simulation cell, from 630MPa for an aspect ratio of 0.8 to 25MPa for aspect ratio of 4. As the aspect ratio is increased, the calculated critical stress converges to 25MPa, which is the true Peierls stress τ_{PN} for edge dislocations in Mo. Comparing to previous calculation of τ_{PN} quoted in the literature [3] which yielded a rather high τ_{PN}, of $400 - 700$MPa, the author believes that the previous calculation gave an over-estimation of true τ_{PN} due to lacking of correction for boundary effects which is an artifact introduce to the simulation by boundary conditions that are used and should be taken out. The corrected τ_{PN} provides a more consistent picture of edge dislocation mobility.

4.1 Background

As have been reviewed in the previous chapter, from experiments people have found that there are two important types of dislocations in Mo. Screw dislocations control the low temperature plasticity while edge dislocations are important at high temperatures because screws become more mobile at elevated temperatures and can annihilate with each other through cross-slip while edge dislocations are confined to their glide planes. In other words, the inability for edge dislocations to climb easily at high temperature resulted in the experimental observation of edge dipoles and elongated dislocation loops, as shown in Figure 3-10.

The slip system most commonly observed for edge dislocations in molybdenum is $(\{110\}\langle 111\rangle$ and this will be the slip system we study in this chapter.

Since edge dislocations are observed to be extremely mobile, it is expected that the lattice resistance to edge dislocation motion, characterized by Peierls stress τ_{PN}, should be rather low. In the literature, we have found no direct measurement of the critical stress to move the edge dislocation in molybdenum; however, a rather crude estimate of τ_{PN} can be made from experimental results. Combining the experimental observations that edge dislocations move $\sim 25 - 40$ times faster than screws [69] and that the yield stress of Mo at low temperatures which is controlled by screws has an extrapolated value of ~ 800MPa at 0K, a rough estimate of lattice resistance to edge dislocation can be made to be ~ 30MPa. However, previous calculation of τ_{PN} by Duesbery and Xu [3] yielded a τ_{PN} of $400 \sim 700$ MPa for edge dislocation in molybdenum using Finnis-Sinclair potential [20]. This value is rather high and intuitively contradictory to the experimental knowledge of edge dislocations in Mo. Although the authors argued that kinks on edge dislocation can be used to explain the high mobility of edges since the critical stress required to move a kink on edge dislocation is much lower than the value calculated for straight edge dislocations, the argument is not convincing and the overall picture for edge dislocation mobility become a confusing one.

On the other hand, with the tools (PBC image effect evaluation) and insights we

gained (magic box geometry that makes image effect diminish) in Chapter 2, it seems necessary and natural to apply the new methods to re-calculate the τ_{PN} for a more reliable number. This is the main task of this chapter and will be discussed in details soon.

4.2 Core Structure of Edge dislocation

Using an improved version of Finnis-Sinclair potential for molybdenum [20, 96], the ground state of edge dislocation core in Mo is calculated by first preparing an atomic configuration that contains an edge dislocation dipole under PBC and then relaxing it (minimizing total energy of the simulated system).

The dimension of simulation cell is chosen to be $20a[111]$ (109Å) in $\vec{X}$ direction, $80a[\bar{1}01]$ (356Å) in $\vec{Y}$ direction, and $3a[1\bar{2}1]$ (23Å) in $\vec{Z}$ direction, with a total of 58320 Mo atoms. The edge dislocation dipole is introduced and the location of the two edge dislocations are $(0.25, 0.25)$ and $(0.25, 0.75)$ in the reduced coordinates. Burgers vector is $\vec{b} = \frac{a}{2}[111]$ with length $b = \frac{\sqrt{3}}{2}a = 2.7256$Å.

The cell dimension in $\vec{X}$ and $\vec{Y}$ are chosen such that the aspect ratio is approximately 3.5 and as predicted by anisotropic linear elasticity as well can be confirmed by real atomistic static relaxation calculations, the artificial image energy barrier for the single dislocation when it is moving along the glide plane is approximately 5×10^{-4} eV/Å, shown in Figure 4-2. Therefore, the image effect introduced in this simulation settings is negligible. This ensures that during the relaxation process, the edge dislocation will be indeed pinned down at the lattice site where it was introduced into by the lattice energy barrier, rather than the image energy barrier that is introduced artificially due to the periodic boundaries.

Indeed, if the image energy variation is big, see Figure 4-1, it is also possible that the whole energy landscape is dominated by this artificial variation and the dislocation introduced at the initial lattice site may become unstable and move during the process of relaxing the configuration. Even worse is that it will not stop at the global minimum, instead it may stop in the midway and get trapped by the
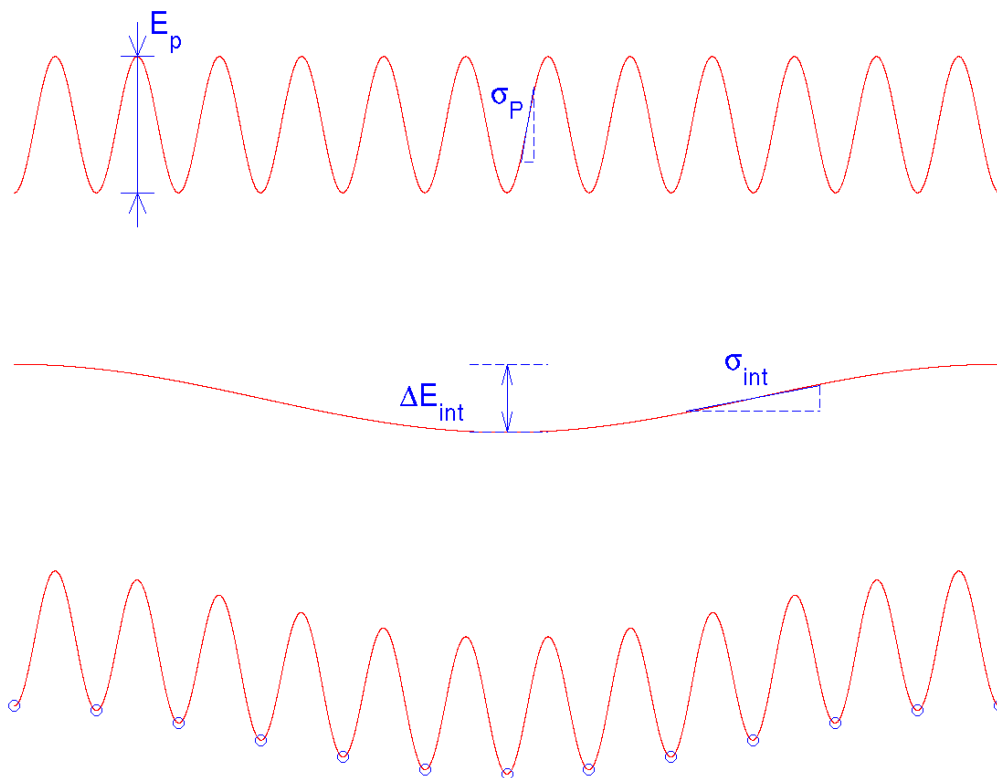
Figure 4-1: Top figure shows the ideal picture of periodic energy variation as a function of dislocation position along the glide plane in the Peierls framework. This is impossible to reproduce in simulations because of boundary effects introduced. In the case of periodic boundaries, the energy landscape will be modified by a superposition of the original energy landscape (which has the periodicity of $1b$ and the artificial image energy curve (which has the periodicity exactly equal to simulation cell dimension in the gliding direction. The image energy variation, shown in the center figure, could be big depending on the geometry of the cell, especially aspect ratio. The modified energy landscape may be far from the ideal one and cause wild behavior of dislocations both during the process of atomistic relaxation or molecular dynamics calculations. The calculated value for Peierls stress will also be affected, as shown in the figure.
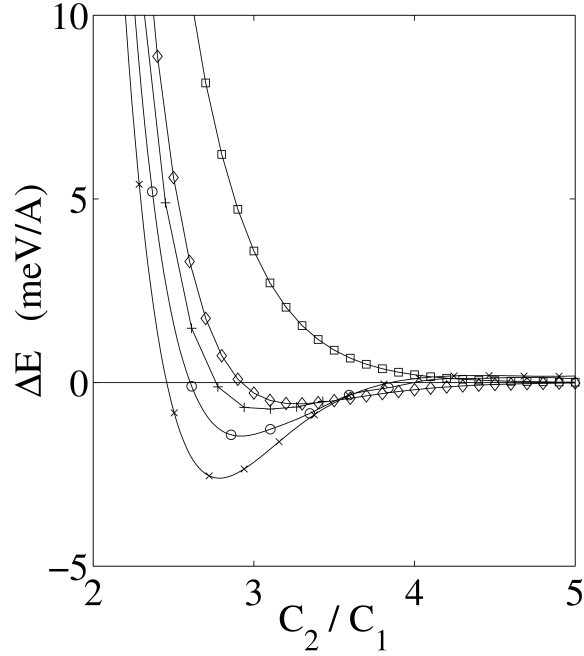
Figure 4-2: Artificial image energy variation is mainly a function of the aspect ratio of the simulation cell. An elongated cell will give much smaller image effect than a square-shaped cell. Aspect ratio of 3.5 is adopted in all the studies presented in this chapter and the image effect is negligible. ($\diamond$: anisotropic linear elasticity prediction; $\square$: isotropic linear elasticity prediction; $\times$, $\circ$ and $+$: atomistic calculations with $c_1 = 15, 20$ and $30[111]$.)

balance between the artificial image energy and the Peierls energy variations. That is something one should definitely avoid.

After conjugate-gradient energy minimization of this carefully chosen configuration, the relaxed configuration is viewed using AtomEye [103, 104]. With the atoms color-coded by local strain, the atomic configuration which contains two dislocations under PBC is shown in Figure 4-3, with detailed picture of the core shown in Figure 4-4.

As is evident from the pictures, the edge dislocation core is of planar shape and the highly-strained atoms only show up on the two atomic rows that are immediately above and below the glide plane. Further above and below the glide plane, one can see the difference in the compressive strain field and the tensile strain field that is characteristic of edge dislocations.

95
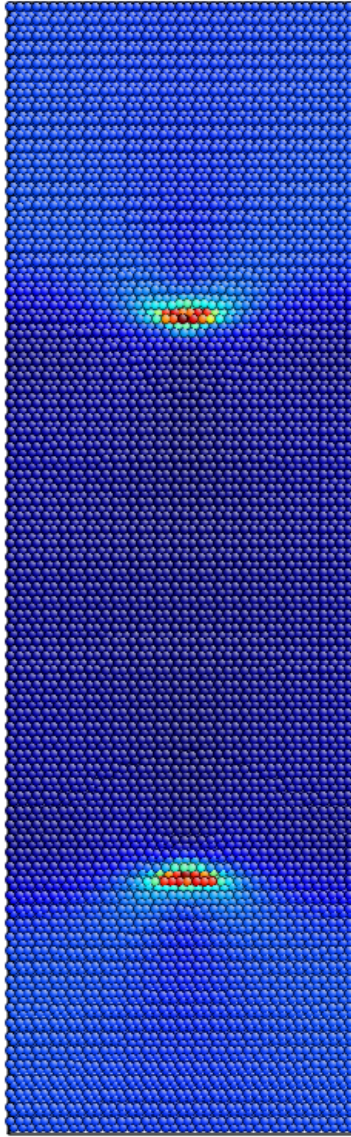
Figure 4-3: Relaxed edge dislocation dipole configuration with atoms color-coded according to local strain. The dimension of simulation cell is $20a[111]$ (109Å) in $\vec{X}$, $80a[\bar{1}01]$ (356Å) in $\vec{Y}$, and $3a[1\bar{2}1]$ (23Å) in $\vec{Z}$ direction, with a total of 58320 Mo atoms.
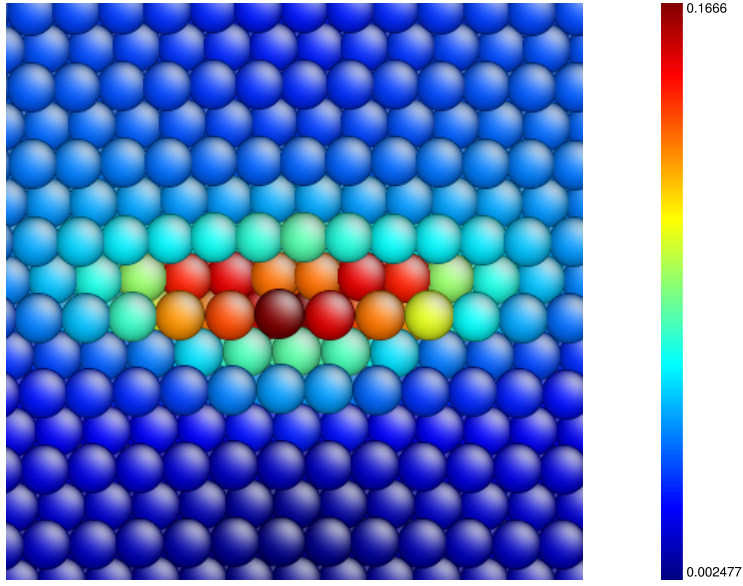
Figure 4-4: Core region magnified for atomic configuration in Figure 4-3. Again, atoms are color-coded by local strain.

Aside from the qualitative picture in Figure 4-3, one can actually take the two atomic rows that are immediately above and below the glide plane and calculate the misregistry between them. From the misregistry curve, one can quantitatively determine the edge dislocation core profile and therefore the core width. This is shown in Figure 4-5.

Using the Peierls-Nabarro model [105, 106, 10, 107, 108, 109]:

$$\tau_{PN} = A \cdot exp(-\frac{\alpha\zeta}{b}) \tag{4.1}$$

where $\mu = 151.5$GPa is the shear modulus, $\zeta = 5.5$Å is the dislocation half-width that we get from the atomistic relaxation described above, $\nu = 0.31$ is the Poisson ratio, $b = \frac{\sqrt{3}}{2}a = 2.7256$Å is the burgers vector, $A = 2\mu/(1 - \nu) = 439.1$GPa, and $\alpha = 2\pi$ for edge dislocations, one can estimate the Peierls stress for the edge dislocation to be:

$$\tau_{PN} = 1.3 \text{ MPa}$$

This is indeed a rather small number and indicates an extremely low lattice resistance
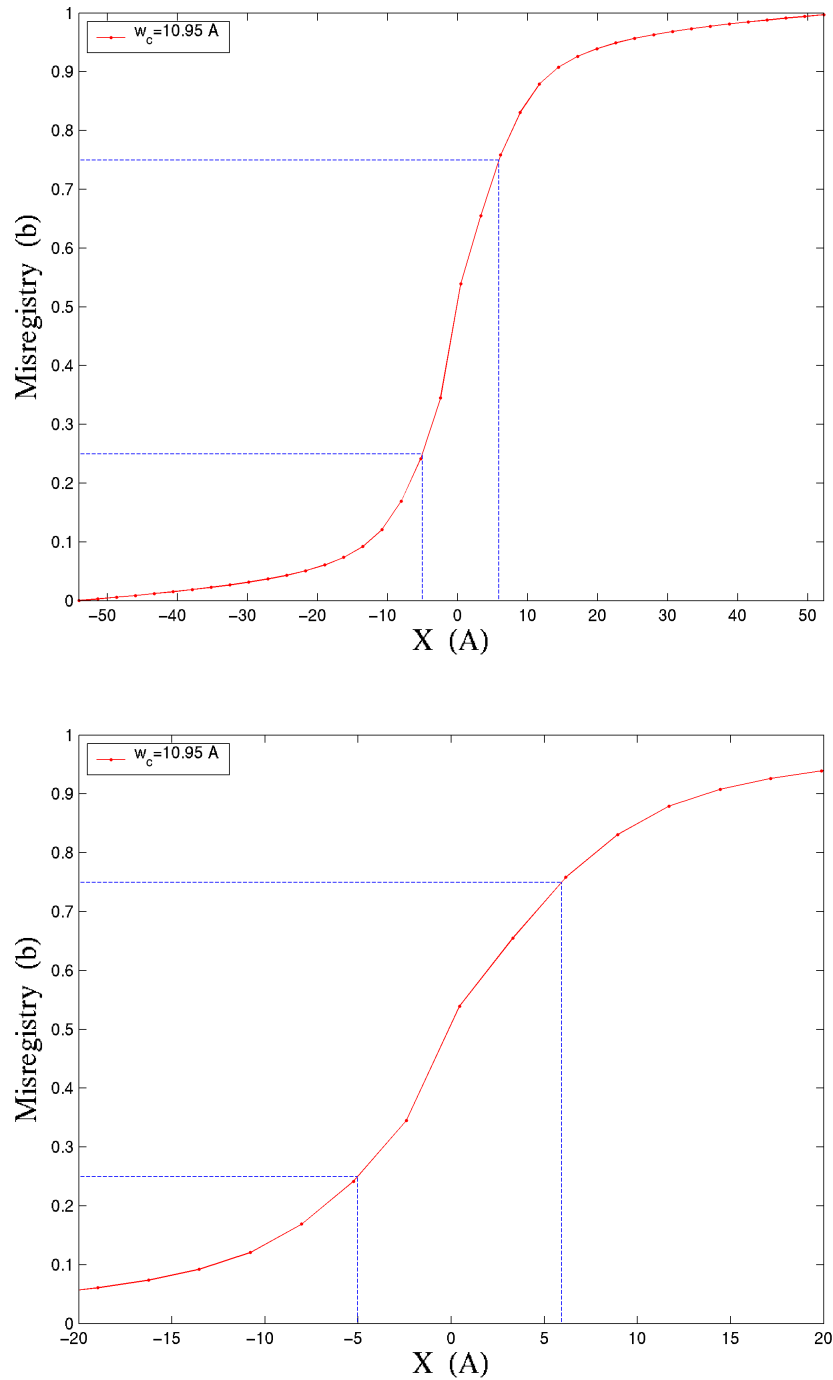
Figure 4-5: Misregistry along [111] direction. This value is calculated for the two atomic rows between which the edge dislocation resides. Edge dislocation core, defined as the region where misregistry is between $\frac{b}{4}$ and $\frac{3b}{4}$, has a width of ~ 11Å. Top figure shows the whole curve, while the bottom figure shows the details around the core.

to edge dislocations in molybdenum. Since this model assumes a sinusoidal form which is highly idealized, it may give inaccurate τ_{PN}. Also worth mentioning is the fact that the model is extremely sensitive to the core halfwidth value ζ simply because ζ is in the exponent term. Using $\zeta = 5.5$Å will give you $\tau_{PN} = 1.3$MPa, but using $\zeta = 4.5$Å will give you $\tau_{PN} = 13.7$MPa. However, the core width value itself is not of high accuracy and may indeed have small changes when the dislocation moves. Therefore, the number we just computed is highly approximate and can only be trusted probably within 1 order of magnitude.

In the recent work of Wang [110], after correcting an error in the original Peierls-Nabarro model, prediction of Peierls stresses for a large number of different crystals have been made and reasonable agreement with experimental data is observed. For edge dislocation in BCC Mo, τ_{PN} is predicted to be ~ 130MPa. This value is higher than the estimations made above by $1 - 2$ orders of magnitude and the discrepancy is mainly due to an under-estimation of the core width. The values we have just obtained above made use of the core width results from atomistic relaxations and therefore is expected to yield a more accurate value. As a matter of fact, with the introduction of γ-surface information, various schemes have been designed to evaluate τ_{PN} more accurately without full atomistic calculations and among them, the semi-discrete variational Peierls framework by Bulatov et al [111] has shown to produce highly accurate results. As one takes in more atomistic information and relaxes more assumptions which were made in the Peierls model, it is expected that the predicted value of Peierls stress will be closer to true τ_{PN}. However, this is not the main theme of this chapter and below we will instead use full atomistic calculations to calculate τ_{PN}. It is generally expected that such atomistic calculation will yield more accurate predictions of τ_{PN} and indeed we will get a definitive number for τ_{PN} of edge dislocation in Mo. However, It should also be noted that even when using full atomistic calculations, extra caution needs to be taken in setting up the simulation to avoid large errors in the simulation results.

In the following section, we will calculate τ_{PN} directly with atomistic methods, namely, by static relaxation method using Finnis-Sinclair potential [20, 112]. The

τ_{PN} value we get will be corrected for image effect and is much more accurate than the above Peierls-Nabarro model estimation. But it is always helpful to get some rough numbers first to get a qualitative picture.

4.3   Peierls Stress of Edge Dislocation

As have been introduced at the beginning of this chapter, the motivation of this calculation is really two-fold: (1) Previous calculations in the literature [3] gave a rather big number for τ_{PN} of edge dislocation in molybdenum which seems to be contradictory to experimental observations. There is a good reason to suspect the calculated number was inaccurate since the effect of the boundary conditions that they used in that calculation was not evaluated and could potentially be big. (2) In Chapter 2, we have just developed the tools that enables us to quantify the image effect due to the periodic boundary conditions. It shall be natural to make use of the newly acquired machinery to try to clarify the issue of τ_{PN} for edge dislocations in molybdenum.

Indeed, a single parameter ΔE (as defined in Figure 2-8) was defined and used to represent the magnitude of the image effect. This parameter ΔE can be calculated either from linear elasticity using the image summation method developed in Chapter 2 and described in more details in [7, 8, 9], or from atomistics where you prepare a number of dislocation configurations and use static relaxation method to discretely sample the total energy variation with respect to relative displacement between the two dislocations in the simulation cell. The atomistic approach is more accurate and self-consistent. The beauty of it is that it does not need anything from continuum theory and everything is done in a "fully atomistic" way. The drawback is that requires more computation. Either approach would give you the result of ΔE as an indication of image energy variation as the dislocation moves. A large ΔE value should be taken as a serious warning against adopting the current cell geometry. In the following studies, we will use several different cells that have different aspect ratios $\eta = \frac{C_2}{C_1}$ but the same size ($C_1 \times C_2$ is constant) to see whether they will give rise to

different τ_{PN} results and how big a different it makes to use different aspect ratios.
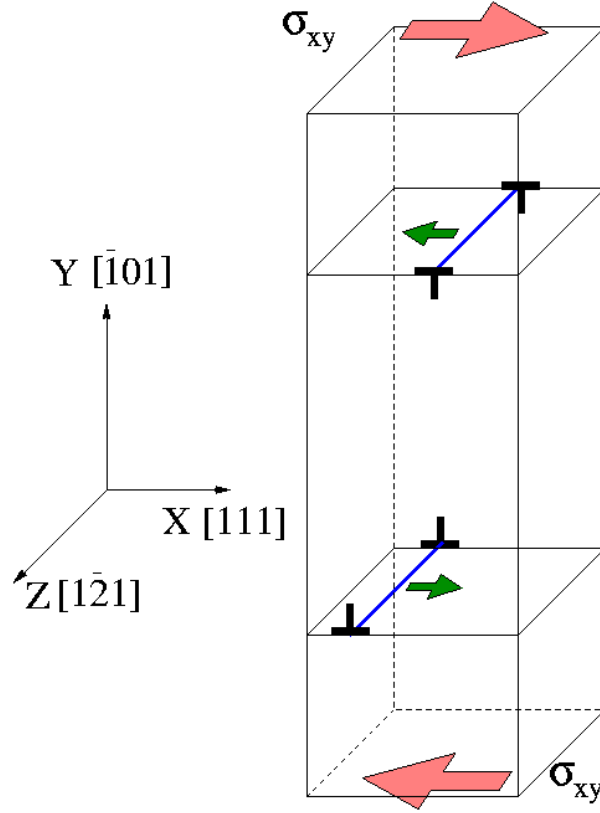
Figure 4-6: Calculate Peierls stress by applying shear stress σ_{xy} to the simulation cell until the dislocations are able to move across the PBC cell.

4.3.1 Method for calculating τ_{PN}

Using Parrinello-Rahman method [113] combined with static relaxation technique, i.e., energy-minimization using conjugate-gradient plus steepest-descent methods, we apply a shear stress σ_{xy} (as shown in Figure 4-6) to the simulation cell that was set up to contain an edge dislocation dipole separated by exactly half the box height, i.e., $\frac{C_2}{2}$. The dislocation may start moving at certain applied shear stress value σ_1. However, this value is not recognized as the critical stress. Because the initial setting of the dislocation dipole where the two dislocations have zero relative displacement in

$\vec{X}$, i.e., [111] direction is indeed an energy maximum if one considers the image energy variation only (the setting where the relative displacement in $\vec{X}$ is $\frac{C_1}{2}$ corresponds to an energy minimum in the image energy variation curve). So the initiation of motion at this point may have some help from the image stress (if aspect ratio is chosen to be inferior) and stress at this point σ_1 will be an under-estimate of the true Peierls stress value τ_{PN}. At this stress, the dislocation will move by one or several Burgers vectors before the decreased image stress cause the dislocation to stop motion and get trapped at another lattice position. As we further increase the applied stress σ_{xy}, the dislocation may move further. Above certain critical stress value σ_2, the dislocation is able to move beyond the image energy minimum and from there on a continuous motion of dislocation is assumed. We will record σ_2 as the critical stress needed to move the edge dislocation.

Realizing the symmetric property of the image energy curve (the middle curve in Figure 4-1), one should also be able to see that:

$$\sigma_1 < \tau_{PN} < \sigma_2 \tag{4.2}$$

and:

$$\tau_{PN} \sim \frac{\sigma_1 + \sigma_2}{2} \tag{4.3}$$

if the difference between σ_1 and σ_2 is negligible compared to the absolute value of tau_{PN}.

σ_1 is an under-estimation of τ_{PN}, whereas σ_2 is an over-estimation of τ_{PN}. The method of recording σ_2 as "the" Peierls stress is consistent with the notion that Peierls stress is indeed a critical stress needed to move the dislocation across the lattice sites, however, it will always give us a value larger than or equal to true τ_{PN}. The best scenario that makes $\sigma_2 = \tau_{PN}$ is when $\Delta E = 0$ and image effect diminishes. Otherwise, $\sigma_2 > \tau_{PN}$ and the difference between the two is a monotonic increasing function of ΔE.

One may be tempted to use $\frac{\sigma_1 + \sigma_2}{2}$ as an estimation for τ_{PN}. Certainly this would a valid option since this number in some cases is closer to true τ_{PN} than both σ_1 and

σ_2; however, $\tau_{PN} \approx \frac{\sigma_1+\sigma_2}{2}$ is only true for small ΔE scenarios. If ΔE is large, then this relation does not hold and the average value of σ_1 and σ_2 will not be a good representation of τ_{PN}.

To be self-consistent, σ_2, the minimum stress required to move dislocation across the periodic box, will be used in all the following calculations.

4.3.2 True Peierls Stress and Effect of Cell Aspect Ratio

Now we look at the result of calculated critical stress (to be exact, σ_2) with varying simulation cell shape. All the simulation cells we used have about the same cross-sectional area in xy plane ($C_1 \cdot C_2 \approx 4 \times 10^4$ Å^2), but the aspect ratios are different, ranging from 0.8 to 3.8. The variation of calculated critical stress that may be taken as an estimation of τ_{PN} with aspect ratio is shown in Figure 4-7, where the effect of PBC on calculated critical stress is quantified for the first time.

The calculated critical stress value that one may naively take as τ_{PN} changes by more than one order of magnitude (a factor of ~ 30 between the lowest and the highest value of critical stress) from ~ 700 MPa to ~ 25 MPa as the cell shape is changed from an almost-square shape to an elongated shape. As one can see, at low aspect ratios, calculated stress value increases monotonically with decreasing aspect ratio and it is expected that even larger stress values will be produced if we keep lowering aspect ratio.

The previous value of $400 - 700$ MPa corresponds to the high value portion of the curve in Figure 4-7. It is about 20 times the true Peierls stress value $\tau_{PN} = 25$ MPa.

4.3.3 Conclusion and Insights

On the core structure and Peierls stress for edge dislocations in molybdenum, a careful recalculation of Peierls stress τ_{PN} using Finnis-Sinclair potential yield a converged value of 25 MPa. In contrast to the previously reported value of $400 - 700$ MPa, this value is a true representation of the Peierls stress (within the physical picture described by Finnis-Sinclair potential model) and is drastically lower. This value sig-
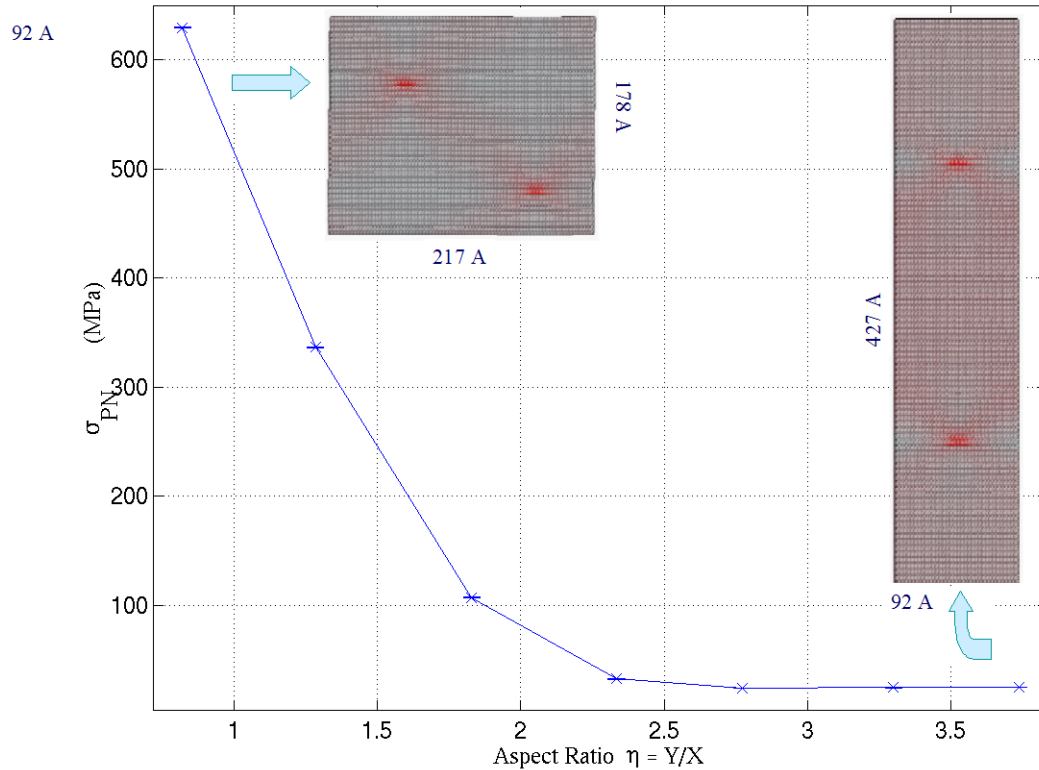
Figure 4-7: Calculated critical stress using the method as described changes by more than one order of magnitude when the cell shape is changed from an almost-square shape to an elongated shape. The converged value of critical stress at large aspect ratios is ~ 25 MPa.

nifies the extremely low lattice resistance to edge dislocations in BCC metal molybdenum. It also implies that earlier proposition of kink mechanisms operating on edge dislocation is unnecessary and most possibly untrue. Due to their low τ_{PN}, edge dislocations in molybdenum are unlikely to support stable kinks. As will be demonstrated in next chapter, edge dislocation mobility is not changed with the introduction of an pre-existing kink. It will be yet another direct proof that kinks do not play a role in the edge dislocation mobility picture.

As we have stated above, all the simulation cells adopted in this calculation only differ in aspect ratio but not in size, yet they produced critical stress values that differ by more than a factor of 30. If there is anything it proves, it is the common

104

notion among atomistic researchers that as long as you use a large atomistic model, all the artificial effects would diminish. This is not true. In this case, even when a one-million-atom configuration is used to calculate Peierls stress, one could still get totally wrong results if the aspect ratio $\eta = \frac{C_2}{C_1}$ is not chosen appropriately. On the other hand, in many cases bigger model size will give you better results, e.g., larger distance to the surface will make the surface effect smaller, etc. However, one shall always go through the trouble of proving something before naively trust something and start the simulation blindly.

The above calculation of the convergence behavior of calculated τ_{PN} with increasing aspect ratio is also a direct validation of the image energy variation model that we presented earlier in Chapter 2.

We have calculated τ_{PN} for several configurations. Indeed, in order to get the correct value for τ_{PN}, one does not need to reproduce the whole curve as shown in Figure 4-7. A single calculation with an appropriately large aspect ratio is guaranteed to produce an accurate measurement of τ_{PN} for intended dislocations.

Chapter 5

Mobility of Edge Dislocations in Mo

In this chapter, we will discuss our simulation results on edge dislocation mobility in BCC molybdenum. In contrast to the previous two chapters, this is a discuss on dynamics of dislocations rather than static mobility measures such as zero-stress zero-temperature core structure and Peierls stress. Static relaxation technique is replaced by finite temperature molecular dynamics simulations and the measured quantity also changes from Peierls stress (τ_{PN}) to dislocation velocity (v). In the simulated stress regime, edge dislocation exhibited high mobility and its motion is governed by viscous drag, with drag coefficients in the 10^{-5} Pa·s range. At high velocities (greater than half shear wave velocity, i.e., $v > c_s/2$), relativistic effect will appear and increase the drag coefficient approximately linearly and lead to an asymptotic behavior of dislocation velocity towards shear wave velocity.

We being this chapter with a briefly review of experimental mobility measurements in BCC molybdenum. In the second section we discuss the technical details of the simulation, including the geometry setup of the simulation cell and the methods of locating dislocation position and extracting dislocation velocity from it. In the third section, we present the mobility results, namely the functional dependence of dislocation velocity over a range of temperatures and stresses, importance of kinks.

5.1 Review of Experimental Mobility Measurements

As we have reviewed in the previous chapter, from experiments people have found that there are two important types of dislocations in Mo: screw dislocations control the low temperature plasticity while edge dislocations are important at high temperatures simply because screws become more mobile at elevated temperatures and can annihilate with each other through cross-slip while edge dislocations are confined to their glide planes. In other words, the inability for edge dislocations to climb easily at high temperature resulted in the experimental pictures that we in Figure 3-10 and alike.

In Chapter 3 we have reviewed the several most important aspects of BCC plasticity. Now let us briefly review the experimental understanding on dislocation mobility, which concerns both edge and screw dislocation, and other types of dislocations, too.

Individual dislocation mobility measurements could not only provide valuable information and insight towards our fundamental understanding of mechanical strength, but can also serve as a reference point for the atomistic models of dislocations that we developed from computer simulations. However, due to the high expense and experimental difficulty in obtaining high purity molybdenum single crystal samples and the difficulty in introducing single dislocations and accurately measuring their mobility, not much data are available for single dislocation mobility.

One of the earliest measurements of individual dislocations mobility in molybdenum was performed by Prekel et al. [72]. Edge dislocations were introduced by indenting the surface using a sharp sapphire stylus rather than surface scratching [114] because dislocations nucleated near the scratch surface were previously found to be not moving unless stress is so high that grown-in dislocations move as well. Dislocation positions, as revealed by etch pits, are shown in Figure 5-1(a). In Figure 5-1(b) dislocation velocity as a function of resolved shear stress on {110} and {112} planes. Mobility of edge dislocations is seen to be higher on {112} planes, and to be increasing with increasing temperature. The authors found the dislocation velocity data are in support of the kink mechanism with kink activation energy fitted to be
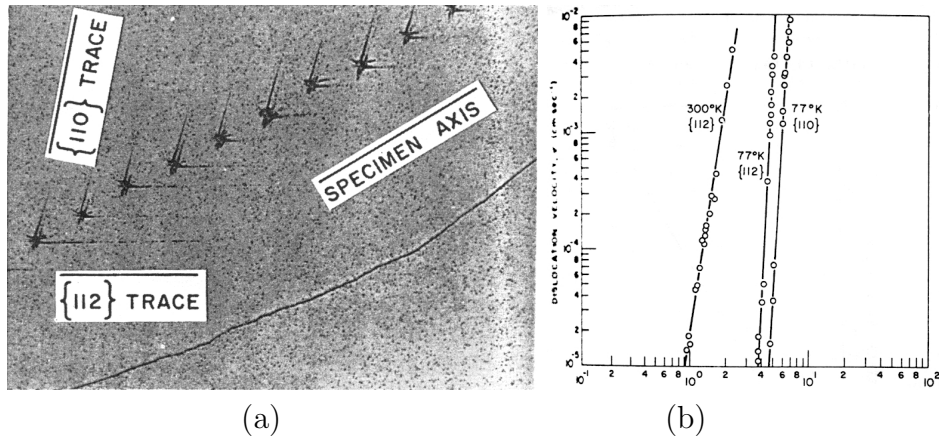
Figure 5-1: Early edge dislocation mobility measurements with etch pit method by Prekel et al. [72]. (a) Dislocation etch pits from the indenter, revealing the positions of dislocations. (b) Dislocation velocity measurements as a function of stress in unit of (kg/mm^2) at different temperatures and slip planes.

0.63eV. However, as we have shown in the previous chapter, even straight edge dislocations have very low lattice resistance and kink mechanism is not considered to play any role in edge dislocation motion; therefore this experimental result appears to be in conflict with our atomistic results. The reason of the obvious disparity may well be explained by the artifacts in the experimental measurements from interactions of the edge dislocation with the surface, as was found in [74] where a thin surface film always appeared on etched Mo sample and strongly impeded dislocation motion. Grown-in dislocations and point defects in the sample could also have contaminated the experimental results.

On the other hand, early experimental reports by Leiko [73, 115, 116, 117] where screw dislocations are shown to have high mobility is also inconsistent with current atomistic understandings of screws where straight screw dislocations are believed to have critical stress at $2 - 3$ GPa and can therefore not move readily without assisting kink mechanisms. As we plot the results from Leiko (supposedly for screw) and Prekel (supposedly for edge) together, as did by Nadgornyi [74] (Figure 5-2, a confusing picture is presented where screw dislocations are shown to be much mobile than edges. Most like these results have been contaminated by surface effects, as

109
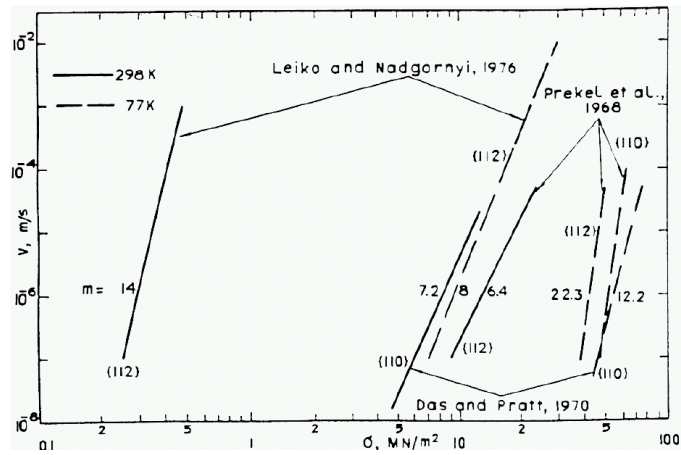
Figure 5-2: A confusing picture generated by comparing dislocation velocity measurements of edge (from Prekel et al.) and screw (from Leiko et al.) as a function of stress[74]. It is inconsistent with atomistic understanding of the much higher lattice resistance for screws than edges.

suggested by Matsui [118], where screw dislocations intersecting with the free surface may be forced to bend toward a mixed configuration thus substantially increase their mobility. Therefore, both velocity measurements may contain substantial errors and should not be trusted.

(a)   (b)
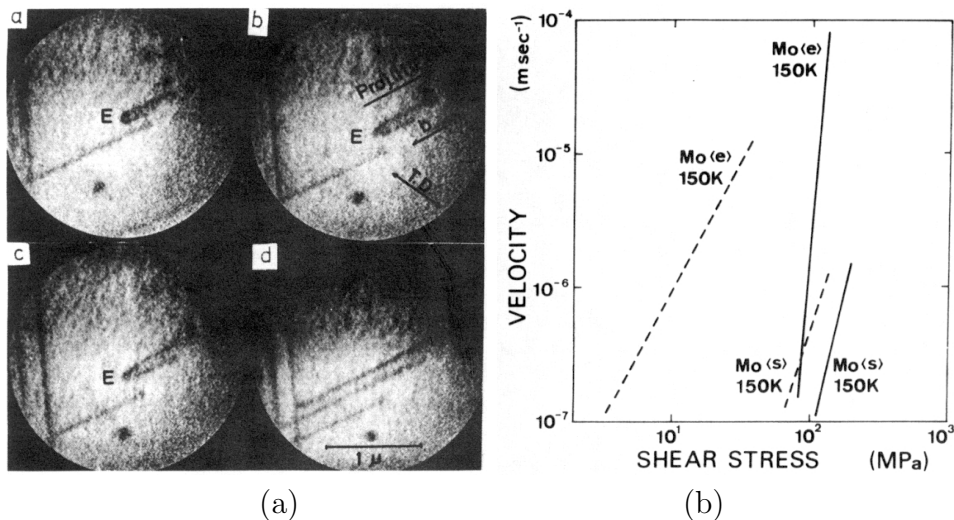
Figure 5-3: Dislocation mobility in Mo by *in situ* high voltage electron microscopy[69] is sufficiently free from surface effects and provides a more consistent picture of dislocation mobility in Mo.

More recent *in situ* TEM observations, as shown in Figure 5-3, are sufficiently free from artificial surface effects and seem to provide convincing results [69].

All these experiments, however, measure dislocation velocities from a different time scale than we have in simulations and the magnitude of dislocation velocity are not directly comparable. On the other hand, we believe developments on simulation techniques, e.g., MD acceleration techniques by Voter et al [119, 120], may soon make the direct comparison of the two possible.

5.2 Difficulty and Motivation fo Dislocation Mobility Simulations

Due to various reasons, not much has been done in the area of MD simulation of dislocation mobilities, except for the early work of Baskes and Clapp [4, 5] and recent work of Gumbsch and Gao [6].

The main reason is probably that due to the limited size of atomistic simulations, it is hard to measure accurately the steady-state velocity of a dislocation, not mentioning whether you can actually reach the steady-state. This will been shown in the later analysis of our MD simulation results of edge velocities and also is evident from the early work of Baskes and Clapp [4, 5] where one can clearly see that the velocity of the dislocation may be still in the process of climbing up to equilibrium velocity before the simulation had to be terminated due to computational limitations.

Another challenge is to keep track of the dislocation position as it moves within the simulation cell. As will be shown later, this can be done by either geometry analysis of misregistry or energy analysis. In both cases, reasonable amount of work need to be done to locate the dislocation core as it moves and large amount of simulation data need to be processed and analyzed in real time. If simulation box is tilted, the tilting also need to be considered in arriving at the real position change of the dislocations.

The factor that severely limits the simulation capability is the computational cost of such simulations of dislocation mobility. Firstly, the simulation cell size must

be sufficiently large to minimize core-overlapping, dislocation-dislocation interaction, and other artifacts such as surface effect if free surface is used. If dislocation operates in the viscous drag regime, then kinks are not important and simulation cell size can be reduced in the dislocation line direction. Otherwise, the dimension of the simulation box in dislocation line direction has to also be reasonably large to allow for kink nucleation and migration. Indeed, single kink migration shall be reasonably well approximated by a small cell, but double kink nucleation shall need a large cell dimension in the direction of dislocation line. Secondly, the simulation has to be run long enough for the dislocation to reach steady-state motion. This usually takes several picoseconds and is not a severe problem. Thirdly, after the dislocation reached steady-state motion, its motion shall be simulated for sufficiently long (large number of timesteps) to reduce measurement errors which is approximately proportional to the square root of length of simulation time. Because of all these requirements, the simulations of dislocation mobility could be potentially very expensive. In the studies presented below, each of the simulations of edge dislocation mobility takes from half a day to one week of CPU time on a AMD Athlon 1.33GHz personal computer. Realizing this is still simulation in the phonon drag regime, one can immediately see how expensive a realistic simulation of dislocation motion through kink mechanism can be. No doubt it requires massive power of modern parallel computers and it is arguably worth doing since probably same insights could be drawn from static calculations as well, most likely at significantly lower cost of hardware, software, and man power. However, one has to realize that such dynamic simulations will not only provide valuable insights into the dynamic behavior of dislocations, but can also provide larger-scale modeling, e.g., dislocation dynamics, with parameters that can not be determined by other means, e.g., drag coefficients. This is indeed the motivation of the work presented here for edge dislocations in molybdenum [21, 121, 122].

5.3   Setting Up the MD Simulation

Molecular dynamics simulation is a powerful method for probing the structure and dynamics of extended crystalline defects like grain boundaries [123] and dislocations. While the velocity of an isolated dislocation in an FCC metal has been obtained using fixed border conditions to transmit the driving force [4, 5], very little is known about the underlying mechanistic details, such as the role of kinks on the mobility of a straight dislocation, and steady-state velocity measurements were not obtained either. Another issue that has not been addressed adequately is how a specific border condition modifies the local driving force acting on the defect core.

In this study we simulate by molecular dynamics (MD) the motions of edge dislocations in a BCC metallic molybdenum lattice. Most of the discussions focus on the mobility of an initially straight edge dislocation and some results on edge dislocations with pre-existing kinks will also presented. In this section, we first discuss the methodological issues of properly setting up the MD simulation and extracting the dislocation position and velocities.

5.3.1   Geometry Settings of Initial Configuration

The first thing that is of foremost importance is to decide which boundary condition to choose. We use periodic boundary conditions in all the studies that follow. The decision to adopt the periodic boundary conditions (PBC) stems mainly from the fact that with periodic boundaries constant motion of dislocation could be achieved since there is no real space boundary that the dislocation have to stop at and as the dislocation traverses the simulation box and exits the simulation cell it essentially enters the cell from other end. In other words, we will be simulating the relative shifting of two infinite dislocation arrays, one positive and the other one negative, and the simulation can go on forever.

Another important reason for adopting the periodic boundary conditions is that the image interaction effects associated with PBC have recently been clarified [7, 8, 9], to the extent that one can now accurately and self-consistently quantify these effects,

as have been discussed in Chapter 2.

It shall also be decided as to how we put the dislocations in the PBC cell. In this case, an edge dipole need to be present and there are mainly two options. One is to put them on the same glide plane, but this would be an inappropriate choice for this simulation because the two dislocations of opposite signs will start moving in opposite directions and will soon annihilate with each other which will make the simulated system become perfect crystal [1]. The other option is to place them on different glide planes so that they can not annihilate with each other unless through climb motion which should be very difficult due to high energy barriers. The latter shall be adopted. But how far apart should their glide planes be? To minimize interaction between the two dislocations, they should be set apart from each other by exactly half the box dimension in Y direction (perpendicular to both the dislocation line direction and the Burgers vector direction).

It is also important to make the decision on how the simulation cell geometry is. As we have shown in Chapter 2 and Chapter 4, the aspect ratio plays a big role in determining the magnitude of the image effect due to the periodic boundaries. A good aspect ratio should be at least larger than 2, which means the edge dislocation configuration will have an elongated shape in Y, i.e., [110] direction.

The initial position of each of the dislocations on their respective glide planes does not matter much, because the dislocation will start moving and their relative displacement will change during the simulation anyway.

Now we should create the dislocation configuration. Figure 5-4 shows the specific procedure we are adopting to create a particular edge dislocation dipole. Starting with a rectangular atomic cell with box vectors at $20[111]$, $80[\bar{1}01]$ and $3[1\bar{2}1]$ respectively, we first remove a layer of atoms on an (111) plane (the shaded region) and then displace all other atoms according to the linear elastic displacement field of a dislocation dipole in a periodic cell, the solution to which can be obtained using the

---

[1]In fact, if the lattice resistance to dislocaiton motion is large, then it may be possible for the dislocations of opposite signs to be trapped in their initial lattice positions. That is not the case here, since edge dislocations in molybdenum has a very low Peierls stress value: $\tau_P = 25$MPa.
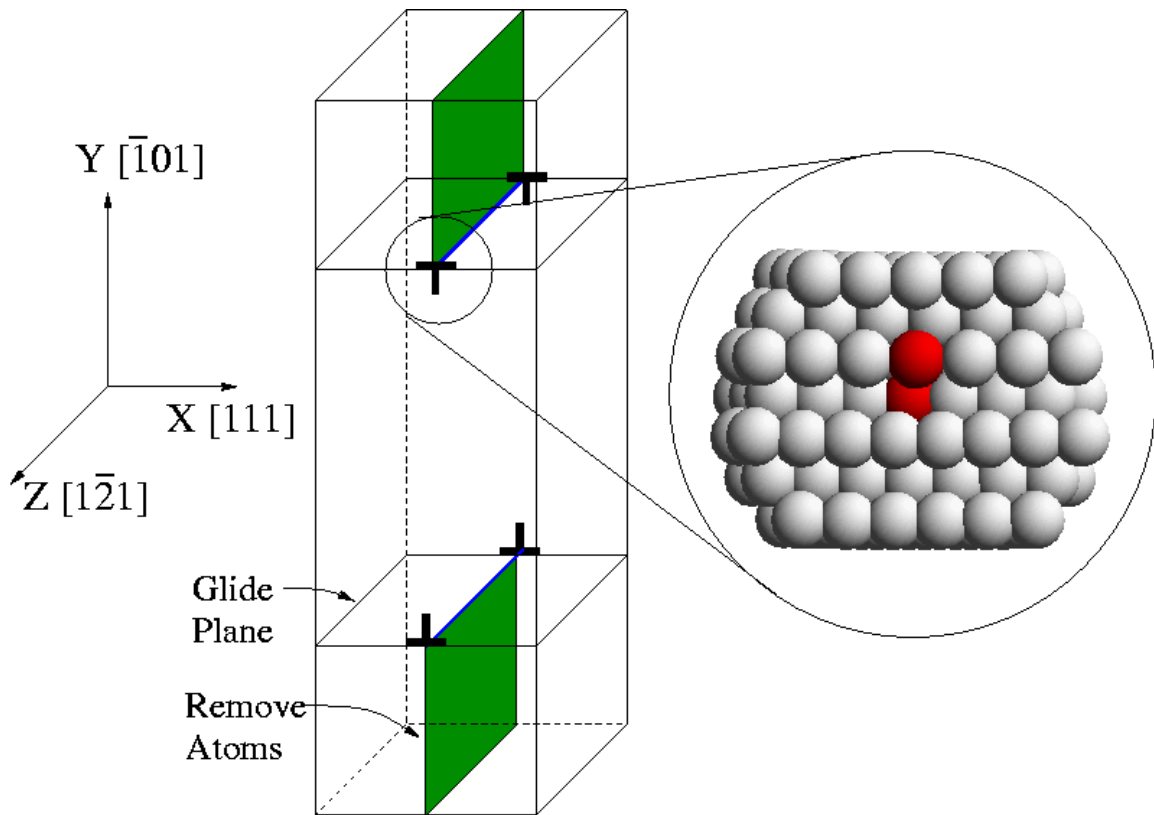
Figure 5-4: Setting up an edge dislocation dipole by removing a layer of atoms in the shaded plane, and displacing the atoms according to displacement field prepared using methods described in Chapter 2, followed by conjugate gradient force relaxation. Atomic arrangement around the dislocation core is shown with the core atoms (highlighted) having the largest potential energy as well as maximum disregistry across the two atomic layers on the either side of the glide plane.

method outlined in Chapter 2 and [7, 8, 9]. After conjugate gradient relaxation , we obtain an atomic configuration with two edge dislocations with opposing Burgers vector $a/2[111]$, each lying on a $(\bar{1}01)$ glide plane and separated from the other by a distance of $40[\bar{1}01]$. The inset in Figure 5-4 shows the detailed relaxed atomic arrangement around the dislocation core.

5.3.2 Extracting Dislocation Position and Velocity

To extract dislocation velocity from the MD trajectories, we need to identify the position of the dislocation core as a function of simulation time. Atomic position

data can be saved at various time intervals and geometrical analysis is performed off-line; however, this would require very large disk space and is not an optimal solution. Since only velocity data are desired, we can carry out the geometrical analysis on-line to determine the core position for every dislocation segment at each MD time step, and save this information to data files.

Given the system configuration, we would like to quantitatively estimate the dislocation position. Since the dislocation line is approximately parallel to Z-axis, we divide the simulation cell along Z-axis into slices each of which contains only one layer of atoms. For each slice, we first find out the two rows of atoms which are immediately above and below the slip plane. Then we calculate the disregistry between these two rows as a function of X-coordinate. This function periodically extends to infinity due to the periodicity along X-axis. In Figure 5-5 this function is plotted within 3 periods for both the upper dislocation segment and the lower segment. The point which corresponds to maximum misregistry is then identified and taken to be an estimate of the core position. For a more numerically consistent estimation, we use several points near this maximum and do local parabolic fitting. The peak of the fitted parabola indicates the estimated core position of this dislocation segment. The procedure of fitting is also shown in Figure 5-5 where we used 4 data points for the parabolic fitting.

From the estimates of the dislocation core positions for all the segments, we construct the profile of the dislocation line, and by repeating the procedure at successive timesteps, we can follow the time evolution of the dislocation profile. Thus we can observe the details of dislocation glide. Shown in Figure 5-6 is a dislocation profile evolution plot. This 3D plot shows how the dislocation line shape changes with time. (The dislocation line is 36 repeat distances long.) This information is not of much use in this case, since in the stress regime that we are going to study, the edge dislocations exhibit high mobility and kinks do not play a role in the mobility picture. However, evolution of the dislocation line profile with time may uncover important features of dislocation motion in other cases. For example, see Figure 5-7 for a dislocation profile evolution picture that clearly shows the double kink nucleation and migration
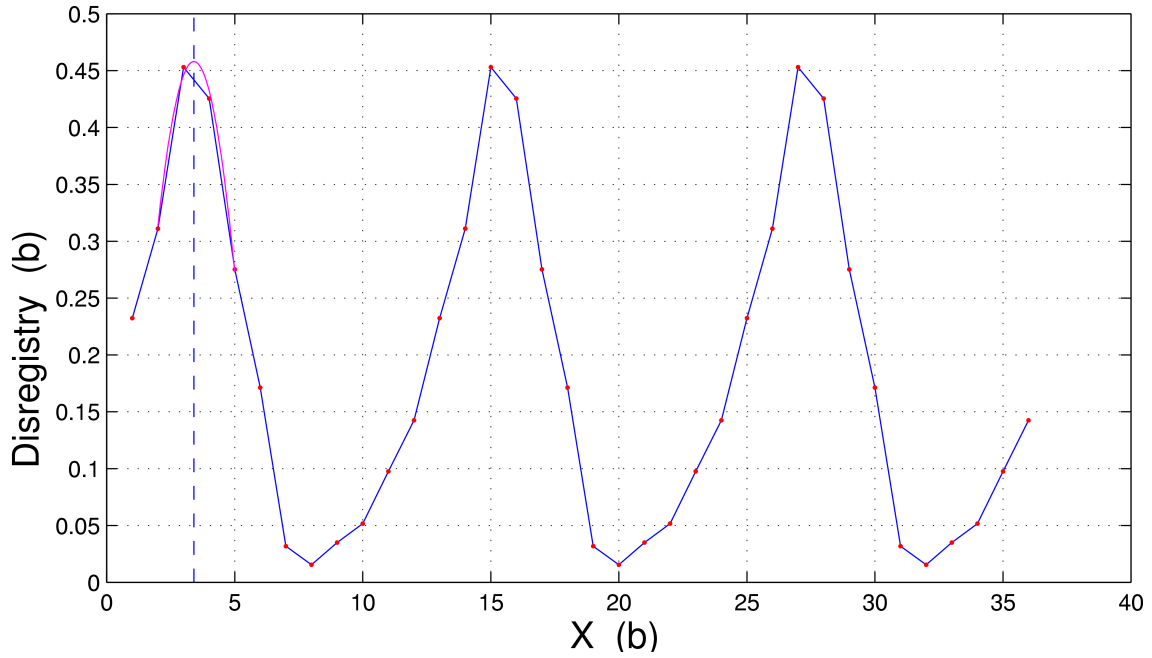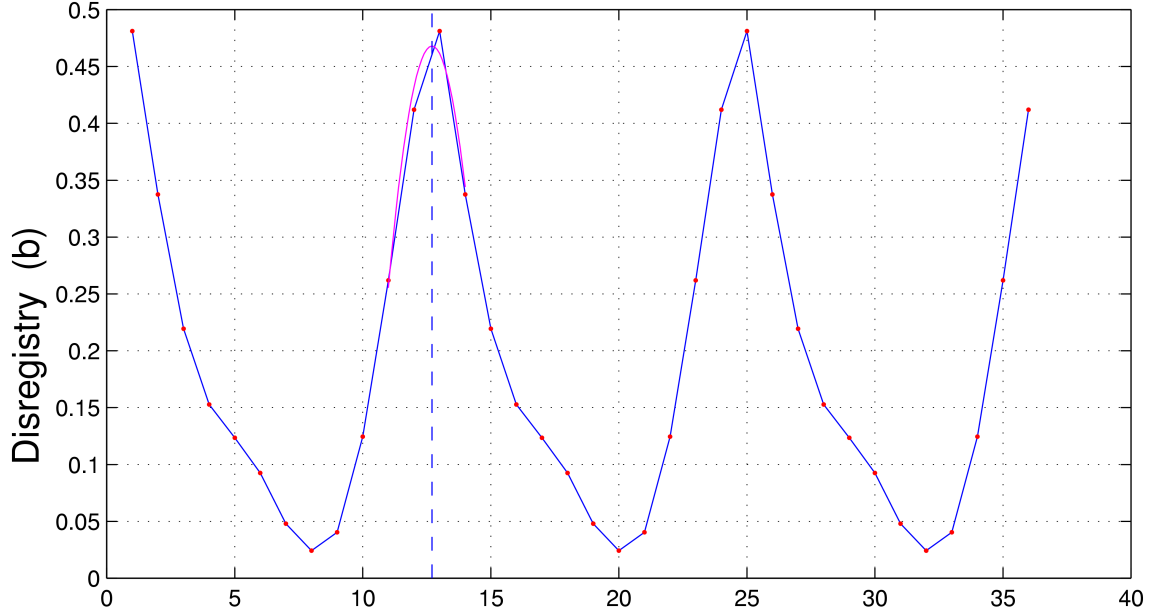
Figure 5-5: Disregistry as function of X-coordinates for both the upper dislocation segment and the lower one. Four-point parabolic fitting is used to determine the position of dislocation core.

behavior of screw dislocations in semiconductor silicon.
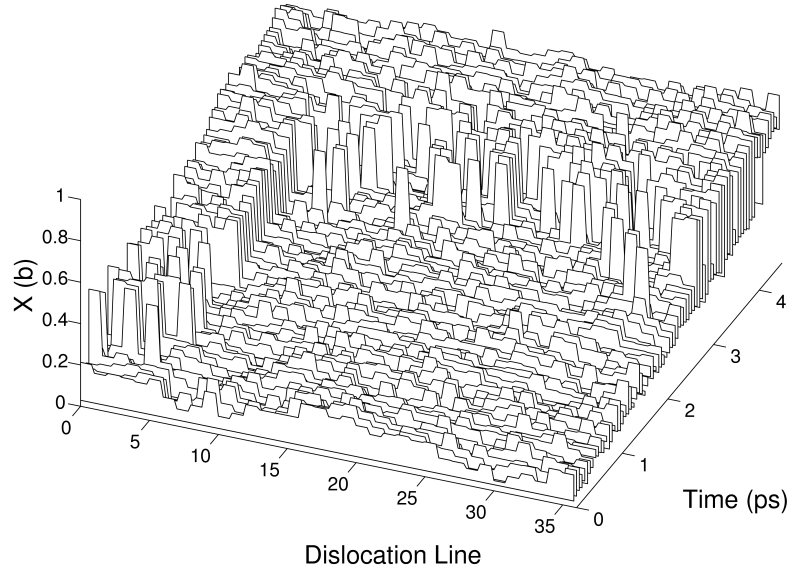
Figure 5-6: Evolution of dislocation profile ($T = 20K$, $\sigma = 0.07GPa$).

By averaging along the dislocation line, we get the average line position of disloca-
tion. Plotting against time and fitting to a straight line gives the dislocation velocity
as the slope of the fitted line [2].

As shown in Figure 5-8, dislocation position variation can be directly translated
to instantaneous velocity of the dislocations. After the initial incubation stage, dis-
location velocity stays around an equilibrium value under constant stress. It is also
shown that the initial large variation of virial stress quickly disappeared and the
applied shear stress is controlled well by the Parinello-Rahman method. Therefore,
excluding the initial incubation time, both velocity and stress can be obtained with
certain precision.

---

[2]The incubation time portion of the curve should be disgarded since that part represents a stage
where velocity gradually increases from 0 to steady-state value.
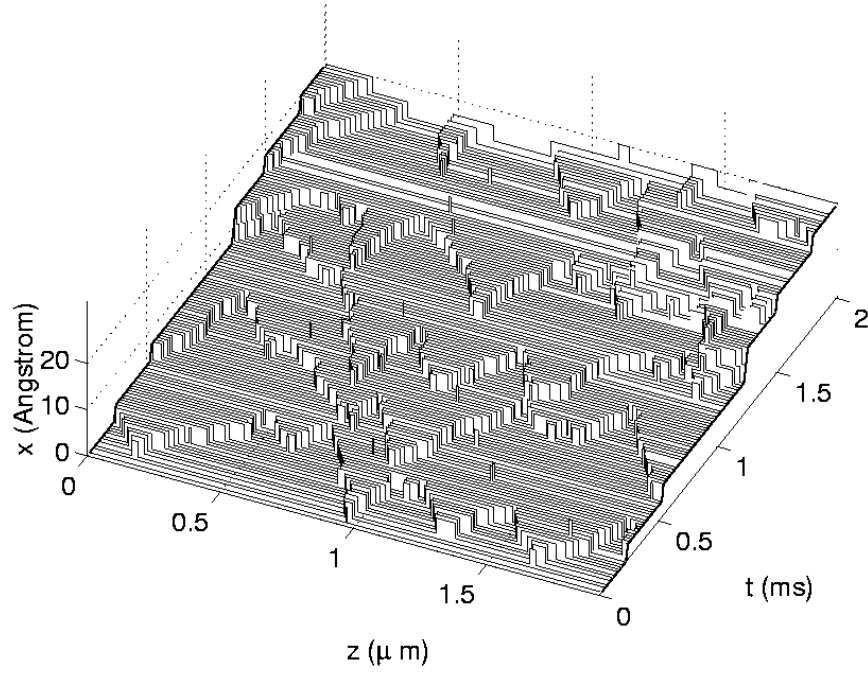
Figure 5-7: Evolution of dislocation profile for screw dislocations in silicon. Generated by kinetic Monte Carlo simulation by Cai et al. Double kink nucleation and migration processes are clearly seen from this dislocation profile evolution picture.

5.3.3 The Potential Model

The MD results we present in this chapter are obtained using the Finnis-Sinclair empirical potential model [20] as revised by Ackland and Thetford [96].

The function form of the FS potential is given below,

$$V(\{\vec{r}_i\}) \;=\; V_N + V_P, \tag{5.1}$$

$$V_N \;=\; -A\sum_i \sqrt{\rho_i}, \tag{5.2}$$

$$\rho_i \;=\; \sum_j \phi(r_{ij}), \tag{5.3}$$

$$V_P \;=\; \frac{1}{2}\sum_{ij} v(r_{ij}) + v_c(r_{ij}), \tag{5.4}$$

$$\phi(r) \;=\; \begin{cases} (r-d)^2 + \beta(r-d)^3/d, & r \le d \\ 0, & r > d \end{cases} \tag{5.5}$$

119
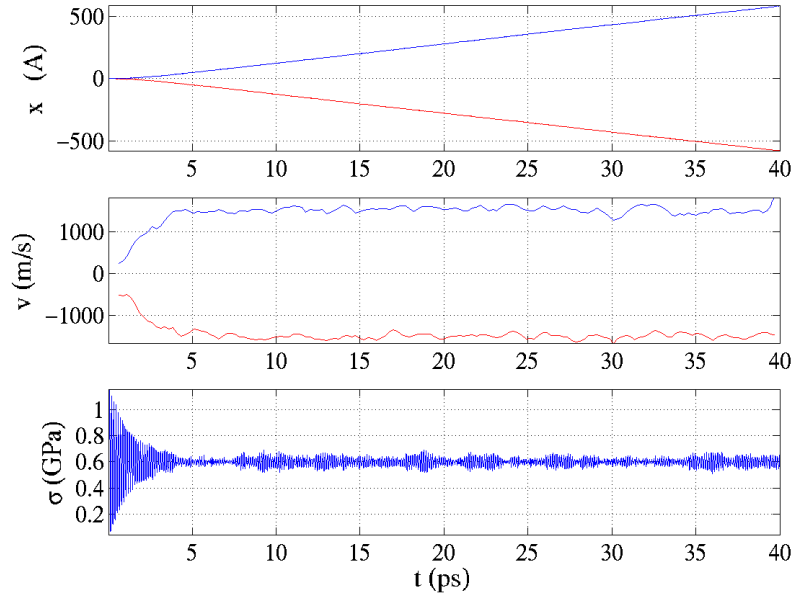
Figure 5-8: Dislocation position, velocity and virial stress variation in a MD simulation at $T = 300K$ and $\tau = 600MPa$ under zero pressure. The two separate data lines correspond to the upper and lower dislocations in the simulation cell respectively.

$$v(r) = \begin{cases} (r-c)^2(c_0 + c_1 r + c_2 r^2), & r \leq c \\ 0, & r > c \end{cases} \tag{5.6}$$

$$v_c(r) = B(b_0 - r)^3 \exp(-\alpha r), \tag{5.7}$$

where V_P represents a pairwise repulsive interaction accounting for the core electron overlap and V_N describes metallic cohesive energy. The cohesive energy per atom varies as the square root of the effective electron charge density ρ_i. Although the theoretical justification of the functional form of FS potential was thought to be valid only for metals with nearly half filled d band, such as VIB metals Mo, W, etc, it was later shown by Ackland et al. [124] that it is applicable for all band fillings after charge neutrality of each atom is considered, so that the square root form can be used for noble metals and Ni as well.

The Finnis-Sinclair potentials were constructed for seven BCC metals, V, Nb, Mo, Ta, Cr, Fe, W. It is a EAM-type many-body potential that has 7 parameters

that are fitted to experimental results on lattice constants a, cohesive energy E_{coh} and three elastic constants C_{11}, C_{12}, C_{44}. Computationally this is a rather efficient potential model since this many-body potential has a small potential cut-off radius between 2nd and 3rd neighbors and the energy evaluation does not involve angular calculations. However, as have been reported in [125], it results in low thermal expansions and describes surfaces poorly. As pointed out in [126], angular terms need to be introduced and indeed this was done by Moriary at LLNL, who constructed a new potential called MGPT potential [127] based on the Generalized Pseudopotential Theory [128, 129, 130]. This potential was constructed for molybdenum. Unfortunately, this potential is rather slow because it has not only 2-body and 3-body interaction but also 4-body interaction terms. With all this added computational cost, this potential can only be used for static relaxations in simulating atomistic dislocation systems [3, 90]. Finite temperature MD simulation of dislocations requires fast potentials and MGPT is not an option.

The version of Finnis-Sinclair potential we use is from the 1987 Phil. Mag. paper by Ackland and Thetford [96]. They found out that the original version of FS potential give unphysical results for system under large compression, and added an extra 2-body term to correct for this. The correction term would not show when the system is under tension. This revision is only for five of the metals: V, Nb, Ta, Mo and W.

5.3.4   Image Effects in A Periodic Simulation Cell

The problem of dislocation motion generally refers to the movement of a single dislocation moving in an infinite lattice. To relate this problem to that of a dislocation dipole, two effects need to be considered, one is the interaction between the two dislocation forming the dipole and the other is the interaction between these two dislocations and their images which are introduced by the periodic boundary conditions. Both interactions may be treated in the framework of linear elasticity. We will denote the interaction energy associated with these two effects as E_{elas}; it is actually an energy per unit length of dislocation. Refer to Chapter 2 for the method of calculating E_{elas}. We will apply this result to give an estimate of local driving force acting on the

dislocation.

From linear elasticity and atomistic simulations we find that E_{elas} varies in an oscillatory manner with the offset x (along X direction in Figure 5-4) between the two dislocations forming the dipole. We can define the maximum slope $\max dE_{\mathrm{elas}}/dx = \sigma_{\mathrm{int}}b$ as a measure of the total effect of PBC, where σ_{int} is the maximum internal stress acting on the dislocation with b the Burgers vector. For the simulation cell shown in Figure 5-4, the variation of E_{elas} can be well represented by a sinusoidal function, $E_{\mathrm{elas}} = A\sin(\frac{x}{12b}) + \mathrm{const.}$, where $A = 0.98 \times 10^{-3}\mathrm{eV/\mathring{A}}$. The corresponding maximum internal image stress is $\sigma_{\mathrm{int}} = 6.7\mathrm{MPa}$, which is much smaller than the typical values of applied shear stresses ($40 \sim 7000\mathrm{MPa}$). For this particular case it appears that the image effects due to the periodic cell are quite small.

The following studies on dislocation velocity all use a simulation that is $40b$ long along $\vec{X}$ direction, i.e., [111] direction. We can also calculate the maximum image stress value by approximating the image energy curve as a sinusoidal curve. $E_{\mathrm{elas}} = A\sin(\frac{x}{40b}) + \mathrm{const.}$, where $A = 0.4 \times 10^{-3}\mathrm{eV/\mathring{A}}$. The corresponding maximum internal image stress is $\sigma_{\mathrm{int}} = 1\mathrm{MPa}$, which is negligible compared to the applied shear stress on the simulation cell. values of applied shear stresses ($40 \sim 7000\mathrm{MPa}$). Therefore, the image effect is essentially zero for the simulation cell geometry we have adopted.

5.4 Velocity Simulation Results

By varying the temperature and stress values we apply to the simulation, we get different velocity outputs and can compile this output data into a velocity surface as a function of stress and temperature, as shown in Figure 5-9.

One can rotate this velocity surface around to explore its features, mainly the stress dependence and temperature dependence of velocities.

5.4.1 A Discussion on the Four Regimes

The dynamic properties of dislocations are determined by not only the intrinsic properties of the dislocation in the crystal but also the magnitude and distribution of
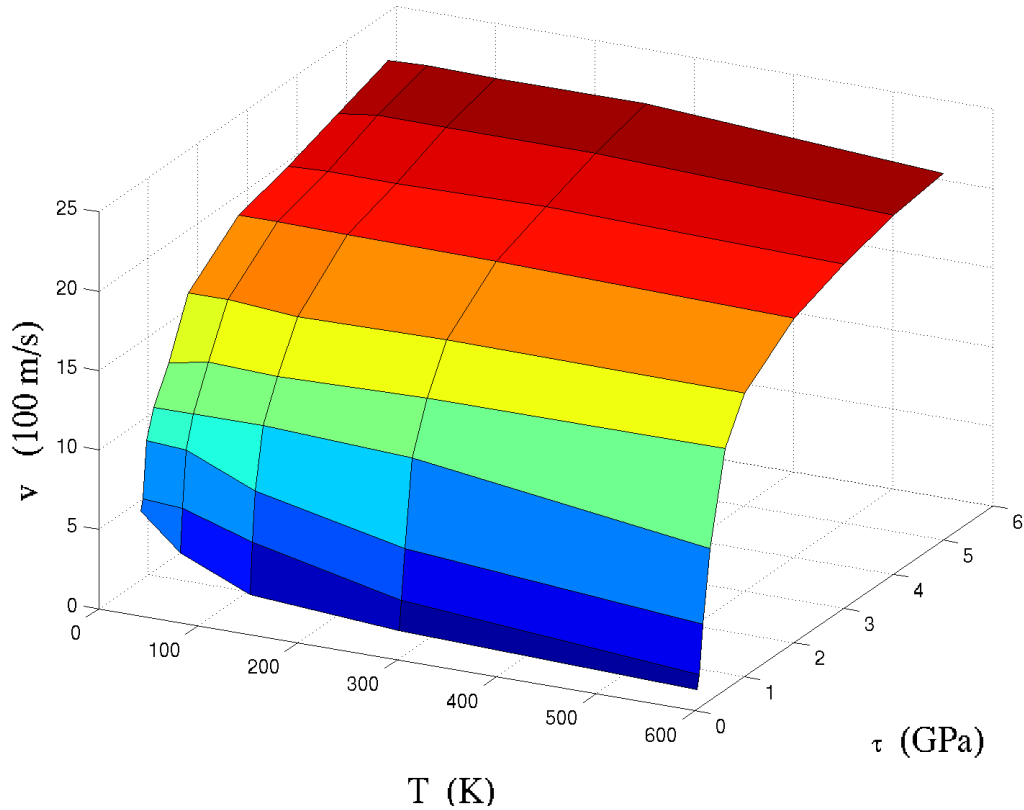
Figure 5-9: By simulating a range of temperature and stress conditions, we have obtained a data array of velocies that can be plotted as a velocity surface.

driving forces. At zero temperature, continuous glide motion of dislocations occurs only if the applied stress σ exceeds a critical stress σ_{c_0} which is equal to the maximum glide resistance $\hat{\sigma}$. (σ_{c_0} should be equal to τ_{PN} for a single dislocation gliding in infinite medium.) The value of $\hat{\sigma} = \sigma_{c_0}$ depends on the type and the distribution of the glide resistance peaks. At finite temperatures, however, macroscopic continuous glide of a dislocation can occur with the help of fluctuations at any stress up to $\sigma_c \leq \sigma_{c_0}$. In bcc metals, four specific regions of the dislocation velocity can be demarcated[131, 132]. In the first region, the motion is controlled by the thermal release of dislocation from some equilibrium positions in the obstacle resistance profile. This is the thermally activated region at $v \leq 10^{-5}c_s$ (c_s is the velocity of sound in the solid) where the dislocation motion is jerky and the dependence $v(\sigma)$ is highly non-linear. Also the

velocity increases with temperature, and imperfections affect the dislocation motion greatly. The second region, at $10^{-5} < v/c_s < 10^{-2}$, is regarded as a continuation of the previous region, the motion being sensitive to all the contributions to the glide resistance. In both, the applied stress σ is below the mechanical threshold $\hat{\sigma} = \sigma_c$. In the third region where $v \geq 10^{-2}c_s$, the drag resistance is predominant. Here $\sigma > \sigma_c$, the dependence $v(\sigma)$ is linear, the velocity decreases with temperature and depends weakly on the concentration of imperfections. Lastly, in the fourth region at $v \sim c_s$, some relativistic effects can be observed.

5.4.2   Temperature Dependence of Dislocation Velocity

In Figure 5-9, the temperature effect on velocity is found to be minimal at high stress values. For example, dislocation velocity at applied shear stress of 5 GPa keeps constant for different temperatures simulated.

It is only at low stress values that the temperature effect becomes evident. For shear stress at 40 MPa, measured dislocation velocity is a monotonic decreasing function of temperature. This shows us that the dislocation motion is not governed by a thermally-activated process; rather, it is governed by viscous drag in the studied stress regimes. Since Peierls stress for edge dislocation is only ~ 25MPa, the applied shear stress values are all greater than Peierls stress and therefore dislocation motion is only impeded by phonon drag. The drag coefficient B, which is defined as $B = \sigma \cdot b/v$, is an important parameter to characterize the behavior of dislocation in this regime.

Although there is no experimental data on the temperature dependence of the drag coefficient for molybdenum, experiments on other materials have shown a similar behavior, e.g., experiments in copper [133] have produced a monotonic increasing drag coefficient B with increasing temperature. Theoretical calculations on phonon drag is discussed in details in [134] and qualitative trend is found to agree with the simulation results.
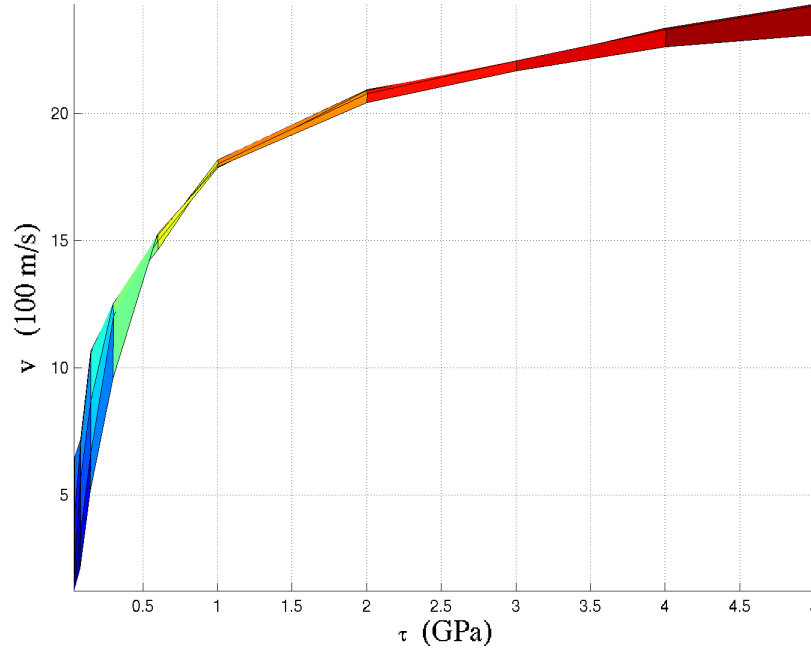
Figure 5-10: Stress-dependence of dislocation velocity shows a decreasing stress exponent m, as defined by $v \propto \sigma^m$. At low stresses, $m = 1$, while as stress increases to 6 GPa, m decreases to approximately 0.25.

5.4.3 Stress Dependence of Dislocation Velocity

Figure 5-10 shows that in the stress range we have studied, the stress sensitivity coefficient as defined by $v \propto \sigma^m$, decreases from $m = 1$ for low stress values to $m = 0.25$ for high stress values up to 6GPa.

The initial linear dependence of $v(\sigma)$ is a distinctive feature of the third regime that we discussed earlier in this section. This is best characterized by looking at the drag coefficient $B = \sigma \cdot b/v$. Indeed, as shown in Figure 5-11, drag coefficient in this stress regime remains approximately a constant at $6 \times 10^{-5} Pa \cdot s$.

At higher stresses ($\sigma > 400$ MPa), drag coefficient B shows an approximate linear growth with increasing stress. One should also notice a small positive curvature that indicates an even higher slope for drag coefficients at higher stresses. The first-order transition point where drag coefficient start to grow almost linearly corresponds to
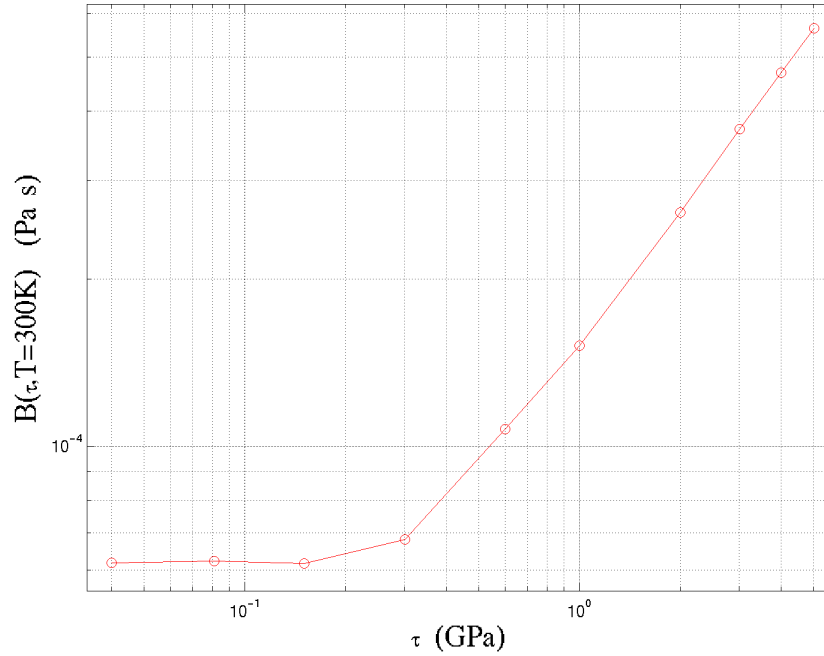
Figure 5-11: Stress-dependence of dislocation velocity is best shown by plotting the drag coefficient B against stress. B is defined as $B = \sigma \cdot b/v$. At low stresses ($\sigma < 0.4$ GPa), drag coefficient remains constant, whereas at higher stresses, drag coefficient B starts to grow in an approximately linear fashion, with a small positive curvature.

a dislocation velocity value of approximately half the shear wave speed, c_s. Indeed, this transition is caused by the relativistic effect when the velocity of dislocation approaches sound velocity.

5.4.4 Pressure Dependence of Dislocation Velocity

Figure 5-12 shows that as pressure is increased, mobility of dislocation is decreased monotonically. The rate of the decrease is more than linear.

Reason for the decrease in mobility can be traced to the change that take place in γ-surface. As the lattice is pushed tighter and tighter, the energy barrier in the γ-surface (unstable stacking fault energy) does not increase much, but due to decreased lattice spacing, shear modulus, i.e., the slope of the γ-surface at lattice origin, will be increased. The ideal shear strength will increase as well. This shall lead to an

126
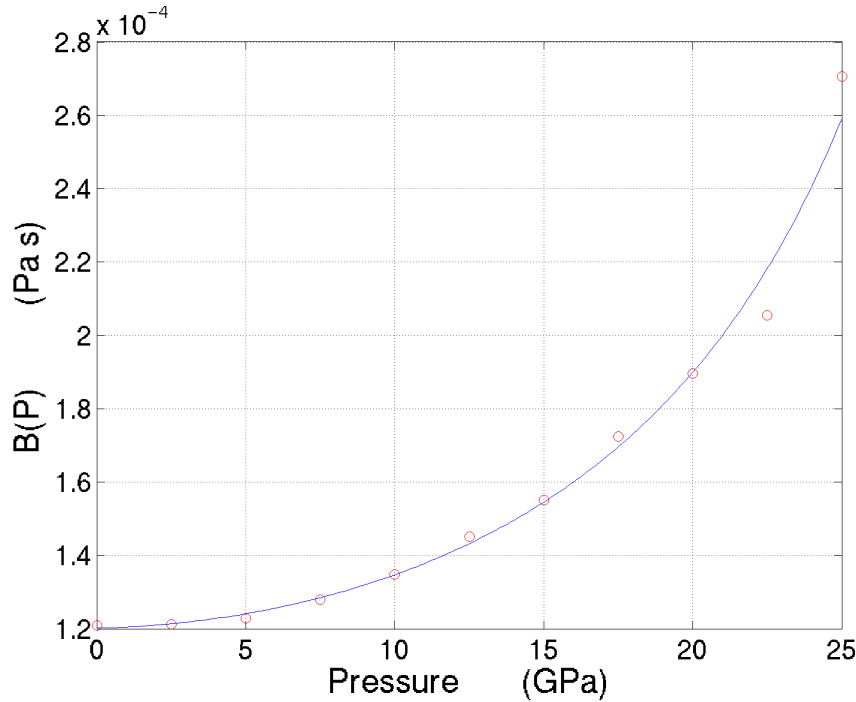
Figure 5-12: Pressure-dependence of dislocation velocity is shown by plotting the drag coefficient B against pressure. The decrease in dislocation mobility (increase in drag coefficient B), is due to both a smaller lattice spacing under compression, and the increase in shear modulus.

increase in the critical stress of dislocation and will lower the dislocation mobility.

5.4.5   Importance of Kink Mechanism

For edge dislocations, due to extremely low lattice resistance, it is quite possible that no stable kinks can be supported on an edge dislocation, not mentioning whether their nucleation and migration would actually play a role in edge mobility. In this study, a pre-existing kink is introduced to the edge dislocation, as shown in Figure 5-13 and measurements of dislocation velocity are compared with the one where there was no pre-existing kink.

It is found that the dislocation velocity does not change with the introduced pre-existing kink compared to no initial kinks. This indicates that kink mechanism is not the controlling mechanism in the simulated stress regime.
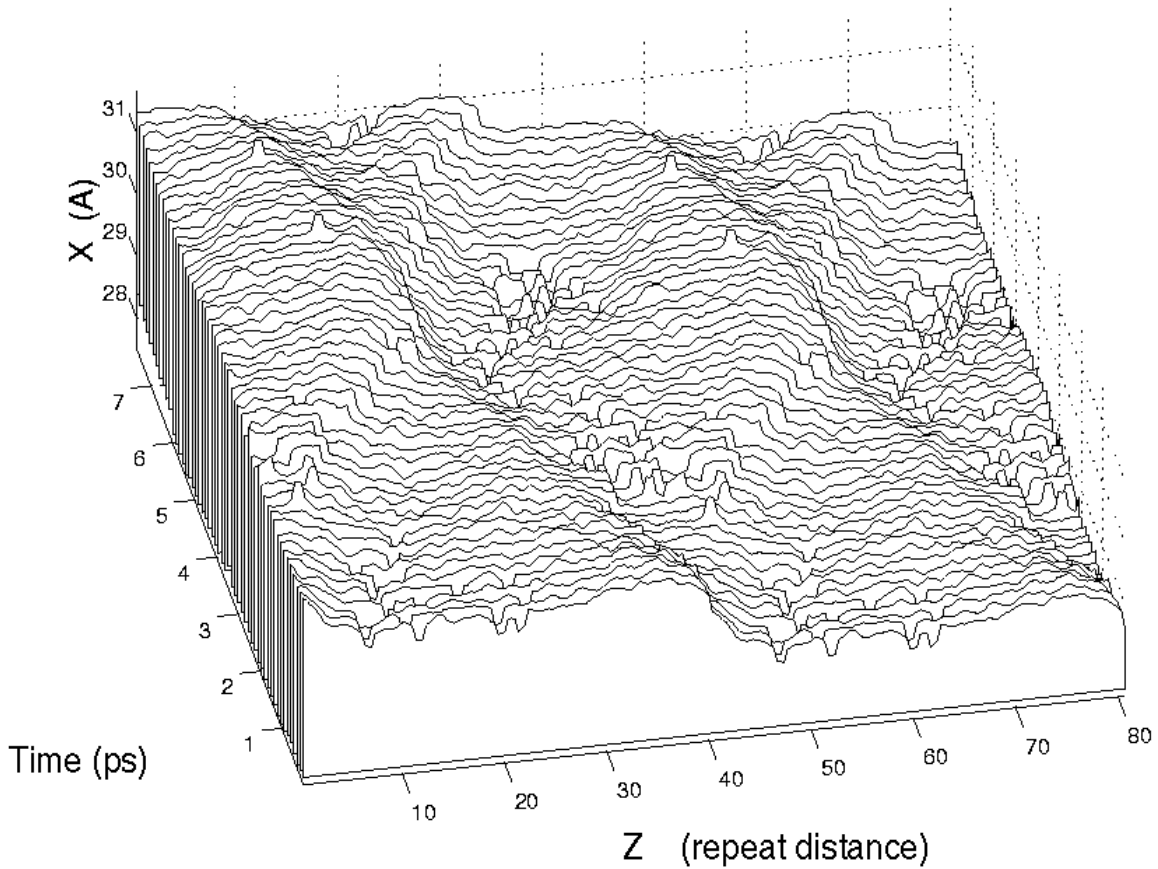
Figure 5-13: Pre-existing kinks introduced to initial configuration did not enhance edge dislocation mobility, indicating that kinks on edge dislocations in Mo is not important and kink mechanism is not the controlling mechanism, in the studied stress regime.

5.5 Summary

In this chapter, we have simulated the dynamics of single edge dislocation by simulating its motion, observing its dislocation line profile, and extracting dislocation velocity data to analyze the dependence of dislocation mobility on stress, temperature and pressure. Temperature-dependence reveals the phonon-drag mechanism in low-temperature region. Stress-dependence shows up in the low-velocity region as a constant drag coefficient; but for velocities higher than $\frac{c_s}{2}$, relativistic effect will cause the drag coefficient to grow approximately linearly, with a small positive curvature. In the simulated stress and temperature ranges, kink mechanism is not found to be

an important factor in determining edge dislocation mobility.

The calculated drag coefficients can be passed on to dislocation dynamics codes (DD) as valuable inputs to allow the DD simulation to incorporate finite temperature velocity behavior of dislocations, or to any other dynamic models that need to consider the velocity stress relationship at finite temperature.

Chapter 6

Deformation Twinning in BCC Molybdenum

In the previous three chapters, we have discussed the static and dynamic measures of dislocation mobility in molybdenum. In this chapter, another important plastic deformation mechanism in BCC metals, deformation twinning, is studied using atomistic methods. First, MD results on atomistics of twinning nucleation and growth in BCC molybdenum is presented. Then, to analyze the nucleation of twins, 1-D chain model is developed and a simple form energy criterion for describing competition between twinning nucleation and dislocation-based slip is presented. Minimum-energy path analysis for twin nucleation reveals different stages for the perfect crystal to nucleate the twin. A general 4-stage wave steepening model to describe the strain-localization (energy-localization) process is proposed. Putting an small sinusoidal shear wave perturbation on top of the strain field of the 1-D chain near the critical point where the defect nucleation occurs, we follow the dynamics of the 1-D chain and the four stages of strain localization is clearly demonstrated. Beyond current problem of twinning nucleation, the 4-stage wave-steepening model can find its application in nucleation of other types of defects.

6.1   Background

Deformation twinning and slip are the main plastic deformation mechanisms through which crystals can accommodate large strains. Deformation twins have long been identified in BCC, HCP, and lower symmetry metals and alloys, and are now found to be formed in many FCC metals and alloys, in ordered alloys and other inter-metallic compounds, in elemental semiconductors and compounds, in other non-metallic compounds such as calcite and sodium nitrate, and even in complex minerals and crystalline polymers [135, 136].
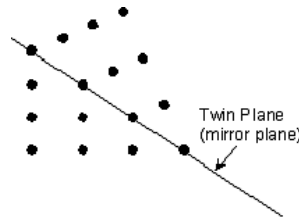
Figure 6-1: Mirror symmetry about the twin plane is characteristic of twins.

Experiments with single crystals have shown that some structures e.g., FCC metals, do not normally twin unless under appreciable strain or very high strain rates, while in others, e.g., BCC and HCP metals, twins are easier to form. Twinning is often characterized by very rapid formation of twinned regions and gives large load drops in the stress-strain curves. The relative contribution of twinning to the overall strain increases when temperature is lowered or strain rate is increased. In general, deformation twinning operates at low temperature, high stress(strain), high strain rate, and in crystals of lower symmetry where number of slip systems are limited.

The classical definition of twinning requires that the twin and parent lattices are related by a mirror reflection in the twin plane [1], as shown in Figure 6-1. A real atomic configuration of twinning is shown in Figure 6-2, where a twinned region is enclosed by the twin boundaries.

---

[1] This is usually referred to as Type I twin, whereas in some cases, twin and parent lattices are related by a rotation of $180°$ and it is usually referred to as Type II twin.
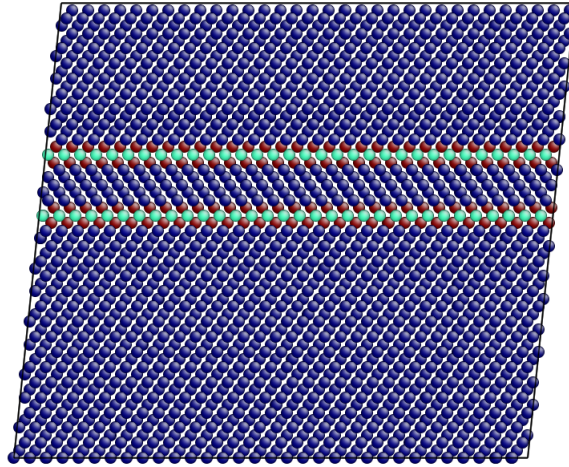
Figure 6-2: Atomistic configuration that shows a twinned region enclosed by the twin boundaries (the green atoms). Atoms are color-coded by local shear strain.

(a)   (b)   (c)
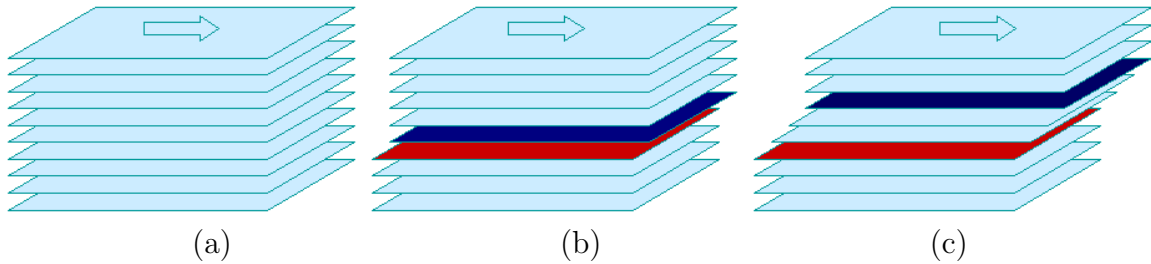
Figure 6-3: Schematics of slip and twinning. (a) Undeformed crystal; (b) Deformation through slip; (c) Deformation through deformation twinning.

The schematic plot in Figure 6-3 shows the difference between deformation twinning and slip. As the perfect crystal shown in Figure 6-3(a) is sheared, the excessive shear strain can be relieved by either slip or twinning. In the case of slip, as shown in Figure 6-3(b), relative displacement happens between two layers only, one immediately above the slip plane and one below. Atoms move by whole numbers of lattice spacing, and lattice orientation remains unchanged. In the case of twinning, as shown in Figure 6-3(c), deformation twins form by highly co-ordinated individual atom displacements the magnitude of which is of fractional lattice spacing, and the lattice orientation of the twinned region is changed.

Crystallographically, an operative slip mode is usually, but by no means invariably,

characterized by the closest packed plane and direction of the structure. The operative twinning modes can be similarly selected by a combination of easy atomic "shuffling" and minimum magnitude of the associated shear [137]. The assumption of minimum shear with no shuffles, in fact, leads to the correct prediction of the actual twinning modes of almost all the metallic single lattice structures. However, the twinning elements selected by crystallographic considerations may not be fully accurate since the operative twinning mode is determined by the energy of the interface, rather than the magnitude of the twinning shear.

In FCC metals, the twin lattice points are on coincidence sites and a deformation twin may be regarded as a stack of intrinsic stacking faults. The energies of an intrinsic stacking fault and the {111} twin boundary are similar and small. However, in BCC metals, it has been found by Vitek [138] that the twin lattice points are translated away from coincidence sites by a non-repeat lattice vector to form a "isosceles" type interface that destroys the reflection symmetry across twin boundary, and the minimum number of faults that would be mechanically stable is three. However, the calculations were carried out using a pairwise potential that is inadequate in describing the BCC metals and the lowest energy structure predicted may be unreliable.

Similar to most first order phase transformations which are divided into nucleation and growth stages, it is usually assumed that separate consideration should be given to the formation of a small twin region and to its subsequent growth into a large twin. The reason is two-fold: (1) the spontaneous formation of a large twin is difficult to envisage; (2) the finite positive energy of the twin interface implies an energetic barrier to the formation of a very small volume of twinned crystal. The analogy with phase transformation may be extended in that twin nuclei may form under the action of an applied stress in a region of near-perfect crystal (homogeneous nucleation) or form from a suitable pre-existing defect configuration (heterogeneous nucleation). Twinning is normally nucleated heterogeneously from some defect configuration, but in highly prefect crystals homogeneous nucleation of twins have been observed to occur, e.g., in cadmium and zinc [139] and the stresses to induce twinning are an

order of magnitude higher than those usually measured on macroscopic specimens. The focus of this thesis will be on the homogeneous nucleation of twins.

In classical nucleation theory, the energy of a small embryonic twin which is assumed to be separated from the parent phase by a sharp interface is calculated by assuming that the embryonic region has a defined volume and surface area and that macroscopic parameters such as surface free energy or elastic stiffness are relevant. A general assumption is that the shape is an ellipsoid with three axes, two of them in the twin plane and one normal to twin plane. This problem can be solved within the framework of anisotropic elasticity. However, due to the high non-linearity at the interface, the twin interfaces should be treated with atomistic methods, either semi-empirical potentials or more accurately, first principle calculations.

The critical stress required for growth of twins by spontaneous nucleation of successive loops of twinning dislocation is generally believed to be much smaller than the corresponding estimate for formation of a twin nucleus, and growth by spontaneous nucleation of new layers is considered to be a possible mechanism.

Furthermore, existing models on defect-assisted nucleation and growth of twins, which is of great importance but will not be covered in this thesis, are discussed in details in [136]. To briefly summarize, most models of defect-assisted twin nucleation are based on the dissociation of some dislocation configuration into a single- or multi-layered stacking fault which then serves as the twin nucleus, whereas models of twin growth involve either repeated nucleation of successive layers or a pole mechanism or cross-slip "source" mechanism which allows a single twinning dislocation to move through successive twin planes. Since appreciable core overlap is usually present, linear elastic theory is inadequate and atomistic calculations are required to verify the models, e.g., the pole mechanism; however, few work has been done in this aspect due to the large simulation size required for testing these models, difficulty in setting up the desired defect configuration atomistically, and difficulty in treating the simulation boundaries properly.

The twinning system observed in experiments for BCC molybdenum [140] is $\{112\}\langle 111 \rangle$. We will focus on this orientation in the following atomistic studies,

sometimes using the $\{110\}\langle 111 \rangle$ slip system for comparison.

6.2 MD Simulation of Twinning Nucleation and Growth

Using finite temperature molecular dynamics simulations, the nucleation and growth of deformation twins can be directly observed and analyzed.

We begin our atomistic study of deformation twinning in Mo by quasi-2D molecular dynamics simulations in two different kinds of loading condition: mode-I loading with pre-existing crack, and shear loading with no pre-existing defects. Then we extend the atomistic study to full 3D. A 3D atomistic picture of twin nucleation and growth is presented for the first time and mechanistic insights are gained from the full 3D simulation.

6.2.1 Quasi-2D Model-I Loading with Pre-Existing Crack

In this simulation, we set up an atomic configuration that is perfect BCC crystal except for an ellipsoidal void in the center, as shown in Figure 6-4(a). To favor twinning, we choose the X,Y,Z axes to be along $[\bar{1}\bar{1}0]$, $[001]$, and $[\bar{1}10]$ respectively. The ellipsoidal void has a dimension of 60Å in X and 30Å in Y and is introduced by removing atoms in the ellipsoidal region. Uniaxial tension is applied in Y direction and this is essentially a mode-I loading if we consider the two horizontal edges of the void which are separated by 60Å to be two separate blunt cracks.

The maximum resolved shear stress plane is the 45° plane which has a Schmid factor of 0.5. The $(11\bar{2})$ twin plane is at an angle of $\phi = 35.3°$ with X and the Schmid factor is $cos(\phi) \cdot cos(90° - \phi) = 0.47$. As uniaxial tension is applied, equivalent shear on $(11\bar{2})$ plane is of twinning sense and twin nucleation and growth will be favored. If we apply uniaxial compression or rotate lattice orientations by 90°, then equivalent shear on $(11\bar{2})$ plane will be of anti-twinning sense and dislocation-based slip will be favored.

The overall dimension of the simulation cell is 231.4Å in X (along $[\bar{1}\bar{1}0]$), 232.9Å in Y (along $[001]$), and 8.9Å in Z (along $[\bar{1}10]$). The thickness in Z is minimal and

137
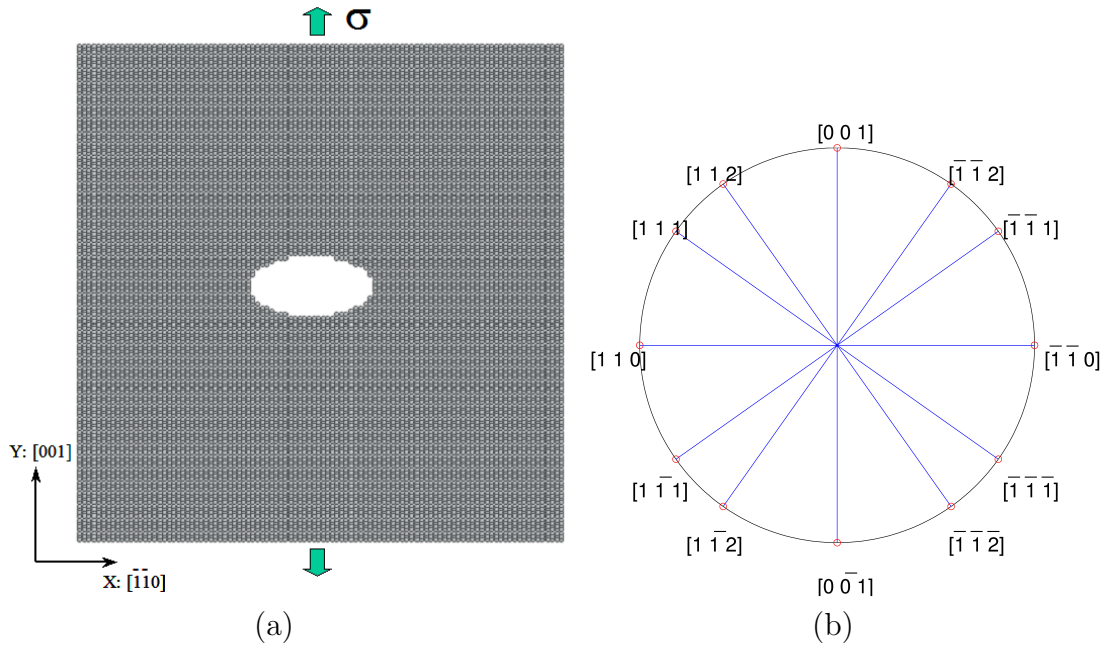
Figure 6-4: (a) The initial atomic setup of the quasi-2D simulation. The simulation cell is 231.4Å in X direction (along $[\bar{1}\bar{1}0]$), 232.9Å in Y direction (along $[001]$), and 8.9Å in Z direction (along $[\bar{1}10]$). Uniaxial tension is applied in Y direction. (b) A zonal plot that shows the important crystallographic directions on the xy plane. The angle between the $(11\bar{2})$ twin plane and X direction is $\phi = 35.3°$, whereas the angle for (110) slip plane is 90°. As an uniaxial tension stress is applied in Y, the Schmid factor for $(11\bar{2})$ plane is $cos(\phi) \cdot cos(90° - \phi) = 0.47$.

therefore this is a quasi-2D simulation.

As shown in Figure 6-5, twin is nucleated at crack tip and grows into the bulk on $(11\bar{2})$ plane in $[111]$ direction. The twin region can be distinguished from the untwinned region by either geometry analysis or by energy analysis. In Figure 6-5, we have color-coded the atoms by individual atomic energy and atoms in the twin region have higher energy than the bulk and therefore have different colors from the bulk.
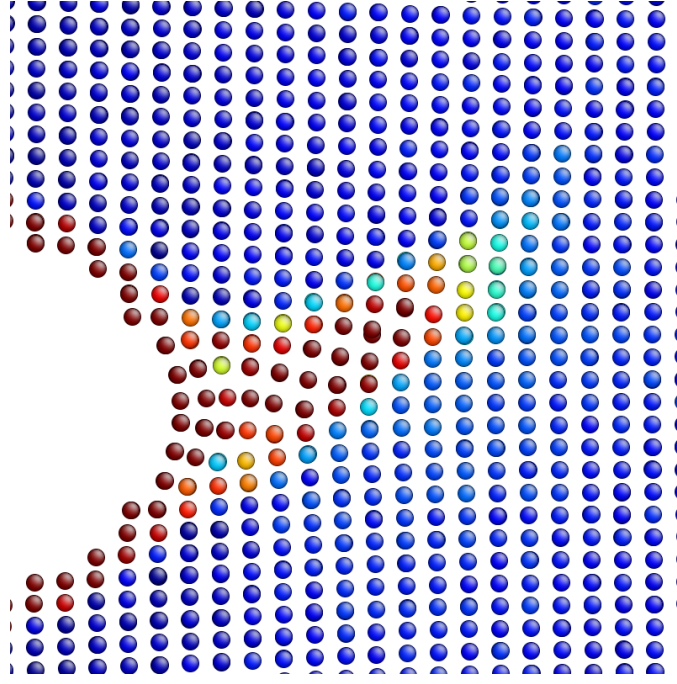
Figure 6-5: Crack-tip region magnified. Showing the twinned region by using energy color-coding on atoms.

The stress matrix at the point when twin is nucleated is:

$$\sigma = \begin{bmatrix} \sigma_{11} & \sigma_{12} & \sigma_{13} \\ \sigma_{21} & \sigma_{22} & \sigma_{23} \\ \sigma_{31} & \sigma_{32} & \sigma_{33} \end{bmatrix} = \begin{bmatrix} -2.74 & 0 & 0 \\ 0 & -10.03 & 0 \\ 0 & 0 & -2.78 \end{bmatrix} GPa$$

This stress matrix is in the Cartesian coordinate system that we adopted in the simulation, with axes $\bar{x}_i, i = 1, 2, 3$. To transform this stress matrix into another Cartesian coordinate system with axes $\bar{x}_i^*, i = 1, 2, 3$, where $\bar{x}_1^*$ aligns on the $(11\bar{2})$ twin plane, we first calculate the direction cosine matrix c, where $c_{ik} = cos\angle(x_i^*, x_k)$:

$$c = \begin{bmatrix} cos(\phi) & cos(90° + \phi) & 0 \\ cos(90° - \phi) & cos(\phi) & 0 \\ 0 & 0 & 1 \end{bmatrix} = \begin{bmatrix} 0.816 & -0.578 & 0 \\ 0.578 & 0.816 & 0 \\ 0 & 0 & 1 \end{bmatrix}$$

where $\phi = 35.3°$. Therefore, the transformed stress matrix in the twinning coordinate

system is:

$$\sigma^* = c\sigma c^T = \begin{bmatrix} -5.17 & 3.44 & 0 \\ 3.44 & -7.60 & 0 \\ 0 & 0 & -2.78 \end{bmatrix} GPa$$

The critical resolved shear stress is therefore 3.44GPa with the pre-existing crack. As we will show in the next simulations, when there is no pre-existing defects (dislocations, cracks, etc.) in the crystal lattice, a much larger CRSS is required to nucleate twins.
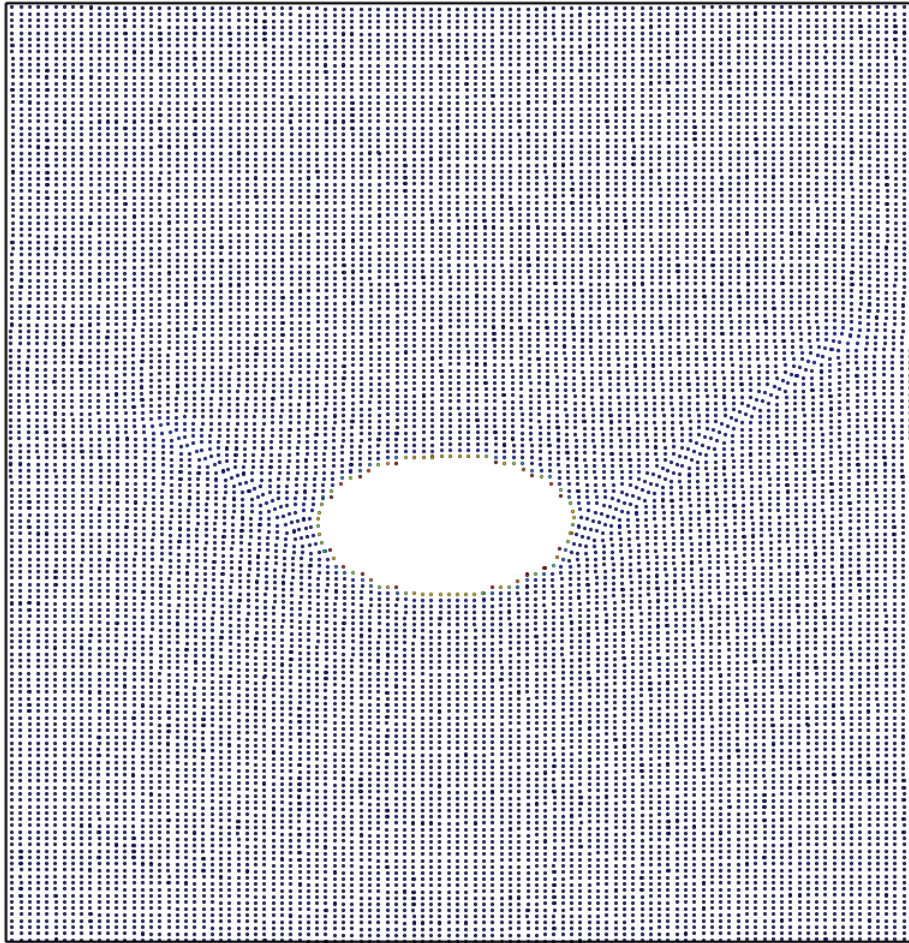
Figure 6-6: A picture of the full atomistic simulation cell. At this stage, twin is already nucleated at the crack tip and have propagated by significant length. The twinned region is clearly visible due to different lattice orientation from the bulk.

As shown in Figure 6-6, after the initial twin nucleation at the crack tip, the

twins have propagated by significant distances on $\{11\bar{2}\}$ planes. The twinned region is clearly visible due to its different lattice orientation from the bulk, and the mirror symmetry about the twin boundary is also evident.

Shown in Figure 6-7 are the snapshots of the atomic configuration during the twin propagation.

Under shear stress of ~ 3.5GPa, the nucleated twin starts to propagate and its speed increases quickly in about 0.3 nanosecond to steady-state velocity of ~ 2300m/s. However, due to the periodic boundary condition, eventually the propagation of the twin is impeded and stopped, as the final atomic configuration shows.

As we analyze the atomic structure of the twin in Figure 6-7 and Figure 6-8, we see that slightly away from the propagating front of the twin the twinned region is of two-layer structure [2], whereas the structure of the propagating front of the twin is of partial edge dislocation character. Away from the propagating front, the twinned region becomes more and more thicker, from 2 layers to 6 layers.

As have been discussed at the beginning of this section, we can rotate the loading orientation by 90° so that the equivalent shear is of anti-twinning sense. As shown in Figure 6-9, the new loading orientation in the anti-twinning sense no longer favors twinning and dislocation emission from crack tip is instead observed. The CRSS for dislocation emission can also be calculated by transforming the stress matrix at critical point to the $(11\bar{2})$ plane coordination system. The transformed stress matrix is

$$\sigma^* = c\sigma c^T = \begin{bmatrix} -9.03 & 2.05 & 0 \\ 2.05 & -7.93 & 0 \\ 0 & 0 & -6.72 \end{bmatrix} GPa$$

and CRSS on $(11\bar{2})$ plane is 2.1GPa, lower than the twinning CRSS of 3.5GPa obtained in previous simulation. The dislocations emitted from the crack tip are pure $\frac{a}{2}[111]\{11\bar{2}\}$ edge dislocations. Interested readers can refer to [141, 142] for current models of dislocation nucleation at crack tip.

---

[2]As will be shown in later 1D chain analysis, two-layer structure is the minimum structure that is energetically meta-stable.
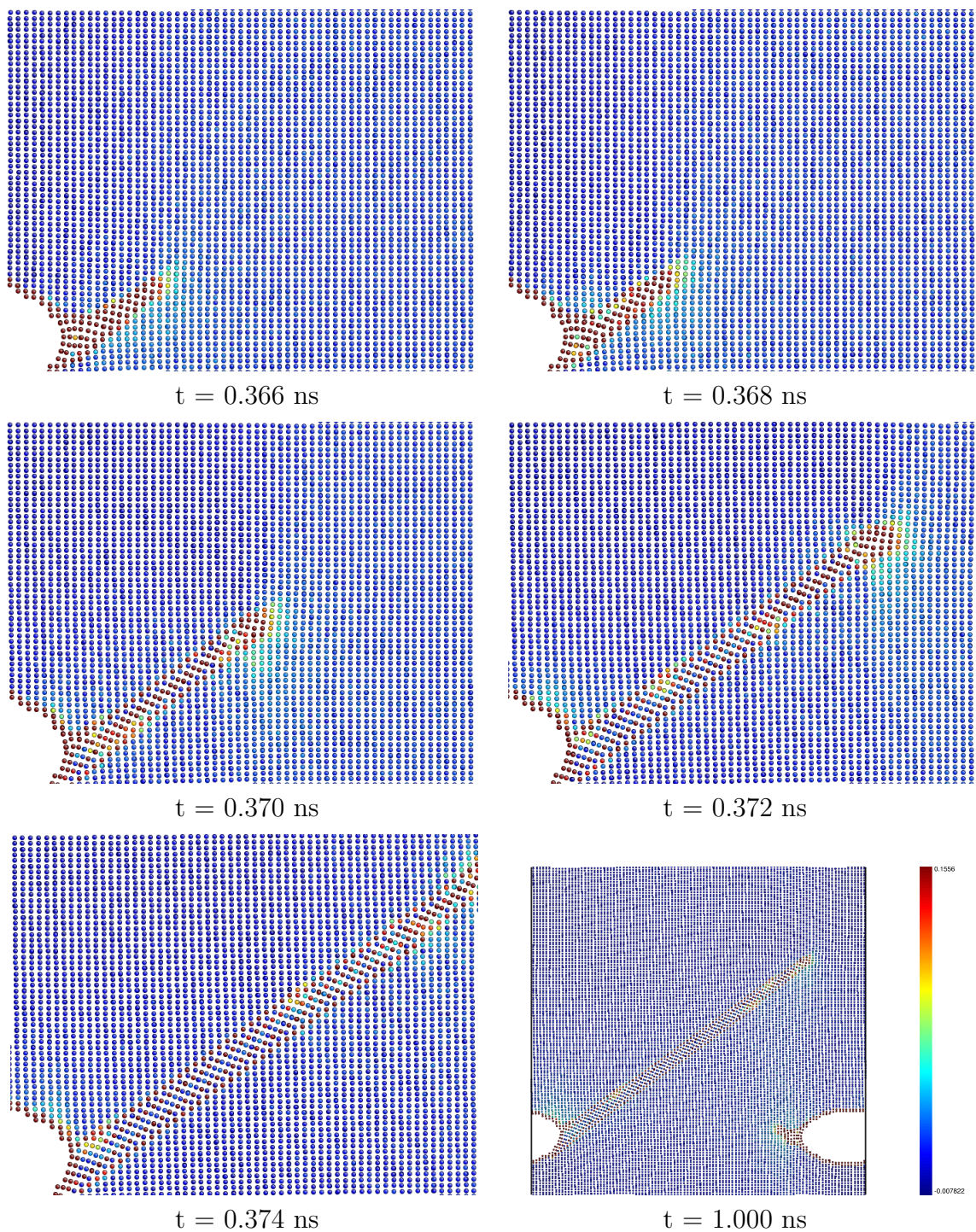
Figure 6-7: Sequence of atomic configurations during MD simulation. Atoms color-coded by energy with the color map shown above.
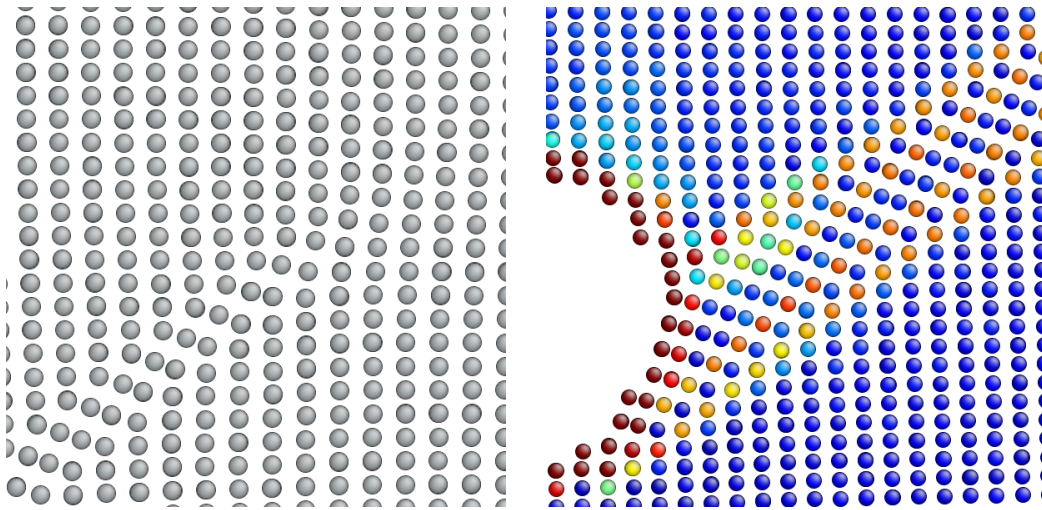
Figure 6-8: Atomic details at the propagating front of the twin and at the crack tip.
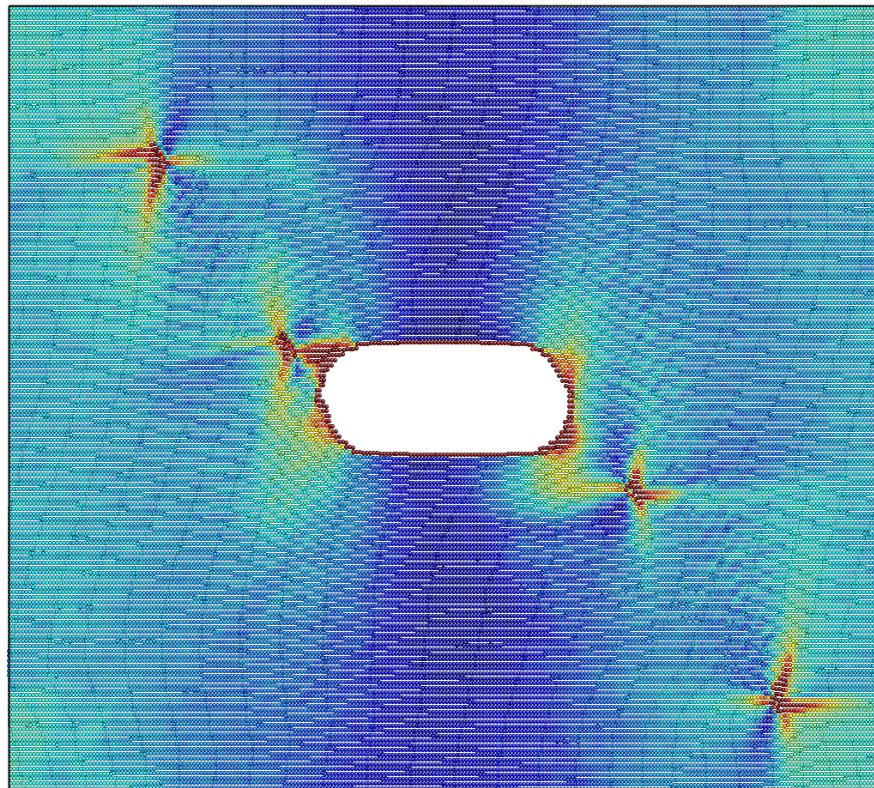
Figure 6-9: Loading orientation changed to anti-twinning sense and dislocation emission from crack tip is observed.

6.2.2 Quasi-2D Shear Loading on Perfect Crystal

In this section, we simulate twin nucleation and growth in perfect crystals that has no pre-existing defects embedded in.
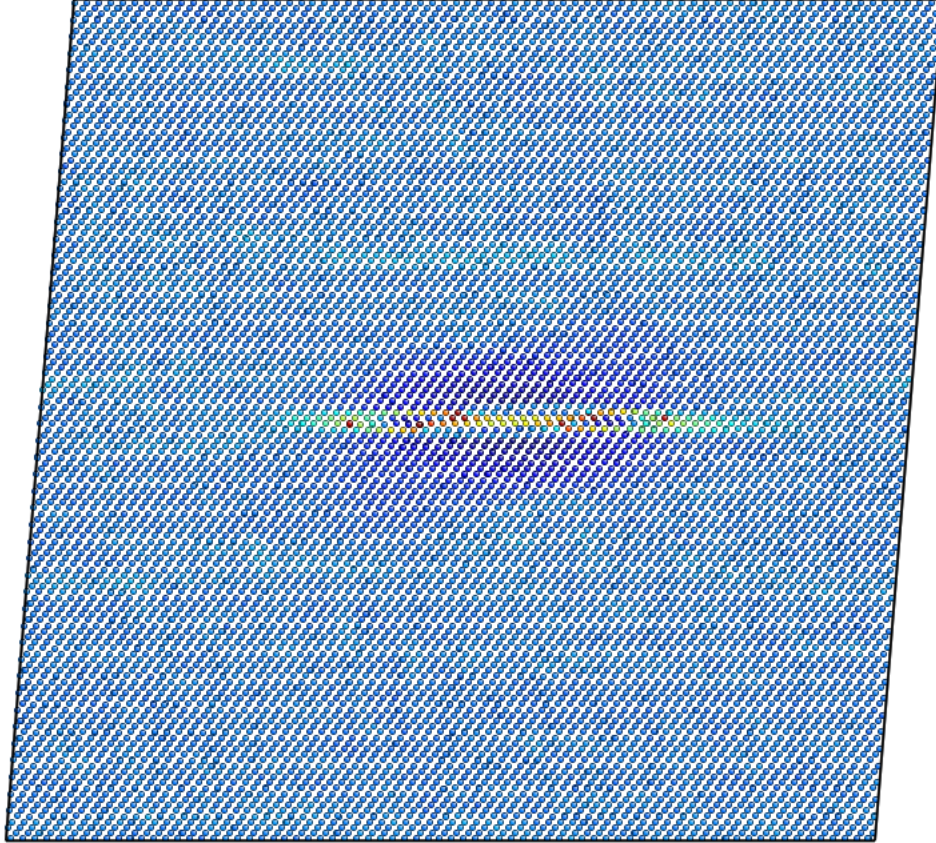
Figure 6-10: A picture of the early stage of twin growth. The twin has already been nucleated.

In this simulation, we set up an initial atomic configuration of molybdenum that has perfect BCC crystal structure. For convenience, we choose the X,Y,Z axes to be along [111], [10$\bar{1}$],and [$\bar{1}$2$\bar{1}$] respectively. The dimension of the simulation cell is 199.0Å in X (along [111]), 192.7Å in Z (along [$\bar{1}$2$\bar{1}$]), and 8.9Å in Y (along [10$\bar{1}$]). The thickness in Y is minimal and therefore this is a quasi-2D simulation.

Shear loading is applied at a constant rate of 1×10^8 s^{-1} on ($\bar{1}$2$\bar{1}$) plane, i.e., the xy plane, in [111] direction. This is the twinning direction whereas the opposite will be the anti-twinning direction.

As the shear loading is increased, the deformation of the crystal changes from linear elastic to nonlinear elastic, and finally plastic deformation occurs through twin nucleation growth, as shown in Figure 6-10.
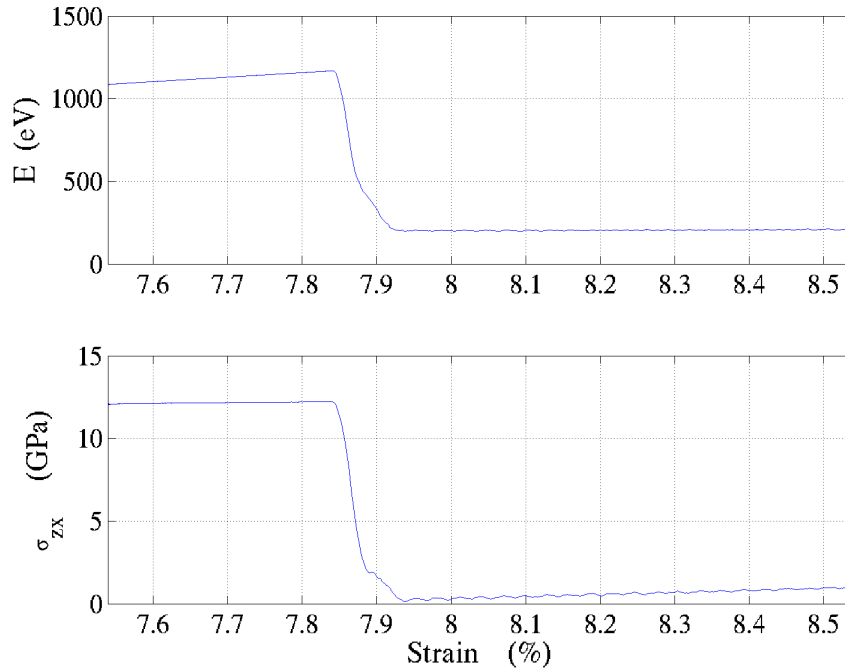
Figure 6-11: The energy and shear stress curve with respect to applied strain. The large energy and stress relief due to twin nucleation and growth is evident.

We plot the energy and shear stress data as a function of applied shear strain in Figure 6-11. Evident from the plot is that both energy and shear stress will start decreasing at critical strain of 7.84% due to twin nucleation, and as the twin grows, both of them continue to decrease until finally the twin band is fully formed and no longer grows. From then on, the stress-strain relation becomes linear elastic again. The energy drop is as much as 1000 eV and the shear stress drops from 12.4GPa to close to zero.

Next we look at the atomic structure of the nucleated twin embryo at critical stress of 12.4GPa and critical strain of 7.84% in Figure 6-12. The central portion of the twin embryo has a thickness of 2-3 layers while its edge is thinner. If one considers
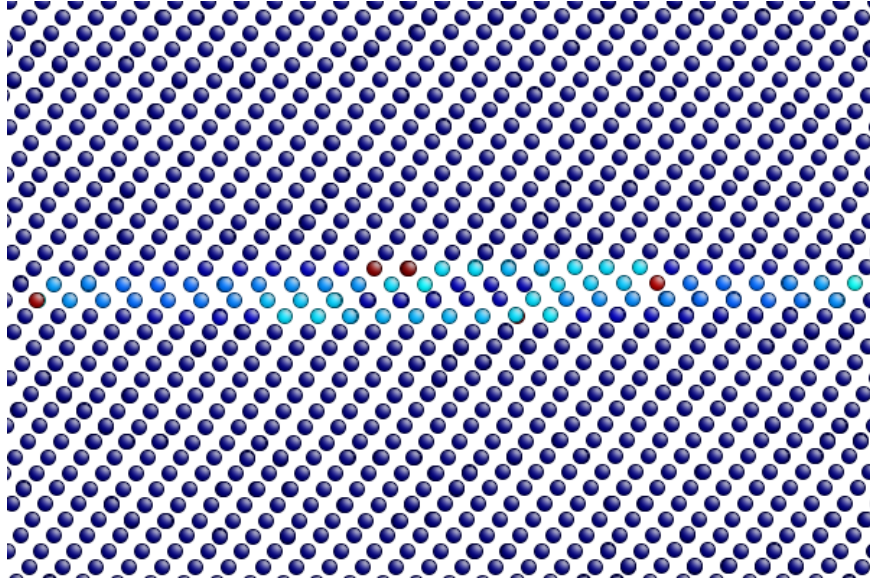
Figure 6-12: A closer look at the twin embryo.

the edge to be 1-layer thick then it can be considered as a twinning dislocation that is a partial edge. The propagation of this twinning dislocation controls the rate at which the twinned region grows in the {112} plane. From the MD simulation data, we estimate the velocity of the twinning dislocation to be $\sim$ 6000 m/s, which is comparable to the longitudinal wave velocity in Finnis-Sinclair Mo (6700 m/s) and in the transonic region.

The out-of-plane growth of nucleated twin is much slower than the in-plane growth and its velocity is estimated to be a factor of $\sim$ 30 times lower.

Since we are using periodic boundary conditions, the two propagating fronts of the twinned region will eventually encounter each other and merge together to finally form a flat twin band, as shown in Figure 6-13. The twinned region has a structure of 11 layers. We analyze the layer-by-layer relative displacements in Figure 6-14. Relative displacements are plotted in units of Burgers vector: $1b = 2.73$Å against the layer index. (The atomic layers that are in the bulk and are away from the twin boundaries all have relative displacements close to zero and are not shown in the plot.) The relative displacement distribution of the twin is essentially: $(0, ..., 0, \frac{b}{3}, \frac{b}{3}, ..., \frac{b}{3}, \frac{b}{3}, 0, ..., 0)$. This is in agreement with results from the 1D chain analysis which we will discuss
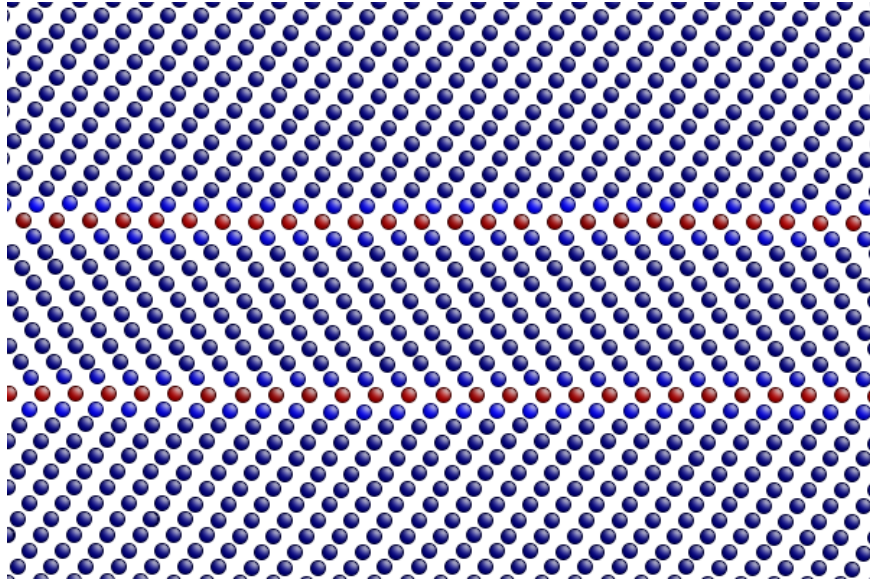
Figure 6-13: 11-layer twin structure after the twinned region merged with itself due to PBC.
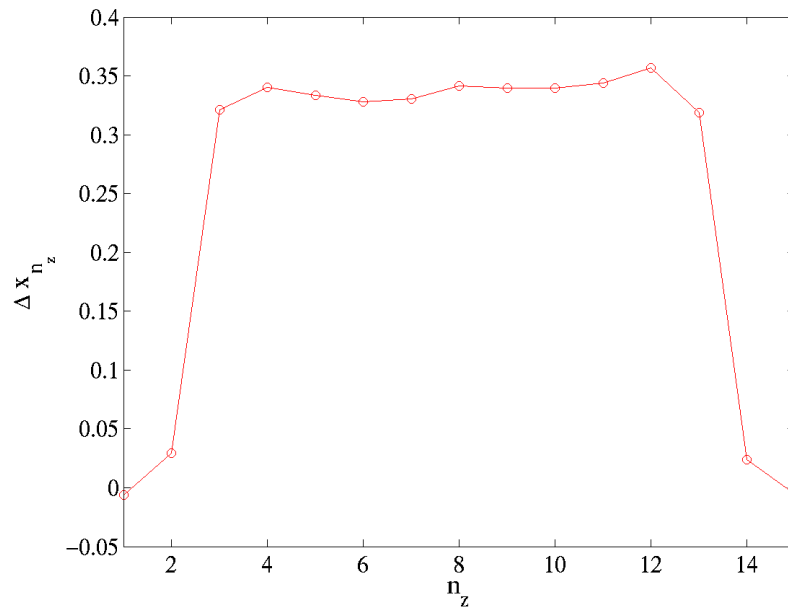
Figure 6-14: The relative displacement curve for the 11-layer twin structure.

later in the chapter.

6.2.3 3D Shear Loading on Perfect Crystal

The quasi-2D simulation that we discussed in the previous two sections have provided some useful information on the twin nucleation and growth; however, the quasi-2D model is highly restrictive and may miss important features that can only be observed and studied in a full 3D model.

In this section, we set up a full 3D atomistic model that removes the restrictions imposed by quasi-2D models and simulate twin nucleation and growth in a more realistic settings.

The initial atomic configuration of molybdenum has the perfect BCC crystal structure. Same as the previous simulation of quasi-2D shear simulation on perfect crystal, we choose the X,Y,Z axes to be along $[111]$, $[10\bar{1}]$,and $[\bar{1}2\bar{1}]$ respectively. The dimension of the simulation cell is 199.0Å in X (along $[111]$), 192.7Å in Z (along $[\bar{1}2\bar{1}]$), and 198.6Å in Y (along $[10\bar{1}]$). Now we have enough thickness in Y and certain important features of twin nucleation and growth that are impossible to appear in quasi-2D simulations,, e.g., dislocation loop nucleation, can now be modeled in this 3D simulation.

The simulation temperature is kept constant at $T = 10$K. At this low temperature, atomistic pictures of twinning suffer very little from thermal fluctuations and appear in a clear manner which will make the geometry analysis much easier and less prone to error. Shear loading is applied at a constant rate of $3 \times 10^6 \ s^{-1}$ [3] on $(\bar{1}2\bar{1})$ plane, i.e., the xy plane, in $[111]$ direction. This is the twinning direction whereas the opposite will be the anti-twinning direction.

As shown in Figure 6-15 and Figure 6-16, twin nucleation and growth occurs above a critical shear stress of 12GPa and a critical shear strain of 8%. Both energy and shear stress experience sharp drop as the twin is nucleated and grows, as shown in Figure 6-17.

In Figure 6-15 we look at the twin from above the simulation cell with a view angle of approximately 45° and can see the twin region is quite flat and has a ellipsoidal

---

[3]We were able to achieve this low strain rate by first bringing the system to a point that is close to critical point using a high strain rate, and then changing the strain rate to a much smaller value.
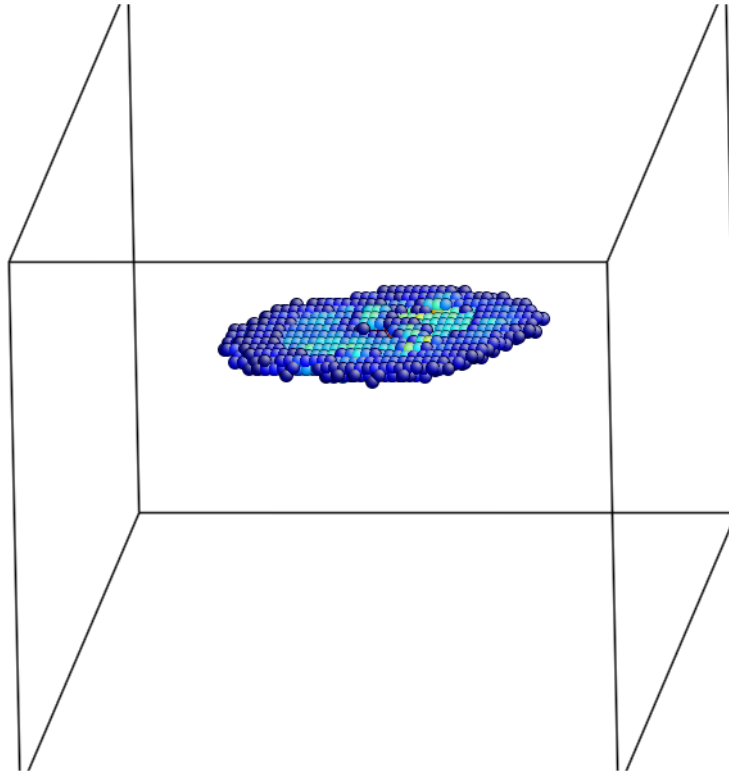
Figure 6-15: A picture of the twin disk in the middle of its growth. Its form is that of a ellipsoidal disk. However, the edges of the disk is as thin as 1 layer and the center of the disk is the thickest.

shape. (Only the atoms in the twinned region are shown whereas the bulk atoms have been removed for viewing convenience.)

In Figure 6-16 we look at the atomic configuration from the side, i.e., shown in the picture is a xz plane that was obtained by making a cut through the center of the twin and the normal-to-paper direction is parallel to Y axis. The twin boundary can be identified by following the light-colored atoms which have different colors from the bulk atoms due to their higher local strain values. With the twin boundary identified, one can see that the twin is thickest at the center while becoming thinner and thinner off the center. Overall shape of the twin is roughly like that of a spaceship or a football, except it is much thinner. (One may attempt to describe the twin to have a penny shape, but it is not accurate either due to the difference in thickness of the twin at the center and at the edge.) The shaded area surrounding the twin corresponds
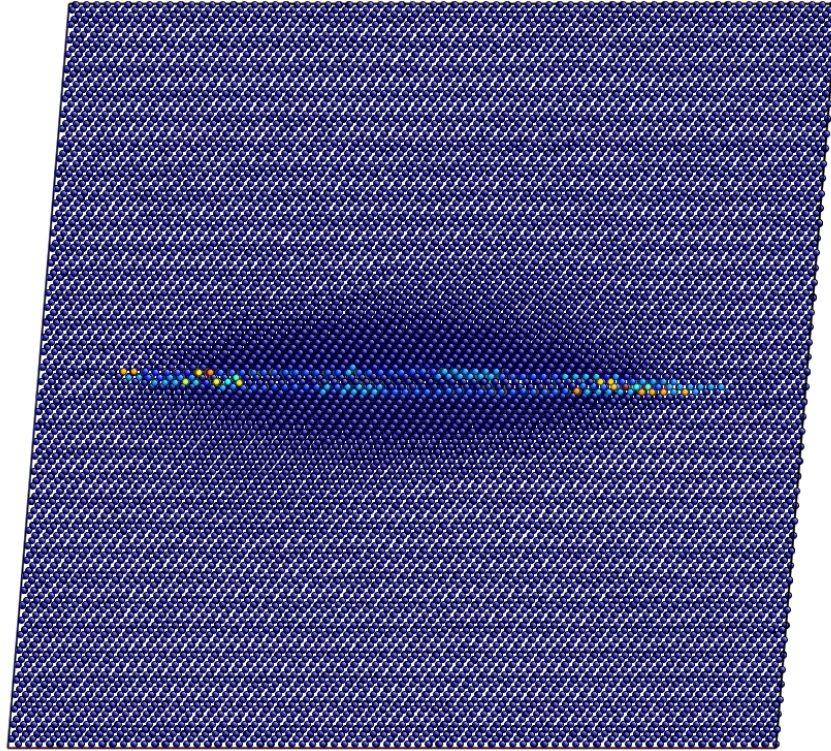
Figure 6-16: A side-view picture of the twin disk in the middle of its growth. From this angle, its shape is more like that of a spaceship. The edges of the disk is as thin as 1 layer and the center of the disk is the thickest.

to atoms having relative large elastic displacements and its shape better resembles a spaceship.

This is the first time that detailed information on the shape of homogeneously nucleated twins is obtained by a full 3D atomistic simulation. Combining the information one has obtained from these two figures, one can imagine in 3D space what the twin looks like. Indeed, by looking at the twin from various view angles, we have concluded that the twin is a relatively think disk, thickest in the center (multiple layers) and thinnest at the edge (down to one layer), and the twin disk has an ellipsoidal shape.

Now let us take a detailed look at the atomic configurations during the twin nucleation and growth from different view angles.
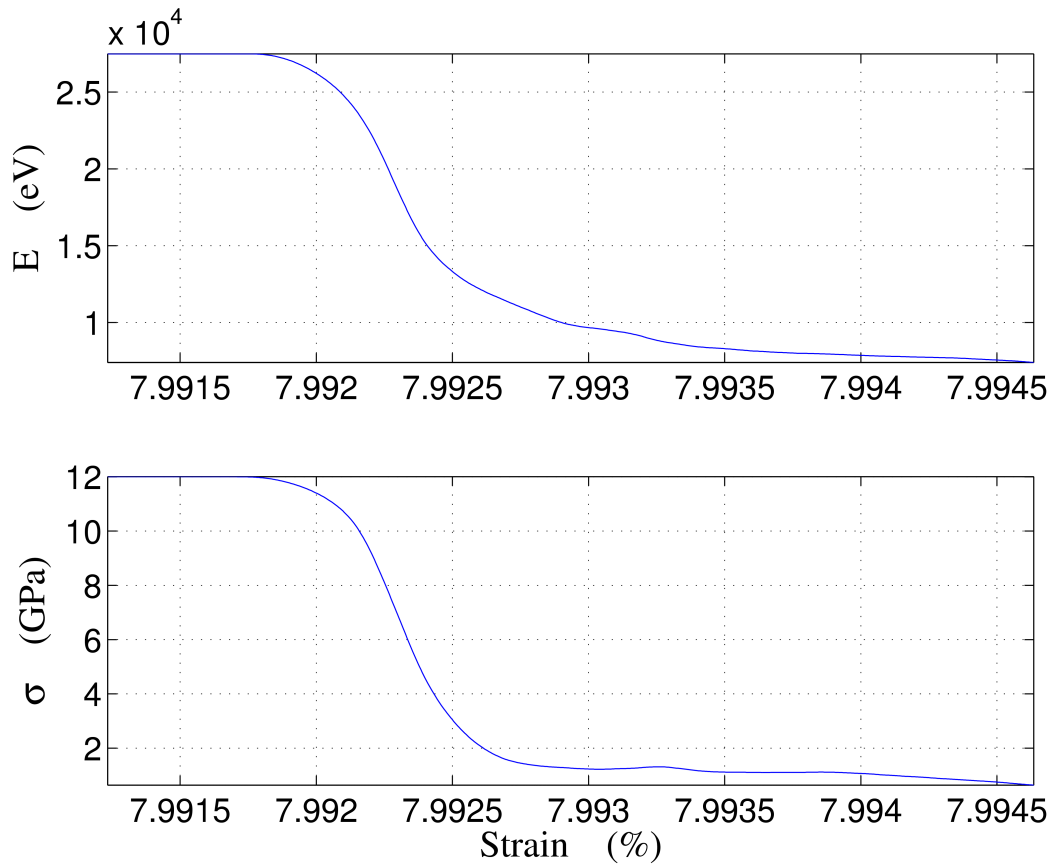
Figure 6-17: Total energy of the atomistic system and shear stress is plotted against the applied shear strain. Drastic drops in both energy and stress accompanies the nucleation and growth of the twin.

1. Top view:

   Shown in Figure 6-18 is the sequence of snapshots of the atomic configuration during the initial stage of twin nucleation and growth. We look at the configuration from the top, i.e., we are looking at xz plane and Y direction is normal to paper.

   From this view angle one can clearly see that the shape of the twin is more like an ellipse rather than a round disk. This is a manifestation of the anisotropy of dislocation mobility in molybdenum, i.e., screw dislocations have much lower mobility than non-screw components. The edge of the twinned region is indeed a loop of twinning dislocations, with the upper and lower edges being of screw

(a)

(b)

(c)

(d)

(e)

(f)

(g)

(h)

(i)

(j)

(k)
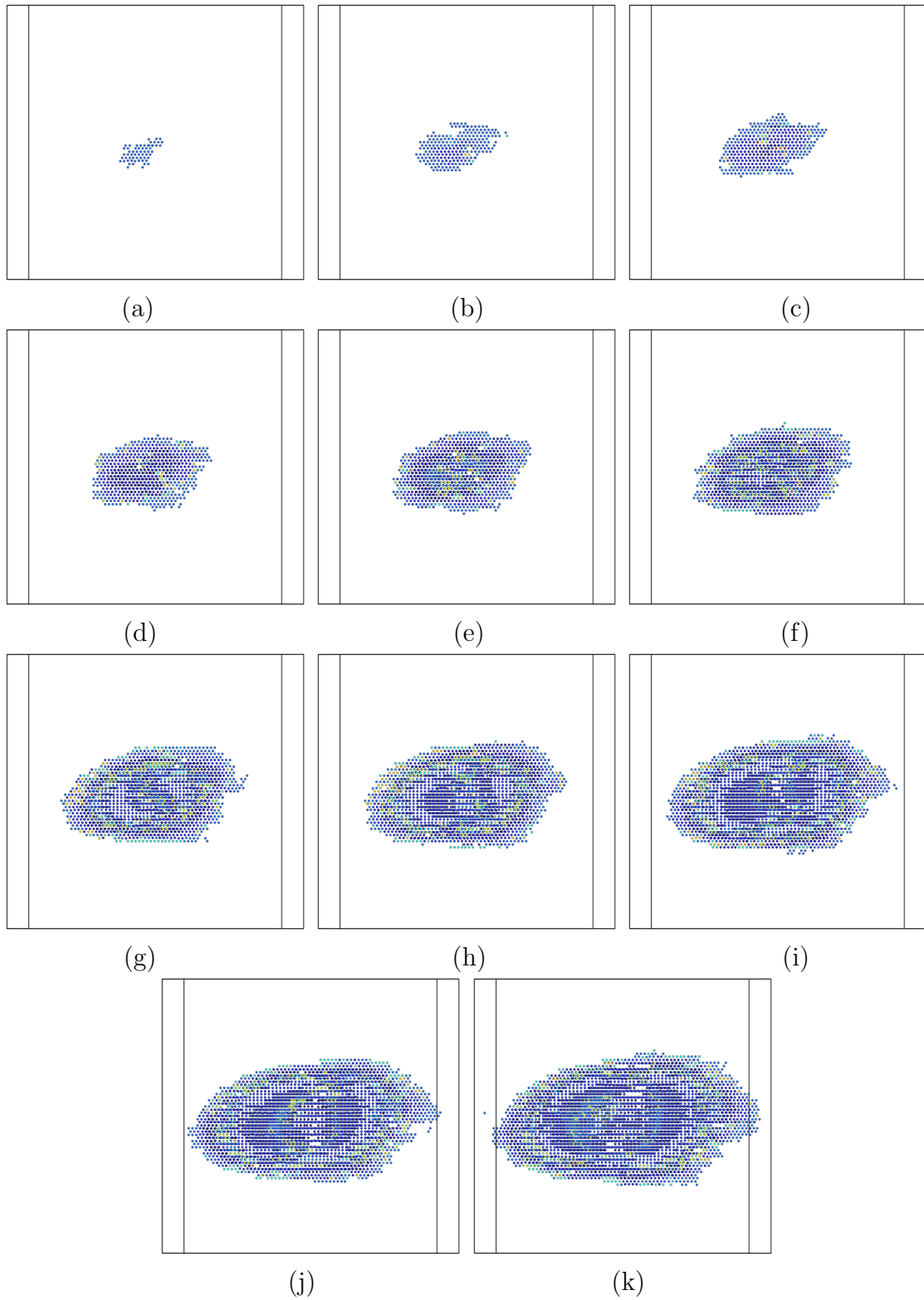
Figure 6-18: Evolution of the twin (top view).

153
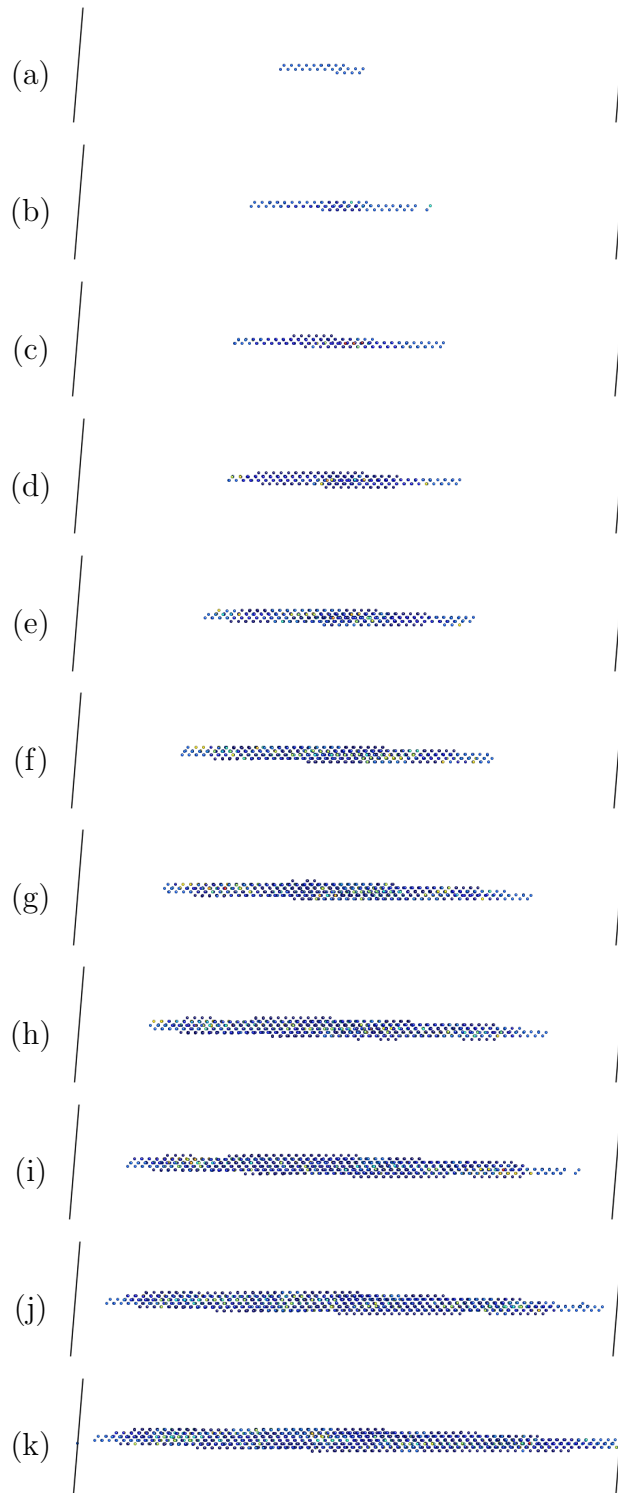
Figure 6-19: Evolution of the twin (side view).

type, the left and right edges being of edge type, and the parts in between being of mixed type. Since screw dislocation has lower energy and lower mobility than other components, it is the slowest during the expansion of the twinning dislocation loop and caused the overall ellipsoidal shape of the twin.

(a)

(b)
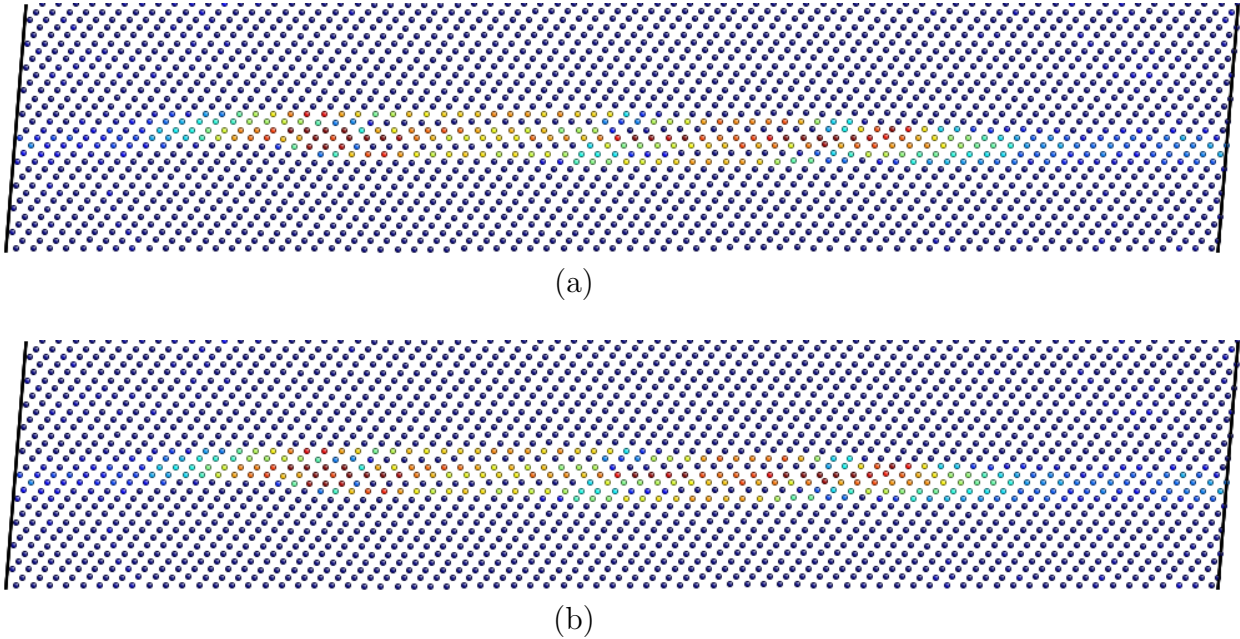
Figure 6-20: Side view of the twin. Only one slab of atoms is shown. (a) The slab is cut normal to Y axis and through center of twin, with the result being that the edge components of the twinning dislocation loop are shown. (b) The slab is cut normal to X axis and through center of twin, thus the screw components of the twinning dislocation loop are shown.

2. Side view:

   We now make a cut normal to Y axis and through the center of the twin, and look at the half configuration from the side. This cross-sectional view of the twin provides us with information complimentary to that from the previous view angle. It is clear from Figure 6-19 that the twinned region is a flat disk that is thickest at the center and gets thinner and thinner approaching the edge.

   Shown in Figure 6-20 is detailed view of the atomic configuration as in Figure 6-19(g). By geometry analysis one can identify the twin boundary and see that the edge of the twin disk is a twinning dislocation loop that has a Burgers vector

of only $\frac{1}{3}\vec{b}$, with a full Burgers vector $\vec{b} = \frac{a}{2}[111]$. Alternatively, one can also consider the edge of the twin disk as a one-layer twin. The twin becomes thicker and thicker approaching the center, becoming two layers within several Å's and then three layers, four layers, etc, becoming thickest at the center.

3. 3d view:

   By now one should be able to fully construct a mental picture of the twin in 3d space from Figure 6-18 and Figure 6-19. As a confirmation, 3d snapshots are also shown in Figure 6-21, where one can see that the previous observations about the shape of the twin are correct. As the twin grows, the expansion of the twin disk in the {112} plane is much faster than its out-of-plane growth. The in-plane growth is also anisotropic, causing the twin disk to resemble approximately the shape of an ellipse.

From the MD simulation, the velocity of the twinning dislocation while the twin disk was in expansion is estimated to be ~ 6000m/s, comparable to longitudinal wave speed in molybdenum, which is between 6000 and 7000 m/s from both experiments and Finnis-Sinclair potential. This is within expectation given the extra-large applied shear stress of 12GPa.

Due to the periodic boundary conditions, the twin disk will grow to merge with itself, similar to that observed in quasi-2D simulation of shear loading on perfect crystal. Simulation observations after that point is of little interest but it is interesting to note that once the twin region is fully formed it relieves large amount of shear strain and can even accommodate extra strain through further elastic deformation.

In summary, we have simulated the nucleation and growth of {112}⟨111⟩ deformation twins in BCC metal molybdenum using a Finnis-Sinclair potential model. Several different loading conditions have been simulated while our main focus is on the 3D simulation of homogeneous twin nucleation and growth in a perfect crystal. It is always dangerous to have prejudgements before looking at simulation results which will inevitably lead one to interpret the results differently, i.e., *you see what you expect to see.* Therefore, I have tried to maintain an objective perspective in
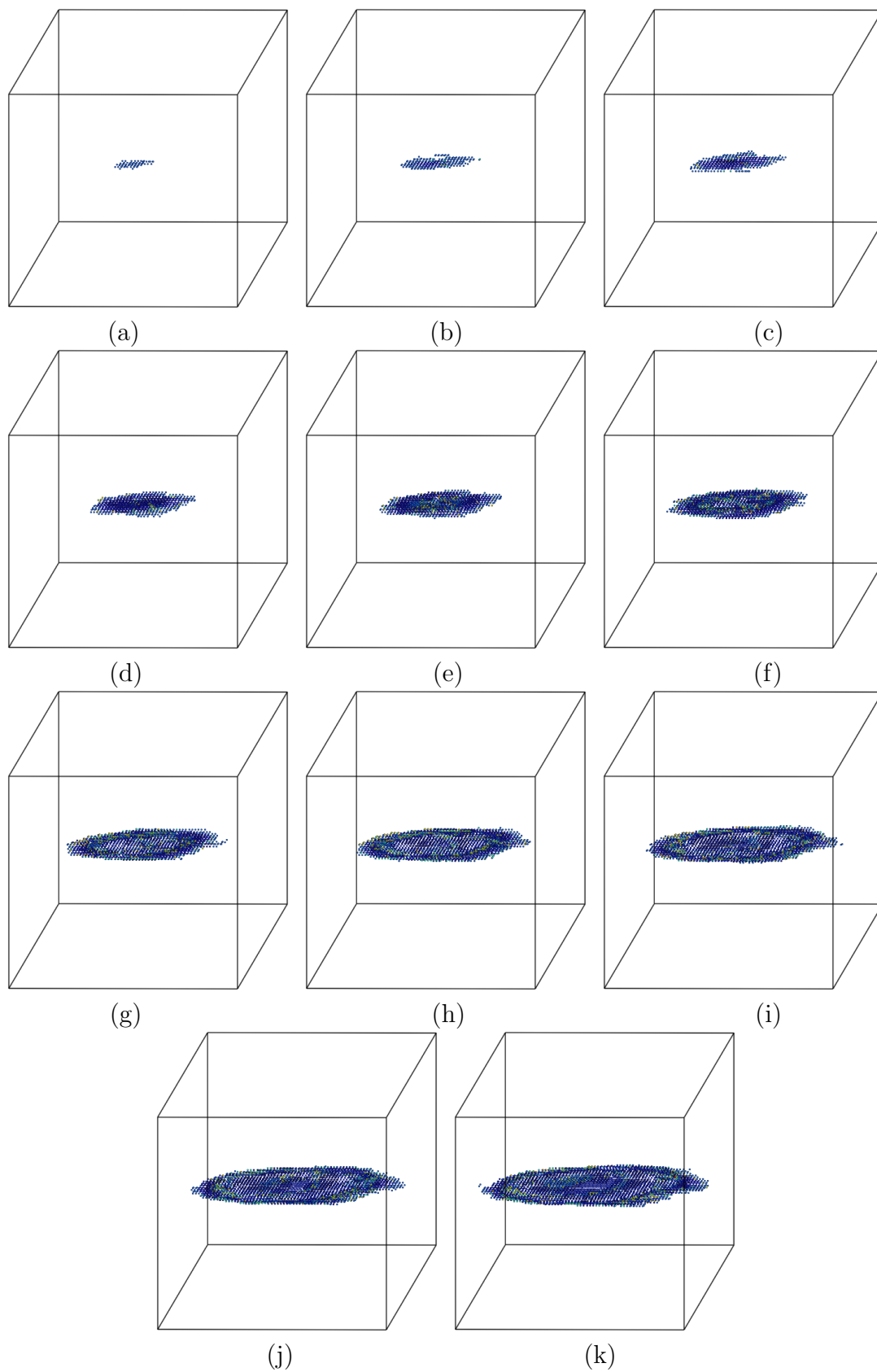
Figure 6-21: Evolution of the twin (a 3d view).

examining the simulation results and I believe the following conclusions can be made from the simulations:

- The nucleated twin is of ellipsoidal disk shape and its thickness gradually decreases from the center to the edge where the twin has only a thickness of only 1 layer and can be considered a twinning dislocation loop that has Burgers vector of $\frac{1}{3}\vec{b}$, where $\vec{b} = \frac{a}{2}[111]$.

- The in-plane expansion of the twin disk is rather fast under the high stresses applied, having a speed comparable to sound velocity; whereas out-of-plane growth of the twin disk is much slower, requiring twinning dislocation loop nucleation on top of the existing twin.

- The critical strain for twin nucleation in perfect crystal is simulated to be around 8% and the critical stress is about 12GPa, compared to much lower values in the pre-existing crack case. In real experiments, with pre-existing defect microstructure as well as a much lower strain rate than the ones used in the above simulations, the strain at which deformation twinning starts to play a significant role will be much lower than the values reported here.

- Across the twin layers, the relative displacement distribution of the twin is approximately: $(0, ..., 0, \frac{b}{3}, \frac{b}{3}, ..., \frac{b}{3}, \frac{b}{3}, 0, ..., 0)$.

In this section we have used large size molecular dynamics simulations to simulate deformation twinning in BCC molybdenum in a finite-temperature settings with relatively high-strain rate. Analysis of the MD results have provided us with valuable information about the geometry and characteristics of the homogeneously nucleated twin. In the next section, we will take a drastically different approach to study twin nucleation, namely, we will abandon the less important degrees of freedom and concentrate on the most important ones to arrive at definitive measures for twinning nucleation at the atomistic level.

6.3 1-D Chain Model Analysis

In this section, we design a simple model, the 1-D Chain Model, to study the twin nucleation problem. The philosophy of the model is to ignore the unimportant degrees of freedom (DOF) and study only the most important DOF's; by doing this, the problem is greatly simplified without losing the true physics and can then be studied thoroughly in a low-dimension space.

We will first elaborate on the motivation for designing this model and describe the model, then proceed to apply the model to 1-layer, 2-layer, and multi-layer calculations. Finally, we will summarize the insights that we have gained from these calculations.

6.3.1 Motivation

From the previous section of MD analysis of twin nucleation and growth, one can see that large-size MD simulations can indeed provide useful informations as to the structure and mobility of the twin. However, due to the large size of the simulations, it is very difficult for human beings to fully understand a defect phenomena in such a high-dimensional space. What human beings can understand, though, is phenomena in low-dimensional space. The so-called "insights" on defect mechanisms, in some sense, is always achieved by a reduction of dimensional space only after which the large amount of information can be made compact and be understood better by human beings. The challenge is: how to achieve the reduction in DOF's without losing essential physics?

We can draw some inspiration from the problem of dislocations. In the study of dislocations, we usually start from the problem of straight dislocation and study its core structure and Peierls stress, which one can call "primary effects", before moving on to consider the "secondary effects" such as kinks, jogs, junctions, etc. Here in the problem of twinning, we can also start from "primary" effects before moving on to "secondary" effects. Considering the change of thickness of the twinned region from 1-layer at the edge of the twin disk to multiple layers at the twin center to

be "secondary" effects, we can then focus on the "primary" effects where the twin thickness is assumed to be the same everywhere. In other words, let us now consider an infinitely extended flat twin. Essentially, this is to ignore the in-plane relaxation and assume all the atoms in the same xy layer are all moving in the same fashion. Considering the fast in-plane relaxation that we observed in the previous section's MD simulations, the most important mode of motion, which I consider to be the layer-to-layer relative shift, is not lost and essence of the problem is preserved. Furthermore, after this model analysis, one can extend the model to incorporate the "secondary" effects to come up with a full-blown model for twin nucleation.

This is indeed the 1-D Chain Model that we will describe below in more details. With this model, we will be able to study the twinning problem in a much lower dimensional space and arrive at quantitative measures and much more thorough analysis than what one can achieve in a larger dimensional space.

The approach we take here in designing the 1-D Chain model and carrying on various analysis in low-dimensional space drastically differs from the approach we have been adopting in the previous atomistic studies that we discussed in the thesis. In the previous calculations we have been always trying to go into more atomistic details to discover something; however, here we take an abstraction approach, stepping back and drastically simplify the problem in an effort to understand better the physics in a low-dimensional space where the essence of the problem resides.

6.3.2   The Model

As have been discussed, the 1-D Chain Model assumes all the atoms on the same {112} layer to be linked together rigidly. As one atom moves, all the other atoms on this layer follow its motion and the whole layer of atoms move in the same direction by the same amount.

Shown in Figure 6-22 is an example of such a 1-D Chain. Each atom represents a whole layer of atoms. Each atom has three degrees of freedom: in x, y, and z. In this problem, the most important DOF is x for each atom, while y and z can be either allowed to relax or held fixed.
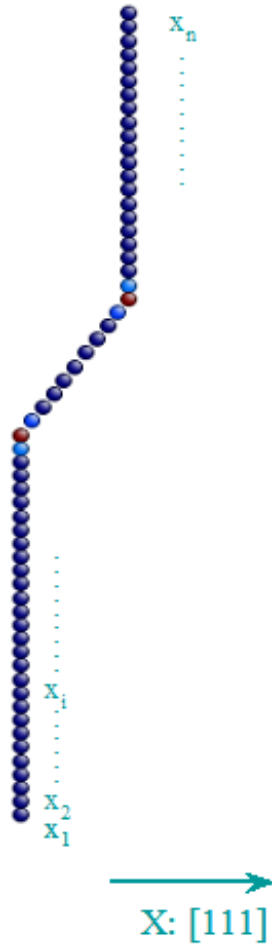
Figure 6-22: 1-D chain model is indeed a MD simulation of an atomic chain that fully represents the real shear displacement behavior of the (112) layers.

For example, in Figure 6-22 we have a 1-D Chain that consists of n atoms. Each of these atom, say, atom #i, has its own coordinates (x_i, y_i, z_i). The absolute value of x_i does not mean much, whereas $\Delta x_i = x_{i+1} - x_i$ is the relative displacements between neighboring layers in [111] direction and is a very important order parameter that we will use in the 1-D chain analysis.

For a N-atom 1-D Chain under PBC, there are N Δx_i's and $3N$ DOF's. The other $2N$ DOF's in y_i and z_i's (or, equivalently, in Δy_i and Δz_i's) shall be allowed to relax with given Δx_i's.

We can write total energy of the system as: $E = E(\Delta x_1, \Delta x_2, ..., \Delta x_i, ..., \Delta x_n)$. It
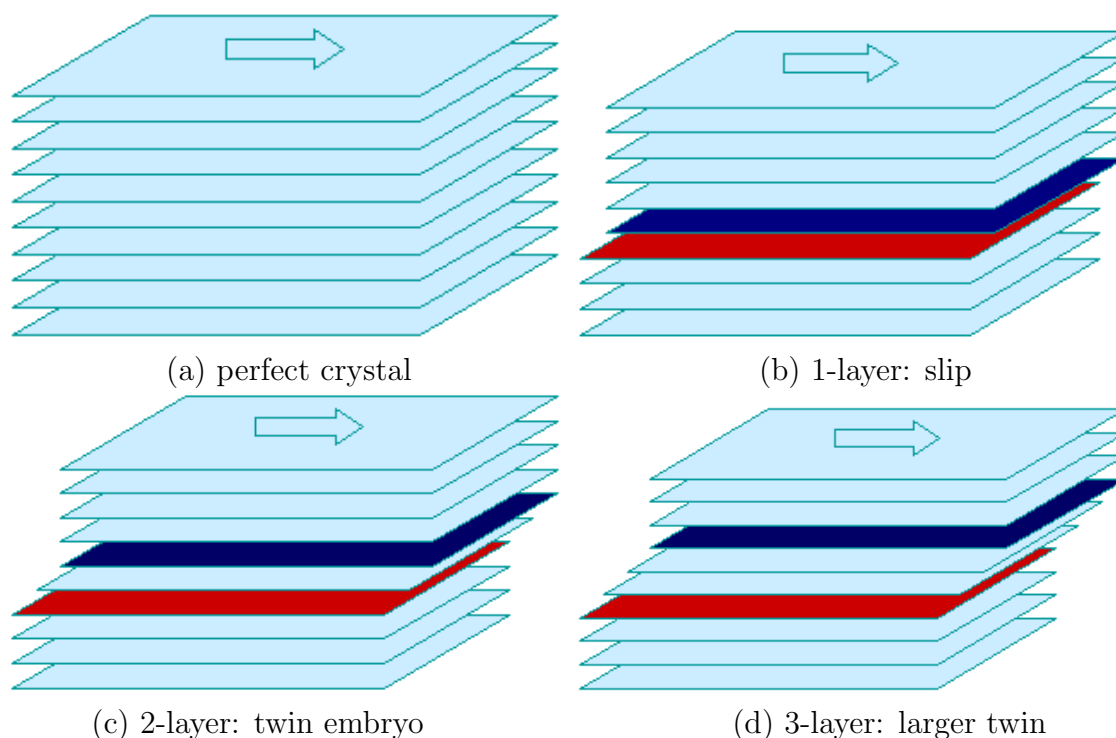
Figure 6-23: Schematics of slip and twinning. (a) Undeformed crystal: all Δx_i's are close to zero. (b) Deformation through slip (1-layer), relative displacement concentrated between two layers and all Δx_i's are close to zero except one of them. (c) A 2-layer twin: All Δx_i's are close to zero except two of them. (d) A 3-layer twin: All Δx_i's are close to zero except three of them.

means for any given configuration $(\Delta x_1, \Delta x_2, ..., \Delta x_i, ..., \Delta x_n)$, we can construct the corresponding atomic configuration and calculate energy for the atomic configuration using semi-empirical potential models or electronic structure calculations [4]. In this case, we use a modified Finnis-Sinclair potential model [20, 112] for all the 1-D Chain calculations.

As shown in Figure 6-23, slip and twinning can both be described by the 1-D Chain model. The perfect crystal in Figure 6-23(a) corresponds to a 1-D Chain where all Δx_i are zero or close to zero. Slip deformation in Figure 6-23(b) corresponds to a

---

[4]One can also use simpler models, e.g., assuming the atoms are harmonic oscillators and write a corresponding Hamiltonian for the system. However, it will be a much poorer representation of the true atomic interactions and shall not be used in this 1-D chain analysis where one often has large local strains which requires more accurate models.

1-D Chain where all Δx_i's are close to zero except for one of them. Therefore, we call this "1-layer" deformation. A two-layer twin in Figure 6-23(c) corresponds to a 1-D Chain where all Δx_i's are close to zero except for two of them. A three-layer twin in Figure 6-23(d) corresponds to a 1-D Chain where all Δx_i's are close to zero except for three of them. One can further extend the consecutive number of non-zero Δx_i's to have multiple-layer twins.

On whether to relax Δy_i's and Δz_i's, the physical answer is yes: one should always allow the DOF's in Y and Z to relax to have a more physical answer. One can immediately see that in 1-layer case, this is essentially the γ-surface calculation. Therefore, one can see this 1-D Chain model calculation as a multi-layer γ-surface calculation: $E = \gamma(\Delta x_1, \Delta x_2, ..., \Delta x_i, ..., \Delta x_n)$.

However, in some cases, the relaxation in Y and Z are not essential and does not change the physics, as will be shown in the example below. In those scenarios, one can save tremendous computing time by not relaxing Y and Z and yet get the physical answer. This consideration may well turn out to be very important in computationally expensive model calculations, e.g., electronic structure calculations.

6.3.3 One Layer Analysis

We begin our 1-D Chain model calculations from the 1-layer case. By fixing all the Δx_i's except for one (Δx_1) to zero and varying Δx_1 from 0 to $1b$, we obtain the energy curve with respect to Δx_1, as shown in Figure 6-26 for $(\bar{1}10)[111]$ slip system and in Figure 6-25 for $(\bar{1}\bar{1}2)[111]$ slip system which is also a twin system. The energy $E = E(0, ..., 0, \Delta x_1, 0, ..., 0)$.

For $(\bar{1}\bar{1}2)[111]$ slip system, we first calculate $E(0, ..., 0, \Delta x_1, 0, ..., 0)$ without relaxing y_i's and z_i's. As shown in Figure 6-24, the energy barrier for slip is 0.84eV, or in terms of energy per unit length in normal-to-paper direction(Y): 0.189eV/Å. Critical shear stress in positive direction is 30.26GPa, whereas critical shear stress in negative direction is 30.27GPa. The difference is minimal, not reflecting the twinning anti-twinning asymmetry characteristic of this slip system.

Then we repeat the calculation with relaxations in Y and Z. As shown in Figure
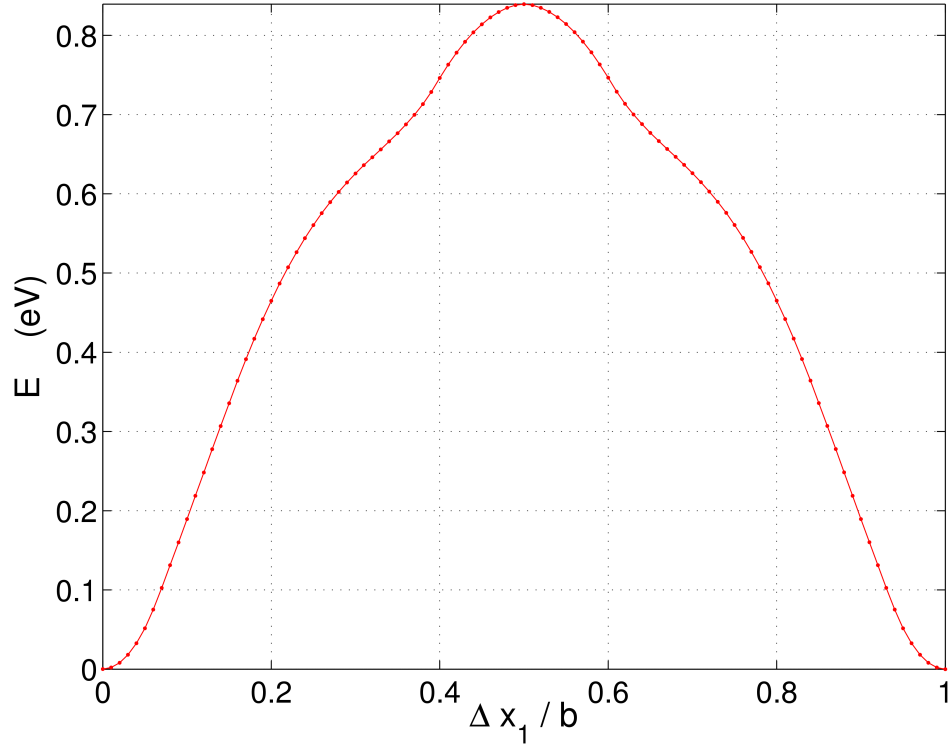
Figure 6-24: 1-layer analysis for $(\bar{1}\bar{1}2)[111]$ twin system, without relaxation in Y and Z.

6-25, the energy barrier becomes 0.82eV, or in terms of energy per unit length in normal-to-paper direction(Y): 0.184eV/Å. Critical shear stress in positive direction is 33GPa, whereas critical shear stress in negative direction is 29GPa. The difference between the two is a result of the asymmetry about $\Delta x_1 = \frac{b}{2}$ in the energy curve in Figure 6-25. The softening in the energy curve at approximately $\Delta x_1 = \frac{b}{3}$ did not result in a meta-stable energy state; however, this is closely related to twin nucleation and in the 2-layer analysis below we will see it turning into a local energy minimum that corresponds to a 2-layer twin. The softening in the positive direction causes the experimentally observed difference in CRSS for twinning and anti-twinning directions, and the twinning anti-twinning asymmetry will be best viewed in the 2-layer or multiple-layer analysis settings that we will soon get to.

For comparison, we also calculate $E(0, ..., 0, \Delta x_1, 0, ..., 0)$ for $(\bar{1}10)[111]$ slip system. As shown in Figure 6-26, the energy barrier for slip is 0.42eV, or in terms of energy

164
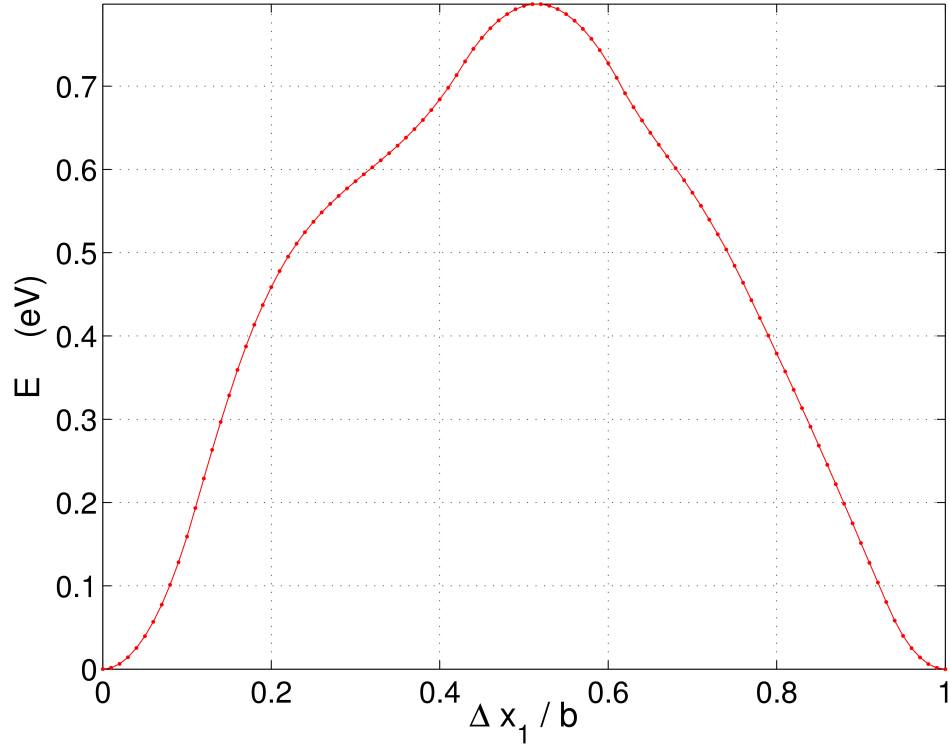
Figure 6-25: 1-layer analysis for $(\bar{1}\bar{1}2)[111]$ twin system, with relaxation in Y and Z.

per unit length: 0.163eV/Å. Ideal shear strength can be identified as the maximum slope in the energy curve to be 15.13GPa. Firstly, the critical stress for this slip system is much smaller than that for $\{112\}\langle111\rangle$, since this slip system is the primary slip system due to the large separation between layers (2.23Å compared to 1.28Å for $\{112\}\langle111\rangle$ slip system). Secondly, the energy curve is fully symmetric about $\Delta x_1 = \frac{b}{2}$ and therefore the resistance to positive and negative shear are the same. This is in contrast to the twinning anti-twinning asymmetry for $\{112\}\langle111\rangle$ slip system.

The 1-layer analysis is similar to the γ-surface calculation where one obtains the misfit energy by a rigid shift between two half crystals along a glide plane. This calculation reveals that there are no meta-stable energy states except for at $\Delta x_1 = n \cdot b$, where n is an integer, which means there are neither stable stacking faults nor stable partial edge dislocations on both slip systems.
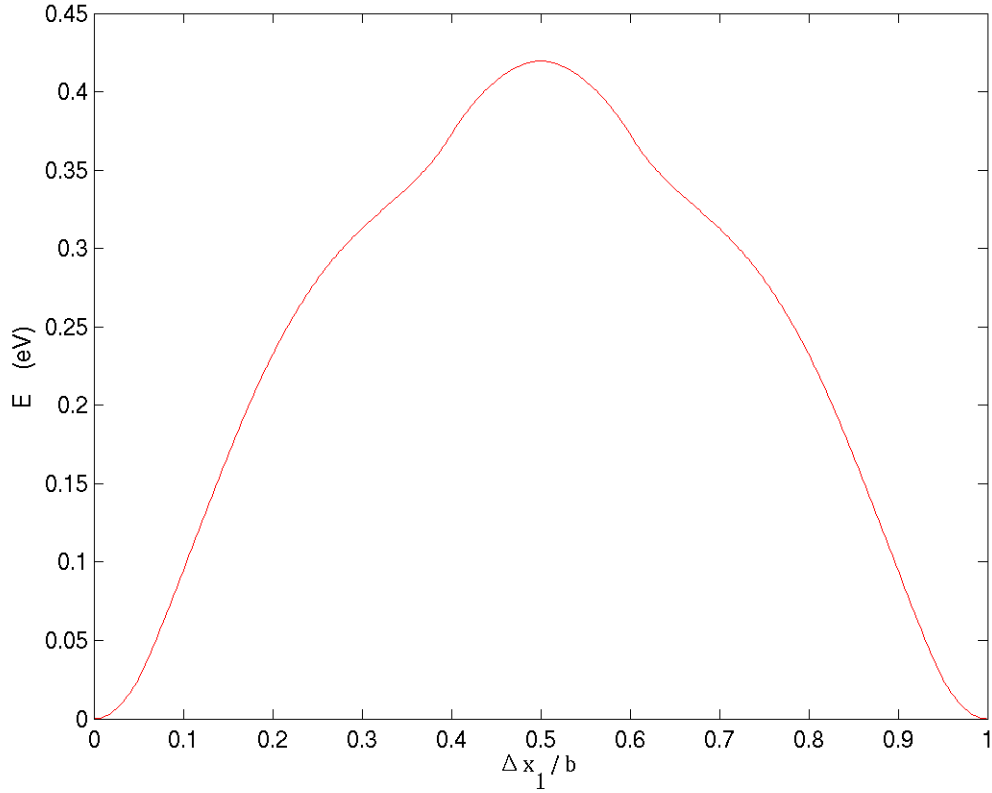
Figure 6-26: 1-layer analysis for $(\bar{1}10)[111]$ slip system.

6.3.4 Two Layer Analysis – Twin Embryo

Next we increase the number of free DOF's so that two of the Δx_i's are allowed to take non-zero values. In this 2-layer analysis, we will calculate $E = E(0, ..., 0, \Delta x_1, \Delta x_2, 0, ..., 0)$.

For $(\bar{\bar{1}}\bar{1}2)[111]$ slip system, we first calculate $E(0, ..., 0, \Delta x_1, \Delta x_2, 0, ..., 0)$ without relaxing y_i's and z_i's. Now we have two independent variables: Δx_1 and Δx_2. When plotting energy as a function of Δx_1 and Δx_2, we can plot it as an energy surface, as shown in Figure 6-27. In the figure, Δx_1 and Δx_2 are both normalized to b, and energy of the 1-D chain is plotted in units of eV. The height of the energy surface at given $(\Delta x_1, \Delta x_2)$ resembles the value of the energy $E(\Delta x_1, \Delta x_2)$. Valleys in the energy surface correspond to local energy minima and hilltops correspond to local energy maxima. Due to lattice periodicity of $1b$, the energy surface is periodic in

166
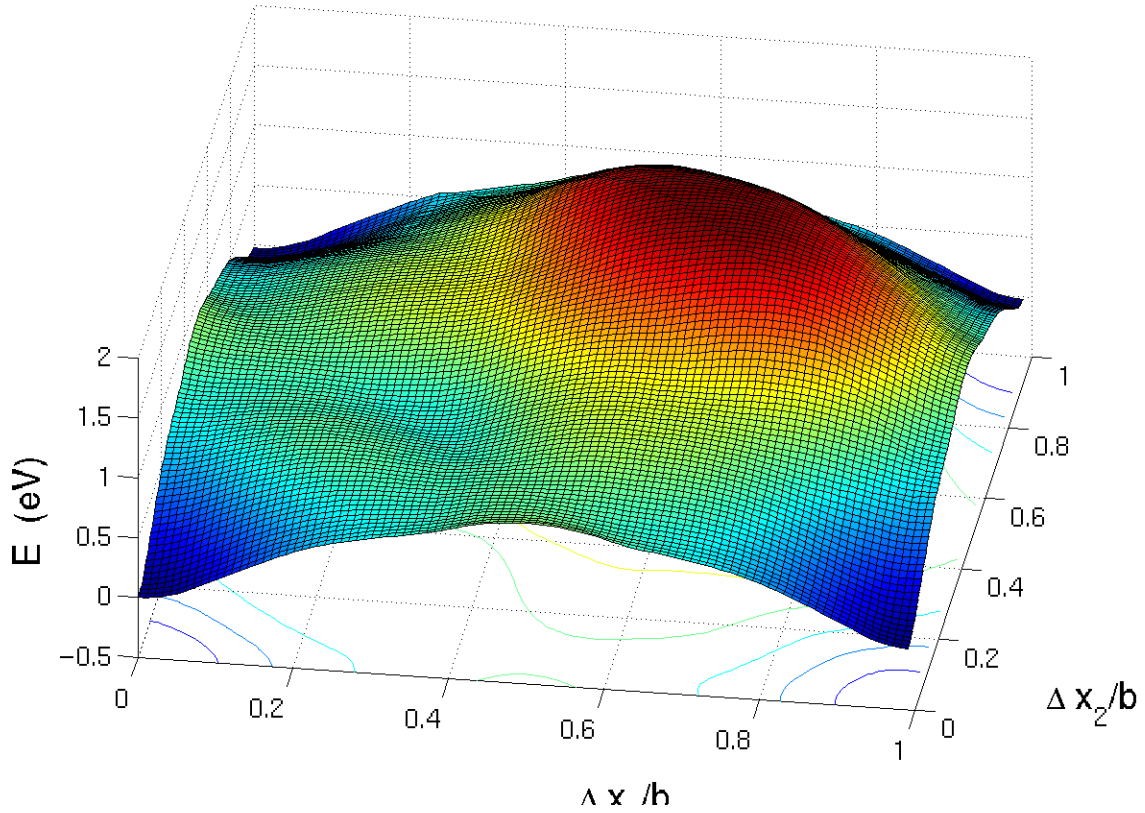
Figure 6-27: Energy surface in 2-layer analysis for $(112)[111]$ twin system, without relaxation in Y and Z.

both Δx_1 and Δx_1 with a periodicity of $1b$ and therefore we only need to calculate the region of $0 \leq \Delta x_1, \Delta x_2 < 1b$, as is shown in the figure.

Two important features emerge from the energy surface plot: one is the existence of a twinning local energy minimum, the other is the twinning anti-twinning asymmetry.

As one can see in Figure 6-27, except for the energy minima at whole numbers of lattice spacings, i.e., $(\Delta x_1, \Delta x_2) = (0, 0), (0, b), (b, 0), (b, b)$, there exists an additional local energy minimum at approximately $(\Delta x_1, \Delta x_2) = (\frac{b}{3}, \frac{b}{3})$ (to be exact, the minimum is at $(0.32b, 0.32b)$.) This local energy minimum corresponds to a 2-layer twin structure. The energy barrier for the system to jump from the $(0, 0)$ energy valley to the $(\frac{b}{3}, \frac{b}{3})$ valley is 0.706eV, with the saddle point located at $(0.36b, 0.16b)$, whereas

the energy barrier for the jump from $(0,0)$ to $(b,0)$ is 0.769eV, with the saddle point located at $(0.5b, 0.1b)$.
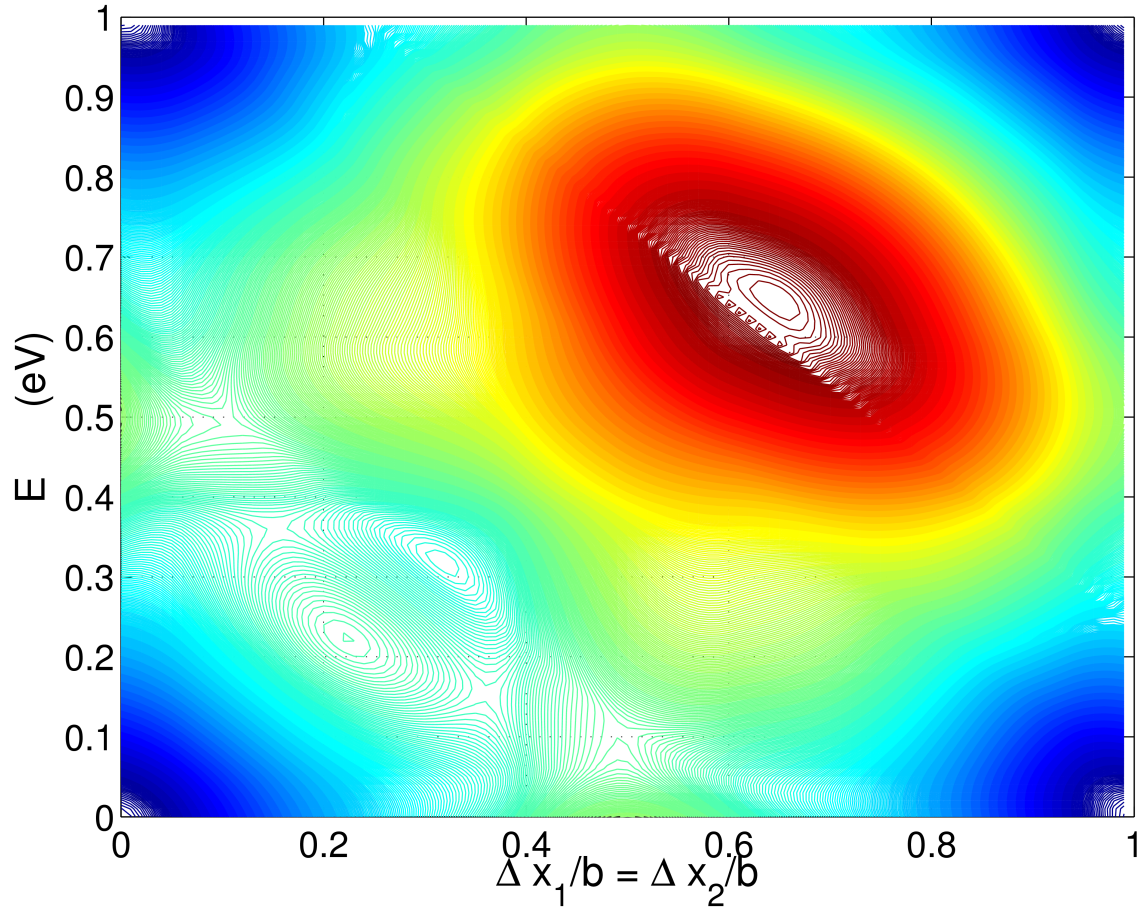
Figure 6-28: Energy contour in 2-layer analysis for (112)[111] twin system, without relaxation in Y and Z.

The energy landscape can be viewed more clearly in a contour plot as shown in Figure 6-28. The contour lines are color-coded by energy, with deep blue being 0eV and deep red being 1.66eV. In Figure 6-29 the energy contour is shown only for $0 \leq \Delta x_1, \Delta x_2 < 0.55b$ so that the details around the twin minimum can be seen more clearly.

From the energy contour plot one should be able to easily identify the local energy minima and maxima which are center of converging circles. The twin minimum is located to be at $(0.32b, 0.32b)$, with the energy being 0.652eV. The nearby local
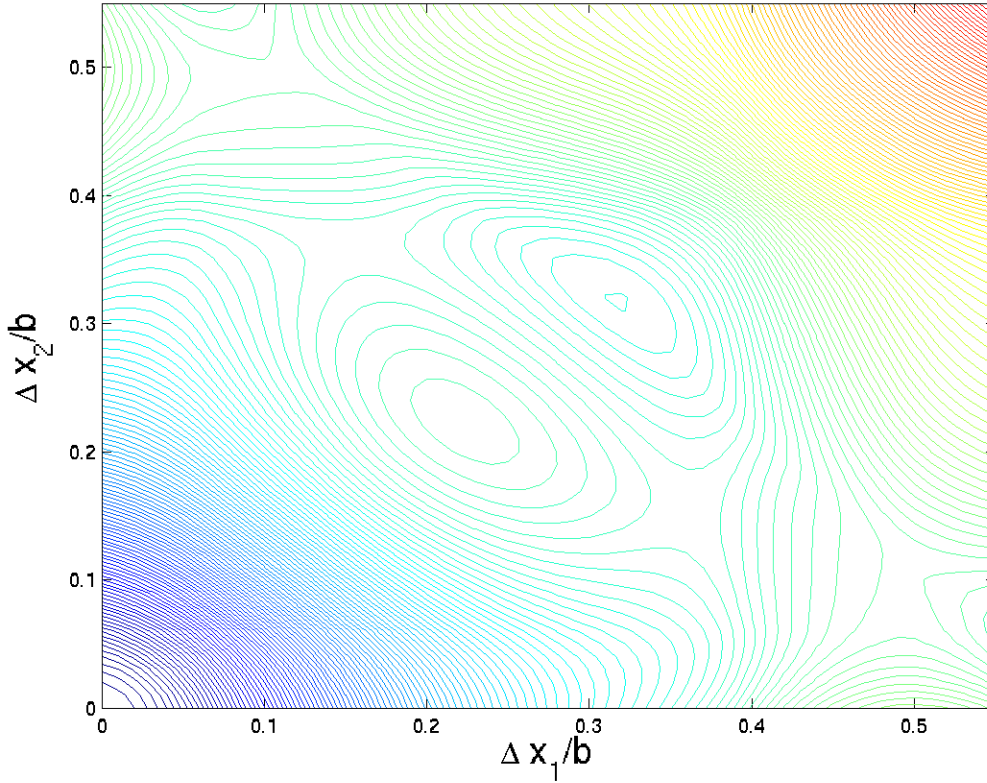
Figure 6-29: Energy contour in 2-layer analysis for (112)[111] twin system, without relaxation in Y and Z. We only show the region $0 \leq \Delta x_1, \Delta x_2 < 0.55b$ so that the details around the twin minimum can be seen more clearly.

energy maximum at $(0.22b, 0.22b)$ with energy of 0.749eV represents the maximum energy barrier to jump from $(0,0)$ to the twin minimum. However, this is not the true energy barrier. Indeed, the saddle point that represents the minimum energy required to complete the transition is located at $(0.36b, 0.16b)$ (or symmetrically at $(0.16b, 0.36b)$), with the true energy barrier determined to be 0.706eV. The lowest energy path that leads the system from $(0,0)$ to the twin minimum passes this saddle point and the whole path can be determined by following the sparsest separation between the energy contour lines, i.e., climbing the energy mountain with the path that has the smallest slope and such a path will be shown later for the relaxed case.

Similarly, we can determine the saddle point for transition from $(0,0)$ to $(b,0)$ to

be at $(0.5b, 0.1b)$, with the energy barrier being 0.769eV.

From these analysis, we can see that the 2-layer twin represents an energetically meta-stable structure that can be formed with an activation energy of 0.7eV per 1-D chain. In the competition with dislocation-based slip which is represented by the transition from $(0,0)$ to $(b,0)$, twinning is guaranteed to win when positive shear is applied, because the energy barrier for the system to jump from $(0,0)$ to $(\frac{b}{3}, \frac{b}{3})$ is 0.706eV, smaller than the energy required for slip (0.769eV).

However, if negative shear is applied, then the transition from from (b,b) to $(\frac{b}{3}, \frac{b}{3})$ has a different path. Notice the huge mountain that separates the two with the mountain top being at 1.66eV. The system will try to bypass the mountain and inevitably fall into the slip minimum at $(b,0)$ or $(0,b)$. Therefore, the system will never twin under negative shear.

The energy barrier for slip under negative shear is even higher than the energy barrier for slip under positive shear: 0.859eV. However, since twinning becomes impossible, this is the only deformation mode and will always be favored.

The difference in energy barrier between positive shear and negative shear highlights the twinning anti-twinning asymmetry on {112} that can be observed in experimental CRSS measurements, as have been discussed in Chapter 2. Here we have shown that the asymmetry is due to the existence of a twinning energy minimum and consequent lower energy barriers when positive shear is applied.

Now we redo the calculation with relaxations in Y and Z and see whether the physics is changed.

As shown in Figure 6-30, the twin minimum again shows up in the energy surface. In Figure 6-31 we take a side view so that the normal-to-paper direction is parallel to Δx_2 axis. From both figures, the twin minimum is clearly visible. The energy for the twin minimum is 0.611eV and the exact location of the twin minimum remains at $(0.32b, 0.32b)$.

Shown in Figure 6-32 is the energy contour plot for the relaxed case. Again, we can determine the energy barriers for transition between the energy minima. Under positive shear, the system can either twin or slip. The energy barrier for twinning is
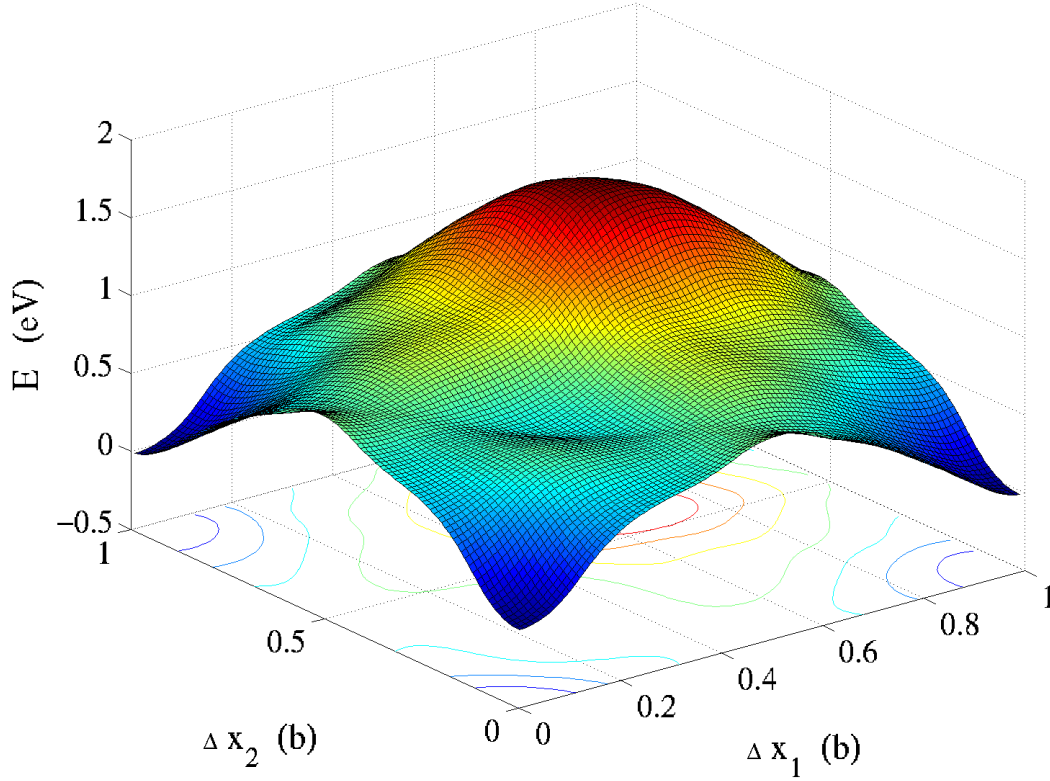
Figure 6-30: Energy surface in 2-layer analysis for $(112)[111]$ twin system, with relaxation in y_i's and z_i's.

0.672eV with the saddle point at $(0.36b, 0.16b)$, whereas the energy barrier for slip is 0.736eV with the saddle point at $(0.5b, 0.09b)$. Under negative shear, the system can only slip, with an energy barrier of 0.808eV.

Utilizing the energy contour, we can also plot out the whole minimum-energy path for either slip or twinning. As shown in Figure 6-33, the minimum-energy path for twinning connects the perfect lattice energy minimum $(0, 0)$ and the 2-layer twin minimum $(\frac{b}{3}, \frac{b}{3})$ whereas the minimum-energy path for slip connects the perfect lattice energy minimum $(0, 0)$ to the slip minimum $(b, 0)$. The two paths bifurcates at $(0.29b, 0.03b)$, before either of the saddle points have been encountered. The system can either twin or slip after the bifurcation point; however, since the twinning path has a lower energy barrier (0.672eV) than the slip path (0.736eV), twinning will be
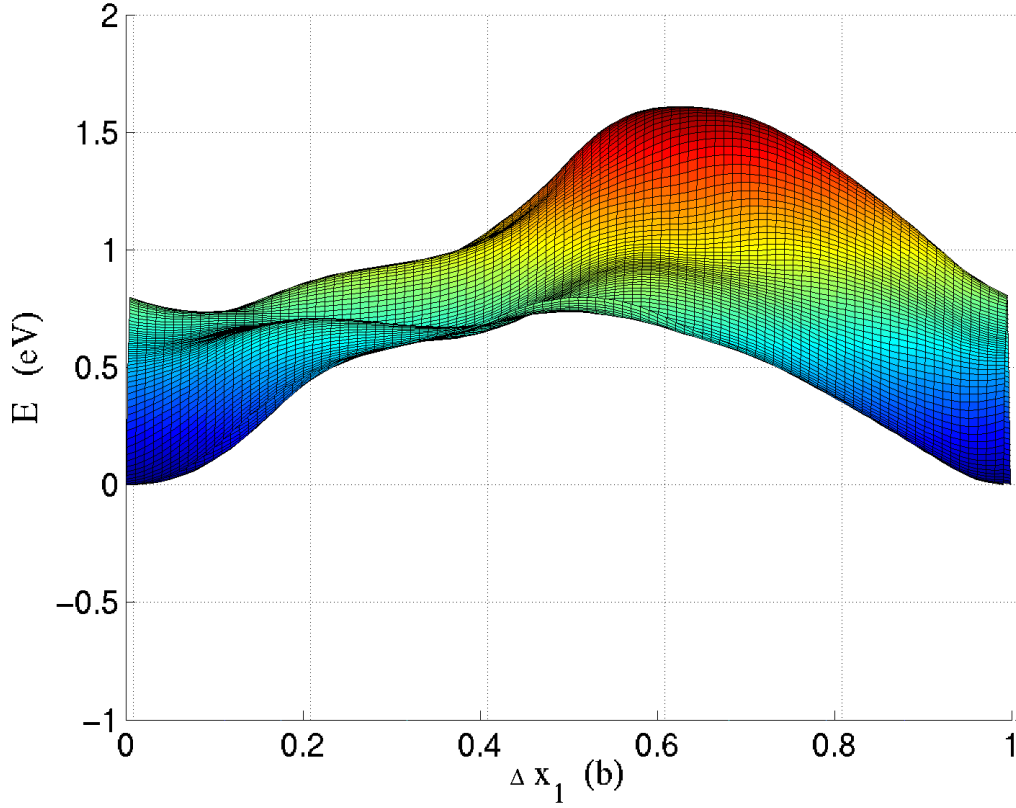
Figure 6-31: Energy surface in 2-layer analysis for (112)[111] twin system, with relaxation in y_i's and z_i's. A side view so that the normal-to-paper direction is parallel to Δx_2 axis.

favored.

From this analysis, we can define a simple energy criterion for competition between twinning and slip. We denote γ_{twin} as the activation energy for the twin nucleation in the 1-D chain model, and γ_{slip} as the activation energy for slip. Then we can compare γ_{twin} to γ_{slip} to see which mode will be favored when they come into competition:

$$\text{Twinning favored, if } \gamma_{twin} < \gamma_{slip};$$
$$\text{Slip favored, if } \gamma_{twin} > \gamma_{slip}.$$

For $(\bar{1}\bar{1}2)[111]$ system, $\gamma_{twin} = 0.672\text{eV} < \gamma_{slip} = 0.736\text{eV}$; therefore, twinning is favored and $(\bar{1}\bar{1}2)[111]$ is a twin system.

This simple energy criterion can be used to identify or confirm twin systems in

172
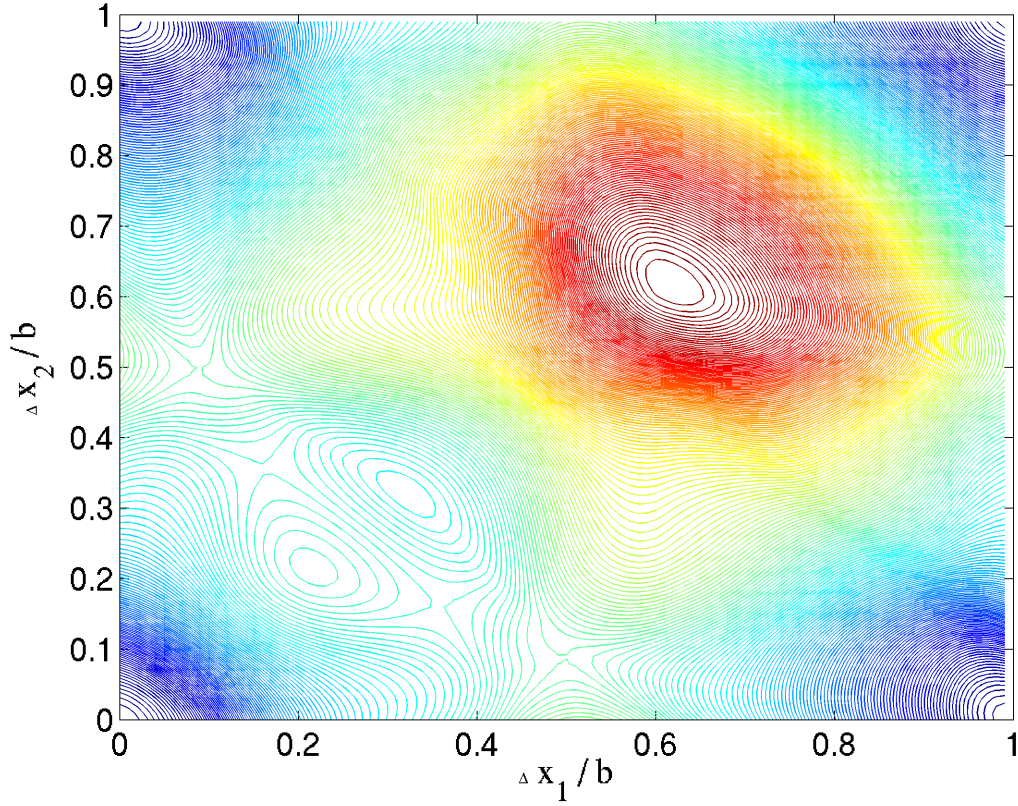
Figure 6-32: Energy contour plot in 2-layer analysis for $(112)[111]$ twin system, with relaxation in Y and Z.

simple and complex structures.

For comparison, we have also calculated the energy surface $E(\Delta x_1, \Delta x_2)$ for $(\bar{1}10)[111]$ slip system. As shown in Figure 6-34, the only energy minima are at $(0,0)$, $(b,0)$,$(0,b)$, and (b,b). There is no twin minimum in the energy surface and the only choice for system under shear is to slip. The energy surface is completely symmetric about $(\frac{b}{2}, \frac{b}{2})$. The energy barrier for $(\bar{1}10)[111]$ slip is 0.422eV, much lower than the energy barriers for $(\bar{1}\bar{1}2)[111]$ slip or twin, again in agreement with the fact that $\{110\}\langle 111\rangle$ is the experimentally observed primary slip system; the minimum-energy path is extremely simple in that it is a straight line connecting $(0,0)$ and $(b,0)$ and the saddle point is the center of the line at $(\frac{b}{2}, 0)$.
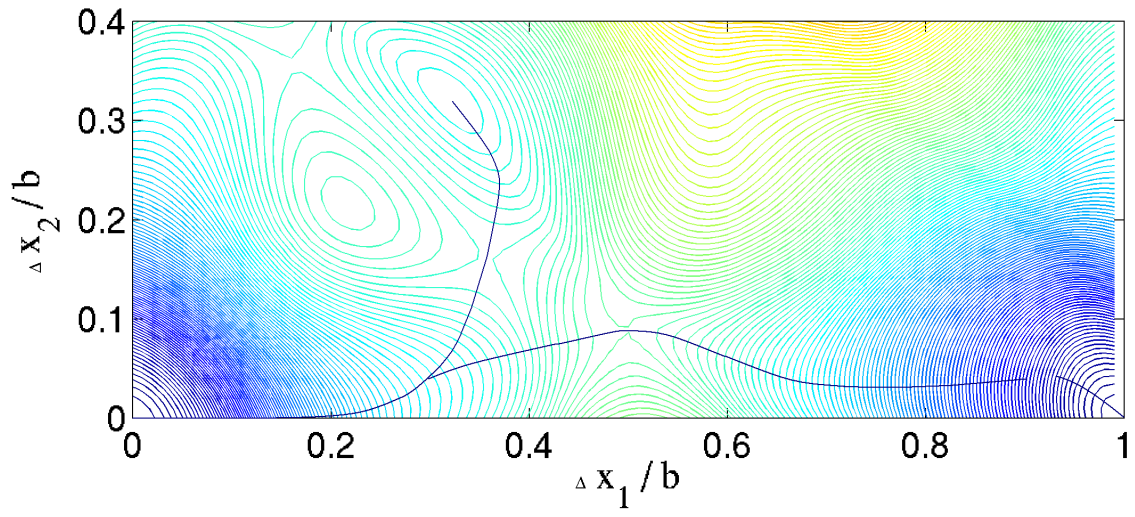
Figure 6-33: 2-layer minimum-energy path analysis for (112)[111] twin system, with relaxation in Y and Z.
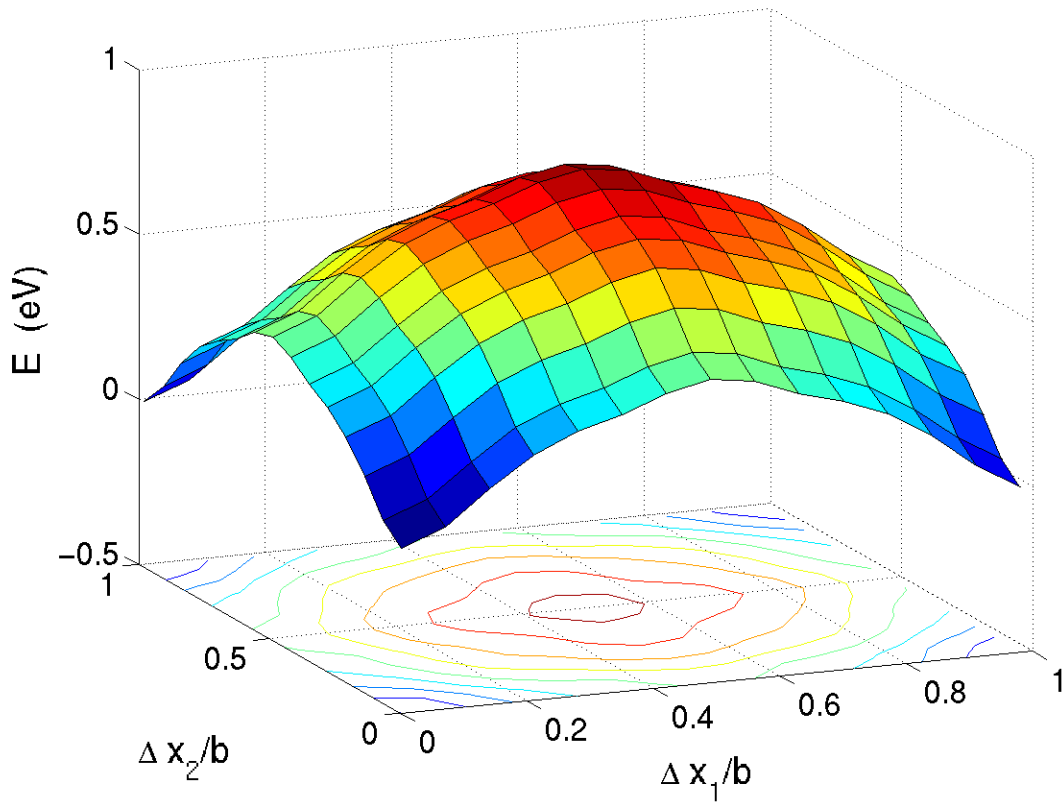
Figure 6-34: 2-layer analysis for (110)[111] slip system.

6.3.5 Multiple Layer Analysis
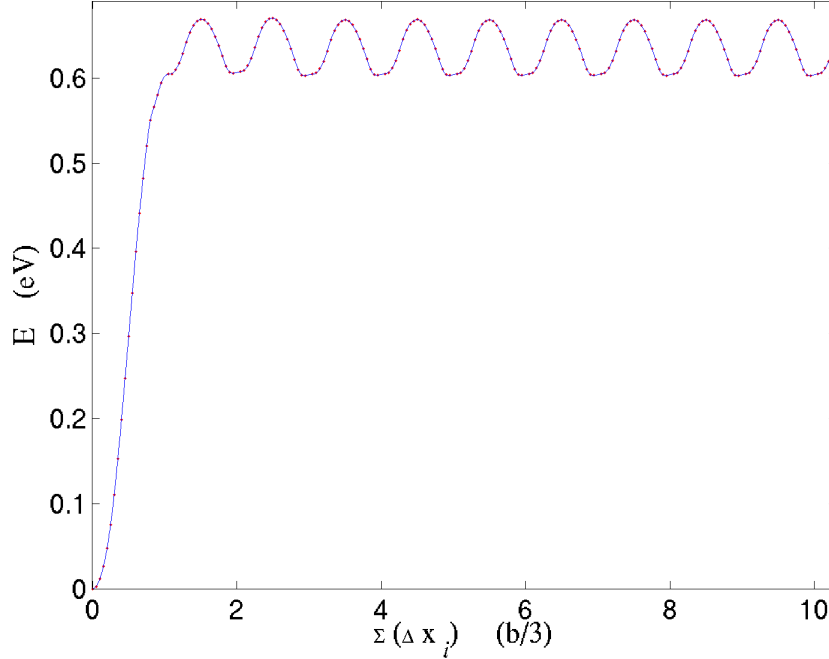
Figure 6-35: Multiple-layer analysis for (112)[111] slip system. Minimum energy is plotted as a function of increasing shear strain imposed on the 1-D chain.

Now let us extend the 1-D chain analysis to multiple layers. Now we allow N of the Δx_i's to take non-zero values ($N > 2$). In this N-layer analysis, we will calculate $E = E(0, ..., 0, \Delta x_1, \Delta x_2, ..., \Delta x_N, 0, ..., 0)$.

Since now we have more than 2 independent variables (nonzero Δx_i's) and together with the dependent variable (energy) the total number of variables is greater than 3 and can not be easily visualized like we did in the 1-layer and 2-layer analysis. Instead of plotting all of the Δx_i's out explicitly, we now plot only the total displacement in X, $\Sigma \Delta x_i$. The minimum-energy path is followed as the total displacement in [111] is increased from 0 to $\frac{b}{3}$, $\frac{2b}{3}$, etc., and the minimum energy is plotted against the total displacement normalized by $\frac{b}{3}$, as shown in Figure 6-35.

Evident from the plot is that there is no meta-stable states for total displacement of $\frac{b}{3}$, but starting from $\frac{2b}{3}$ there are energy minima that correspond to nucleated
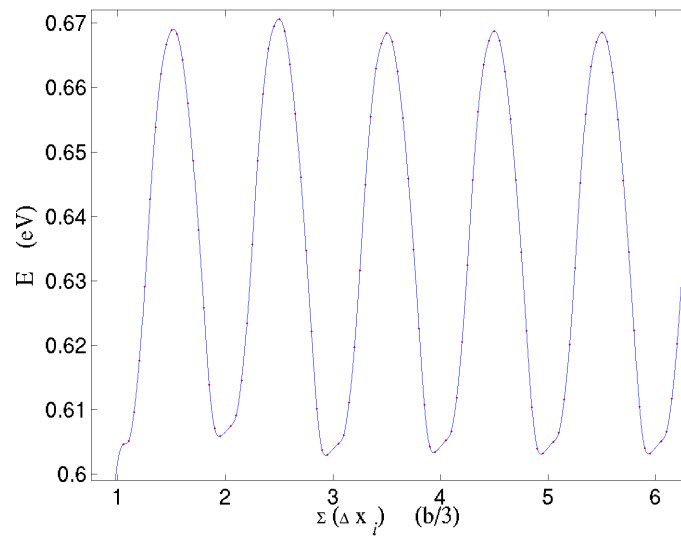
Figure 6-36: Details of the minimum energy curve as a function of increasing shear strain imposed on the 1-D chain.
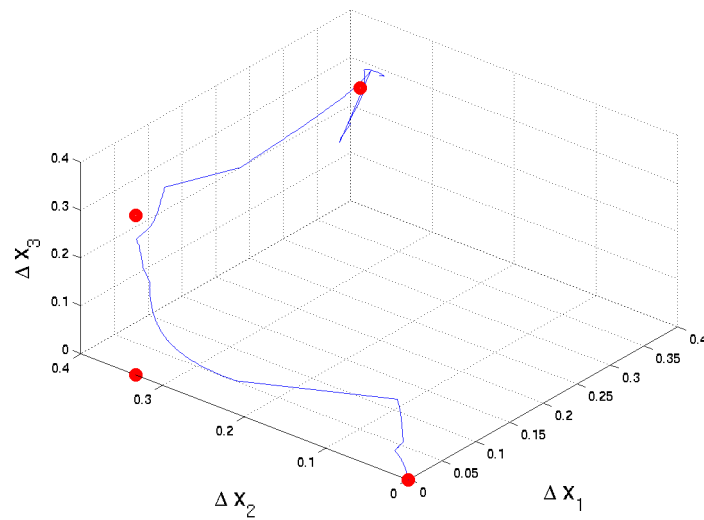
Figure 6-37: Minimum-energy path plotted in 3D space defined by Δx_1, Δx_2 and Δx_3.

176

twins. The energy minimum at $\frac{2b}{3}$ corresponds to a 2-layer twin, the energy minimum at b corresponds to a 3-layer twin, etc. As we impose greater and greater shear strain on the 1-D chain, a 2-layer twin is firstly nucleated which is then followed by subsequent twin growth. The energy barrier for twin growth in the 1-D chain model is approximately equal to the twin nucleation barrier, and the energies of the multiple-layer twins are also approximately the same: from 2-layer twin to 10-layer twin, they all have an energy of about 0.6eV.
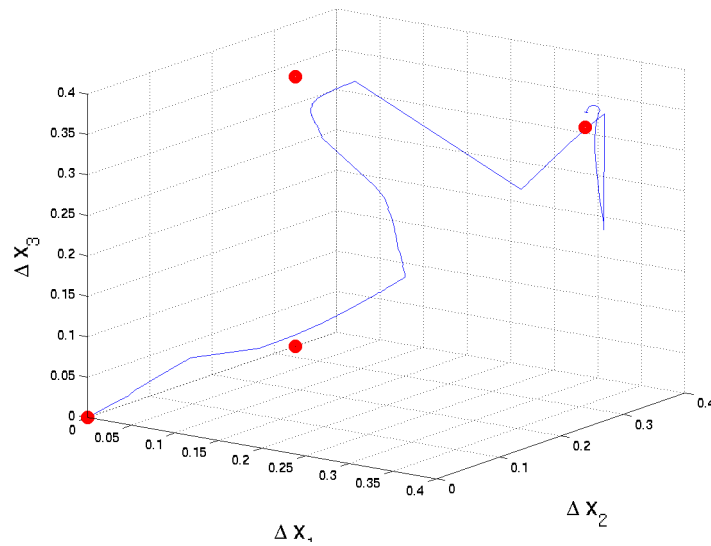
Figure 6-38: Minimum-energy path plotted in 3D space defined by Δx_1, Δx_2 and Δx_3. View angle different from previous figure.

Shown in Figure 6-36 is a more detailed picture of the energy vs. shear strain plot. From this plot one can see that there are small differences between the different layers of twin structure. One obvious feature is that the growth from 2-layer to 3-layer twin is associated with a slightly higher energy barrier and is rewarded with a lower energy minimum at 3-layer structure. One can expect the initially nucleated 2-layer twin to be short-lived due to its higher energy than the 3-layer twin and the fact that usually the externally applied shear will tilt the energy landscape to make the difference more pronounced than shown in the figure. However, the 2-layer twin is the minimum structure for twin nucleation and it is the right twin embryo that we

should study.
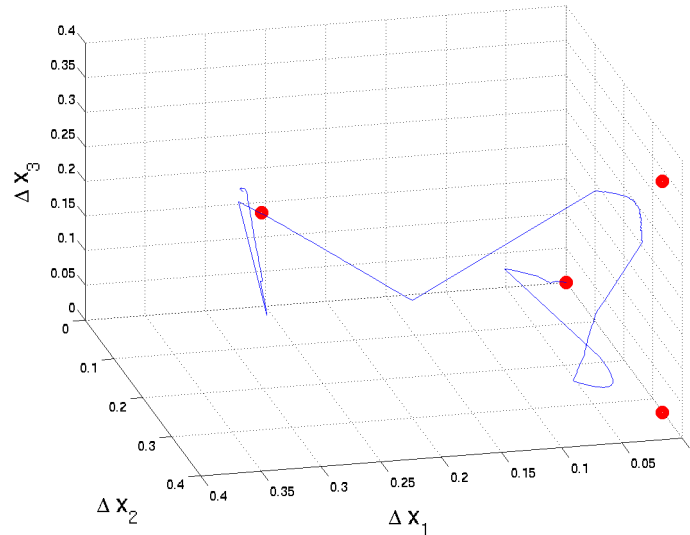
Figure 6-39: Minimum-energy path plotted in 3D space defined by Δx_1, Δx_2 and Δx_3. Still another view angle.

The minimum-energy path analysis is essentially the same for multiple layer calculations, but the visualization of the path becomes much harder than in the 1-layer and 2-layer case. In Figure 6-37, 6-38 and 6-39 we look at the minimum-energy path for the system as the total applied shear strain is increased. The path is plotted in a 3-D space defined by Δx_1, Δx_2, and Δx_3. Starting from 0 total strain, initially all the Δx_i's take on the same amount of shear strain, which shows up as a straight line pointing out from $(0, 0, 0)$ in the direction of $(1, 1, 1)$. Then the system sees that it is more beneficial energetically to distribute the strain unevenly and the result is one of the Δx_i's, in this case, Δx_2, takes a much greater value than the others, this shows up as a turning point in the path plots. Soon Δx_2 grows to approximately $\frac{b}{3}$ and the system comes to the bifurcation point where it needs to decide whether to go down the twinning path or the slip path. Due to the lower energy barrier ahead in the twinning path than in the slip path, the system decide to take the twinning path, overcomes the energy barrier for the twin nucleation, and forms the 2-layer twin. Now the system stands very close to $(0, \frac{b}{3}, \frac{b}{3})$. As shear strain is increased, the

system overcomes the next energy barrier and the 2-layer twin grows to 3 layers. Now the system stands close to $(\frac{b}{3}, \frac{b}{3}, \frac{b}{3})$. Further straining the system will make the twin grow larger, but the action can not be analyzed well in this 3-D plot.

6.3.6   Insights

The 1-D chain model have proven to be a powerful tool to analyze the twin nucleation and growth problem. From the above calculations, we are able to draw the following conclusions and insights:

First, on $\{112\}\langle 111\rangle$ system, two-layer twin structure is stable and shall be considered a legitimate twin embryo. Previous results by Vitek [138] reported that minimum twin structure in BCC molybdenum has three layers is most probably inaccurate due to the pairwise potential used in the calculation.

Second, this 1-D chain model calculation goes much further than the previous calculations of twin structures in that now we can not only find out the stable defect structures by searching for energy minima but can also analyze the energy landscape and find out the minimum-energy path as well as the saddle points. The twinning problem, in this low dimensional space, becomes a well-defined mathematical problem that we can solve with full confidence. The solution we provided is obtained by a combination of optimization techniques including grid search (a mapping of the whole energy landscape at grid points), first-order energy minimization (minimizing energy with the help of first-order derivatives, i.e., the forces), and constrained optimization (given total shear strain, minimize energy). Unlike usual energy minimization studies with normal techniques, e.g., nudged-elastic-band method, which usually suffer from the uncertainties introduced by the initial guess, there is no arbitrariness in the solution we have obtained and the solution is a robust and sound one.

More importantly, using the 1-D chain model, we have formulated a method to identify the twin systems by looking for twin energy minima in low-dimensional space defined by Δx_i's. Once a twin energy minimum is identified, one can proceed to apply the simple energetic criterion to confirm whether twinning will be favored in competition against slip on the particular system: twinning is favored if $\gamma_{twin} < \gamma_{slip}$;

otherwise slip is favored.

Finally, path analysis reveals that system undergoes several stages where distribution of energy(strain) behaves differently. This can be shown more clearly in the 4-stage wave-steepening analysis in the next section.

6.4   4-Stage Wave-Steepening in Defect Nucleation

As have been discussed in the previous section, the minimum-energy path analysis of the 1-D chain under applied shear strain revealed that there are several distinct stages before the 2-layer twin is nucleated. In the initial stage, the applied shear strain is equally partitioned among all the layers; later, one of the layers starts to take on more strain than others; then, the shear strain on this particular layer keeps growing until the system comes to a bifurcation point where the local strain on this layer is already rather large; finally the system decides on which defect structure to form and in the previous case, twin nucleation is favored against slip and a 2-layer twin is nucleated as a result.

This strain localization process can also be understood in the context of energy distribution. Since in the 1-D chain model, energy is closely related to shear strain which is fully represented by the Δx_i's, the process of strain localization is indeed also a process of energy localization.

It is relatively straightforward to understand the strain/energy localization process in the context of energy landscape. By looking at the energy surfaces and energy contours like the ones shown in the previous 2-layer 1-D chain analysis, one can understand the reason for the strain/energy localization is that given the total shear strain, the system will favor the structure that gives the lowest energy. Under small shear strain, lowest-energy structure is the one where strain is equally partitioned. Under high shear strain, lowest-energy structure changes to something that has a local concentration of strain (energy).

In this section, we take a new view angle and analyze the strain/energy localization process in a 4-stage wave-steepening context. The concepts introduced here applies to the universal problem of defect nucleation and may have long-reaching implications.

As shown in the top figure of Figure 6-40, we have an initial perfect crystal structure that has zero strain. The horizontal axis is the $[\bar{1}\bar{1}2]$ direction and the vertical axis is the Burgers vector direction, $[111]$. We impose an initial sinusoidal wave perturbation on the system by displacing the atoms in $[111]$ direction by the amount
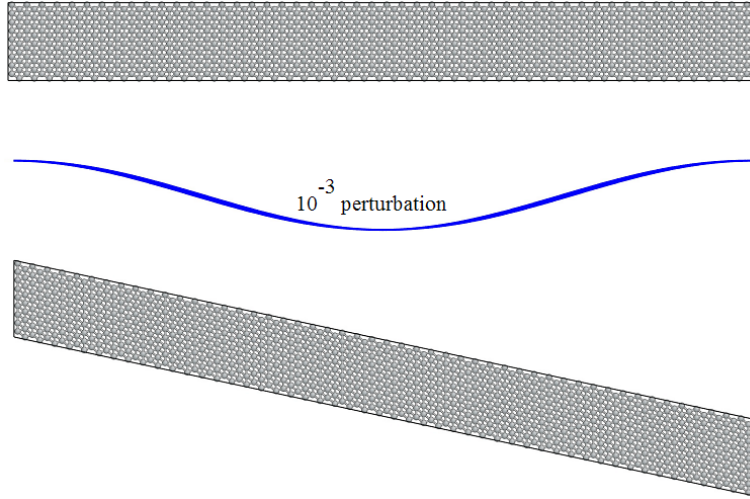
Figure 6-40: Setup of the simulation. The first graph shows the initial crystal structure. We impose an initial sinusoidal wave perturbation on the system by displacing the atoms by the amount designated by the sine function.

designated in the sine curve. Further more, we apply a homogeneous shear strain on the whole system, as shown in the bottom figure of Figure 6-40. After these two steps, we have the atomic configuration whose strain field contains a homogeneous component and a small wave perturbation. We use this configuration as the initial configuration and run MD simulation at a temperature of $T = 10$K. The dynamics of the system is followed and the strain(energy) localization process is analyzed together with the evolution of initial wave that we put in.

Although we have shown more than one atoms for each $(\bar{1}\bar{1}2)$ layer in Figure 6-40, the atoms on the same layer are indeed connected rigidly and the system is a 1-D chain of atoms. In other words, this is a simulation of the dynamics of the 1-D chain under initial small wave perturbation.

In particular, we are interested in the behavior of the system at the critical point, i.e., how does the strain get localized and formed the defect? Therefore, we will use a shear strain of 0.215 which is very close to critical point. With the help from the introduced wave perturbation, defect will be nucleated and let us analyze the different stages of the nucleation process.
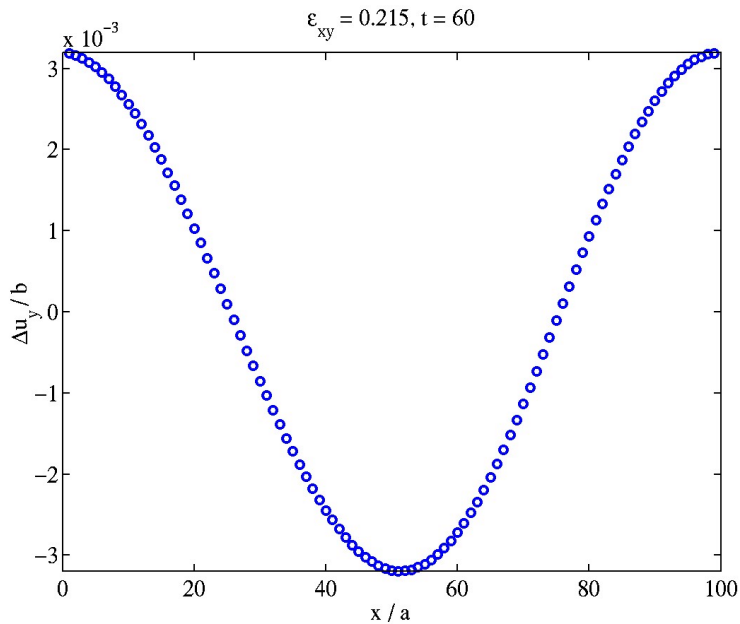
Figure 6-41: First stage: linear growth.

1. Stage 1: Linear Growth

   As shown in Figure 6-41, the initial stage is characterized by the linear growth of the sinusoidal wave. In this stage, the sinusoidal shape of the wave is maintained and the only change to the wave is in the amplitude. This stage can be well described by continuum theory.

   This stage corresponds to the equal-partitioning of the strain (energy) among all the atoms (layers). Strictly speaking, at any given moment, the strain or energy for the different atoms (layers) are not exactly the same. However, no deviation from the equal-partition can last with the oscillation of the wave.

2. Stage 2: Non-Linear Growth

   As the simulation goes on and the amplitude of wave grows larger and larger, the linear description no longer holds and non-linear behavior emerges, as shown in Figure 6-42. This stage is characterized by the non-linear growth of the wave. Now the wave no longer maintains its initial sinusoidal shape and the wave-front steepens due to increasing non-linearity. Despite the steepening,
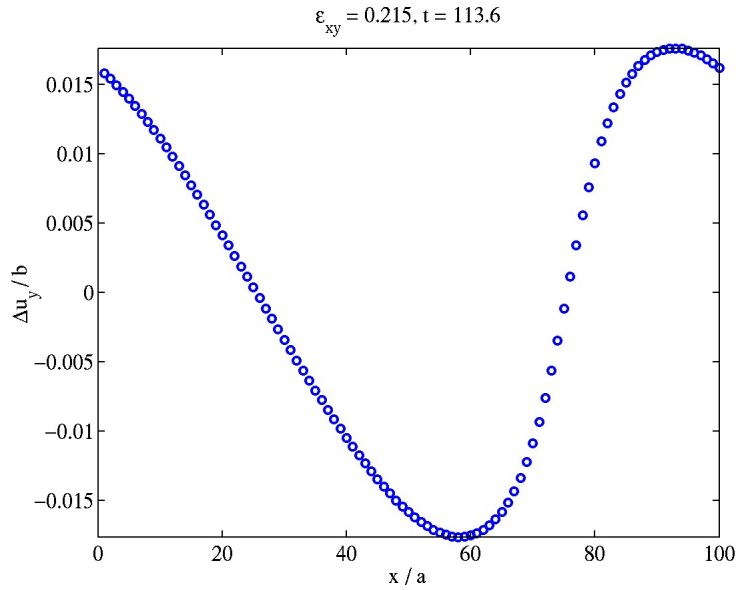
Figure 6-42: Second stage: non-linear growth.

continuum description still holds.

In this stage, the equal-partition of strain (energy) among the atoms has the tendency to become broken. However, it is not yet completely broken.

3. Stage 3: Shear Shock Formation

   In this stage, the wave steepening caused the wave-front to shrink to a level where atomically sharp shock is formed, as shown in Figure 6-43. At this stage, continuum description no longer holds at the shock and the system can only be described in atomistic terms.

   Now the equal-partition of strain as well as energy among the atoms (layers) are completely broken, with a smaller number of atoms (layers) making the sacrifice and taking on much greater strain than the others.

4. Stage 4: Formation of Atomic Defect

   With the shear strain already localized, now the system further proceeds to make a decision to form a local defect (defects), as shown in Figure 6-44. This stage, by no doubt, can only be described atomistically. What type of defect
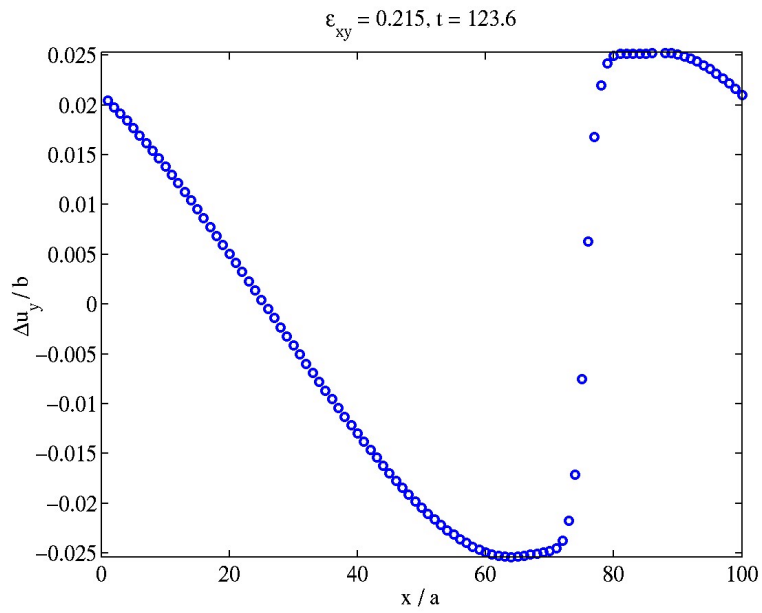
Figure 6-43: Third stage: shear shock formation.
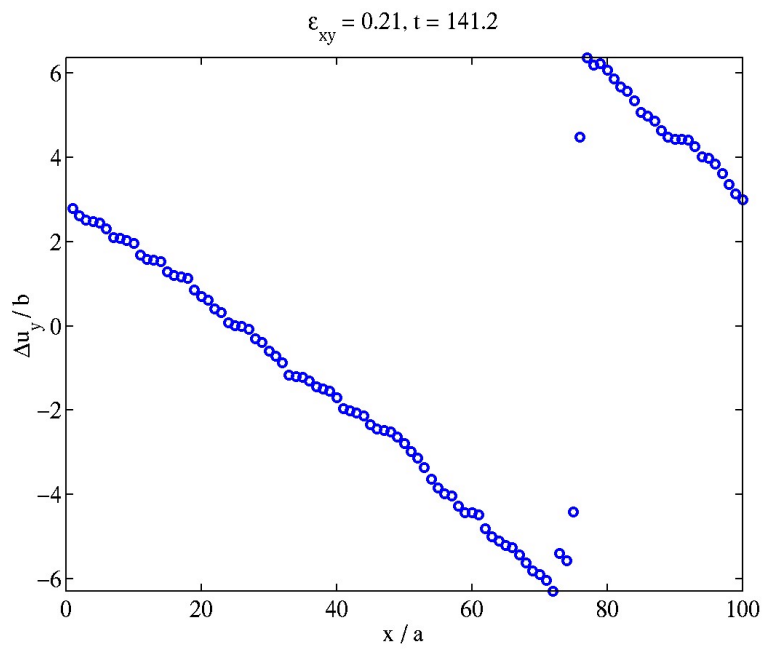
Figure 6-44: Last stage: formation of atomic defect.

is formed is an atomistic decision. Whether it is going to be a dislocation or twins or other kinds of defects, the decision is determined by the atomistic energy landscape. The important parameters that affects this decision are the activation energy barrier for the defect formation and the defect energy itself.

In summary, in the above 1-D chain dynamics simulation, we have introduced a normal mode perturbation wave to probe the behavior of the atomic system close to instability. The introduced perturbation wave is a shear wave that has a wave length of the dimension of the cell, and the probed instability is a shear instability.

From the simulation, we have followed the evolution of the perturbation wave and are able to characterize the process of defect nucleation into four stages: linear growth, non-linear growth, shear shock formation, and finally formation of atomic defect. The wave-steepening process is seen to be intimately related to the localization of strain and energy. It is also worth mentioning that the wave-steepening which results in defect nucleation can not happen without growing non-linearity. A model that has no built-in non-linear considerations will not be able to reproduce these results.

6.5 Summary

In this chapter, we have studied the nucleation and growth of deformation twins in a BCC metal molybdenum using atomistic models.

We began our study by large-size molecular dynamics simulations in both quasi-2D and 3D. In particular, 3D simulation revealed several important features of twin nucleation, namely, the geometry characteristics of the nucleated twin and the speed of twin growth in different directions.

Although the large-size simulations provided a way to directly observe twin nucleation and growth, it is difficult to analyze the simulation results due to the large number of DOF's. A physically-motivated 1-D chain model drastically simplifies the problem yet manages to capture the most important physics. In this chapter, we have shown that the 1-D chain model calculations can be very powerful in completely and thoroughly describe the twin nucleation and growth in a low-dimensional space. Important insights about the initial structure of the twin embryo as well as a simple energetic criterion have been developed from the 1-D chain model analysis. Further ahead we see that combining the 1-D chain model with elasticity would have a great potential in accurately describing the twin nucleation and growth phenomena in given materials.

The process of twin nucleation can be understood in a more general framework. Namely, homogeneous nucleation of any type of defect is closely related to the process of strain (energy) localization. Using 1-D chain dynamics simulation, we have categorized the strain (energy) localization process into four stages where a wave steepening picture provides us a clear view of how the strain is localized. This new perspective is general enough to apply to formation of any kind of defects.

Chapter 7

Summary and Outlook

7.1 Summary of Work

In this thesis, atomistic work on the nucleation and migration of two types of defects, dislocations and twinning, and presented for a BCC metal molybdenum. For dislocations, three contributions are presented, as discussed in Chapter 2, Chapter 3 and 4, and Chapter 5, respectively:

1. PBC Image Correction

Due to the finite size of atomistic models, atomistic studies of dislocations always use certain type of boundary conditions. The result is that the atomistic model differs from the ideal situation of a dislocation in an infinite medium. It not only makes the task of creating initial dislocation configuration more complicated, but also may introduce artificial effects to the simulation. Before discussing any actual calculations, it is important to first clarify how dislocations can be set up in a finite simulation cell and what are the correction effects that need to be considered. In this thesis the Periodic boundary condition(PBC) has been used in all the simulations that have been performed.

Creating a dislocation configuration under PBC involves two steps: (1)Calculate the displacement field $\vec{u}(x, y, z)$ under PBC; (2)Create dislocation configuration $\vec{r_i}$ from $\vec{u}(x, y, z)$. For the first step, one needs to evaluate $\vec{u}(x, y, z)$ due to an infinite

array of dislocations that arise from PBC and the problem is known to be conditionally convergent. One of the solutions is to subtract a linear field from the result that one gets from a finite summation, which then removes the mismatched $\vec{u}(x, y, z)$ at the periodic boundaries [7, 143, 8]. The second step is essentially a mapping between continuous field $\vec{u}(x, y, z)$ and its discrete representation $\vec{r}_i$. I have found that the usual treatment of evaluating $\vec{u}(x, y, z)$ at the lattice sites and then moving atoms from these lattice sites by the same amounts yields inaccurate positions for atoms. The treatment itself is also not self-consistent. A mathematically sound solution for the atomic positions x, y, z that is self-consistent is to require that $\vec{u}(x, y, z) = (x - x_L, y - y_L, z - z_L)$, rather than $\vec{u}(x_L, y_L, z_L) = (x - x_L, y - y_L, z - z_L)$, where (x, y, z) is the real atomic position and (x_L, y_L, z_L) is the nearby lattice site. (The solution to the equation in each bounded region, i.e., between lattice sites, can be obtained using numerical methods like Newtons method, binary search, etc.) This guarantees the uniqueness of the mapping between displacement field and real atomic representation and that appropriate numbers of atoms are generated. This two-step process is illustrated in Figure 2-4 and Figure 2-5.

After an atomic dislocation configuration is generated, one should not start the simulations without quantifying the artificial effect of the image dislocations that are introduced by PBC. Contrary to common belief that using large size simulation cells will make the image effects diminish, the artificial image energy barrier for a dislocation moving within the periodic cell can still be very high, regardless of the simulation cell size. We have evaluated such barriers for edge and screw dislocation dipole configurations under PBC for different cell geometries and found that it is a sensitive function of the aspect ratio of the cell, as shown in Figure 2-8. The optimal aspect ratio, one which minimizes the artificial energy barrier, has been identified and used in later simulations.

2. Core Structure and Peierls Stress for Screws in Mo

Screw dislocations in Mo, due to its importance in low temperature plasticity, have been the object of intense atomistic studies; however, controversies remain even

for the very fundamental problem of core structure and Peierls stress. On the core structure of screw dislocations, it has long since been recognized that it exhibits "3-way splitting" (to be called the "polarized core") and it has been considered the source of high lattice resistance to screw dislocations. However, recently a "symmetric core" ("unpolarized core") has been obtained by density functional theory (DFT) calculations by Arias [144]. In this thesis we have computed the screw core structure using yet another model – the tight-binding model. Since this potential model is less computationally intensive than the DFT calculations, we now can afford a larger simulation cell to make the dislocation packing less dense which results in a better approximation to the real core structure. Adopting a quadrupole configuration that minimizes the image stress, we have obtained a relaxed screw core that shows unpolarized core structure, the differential displacement map of which is shown in Figure 3-11, together with that for polarized core obtained from Finnis-Sinclair and MGPT semi-empirical potentials. Since both DFT and tight-binding model predict an unpolarized core, we believe the ground state of the screw dislocation core to be unpolarized. It is natural to expect that an unpolarized core will be more compact and therefore will exhibit higher mobility. How big a difference this makes and whether this will bring the Peierls stress down to values comparable to experimental critical resolved shear stress (CRSS) of $400 - 700$MPa, will not be known until the Peierls stress is accurately determined.

Traditionally, the Peierls stress (τ_P) is calculated by shearing the simulation cell until the dislocation moves and recording the virial stress at that moment. However, as we have discussed above, the effects of boundary conditions can introduce large errors in the result, affecting the result by more than one order of magnitude. The inaccurate nature of virial stress also adds to the unreliability of the result. To acquire an accurate Peierls stress, we have implemented the local-driving-force method [95] which is based on the Gibbs free energy concept and therefore does not suffer from the problems of the virial stress and image stress effects. Using this method, we have obtained a Peierls stress of ~ 3GPa using tight-binding model. A comparative study using the Finnis-Sinclair semi-empirical potential predicts τ_P to be 1.93GPa.

Since τ_P from tight-binding unpolarized screw core remains rather high, it leads to the conclusion that whether the core is polarized or not does not affect the order of magnitude of τ_P. What we can also learn from this is that although empirical potential models predict incorrectly the fine structure of screw cores, quantitative prediction of Peierls stress does not seem to deviate from the more accurate methods too much and therefore may still be acceptable.

Since the straight screw dislocation indeed has a very high τ_P, it implies that kink mechanisms may be important for screw dislocations in Mo. Using MD, we have simulated migration behavior of kinks on screw dislocations, as shown in Figure 3-22. We find that at applied stresses as low as 40 MPa, the kink on screw dislocation moves at a rather high velocity, with a viscous drag coefficient comparable to that of edge dislocations. This signifies the low lattice resistance of kinks on screw dislocations and also implies that the controlling process is kink nucleation rather than kink migration, since the kink nucleation activation barrier is ~ 0.7 eV, as shown by Ngan [145].

3. Core Structure and Peierls Stress for Edges in Mo

Edge dislocations in Mo, having a planar core structure, are widely believed to be highly mobile and do not contribute much to material plasticity at low temperatures. However, recent atomistic studies by other researchers [3] have found an unreasonably high Peierls stress for straight edge dislocations. This is a rather confusing result although one can hypothesize that the high mobility of edge dislocations observed in experiments is due to kink mechanisms.

We first examine the core structure of the edge dislocation. As in Figure 4-3, the high-energy core atoms consist of two rows of atoms that highlight the planar nature of the edge dislocation in Mo. We also plot the misregistry between these two rows to quantify the core width of edge dislocations. The unrelaxed configuration which was prepared using elasticity and the recipes described above had a core width of only 5Å, while the Finnis-Sinclair relaxed core has a width of ~ 10Å. The wide and planar core structure will naturally lead to low lattice resistance, i.e., τ_P, as predicted by simple Peierls-Nabarro model and will be soon verified using atomistic calculations.

192

Using a PBC dipole setting, we have carefully calculated the Peierls stress (τ_P) for edge dislocation in Mo with varying cell geometry, specifically the aspect ratio of the simulation cell. There are two major findings: (1) The calculated Peierls stress varies significantly (from $700MPa$ to $25MPa$) with the aspect ratio, as shown in Figure 4-7. The 30-fold difference due to the artificial image energy barrier signifies the importance of the correction for boundary condition effects. (2) The converged value of τ_P is $25MPa$, one order of magnitude lower than previously reported, suggesting a large image effect in the previous calculation. This results confirms that edge dislocation has extremely low lattice resistance and is highly mobile even as a rigid line without any assistance from kink mechanisms.

4. Edge Dislocation Mobility and Drag Coefficients

Using Parinello-Rahman MD, we have simulated edge dislocation motion under constant temperature and constant stress conditions with varying loading conditions. At zero pressure, a mobility data array corresponding to a range of stress (40MPa to 7GPa) and temperature (40K to 1000K) has been obtained and we have the following findings: (1) The temperature dependence of dislocation velocity is most pronounced at low stresses, where the behavior of increasing velocity with decreasing temperature signifies that the dislocation motion in the simulated stress regime is not a thermally-activated process but one that is controlled by viscous drag (phonon drag). As applied shear stress increases, temperature dependence of dislocation velocity becomes less visible, giving approximately the same velocity values across different temperatures, as shown in Figure 5-9. (2) Stress dependence of dislocation velocity, which can be characterized using the exponent m if one considers that $v \propto \sigma^m$: Since the simulated stresses are all greater than τ_P of edge dislocations, 25MPa, and the dislocation motion is only impeded by viscous drag, there is a linear relation between v and σ and therefore $m = 1$ in low stress regions ($\sigma < 0.4GPa$). Drag coefficient in this region is approximately a constant, $6 \times 10^{-5} Pa \cdot s$. However, as the stress is further increased, dislocation velocity becomes greater than half the shear wave speed $c_s = 3260m/s$, the relativistic effects kick in and the linear relation between σ and v gives way to an

193

asymptotic behavior where σ theoretically could grow up to theoretical shear strength σ_{max} as v approaches the Raleigh surface wave speed $c_R = 0.9345 \cdot c_S = 3050 m/s$. The exponent m quickly drops to values close to 0.25 and the drag coefficient B is no longer a constant; rather, it becomes an increasing function of σ and exhibits approximately linear growth with σ, as shown in Figure 5-10 and Figure 5-11, growing to a value of $7.7 \times 10^{-4} Pa \cdot s$ at $\sigma = 7GPa$. These simulation results of drag coefficients can be used in a variety of models, including dislocation dynamics, mesoscopic models, and any model that incorporates dislocation mobility in the viscous drag regime. The different behavior of drag coefficient at low and high stresses is also an important discovery that indicates the importance of relativistic effects when dislocation velocity becomes comparable to sound velocity. (3) Dislocation velocity is also found to be a decreasing function of external pressure, as shown in Figure 5-12(d).

Another interesting finding of the present work is that at a velocity close to v_R and stress close to $7GPa$, a discrete jump in dislocation velocity to longitudinal wave speed v_l is observed. This jump in dislocation speed is accompanied by a profound change in the dislocation core, still planar but much wider.

On the subject of twinning nucleation and growth, we have adopted two different approaches.

In the first approach, twinning nucleation process is simulated using MD method. The simulations are done in three different settings: quasi-2D pre-existing crack with mode-I loading, quasi-2D shearing of perfect crystal, and 3D shearing of perfect crystal. In the quasi-2D crack case, twin is nucleated at the crack tip and continues to grow into the bulk on a (112) plane. In the perfect crystal shearing cases, twin is nucleated at a random site (due to lack of pre-existing defects as nucleation sites) at about 12GPa of critical stress and 7.9 percent strain. More importantly, it is found that after the initial nucleation of a circular twin disk, the disk keeps its circular shape during its growth while its sharp edges expand at speeds of roughly 6000 m/s, comparable to the longitudinal wave speed $c_L = 6740$ m/s.

The first approach has its merit in that the full atomistic process of nucleation and growth can be captured; however, it involves an unnecessarily large number of degrees of freedom, most of which may not be essential to the physics. Therefore, a second approach is taken to analyze the twinning process. A 1-D chain model is used to capture the most important degrees of freedom, i.e., the relative shift between the planes as well as relaxation normal to the shift plane, while in-plane relaxations are ignored. With this approach, we have only N parameters if we are to study N layers. In this highly condensed parameter space, the energy surface is calculated and it is revealed that there is no energy minimum that corresponds to meta-stable partial slip when $N = 1$; however, there exists an energy minimum at $(\Delta x_1 = \frac{b}{3}, \Delta x_2 = \frac{b}{3})$ that corresponds to a 2-layer twin embryo, as shown in Figure 6-30. Comparing to earlier results by Vitek using a pair potential that predicted no stable 2-layer twin embryo exists (therefore, the minimum layer of twin is 3), our calculation uses a better potential model and therefore is more likely to provide a more realistic picture. To confirm this a DFT 1-D chain analysis will be undertaken.

With the 2-layer being the twin-embryo, we have studied the energy contour of $(\Delta x_1, \Delta x_2)$ and identified the minimum-energy path that leads from perfect lattice to twinned 2-layer structure, as well as the path corresponding to slip process. The bifurcation point of the two paths is found to be near $(\frac{b}{3}, 0)$. More importantly, the low-energy path clearly shows that initially strain is distributed evenly between different layers and the strain localization only happens at later stage when wave steepening caused by increasing nonlinearity. A four-stage description of the wave-steepening process can offer much insight towards the understanding of the formation of twin embryos. Moreover, the wave-steepening description is applicable to more general problems of nucleation of defects that could include dislocations and defects alike.

Summary

Atomistic studies in dislocation and deformation twinning modeling have been presented to highlight the particular challenge of understanding plastic behavior of

metals at the atomistic level. As we have illustrated in the dislocation modeling contributions, one has to consider the difference between the model and the intended settings and remove or minimize any artifacts arising from these differences. In the deformation twinning modeling contributions, we have clearly shown that a reduction of degree of freedoms leads us directly to the core of the problem and a clear physical picture of the nucleation process. In both cases, atomistic calculations have provided mechanistic understanding as well as quantitative measures for nucleation and migration of the the defects of interest.

7.2   Outlook

The most exciting part of this thesis is the final section on twinning nucleation analysis. One can always find great beauty in simplification and generalization of complex systems and complicated problems. The challenger is how to make the simplifications without loosing the real physics.

The 4-stage defect nucleation process by wave-steepening is another example of generalization. Further along this direction, more research can be and should be done to quantify the criterions for transition from one stage to the next. Good amount of work has been done for the transition from the 1st stage to the second (see Li et al, Nature, 2002), while the others await to be explored.

In the direction of dislocations, a coupling between atomistic and continuum models has been demonstrated to be possible and this is one exciting area where significant progress can be made with the so-called "atomistically-informed" continuum models.

A philosophical issue about atomistic modeling of materials is that since it is a stand-alone simulation approach, one can either do everything with "full atomistic", or try to use knowledge from other levels of modeling, e.g., elasticity theory. I find great beauty in both. An example for the former case is the local-driving-force method derived by Ju Li in his Ph.D. thesis which beautifully calculates the resistance to defect migration by using a very local atomistic region and invariance was demonstrated to hold with respect to size and defect environment. An example for

the latter case is the semi-discrete model work by Vasily V. Bulatov in 1996 where atomistic information is coupled with elasticity theory to accurately produce Peierls stress values and it is demonstrated to be very accurate and powerful. It is my belief that both approaches are critically needed to give the atomistic modeling the much needed predicting power.

Bibliography

[1] W. E. King, G. Campbell, T. Gonis, G. Henshall, D. Lesuer, E. Zywicz, and S. Foiles *Mater. Sci. Eng. A*, vol. 191, p. 1, 1995.

[2] A. S. Argon, ed., *Physics of strength and plasticity.* The M.I.T. Press, Cambridge, Massachusetts, 1969.

[3] M. S. Duesbery and W. Xu, "The motion of edge dislocations in body-center cubic metals," *Script. Metall.*, vol. 39, p. 283, 1998.

[4] M. Baskes, M. Daw, B. Dodson, and S. Foiles, "Atomic-scale simulation in materials science," *MRS Bulletin*, vol. 13, p. 28, 1988.

[5] J. A. R. A. Moncevicz, P. C. Clapp, "Dislocation mobilities in nial from molecular dynamics simulations," *Defects in Materials Symposium*, p. 213, 1992.

[6] P. Gumbsch and H. Gao, "Dislocations faster than the speed of sound," *Science*, vol. 283, p. 968, 1999.

[7] W. Cai, V. V. Bulatov, J. Chang, J. Li, and S. Yip, "Anisotropic elastic interactions of a periodic dislocation array," *Phys. Rev. Lett.*, vol. 86, p. 5727, 2001.

[8] W. Cai, V. V. Bulatov, J. Chang, J. Li, and S. Yip, "Periodic image effects in dislocation modeling," *Phil. Mag. A*, p. in press, 2003.

[9] W. Cai, *Atomistic and Mesoscale Modeling of Dislocation Mobility.* PhD thesis, Massachusetts Institute of Technology, May 2001.

[10] J. P. Hirth and J. Lothe, *Theory of Dislocations, 2nd ed.* Wiley, New York, 1982.

[11] J. Friedel, *Dislocations.* Pergamon, Oxford, 1964.

[12] A. N. Gulluoglu, D. J. Srolovitz, R. LeSar, and P. S. Lomdahl, "Dislocation distributions in two dimensions," *Script. Metall.*, vol. 23, p. 1347, 1989.

[13] H. Y. Wang and R. LeSar, "O(N) algorithm for dislocation dynamics," *Phil. Mag. A*, vol. 71, p. 149, 1995.

[14] X. Blase, K. L. A. Canning, S. G. Louie, and D. C. Chrzan, "Structure and energy of the 90° partial dislocation in diamond: A combined ab initio and elasticity theory analysis," *Phys. Rev. Lett.*, vol. 84, p. 5780, 2000.

[15] S. Ismail-Beigi and T. A. Arias, "Ab initio study of screw dislocations in Mo and Ta: A new picture of plasticity in bcc transition metals," *Phys. Rev. Lett.*, vol. 84, p. 1499, 2000.

[16] D. Wolf, "Reconstruction of NaCl surfaces from a dipolar solution to the Madelung problem," *Phys. Rev. Lett.*, vol. 68, p. 3315, 1992.

[17] E. R. Smith, "Electrostatic energy in ionic crystals," *Proc. R. Soc. Lond.*, vol. A 375, p. 475, 1981.

[18] J. R. K. Bigger, D. A. McInnes, A. P. Sutton, M. C. Payne, I. Stich, R. D. King-Smith, D. M. Bird, and L. J. Clarke, "Atomic and electronic structures of the 90° partial dislocations in silicon," *Phys. Rev. Lett.*, vol. 69, p. 2224, 1992.

[19] K. N. Kudin and G. E. Scuseria, "A fast multipole method for periodic systems with arbitrary unit cell geometries," *Chem. Phys. Lett.*, vol. 283, p. 61, 1998.

[20] M. W. Finnis and J. E. Sinclair, "A simple empirical N-body potential for transition metals," *Phil. Mag. A*, vol. 50, p. 45, 1984.

[21] J. Chang, V. V. Bulatov, and S. Yip, "Molecular dynamics study of edge dislocation motion in bcc metal," *J. Computer-Aided Materials Design*, vol. 6, p. 165, 1999.

[22] J. Chang. unpublished.

[23] F. R. N. Nabarro, ed., *Dislocation in Solids*. North-Holland, Amsterdam, 1986.

[24] M. S. Duesbery, "The dislocation core and plasticity," in *Dislocations in Solids* (F. R. N. Nabarro, ed.), vol. 8, Elsevier, Amsterdam, 1989.

[25] W. Cai, V. V. Bulatov, J. Chang, J. Li, and S. Yip, "Dislocation core effects on mobility," in *Dislocations in Solids* (J. P. Hirth, ed.), vol. 13, Elsevier, Amsterdam, 2003. in press.

[26] M. S. Duesbery and V. Vitek, "Plastic anisotropy in b.c.c. transition metals," *Acta Mater.*, vol. 46, p. 1481, 1998.

[27] 3/6/2001. URL: http://library.thinkquest.org/3659/pertable/42.html.

[28] M. Wen and A. H. W. Ngan, "Atomistic simulation of kink-pairs of screw dislocations in body-centred cubic iron," *Acta Mater.*, vol. 48, p. 4255, 2000.

[29] M. S. Duesbery, "The influence of core structure on dislocation mobility," *Phil. Mag.*, vol. 19, p. 501, 1969.

[30] M. S. Duesbery, V. V. Vitek, and D. K. Bowen, "The effect of shear stress on the screw dislocation core structure in body-centered cubic lattices," *Proc. R. Soc. Lond.*, vol. A 332, p. 85, 1973.

[31] V. Vitek, "Theory of the core structures of dislocations in body-centered-cubic metals," *Cryst. Latt. Def.*, vol. 5, p. 1, 1974.

[32] V. Vitek, "Computer simulation of the screw dislocation motion in bcc metals under the effect of the external shear and uniaxial stresses," *Proc. R. Soc. Lond. A*, vol. 352, p. 109, 1976.

[33] M. S. Duesbery, "On kinked screw dislocations in the b.c.c. lattice — i. the structure and peierls stress of isolated kinks," *Acta Metall.*, vol. 31, p. 1747, 1983.

[34] M. S. Duesbery, "On kinked screw dislocations in the b.c.c. lattice — ii. kink energies and double kinks," *Acta Metall.*, vol. 31, p. 1759, 1983.

[35] M. S. Duesbery and G. Y. Richardson, "The dislocation core in crystalline materials," *Critical Reviews in Solid State and Materials Sciences*, vol. 17(1), p. 1, 1991.

[36] L. P. Kubin *Rev. Deform. Behav. Mater.*, vol. 4, p. 181, 1982.

[37] F. Guiu and P. L. Pratt, "The effect of orientation on the yielding and flow of molybdenum single crystals," *Phys. Stat. Solidi*, vol. 15, p. 539, 1966.

[38] D. Veselý, "The study of slip bands on the surface of Mo single crystals," *Phys. Stat. Solidi*, vol. 29, p. 657, 1968.

[39] C. S. Barrett, G. Ansel, and R. F. Mehl *Trans. ASM*, vol. 25, p. 702, 1937.

[40] G. I. Taylor and C. F. Elam *Proc. R. Soc. London A*, vol. 112, p. 337, 1926.

[41] J. F. L. Vogel and R. M. Brick *Trans. AIME*, vol. 197, p. 700, 1953.

[42] B. Sestak and S. Libovicky *Acta Metall.*, vol. 11, p. 1190, 1963.

[43] F. Guiu, "Slip asymmetry in molybdenum single crystals deformed in direct shear," *Script. Metall.*, vol. 3, p. 449, 1969.

[44] A. Luft and L. Kaun, "Electron microscopic investigation of the dislocation structure in molybdenum single crystals deformed in tension at 293 and 493°K," *Phys. Stat. Solidi*, vol. 37, p. 781, 1970.

[45] C. V. Kopetskii and A. I. Pashkovskii, "Plastic deformation and dislocation structure of molybdenum single crystals upon extending along ⟨110⟩ and ⟨100⟩ axes in the range from 77 to 573°K," *Phys. Stat. Solidi A*, vol. 21, p. 714, 1974.

[46] G. J. Irwin, F. Guiu, and P. L. Pratt, "The influence of orientation on slip and strain hardening of molybdenum single crystals," *Phys. Stat. Solidi A*, vol. 22, p. 685, 1974.

[47] H.-J. Kaufmann, A. Luft, and D. Schulze, "Deformation mechanism and dislocation structure of high-purity molybdenum single crystals at low temperatures," *Cryst. Res. Technol.*, vol. 19, p. 357, 1984.

[48] L. Hollang, D. Brunner, and A. Seeger, "Work hardening and flow stress of ultrapure molybdenum single crystals," *Mater. Sci. Eng. A*, vol. 319-321, p. 233, 2001.

[49] L. Hollang, M. Hommel, and A. Seeger, "The flow stress of ultra-high-purity molybdenum single crystals," *Phys. Stat. Solidi A*, vol. 160, p. 329, 1997.

[50] A. S. Argon to be published.

[51] R. M. Rose, D. P. Ferris, and J. Wulff, "Yielding and plastic flow in single crystals of tungsten," *Trans. AIME*, vol. 224, p. 981, 1962.

[52] A. S. Argon and S. R. Maloof, "Plastic deformation of tungsten single crystals at low temperatures," *Acta Metall.*, vol. 14, p. 1449, 1966.

[53] P. J. Sherwood, F. Guiu, H. C. Kim, and P. L. Pratt, "Plastic anisotropy of tantalum, niobium and molybdenum," *Can. J. Phys.*, vol. 45, p. 1075, 1967.

[54] D. Hull, J. F. Byron, and F. W. Noble, "Orientation dependence of yeild in body-centered cubic metals," *Can. J. Phys.*, vol. 45, p. 1091, 1967.

[55] D. P. Ferris, R. M. Rose, and J. Wulff, "Deformation of tantalum single crystals," *Trans. AIME*, vol. 224, p. 975, 1962.

[56] J. F. Byron *J. Less-Common Met.*, vol. 14, p. 201, 1968.

[57] A. S. Keh and Y. Nakada, "Plasticity of iron single crystals," *Can. J. Phys.*, vol. 45, p. 1001, 1967.

[58] D. F. Stein, "The effect of orientation and impurities on the mechanical properties of molybdenum single crystals," *Can. J. Phys.*, vol. 45, p. 1063, 1967.

[59] M. S. Duesbery and R. A. Foxall, "A detailed study of the deformation of high purity niobium single crystals," *Phil. Mag.*, vol. 20, p. 719, 1969.

[60] F. Ackerman, H. Mughrabi, and A. Seeger, "Temperature and strain-rate dependence of the flow stress of ultra-pure niobium single crystals in cyclic deformation," *Acta Metall.*, vol. 31, p. 1353, 1983.

[61] W. A. Spitzig and A. S. Keh, "The effect of orientation and temperature on the plastic flow properties of iron single crystals," *Acta Metall.*, vol. 18, p. 611, 1970.

[62] D. Brunner and J. Diehl, "Strain-rate and temperature dependence of the tensile flow stress of high-purity alpha-iron above 250k (regime i) studied by means of stress-relaxation tests," *Phys. Stat. Solidi*, vol. 124, p. 155, 1991.

[63] D. Brunner and J. Diehl, "Temperature and strain-rate dependence of the tensile flow str ess of high-purity alpha-iron below 250k," *Phys. Stat. Solidi*, vol. 124, p. 455, 1991.

[64] C. J. Bolton and G. Taylor, "Anomolous slip in high purity niobium single crystals deformed at 77°K in tension," *Phil. Mag.*, vol. 26, p. 1359, 1972.

[65] A. J. Garratt-Reed and G. Taylor, "Optical and electron microscopy of niobium crystals deformed below room temperature," *Phil. Mag. A*, vol. 39, p. 597, 1979.

[66] M. H. A. Nawaz and B. L. Mordike, "Slip geometry of tantalum and tantalum alloys," *Phys. Stat. Solidi A*, vol. 32, p. 449, 1975.

[67] H. Matsui and H. Kimura, "Anomalous (110) slip in high-purity molybdenum single crystals and its comparison with that in V(a) metals," *Mater. Sci. Eng.*, vol. 24, no. 2, p. 247, 1976.

[68] H. Saka, K. Noda, T. Imura, H. Matsui, and H. Kimura, "Hvem in-situ observation of anomalous (101) slip in molybdenum," *Phil. Mag.*, vol. 34, no. 1, p. 33, 1976.

[69] T. Imura, K. Noda, H. Matsui, H. Saka, and H. Kimura, "Direct measurement of mobility of dislocations in high-purity molybdenum," in *Dislocations in Solids*, p. 287, University of Tokyo Press, 1985.

[70] A. Lawley and H. L. Gaigher, "Observations on prismatic and grown-in dislocations in zone-melted molybdenum," *Phil. Mag.*, vol. 8, p. 1713, 1963.

[71] A. Lawley and H. L. Gaigher, "Deformation structure in zone-melted molybdenum," *Phil. Mag.*, vol. 10, 1964.

[72] H. L. Prekel, A. Lawley, and H. Conrad, "Dislocation velocity measurements in high purity molybdenum," *Acta Metall.*, vol. 16, p. 337, 1968.

[73] E. B. Leiko and E. M. Nadgornyi, "Dislocation dynamics of molybdenum single crystals in the microplasticity region," *Kristallografiya*, vol. 19, p. 584, 1974.

[74] E. Nadgornyi, "Dislocation dynamics and mechanical properties of crystals," *Prog. Mater. Sci.*, vol. 31, p. 1, 1988.

[75] W. Cai, V. V. Bulatov, S. Yip, and A. S. Argon, "Kinetic monte carlo modeling of dislocation motion in bcc metals," *Mater. Sci. Eng. A*, vol. 309, p. 270, 2001.

[76] F. Louchet and B. Viguier, "Ordinary dislocations in γ-TiAl: cups unzipping, jog dragging and stress anomaly," *Phil. Mag. A*, vol. 80, p. 765, 2000.

[77] H. Haas, C. Z. Wang, M. Fahnle, C. Elsasser, and K. M. Ho, "Environment-dependent tight-binding model for molybdenum," *Phys. Rev. B*, vol. 57, p. 1461, 1998.

[78] M. S. Tang, C. Z. Wang, and C. T. C. K. M. Ho, "Environment-dependent tight-binding potential model," *Phys. Rev. B*, vol. 53, p. 979, 1996.

[79] A. H. Cottrell and B. A. Bilby *Phil. Mag.*, vol. 42, p. 573, 1951.

[80] J. B. Cohen, R. Hinton, K. Lay, and S. Sass *Acta Metall.*, vol. 10, p. 894, 1962.

[81] F. C. Frank and J. F. Nicholas *Phil. Mag.*, vol. 44, p. 1213, 1953.

[82] P. B. Hirsch in *5th International Conference on Crystallography*, p. 139, Cambridge University, 1960.

[83] V. Vitek and F. Kroupa, "Generalized splitting of dislocations," *Phil. Mag.*, vol. 19, p. 265, 1969.

[84] C. Z. Wang, J. Chang, J. Li, W. Cai, V. V. Bulatov, and S. Yip, "Tight-binding study of the core structure and peierls stress of screw dislocations in mo,"

[85] C. Woodward and S. I. Rao, "Flexible ab initio boundary conditions: simulating isolated dislocations in bcc mo and ta," *Phys. Rev. Lett.*, vol. 88, p. 216402, 2002.

[86] V. Vitek, R. C. Perrin, and D. K. Bowen, "The core structure of $\frac{1}{2}\langle 111 \rangle$ screw dislocations in b.c.c. crystals," *Phil. Mag.*, vol. 21, p. 1049, 1970.

[87] V. V. Bulatov, D. Richmond, and M. V. Glazov *Acta Mater.*, vol. 47, p. 3507, 1999.

[88] Q. Ren, B. Joos, and M. S. Duesbery, "Test of peierls-nabarro model for dislocations in si," *Phys. Rev. B*, vol. 52, p. 13223, 1995.

[89] W. Xu and J. Moriarty, "Atomistic simulation of ideal shear strength, point defects, and screw dislocations in bcc transition metals: Mo as a prototype," *Phys. Rev. B*, vol. 54, p. 6941, 1996.

[90] W. Xu and J. Moriarty, "Accurate atomistic simulations of the peierls barrier and kink-pair formation energy for $\langle 111 \rangle$ screw dislocations in bcc mo," *Comput. Mater. Sci.*, vol. 9, p. 348, 1998.

[91] L. H. Yang, P. Soderlind, and J. A. Moriarty, "Accurate atomistic simulation of (a/2)⟨111⟩ screw dislocations and other defects in bcc tantalum," *Phil. Mag. A*, vol. 81, p. 1355, 2001.

[92] L. H. Yang, P. Soderlin, and J. A. Moriarty, "Atomistic simulation of pressure-dependent screw dislocation properties in bcc tantalum," *Mater. Sci. Eng. A*, vol. 309, p. 102, 2001.

[93] C. Woodward and S. I. Rao, "Ab-initio simulation of isolated screw dislocations in bcc mo and ta," *Phil. Mag. A*, vol. 81, p. 1305, 2001.

[94] W. Sigle, "High-resolution electron microscopy and molecular dynamics study of the (a/2)[111] screw dislocation in molybdenum," *Phil. Mag. A*, vol. 79, p. 1009, 1999.

[95] J. Li, *Modeling Microstructural Effects on Deformation Resistance and Thermal Conductivity*. PhD thesis, Massachusetts Institute of Technology, August 2000.

[96] G. J. Ackland and R. Thetford, "An improved N-body semi-empirical model for body-centered cubic transition metals," *Phil. Mag. A*, vol. 56, p. 15, 1987.

[97] J. Marian. unpublished.

[98] E. Schmid and W. Boas, eds., *Plasticity of Crystals, with Special Reference to Metals*. F. A. Hughes, London, 1950.

[99] E. Schmid, "Yield point of crystals, critical shear stress law," *PICAM*, p. 342, 1924.

[100] M. S. Duesbery, "On non-glide stresses and their influence on the screw dislocation core in body-centered cubic metals i. the peierls stress," *Proc. R. Soc. Lond.*, vol. A 392, p. 145, 1984.

[101] M. S. Duesbery, "On non-glide stresses and their influence on the screw dislocation core in body-centered cubic metals ii. the core structure," *Proc. R. Soc. Lond.*, vol. A 392, p. 175, 1984.

[102] K. Ito, "Atomistic study of non-schmid effects in the plastic yeilding of bcc metals," *Phil. Mag. A*, vol. 45, p. 1247, 2001.

[103] AtomEye visualization software, authored by Ju Li (previously a Ph.D. student and later a research scientist at M.I.T. and now a faculty member at Ohio State University), can be found at the following URL: http://164.107.79.177/Archive/Graphics/A/.

[104] J. Li, "Atomeye: an efficient atomistic configuration viewer," *Modelling and Simulation in Materials Science and Engineering*, in print,2003.

[105] R. E. Peierls *Proc. Phys. Soc. London*, vol. 52, p. 23, 1940.

[106] F. R. N. Nabarro *Proc. Phys. Soc. London*, vol. 59, p. 526, 1947.

[107] J. W. Christian and V. Vitek, "unknown," *Rep. Prog. Phys.*, vol. 33, p. 307, 1970.

[108] B. Joos, Q. Ren, and M. S. Duesbery, "Peierls-nabarro model of dislocations in silicon with generalized stacking-fault restoring forces," *Phys. Rev. B*, vol. 50, p. 5890, 1994.

[109] B. Joos, Q. Ren, and M. S. Duesbery, "Erratum: Peierls-nabarro model of dislocations in silicon with generalized stacking-fault restoring forces," *Phys. Rev. B*, vol. 53, p. 11882, 1996.

[110] J. N. Wang, "Prediction of the peierls stresses for various crystals," *Phys. Stat. Solidi A*, vol. 206, p. 259, 1996.

[111] V. V. Bulatov and E. Kaxiras, "Semidiscrete variational peierls framework for dislocation core properties," *Phys. Rev. Lett.*, vol. 78, p. 4221, 1997.

[112] G. J. Ackland and M. W. Finnis, "Semi-empirical calculation of solid surface tensions in body-centered cubic transition metals," *Phil. Mag. A*, vol. 54, p. 301, 1986.

[113] M. Parrinello and A. Rahman, "Polymorphic transitions in single crystals: A new molecular dynamics method," *J. Appl. Phys.*, vol. 52, p. 7182, 1981.

[114] S. S. Lau and J. T. Vreeland, "The introduction of dislocations and slip bands in molybdenum single crystals," *Phys. Stat. Solidi A*, vol. 20, p. 337, 1973.

[115] E. B. Leiko, D. V. Lotsko, E. M. Nadgornyi, and V. I. Trefilov, "Temperature dependence of the mobility of dislocations in molybdenum single crystals," *Sov. Phys. Solid State*, vol. 17, p. 1814, 1975.

[116] E. B. Leiko, A. Luft, and E. M. Nadgornyi, "Slip rosettes and dislocation structure formed by microindentation in molybdenum single crystals," *Phys. Stat. Solidi A*, vol. 44, p. 285, 1977.

[117] E. B. Leiko and A. Luft, "A combined study of the dynamical properties of dislocations in molybdenum single crystals by etch pitting and interference contrast techniques," *Phys. Stat. Solidi A*, vol. 67, p. 435, 1981.

[118] H. Matsui and H. Kimura, "A mechanism of the 'unexpected (110) slip' observed in bcc metals deformed at low temperatures," *Script. Metall.*, vol. 7, no. 9, p. 905, 1973.

[119] A. Voter, "Hyperdynamics: Accelerated molecular dynamics of infrequent events," *Phys. Rev. Lett.*, vol. 78, p. 3908, 1997.

[120] A. Voter, "Parallel replica method for dynamics of infrequent events," *Phys. Rev. B*, vol. 57, p. R13985, 1998.

[121] J. Chang, W. Cai, V. V. Bulatov, and S. Yip, "Dislocation motion in bcc metals by molecular dynamics," *Mater. Sci. Eng. A*, in print.

[122] J. Chang, W. Cai, V. V. Bulatov, and S. Yip, "Modeling of edge dislocation mobility in a bcc metal,"

[123] V. Yamakov, D. Wolf, S. R. Phillpot, A. K. Mukherjee, and H. Gleiter, "Dislocation processes in the deformation of nanocrystalline aluminum by molecular-dynamics simulation," *Nature Materials*, vol. 1, p. 45, 2002.

[124] G. J. Ackland, M. W. Finnis, and V. Vitek, "Validity of the second moment tight-binding model," *J. Phys. F Metal Phys.*, vol. 18, 1988.

[125] W. Xu and J. B. Adams, "Fourth moment approximation to tight binding: application to bcc transition metals," *Surface Science*, vol. 301, p. 371, 1994.

[126] A. E. Carlsson, "Angular forces in group-vi transition metals: Application to w(100)," *Phys. Rev. B*, vol. 44, p. 6590, 1991.

[127] J. A. Moriarty, "Angular forces and melting-in bcc transition metals: a case study of molybdenum," *Phys. Rev. B*, vol. 49, p. 12431, 1994.

[128] J. A. Moriarty, "Analytic representation of multi-ion interatomic potentials in transition metals," *Phys. Rev. B*, vol. 42, p. 1609, 1990.

[129] J. A. Moriarty and R. Phillips, "First-principles interatomic potentials for transition-metal surfaces," *Phys. Rev. Lett.*, vol. 66, p. 3036, 1991.

[130] J. A. Moriarty, "Ultrahigh-pressure structural phase transitions in cr, mo, and w," *Phys. Rev. B*, vol. 45, p. 2004, 1992.

[131] D. Klahn, A. K. Mukherjee, and J. E. Dorn, "Strength of metals and alloys," *Proc. Second Intl. Conf., Am. Soc. Metals, Cleveland*, p. 951, 1970.

[132] H. Neuhauser, "Strength of metals and alloys," *Proc. Fifth Intl. Conf.*, 1979.

[133] K. M. Jassby and J. T. Vreeland, "Dislocation mobility in pure copper at 4.2k," *Phys. Rev. B*, vol. 8, p. 3537, 1973.

[134] V. I. Alshits and V. L. Indenbom, "Mechanisms of dislocation drag," in *Dislocation in Solids* (F. R. N. Nabarro, ed.), vol. 7, p. 43, North-Holland, Amsterdam, 1986.

[135] G. T. G. III, *Encyclopedia of Mater. Sci. & Eng., Suppl. Vol. 2, p. 859.* Pergamon Press, Oxford, 1990.

[136] J. W. Christian and S. Mahajan, "Deformation twinning," in *Progress in Materials Science*, vol. 39, pp. 1–57, Elsevier Science Ltd., 1995.

[137] J. W. Christian, *The Theory of Transformations in Metals and Alloys, 2nd ed.* Pergamon Press, Oxford, 1975.

[138] V. Vitek, "Multilayer stacking faults and twins on (211) planes in b.c.c. metals," *Script. Metall.*, vol. 4, p. 725, 1970.

[139] P. B. Price *Proc. Roy. Soc.*, vol. A260, p. 251, 1961.

[140] S. Mahajan and A. F. Bartlett, "Influence of prior mechanical and thermal treatments on shock-induced substructures in molybdenum," *Acta Metall.*, vol. 19, p. 1111, 1971.

[141] G. Xu, A. S. Argon, and M. Ortiz, "Nucleation of dislocation from crack tips under mixed modes of loading: implications for brittle against ductile behavior of crystals," *Phil. Mag. A*, vol. 72, p. 415, 1995.

[142] G. Xu, A. S. Argon, and M. Ortiz, "Critical configurations for dislocation nucleation from crack tips," *Phil. Mag. A*, vol. 75, p. 341, 1997.

[143] W. Cai, *Atomistic and Mesoscale Modeling of Dislocation Mobility.* PhD thesis, Massachusetts Institute of Technology, June 2001.

[144] T. A. Arias and J. D. Joannopoulos, "Ab initio theory of dislocation interactions: From close-range spontaneous annihilation to the long-range continuum limit," *Phys. Rev. Lett.*, vol. 73, p. 680, 1994.

[145] A. H. A. Ngan and M. Wen, "Dislocation kink-pair energetics and pencil glide in body-centered cubic crystals," *Phys. Rev. Lett.*, vol. 8707, p. 075505, 2001.